Author:
Mueller, Jason D

Title:
High-power, visible-wavelength twin-beam correlations from four-wave mixing
for practical applications in absorption spectroscopy and imaging beyond the shot-noise limit

High-power, visible-wavelength twin-beam correlations from four-wave mixing

for practical applications in absorption spectroscopy and imaging beyond the shot-noise limit

JASON DONALD MUELLER

UNIVERSITY OF BRISTOL
Department of Physics

A dissertation submitted to the University of Bristol in accordance with the requirements of the degree of DOCTOR OF PHILOSOPHY in the Faculty of Science.

SEPTEMBER 2019

Word count: forty thousand

ABSTRACT

Optical shot-noise is a limiting factor common to all classical imaging and spectroscopy applications. Using quantum-intensity-correlated light beams generated via processes such as downconversion and four-wave mixing, one may surpass this classical limit and obtain greater measurement precision for a given photon flux. However, previous work in quantum-enhanced parameter estimation has primarily used single-photon intensities and infrared-wavelength sources, sometimes obtaining a precision advantage only in a post-selected regime rather than per exposed photon. These specifications are not practical for many applications that require greater optical power and visible wavelengths. In this thesis, we push quantum metrology technologies towards real-world applications with the development of a non-post-selected correlated-intensity photon source at blue and red wavelengths and picowatts to microwatts average power. The photon source which we develop employs a silica, few-mode fiber to produce twin beams via four-wave mixing, demonstrating a low-cost method of accessing novel visible wavelengths.

We first discuss the theoretical foundations of classical and quantum parameter estimation, developing a full theoretical model of our experiment, which includes realistic experimental effects such as loss, optical and detector noise, and thermal intensity fluctuations. We compare three absorption estimators and show how loss and optical noise may reduce their efficacy. This theory is confirmed with experimental data and characterizations of our source and detector. We also show that the photonic crystal fiber and single-mode fiber which we use to generate correlated beams via four-wave mixing can reliably produce visible-wavelength beams at microwatts of average power due to exponential parametric gain. Using this source, we perform an absorption measurement at the shot-noise limit, and show that sub-Poissonian intensity correlations are necessary, though not sufficient, for sub-shot-noise parameter estimation. The main experimental results of this work are a successful demonstration of twin-beam intensity correlations 3 dB below the coherent-state limit, overcoming challenges of using silica fibers such as optical noise from Raman scattering and precise mode coupling.

For Mom and Dad,

who taught me everything I know.

AUTHOR'S DECLARATION

I, Jason Mueller, declare that the work in this dissertation was carried out in accordance with the requirements of the University's *Regulations and Code of Practice for Research Degree Programmes* and that it has not been submitted for any other academic award. Except where indicated by specific reference in the text, the work is the candidate's own work. Work done in collaboration with, or with the assistance of, others, is indicated as such. Any views expressed in the dissertation are those of the author.

SIGNED _____ DATE _____

PUBLISHED WORKS

Publications

"Sub-Poissonian twin-beam correlations at blue and red wavelengths from four-wave mixing" **Jason D. Mueller**, Alex McMillan, Paul-A. Moreau, Javier Sabines-Chesterking, John Rarity, Peter J. Mosley, and Jonathan Matthews. (Poster) CLEO 2018. San Jose Convention Center, San Jose, CA, USA (May 2018) [1]

"High-Power, Sub-Poissonian Twin-Beam Correlations at Blue and Red Wavelengths from Four-Wave Mixing in Photonic Crystal Fiber" **Jason D. Mueller**, Alex McMillan, John Rarity, Peter J. Mosley, and Jonathan Matthews. (Talk) CLEO 2019. ICM Centre, Munich, Germany (June 2019)

"Effects of Noise and Unbalanced Loss on Twin-Beam Intensity Correlations" **Jason D. Mueller**, Nigam Samantaray, and Jonathan Matthews. **in preparation**

"High-Power, Visible-Wavelength Twin-Beam Correlations from Four-Wave Mixing in Photonic Crystal Fiber" **Jason D. Mueller**, Alex McMillan, John Rarity, Peter J. Mosley, and Jonathan Matthews. **in preparation**

Presentations

"Photon pair source at blue wavelengths: Towards applications of quantum metrology in bioimaging" **Jason D. Mueller**. (Poster) Photonic Tools for Quantitative Imaging in Tissues. University of Dundee, Dundee, UK (August 2016)

"Photon Pair Source at Blue Wavelengths" **Jason D. Mueller**. (Poster) Bristol Postgraduate Conference. University of Bristol, Bristol, UK (May 2017)

"Photon Pair Source at Blue Wavelengths" **Jason D. Mueller**. (Poster) Bristol QECDT Conference. University of Bristol, Bristol, UK (May 2017)

"Sub-Poissonian twin-beam correlations at blue and red wavelengths from four-wave mixing" **Jason D. Mueller**, Alex McMillan, Paul-A. Moreau, Javier Sabines-Chesterking, John Rarity, Peter J. Mosley, and Jonathan Matthews. (Poster) CLEO 2018. San Jose Convention Center, San Jose, CA, USA (May 2018) [1]

"Four-Wave-Mixing Intensity Correlations at Visible Wavelengths" **Jason D. Mueller**. (Invited Talk) NIST Boulder Laboratories, Boulder, CO, USA (May 2018)

"Four-Wave-Mixing Intensity Correlations at Visible Wavelengths" **Jason D. Mueller**. (Talk) Bristol QECDT Conference. University of Bristol, Bristol, UK (June 2018)

"High-Power, Sub-Poissonian Twin-Beam Correlations at Blue and Red Wavelengths from Four-Wave Mixing in Photonic Crystal Fiber" **Jason D. Mueller**, Alex McMillan, John Rarity, Peter J. Mosley, and Jonathan Matthews. (Talk) CLEO 2019. ICM Centre, Munich, Germany (June 2019)

"(Almost) Dr. Mueller or: How I Learned to Stop Worrying and Love Metrology" **Jason D. Mueller**. (Invited Talk) Louisiana State University, Baton Rouge, LA, USA (September 2019)

TABLE OF CONTENTS

LIST OF TABLES

TABLE **Page**

LIST OF FIGURES

FIGURE **Page**

LIST OF ACRONYMS

ADC Analog-to-Digital Converter.

AR Anti-Reflection.

BS Beam Splitter.

CW Continuous-Wave.

DM Dichroic Mirror.

EM ElectroMagnetic.

EMCCD Electron-Multiplying CCD.

FM Flip-Mirror.

FVB Full Vertical Binning.

FWM Four-Wave Mixing.

GBP Gain-Bandwidth Product.

HSS Horizontal Shift Speed.

HWP Half-Wave Plate.

KTP Potassium-Titanyl-Phosphate.

LBO Lithium triBOrate.

LN2 Liquid Nitrogen.

LP Linearly Polarized.

MMF Multi-Mode Fiber.

NA Numerical Aperture.

ND Neutral-Density.

NRF Noise-Reduction Factor.

OA Operational Amplifier.

OD Optical Density.

PBS Polarizing Beam Splitter.

PC PhotoConductive.

PCB Printed Circuit Board.

PCF Photonic Crystal Fiber.

PSD Power Spectral Density.

PV PhotoVoltaic.

SHG Second-Harmonic Generation.

SiPD Silicon Photodiode Detector.

SMF Single-Mode Fiber.

SNL Shot-Noise Limit.

SNR Signal-to-Noise Ratio.

SPDC Spontaneous Parametric DownConversion.

UV UltraViolet.

CHAPTER 1

INTRODUCTION AND OUTLINE

Chapter outline: *In this chapter, we give context and motivation to the work performed in this thesis. We conclude with a brief outline of the remaining chapters.*

Declaration of contribution: *This chapter is primarily a summary of existing literature, and contains limited novel work, aside from the calculations performed in box 1.1.*

Theoretical and experimental efforts in quantum-enhanced parameter estimation (*i.e.* measuring sample absorption or phase beyond the classical Shot-Noise Limit (SNL)) began in the 1980s with the work of researchers such as Jakeman and Rarity [2], and Reynaud, Giacobino, and Fabre [3, 4]. The motivation for developing quantum precision-enhanced sensing techniques was, and continues to be for many, imaging and characterization of light-sensitive biological samples.

Ref. [2] proposes a single-photon experiment wherein a heralded photon from downconversion or radioactive decay form probe and reference beams to perform absorption estimation. This technique is similar to classical protocols wherein the two outputs of a laser shone onto a beam splitter are used to account for classical intensity fluctuations [5]. The primary difference is that classical measurements are limited by the coherent-state statistics of the initial pump beam and can only, at best, obtain Poisson-distributed coherent-state measurement statics, the SNL. In a lossless, quantum-correlated twin-beam case, however, the mutual intensities of the probe and reference beams exhibit binomial statistics, as either a probe photon was absorbed or not when heralded by the detection of a reference photon [2, 6]. Given that for a specified mean photon number, the variance of a binomial distribution is less than that of a Poisson distribution, more information is obtained per exposed photon when using twin beams. Indeed, ref. [6] measured the absorption of a biological sample at 1 dB below the classical SNL using an infrared, correlated single-photon source, detected with 69% efficient avalanche photodiodes.

The principle of single-photon sub-SNL correlations may be extended to higher photon-number regimes. Some of the first demonstrations of milliwatt sub-Poissonian correlated beams were performed in ref. [3, 4], wherein infrared twin beams were generated via a nonlinear crystal (type-II phase-matched Potassium-Titanyl-Phosphate (KTP)) in a cavity that acts as an optical parametric oscillator. The authors ultimately measured a noise power between of correlated beams at 0.7 dB to 1.5 dB below the classical limit over a detection bandwidth of 3 MHz to 13 MHz, using 90% efficient photodiode detectors.

More recently, many experiments have been performed which demonstrate measurement precision at or beyond the SNL using intensity-correlated twin beams [6–16]. The primary motivation for such experiments have been imaging and absorption spectroscopy. Four of these experiments in particular were performed by our current research group at the University of Bristol [6, 10, 13, 16].

The most relevant of these, a precursor to the experimental work described in this thesis, is ref. [10]. In this work, 808 nm wavelength single-photon twin beams generated via continuous-wave-pumped downconversion (also type-II phase-matched periodically poled KTP) were shone onto a 90% efficient CCD camera, and the beams' intensities correlated. The authors measured, using a commercially available, air-cooled CCD camera, strong sub-Poissonian intensity correlations 4.2 dB below the classical limit, and estimated a sample's absorption 2.7 dB beyond the SNL, even when compared to using a unit-efficiency detector.

Two of the primary practical limitations of the aforementioned works, however, have been

the lack of wavelength tuneability and low photon flux. Indeed, due to the wider availability of long-wavelength single-photon sources, all of the referenced experiments thus far have been performed at wavelengths greater than 710 nm and at femtowatts of probe power, with two exceptions. The work of ref. [3, 4] is performed at infrared wavelengths and milliwatts of optical power, although the authors did not perform any imaging or parameter estimation experiments with their correlated source and required a 200 mW pump beam to produce sufficiently bright correlated beams. The second exception is the recent work of ref. [17], which produced x-ray correlated beams, although at the single-photon level, and they only obtained quantum-enhanced measurement statistics in the post-selection regime (*i.e.* not in the per-exposed-photon regime).

To develop enabling quantum technologies, we as researchers must consider the practical applications of our work to their intended fields. In the case of imaging and absorption spectroscopy, it is of particular interest in biology and chemistry to use visible wavelengths and optical powers on the order of microwatts to watts (see box 1.1 for technical specifications). In this regime, however, it is known that light can have several negative effects on biological samples of interest in terms of damaging the sample or altering its functions. For example, thermal gradients may alter diffusive transport within a cell. Photochemical effects may change cellular division rates, enzyme activity, or dissociate molecules to produce reactive oxygen species [18]. Therefore, to improve measurement precision at a given practical photon flux, or to obtain a given precision using less photon flux, may have wide implications to the field of bioimaging. In addition to these scientific considerations, new technologies should strive to be affordable, compact, and technically accessible, especially, as is our case, when introducing these technologies to already well-established fields which may not be familiar with the prospects of quantum-enhanced sensing.

BOX 1.1. Optical damage mechanisms and thresholds for biological samples.

An important benchmark for realizing practical quantum imaging devices is the optical energy at which samples of interest undergo deleterious photochemical changes (*e.g.* photobleaching) or are otherwise damaged. The results of ref. [19, 20] suggest that we may be able to damage cells at currently attainable twin-beam powers (see chapter 3). In ref. [19], the authors consider cell damage in a super-resolution microscopy experiment wherein a high-NA oil-submersion lens focuses various short-wavelength (405 nm to 640 nm) beams to image U2OS cell samples (human osteosarcoma cells) onto a CCD camera (Andor iXon Ultra 897, the same model camera which we use throughout our own experimental efforts; see also chapter 3). They considered both Continuous-Wave (CW) and pulsed laser regimes.

They found that cell exposure to shorter optical wavelengths induced greater rates of slowed cell division and cell death than longer wavelengths. For example, given a CW 240 s exposure at 48 kJ/cm^2, cells did not survive when using 488 nm radiation, but all cells

survived at 514 nm with the same 48 kJ/cm^2 exposure, only 26 nm redshifted, although the mechanism by which this occurs for this small wavelength difference is unclear.

Comparing CW and pulsed laser regimes, more cell death occurred in the pulsed regime, for the same irradiation time. When comparing 24 s irradiation times at 405 nm wavelength, $>95\%$ of cells died using 10 ms pulses at 10 Hz repetition rate. However, only $\sim 15\%$ died in the CW regime.

Although the relatively long pulse-width and slow repetition-rate of their laser compared to our 0.75 ns pulse-width, 7 kHz source (see chapter 5) makes a direct comparison difficult, the authors consistently killed 100% of their cells using 1 kW/cm^2 optical intensity, so we will compare our twin-beam intensity to this. Focusing ~ 10 pW average power to a 128 µm beam waist, the maximum attainable peak power at practical focusing conditions before camera saturation, corresponds to 1.5×10^{-5} kW/cm^2, considerably lower than the cell-damage threshold. At the same focusing conditions, the cell-damage threshold is reached at ~ 0.7 µW average power. These optical power requirements, however, necessitate the development of low-noise, high-power optical detectors, which is ongoing work discussed in chapter 5.

In ref. [20], the authors similarly measured myelin sheath damage in spinal tissue with varying optical power, although in the megahertz regime, relatively faster than our kilohertz laser repetition rate. Imaging using coherent anti-Stokes Raman scattering with 2.5 ps pulses, 15.6 MHz repetition rate, and pump and Stokes wavelengths 704 nm and 880 nm, they induced cell damage at pump and Stokes peak powers of 38 W and 19 W, respectively (~ 750 µW average power). Again, these optical powers are similar to our own attainable peak and average powers – ~ 75 W peak anti-Stokes power, corresponding to 400 µW average power – that we report in chapter 3.

More generally, ref. [21] states that for optical imaging of living biological samples, shorter wavelengths are typically more damaging, and low-power measurements are desirable. The author proposes that living cells begin to be damaged when exposed to more than a 'single sun' of irradiance, the natural environment in which the cells live, ~ 1 nW/µm^2 in central Europe. This is consistent with the results of ref. [19] at 405 nm, which employs optical powers that we previously mentioned are attainable with our twin-beam source.

There are several pathways to cell damage and photobleaching, which depend on the sample of interest and its environment. For example, cellular heating of red blood cells when exposed to a strongly absorptive optical wavelength may denature proteins and cell membrane lipids, affecting the deformability of the red blood cells [22]. For artificially pigmented retinal pigment epithelial cultures, thermal heating from infrared and blue lasers was found to damage cells at several watts per square centimeter. It was also found

that preparing the cultures in anti-oxidant ascorbic acid reduced oxidative stress on the cell structure when exposed to blue light [23]. Finally, photobleaching, a process whereby a fluorophore stops fluorescing after some characteristic lifetime, occurs widely in microscopy applications [24, 25]. Although the mechanism by which photobleaching occurs depends on many factors and is not totally understood, it typically involves the excitation of the fluorophore to some excited singlet state, which nonradiatively relaxes to an excited triplet state outside of the fluorescence cycle.

The aim of the work described in this thesis is to develop a high-power twin-beam source at visible wavelengths for practical applications in bioimaging. We strive to perform a sub-SNL absorption measurement on a biologically relevant sample, demonstrating improved measurement precision at reduced sample damage. We ultimately measure strong evidence of quantum intensity correlations 3 dB below classical coherent-state statistics at visible wavelengths 450 nm and 650 nm, picowatts of average power, generated via four-wave mixing in user-friendly nonlinear fiber sources, and use the twin-beam source to estimate a sample absorption at the SNL. The methods used to obtain these results are the subject of this thesis, which is organized into five primary chapters as follows.

In chapter 2, we introduce the method by which we generate our intensity-correlated beams, as well as the underlying theory of how we quantify their correlations and estimate sample absorption. In chapter 3, we characterize the general experimental features of the photon source and detector. These characterizations are referenced accordingly throughout the remainder of the experimental work presented in this thesis. In chapter 4, experimental progress towards measuring picowatt intensity correlations and SNL absorption estimation is detailed chronologically, systematically demonstrating the effects of various source and detector modifications throughout the course of this PhD. Chapter 5 reviews ongoing work in the development of low-noise silicon photodiode detectors for measuring microwatt and milliwatt intensity correlations. Finally, we conclude this work with a summary in chapter 6, as well as an outlook for future experiments in the field of quantum-enhanced imaging and spectroscopy. Datasheets for key components of the experiments described in this thesis are included following chapter 6, for posterity.

As the nature of this experimental work is collaborative, I have written *declarations of contribution* at the beginning of each chapter to distinguish my own novel work and credit those who helped achieve the goals of this thesis.

CHAPTER 2

CONCEPTUAL AND THEORETICAL BACKGROUND

Chapter outline: *In this chapter, we discuss the theoretical underpinnings of the experiments performed for this thesis. First, we introduce the nonlinear optical process by which we generate intensity-correlated twin beams. Second, we describe how to quantify these correlations, and the effects of noise on such measurements. Finally, we discuss several absorption estimators and how to compare the performance of our experiment to an ideal classical one.*

Declaration of contribution: *This chapter is primarily introductory text, but contains significant novel research contributions. I performed the simulations shown in fig. 2.3 and fig. 2.4 (a). I myself developed the theoretical framework described in sec. 2.2, which predicts measured correlations based on realistic experimental parameters, as well as performed the related simulations. Discussions with postdoctoral colleague Dr. Nigam Samantaray enabled the extension of theoretical work from ref. [14] on absorption estimators, discussed in sec. 2.3, to show their sub-optimal performance when considering uncorrelated noise and unbalanced detection efficiency. I also performed the theoretical work showing the improved accuracy of multi-beam absorption estimators over the direct absorption estimator.*

2.1 Four-Wave Mixing Theory and Simulations

Four-Wave Mixing (FWM) is traditionally avoided in classical communication networks, as it may be a source of interchannel crosstalk in wavelength-division multiplexing systems [26–28]. It has, however, become a staple in quantum technologies and other classical applications. FWM has been used, for example, as a pair-photon source in on- and off-chip quantum technologies [29–31], which has applications in quantum computation, quantum key distribution, and quantum metrology [2, 6, 10, 14, 32]. Experimental efforts throughout this thesis almost exclusively employ in-fiber FWM as a means to generate intensity-correlated beams for quantum metrology applications. In this section we will discuss the basic theory underlying spontaneous and stimulated FWM photon generation in optical fiber, as well as several experimental efforts to push these techniques to shorter visible and UltraViolet (UV) wavelengths. We will also discuss Raman scattering, a source of noise photons in our experiment, commonly observed in optical fiber experiments.

2.1.1 Theoretical Description and Origins of Four-Wave Mixing

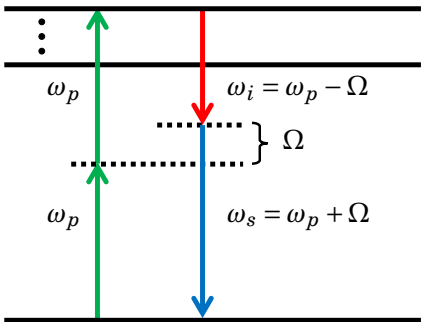

FIGURE 2.1. A schematic showing the general principle of degenerate FWM. Two monochromatic pump photons at optical frequency ω_p annihilate to produce two FWM photons at frequencies ω_s and ω_i, with frequency detuning Ω.

FWM, in the most general case, is the interaction of three ElectroMagnetic (EM) fields to produce a fourth. Consider, for example, three EM fields interacting in a dielectric medium. The first field will produce Rayleigh scattering, as the oscillating polarization within the dielectric will re-radiate with some phase shift. The second field also drives the dielectric's polarization, which interferes with the first field, producing harmonics in the polarization at the sum and difference frequencies. The third field beats with the sum and difference fields, acting as a source field for the fourth wave [33].

In a quantum-mechanical picture, one of these three interacting fields, which produces the fourth, may be vacuum fluctuations. This process is called spontaneous FWM, which becomes stimulated FWM after reaching a threshold intensity, discussed later in this section.

An essential quantum mechanical picture of FWM is shown in fig. 2.1. This process is similar to downconversion, a three-photon technique widely used in quantum optics to generate degenerate photon pairs via energy and momentum conservation [34–36]. In FWM, however, two pump photons, instead of only one, interact with the nonlinear gain medium to produce a signal and idler photon pair. By energy and momentum conservation, FWM photons are always generated in pairs. Therefore, detecting the presence of one photon necessarily heralds the presence of the other,

similar to downconversion [37].

To make this description a bit more rigorous, and to describe the specific pathway by which FWM photons are produced rather than the myriad of other nonlinear interactions supported in optical fibers, we will follow the theoretical work presented in ref. [28, 31, 33, 38]. We begin by considering the induced dipole moment of a single atom,

$$\mathbf{p} = \epsilon_0 \chi_E \mathbf{E}_{\text{loc}}, \tag{2.1}$$

where ϵ_0 is the vacuum permittivity, χ_E is the polarizability of the atom, and $\mathbf{E}_{\text{loc}}$ is the locally applied field. Now considering a material with N atoms, we may rewrite eqn. 2.1 for the polarization of a linear, isotropic, homogeneous dielectric as

$$\mathbf{P} = \epsilon_0 \chi \mathbf{E}, \tag{2.2}$$

where χ is now called the electric susceptibility of the material, $\mathbf{E}$ is the total electric field, and $\chi\mathbf{E} = N\chi_E\mathbf{E}_{\text{loc}}$ [38].

We Taylor series expand eqn. 2.2 in terms of $\mathbf{E}$ to yield an expression for the polarization of the dielectric in the $i \in \{x,y,z\}$ direction in terms of the material's linear response $\mathbf{P}_{\text{L}}$ and its higher-order nonlinear response $\mathbf{P}_{\text{NL}}$ to the applied EM field in the $j,k,l \in \{x,y,z\}$ direction:

$$\begin{aligned} \frac{P_i}{\epsilon_0} &= \sum_j \chi^{(1)}_{ij} E_j + \sum_{jk} \chi^{(2)}_{ijk} E_j E_k + \sum_{jkl} \chi^{(3)}_{ijkl} E_j E_k E_l + \ldots \\ &= \mathbf{P}_{\text{L}} + \mathbf{P}_{\text{NL}}, \end{aligned} \tag{2.3}$$

where, for convergence, $\chi^{(n)} < \chi^{(m)}$ when $n > m$, and assuming no permanent dipole moments present.

Each $\chi^{(n)}$ is a tensor which relates the direction and frequency of the applied EM fields to the direction and strength of the induced polarization. For a silica glass fiber waveguide, because it has inversion symmetry (*i.e.* EM fields have no preferred longitudinal direction of travel in the fiber), we have $\chi^{(2)} = 0$. Thus, the most significant nonlinear contribution is from $\chi^{(3)}$, a fourth-rank tensor with 81 elements, each element having 48 terms. Note that in a silica glass waveguide, one may reduce the number of nonzero elements due to the isotropic nature of the silica fiber [38].

Let us consider the case when all of the coupled EM fields are plane waves polarized in the same $\hat{\mathbf{x}}$ direction:

$$\mathbf{E}_{\text{tot}} = \hat{\mathbf{x}} \frac{1}{2} \sum_{m=1}^{4} \left(E_m \exp\left[i(\beta_m z - \omega_m t) \right] + c.c. \right),$$

where $c.c.$ is the complex conjugate, and $\beta_m = \tilde{n}_m \omega_m$ is a constant which depends on the effective index of refraction $\tilde{n}$ of the fiber at frequency ω_m, discussed in the following section. We may similarly write the polarization of the medium as

$$\mathbf{P}_{\text{NL}} = \hat{\mathbf{x}} \frac{1}{2} \sum_{m=1}^{4} \left(P_m \exp\left[i(\beta_m z - \omega_m t) \right] + c.c. \right). \tag{2.4}$$

Note the strength of the nonlinear susceptibility is less when the fields are not all co-polarized, but here we will only be considering the ideal case of co-polarization for simplicity [28, 33].

Comparing the P_4 amplitude of eqn. 2.4 with eqn. 2.3 yields the following:

$$P_4 = \frac{3}{4}\epsilon_0 \chi^{(3)}_{xxxx}\left[|E_4|^2 E_4 + 2(|E_1|^2 + |E_2|^2 + |E_3|^2)E_4 \right. \\ \left. + 2E_1E_2E_3\exp(i\theta_+) + 2E_1E_2E_3^*\exp(i\theta_-) + ...\right], \tag{2.5}$$

where

$$\theta_+ = \left[\beta(\omega_1) + \beta(\omega_2) + \beta(\omega_3) - \beta(\omega_4)\right]z - (\omega_1 + \omega_2 + \omega_3 - \omega_4)t$$
$$\theta_- = \left[\beta(\omega_1) + \beta(\omega_2) - \beta(\omega_3) - \beta(\omega_4)\right]z - (\omega_1 + \omega_2 - \omega_3 - \omega_4)t$$

are called phase-matching conditions [28, 33].

The first two terms of eqn. 2.5 represent self-phase modulation and cross-phase modulation, respectively. The term associated with θ_+ is called sum-frequency generation, maximized when $\theta_+ = 0$. It represents three photons interacting to produce a fourth at frequency $\omega_4 = \omega_1 + \omega_2 + \omega_3$. In step-index fiber designed to support few modes at ω_4, this phase-matching is difficult to achieve at short wavelengths due to fabrication issues associated with sub-micron core radius r fibers ($r \approx 0.2\,\mu$m for wavelength $\lambda_4 = 450$ nm). This process may occur in multi-mode fibers, but with low efficiency for the same reason as the single-mode fiber case [28].

The θ_- term is FWM, and occurs when two pump photons annihilate to produce a signal and idler pair. If we pump with a monochromatic source such that $\omega_1 = \omega_2 = \omega_p$, from energy conservation we get $\omega_p - \omega_i = \omega_s - \omega_p = \Omega$. Here, Ω is the signal and idler detuning, and $\omega_i < \omega_p < \omega_s$. This represents degenerate FWM, shown in fig. 2.1, because the two pump frequencies coincide. Note that in general, non-degenerate FWM is possible with dual-pump experiments.

We can write the FWM phase-matching condition as

$$\kappa = \Delta\beta + 2\gamma P_p,$$

where $\Delta\beta = \beta(\omega_s) + \beta(\omega_i) - 2\beta(\omega_p)$, γ is the nonlinear coefficient of the fiber at wavelength ω_p, and P_p is the peak pump power (assuming no pump depletion). The γP_p term accounts for self- and cross-phase modulation, as these two effects alter the phase of the interacting fields. We also note here that γ depends on the spatial modes of the interacting fields in the fiber [28, 30, 37], but for our conceptual understanding here we only consider the ideal case wherein all four fields are in the same mode. Supported fiber modes are discussed later in this section.

As with sum-frequency generation, FWM is most efficient when $\kappa = 0$. We can control the phase matching condition of a particular fiber and achieve FWM at various optical frequencies by tailoring our fiber materials and dimensions accordingly, discussed further in sec. 2.1.4 [30, 39].

When not seeded at ω_s or ω_i, FWM occurs spontaneously due to vacuum fluctuations [28]. Spontaneous emission produces single photon pairs, used as non-classical sources for quantum

metrology, information, and communication [29, 37, 40]. These spontaneously emitted photons further stimulate FWM in the nonlinear gain medium, akin to stimulated emission in a laser cavity. By energy and momentum conservation, and in the absence of loss and noise sources, the signal and idler intensities are perfectly correlated, with gain G of fiber with length L given by [28]

$$G = 1 + \left(\frac{\gamma P_p}{g}\right)^2 \sinh^2(gL) \tag{2.6}$$

$$\approx 1 + (\gamma P_p L)^2 + O\left(L^4\right) \tag{2.7}$$

$$\approx \left(\frac{\gamma P_p}{2g}\right)^2 \exp\left(2gL\right), \tag{2.8}$$

and parametric gain $g = \sqrt{(\gamma P_p)^2 - (\kappa/2)^2}$, which depends on the phase-mismatch κ. Taylor-series expanding G around $L = 0$, as in eqn. 2.7, we find that the signal and idler intensities initially increase quadratically. While approximating G for large L, eqn. 2.8, FWM is expected to increase exponentially, allowing access to high-power intensity-correlated beams. This exponential regime, as we will discuss later in sec. 3.1.2, is where our correlated-intensity experiments operate.

We also note here that for narrower FWM spectral linewidths, we expect to reach the threshold for stimulated exponential gain at lower P_p, as more energy is initially confined to a narrower spectral bandwidth [37]. This concept will be important for discussions in sec. 4.12.

To summarize, FWM is a $\chi^{(3)}$ nonlinear process wherein essentially three EM fields interact to produce a fourth. Degenerate FWM is when the output photons are distinct wavelengths, pumped by a bright, monochromatic source. These signal and idler pairs must satisfy energy conservation and the following phase matching conditions:

$$2\omega_p = \omega_s + \omega_i \tag{2.9}$$

$$\beta(\omega_s) + \beta(\omega_i) - 2\beta(\omega_p) + 2\gamma P_p = 0, \tag{2.10}$$

where ω is the optical frequency, $\beta(\omega)$ is the frequency-dependent wave vector, γ is the nonlinear coefficient of the fiber at ω_p, and P_p is the peak pump power. When these conditions are well-satisfied, FWM is initially spontaneous, and the intensity increases quadratically, followed by exponential gain as the spontaneous emission is amplified to stimulated FWM.

2.1.2 Supported Fiber Modes and Effects of Waveguide Dispersion

As mentioned briefly in the previous section, the efficiency of fiber FWM depends on the spatial modes of the pump and FWM photons. In fact, the number of spontaneously emitted photons varies quadratically with the overlap integral of the four beams' transverse spatial modes, and exponentially in the stimulated FWM regime [28, 37]. Not only this, but the fiber dispersion β from the phase-matching condition eqn. 2.10 also depends on the fiber mode in consideration [28, 41]. What are the supported fiber modes, however?

In general, for a lossless, radially-symmetric step-index fiber, optical interference may occur at the core-cladding interface because of the refractive index difference. This affects the transverse intensity profile of the guided optical field down the length of the fiber. There exist, however, transverse intensity profiles which are longitudinally unaffected by the index difference, and these are the supported fiber modes. The procedure for determining these modes is covered extensively in ref. [28, 41–43], and here we will outline this procedure and state the relevant results for the work in this thesis.

To describe the transverse fiber modes for a radially-symmetric step-index fiber of core radius ρ, one begins with the wave equation for the complex electric field $\mathbf{E}(r,\phi,z)$, written in cylindrical coordinates as

$$\frac{\partial^2\mathbf{E}}{\partial r^2}+\frac{1}{r}\frac{\partial\mathbf{E}}{\partial r}+\frac{1}{r^2}\frac{\partial^2\mathbf{E}}{\partial\phi^2}+\frac{\partial^2\mathbf{E}}{\partial z^2}+\beta_{\nu m}\mathbf{E}=0, \tag{2.11}$$

where $\beta_{\nu m}=k\tilde{n}$ is the modal dispersion according to the effective refractive index $\tilde{n}$, which accounts for material and waveguiding effects, and $k=\omega/c=2\pi/\lambda$ is the wavenumber for the free-space optical wavelength λ. Eqn. 2.11 has solutions when $kn_{\mathrm{cl}}<\beta_{\nu m}\leq kn_{\mathrm{co}}$, where $n_{\mathrm{cl}}<n_{\mathrm{co}}$ are the cladding and core material refractive indices, respectively. When $\beta_{\nu m}\approx kn_{\mathrm{cl}}$, the transverse mode propagates well in the fiber cladding. Similarly, when $\beta_{\nu m}\approx kn_{\mathrm{co}}$, the transverse mode propagates well in the fiber core, with exponentially decreasing intensity in the cladding, which is the condition we wish to satisfy [28, 43].

The general solution to eqn. 2.11 may be written as [41]

$$\left(\frac{J_\nu'(U)}{UJ_\nu(U)}+\frac{K_\nu'(W)}{WK_\nu(W)}\right)\left(\frac{J_\nu'(U)}{UJ_\nu(U)}+\frac{n_{\mathrm{cl}}^2K_\nu'(W)}{n_{\mathrm{co}}^2(\omega)WK_\nu(W)}\right)=\left(\frac{\nu\beta_{\nu m}}{kn_{\mathrm{co}}}\right)^2\left(\frac{\sqrt{U^2+W^2}}{UW}\right)^4, \tag{2.12}$$

where J_ν and K_ν are the Bessel function of the first kind and the modified Bessel function of the second kind of order ν, respectively, and the primes denote their derivatives. U and W are given by

$$U=\rho\sqrt{\omega^2n_{\mathrm{co}}^2-\beta_{\nu m}^2}$$
$$W=\rho\sqrt{\beta_{\nu m}^2-\omega^2n_{\mathrm{cl}}^2}.$$

One can approximate eqn. 2.11 without the z-component, as the transverse polarizations of the fiber dominate. In this approximation, solutions to this equation are called Linearly Polarized (LP) modes. LP modes are denoted $\mathrm{LP}_{\nu m}$, where ν and m are positive integers referring to the azimuthal and radial indices. Fundamental modes are those for which $\nu=0$, whereas higher-order modes satisfy $\nu>0$. Examples of fundamental and first-order modes are shown in fig. 2.2. We see, in particular, that the LP_{01} mode is approximately Gaussian, and indeed is Gaussian in the limit of $n_{\mathrm{co}}\to n_{\mathrm{cl}}$ [43].

Now we will discuss how these modes affect the FWM phase-matching condition eqn. 2.10. First, the material refractive index for fused silica is calculated according to the empirical Sellmeier equation. Solving the eigenvalue eqn. 2.12, one can infer $\tilde{n}$ from $\beta_{\nu m}$ for a given fiber

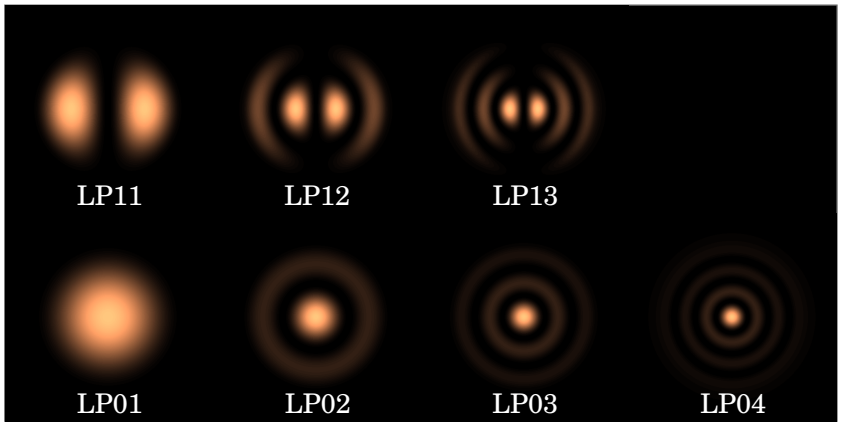

FIGURE 2.2. A chart showing simulated intensity profiles of fundamental and first-order LP modes of a silica fiber.

mode, which encapsulates both material and waveguiding effects. Comparing n_{co} and $\tilde{n}$ for a given mode, as in fig. 2.3, the modal and material dispersion may deviate significantly for longer wavelengths. Correct modeling of the effects of modal dispersion for a particular fiber cross-section is, therefore, critical to precisely simulating the fibers phase-matching conditions.

Finally, if the index contrast of the core and cladding materials is large, then there may be many supported fiber modes, as $\beta_{\nu m}$ may take multiple values. The number of modes which a step-index fiber supports is quantified by its V parameter:

$$V = k\rho\sqrt{n_{\text{co}}^2 - n_{\text{cl}}^2}. \tag{2.13}$$

This parameter is not only dependent on the refractive indecies of the core and cladding, but also the wavelength and fiber radius. Larger values of V indicate that the fiber supports more modes, and a fiber is said to be single-mode at a particular wavelength when $V < 2.405$. For example, a step-index silica fiber in air is single-mode at telecommunications wavelength 1550 nm when the core diameter is smaller than $\sim 1.2\,\mu$m. We can increase the number of supported modes by, for example, using a larger-diameter fiber or shorter wavelengths.

2.1.3 Optical Noise Processes in Fiber

Aside from FWM, there are many other processes which can occur in optical fibers [28, 33, 38]. We have already briefly mentioned self- and cross-phase modulation, but more relevant to our efforts at measuring intensity-correlated beams are processes which generate uncorrelated noise photons that overlap in wavelength with our FWM signal, namely Raman scattering. Raman scattering is an active process stimulated by the molecular vibrations of the fiber material, wherein pump photons are typically converted to lower-energy photons. Due to the amorphous, noncrystalline nature of silica glass, we expect scattering over a large frequency bandwidth [28], supported by our own experimental observations, discussed in sec. 3.1.1.

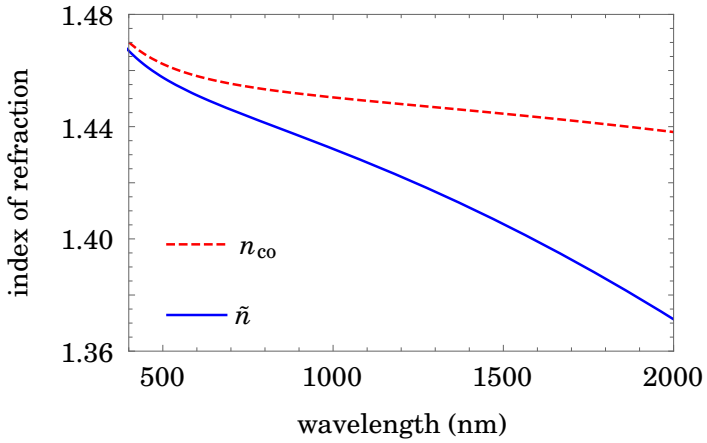

FIGURE 2.3. A simulation we performed comparing material refractive indices with and without accounting for waveguide dispersion, $\tilde{n}$ and n_{co}, respectively.

To avoid confusion, we briefly note here the distinction between Raman scattering and fluorescence. Fluorescence is a resonant process, wherein an absorbed pump photon excites a stable electronic transition in a molecule, and the molecule re-emits a photon after some fluorescence lifetime. During this lifetime, the molecule may exchange energy with its environment, shifting the frequency of the re-emitted photon, typically to lower energies. By contrast, Raman scattering is not a resonant process, in that when a photon interacts with a molecule, an electron is promoted to an unstable virtual state. Rather than pump photons being absorbed by molecules, they scatter via inelastic collisions with them, with elastic collisions representing Rayleigh scattering.

Raman photons in our source, which are uncorrelated with the signal photons, overlap in wavelength with our idler beam. Super-Poissonian noise can increase the FWM and Raman gain intensity noise [44, 45]. As well, the Stokes (long-wavelength) component of FWM can be amplified by Raman, leading to asymmetric FWM sidebands [28]. Therefore, we would like to explore the temperature dependence and intensity scaling of our Raman scattering in optical fiber as a means to increasing our signal-to-noise ratio, which would improve our measured FWM intensity correlations.

Because Raman scattering is light modulated by molecular vibrations, we expect it to be a temperature T dependent process, as increased molecular vibrations in our silica fiber increase the amplitude and bandwidth of our Raman gain, and *vice versa*. In the language of quantum mechanics, when a pump photon scatters from a molecule, it creates an optical Raman photon at frequency shift $\Delta\nu$ from the pump, as well as a phonon, due to conservation of energy. Thus our Raman emission rate I_R depends on the phonon population factor $n(\Delta\nu, T)$, or vibrational density of states, and Raman gain spectrum $g_R(\Delta\nu)$ as [45]

$$I_R(\Delta\nu, T) \sim I_0(\Delta\nu) g_R(\Delta\nu)[1 + n(\Delta\nu, T)], \tag{2.14}$$

where I_0 is the 0 K emission rate, and

$$n(\Delta\nu, T) = \frac{1}{\exp(h\Delta\nu/kT) - 1}. \tag{2.15}$$

The functional form of $n(\Delta\nu, T)$ implies that for frequencies near the pump, we expect a greater reduction in Raman-scattered photons than for disparate frequencies. We experimentally explore this result further in sec. 4.12.

The Raman gain spectrum depends on a number of factors: fiber material, dopants, pump and Stokes polarization, and optical frequency. Similarly to FWM, Raman scattering may also be stimulated, though actively by the fiber material, rather than parametrically as is the case with FWM. Importantly for us, $g_R(\Delta\nu)$ scales inversely with λ_p [28]. This means that although Raman intensity scales exponentially with pump power (and fiber length), in the case where our idler wavelength is far from the pump, where the phonon population is low, we are unlikely to reach the exponential threshold power in our experiments. Compared to the quadratic increase in FWM intensity for weak pumping, Raman power scales approximately linearly with low pump powers because it is a single-photon scattering event. This discussion is experimentally validated in sec. 3.2.1.

2.1.4 Simulations of Four-Wave Mixing Phase-Matching in Optical Fibers

To simulate FWM in fiber, satisfying the phase-matching conditions from sec. 2.1.1, several common approaches are taken depending on the physical structure of the nonlinear fiber and its supported modes [28, 30, 39, 41, 46].

The most straightforward approach is to consider a step-index fiber – a strand of silica, clad in air. In this case, each β from eqn. 2.10 is calculated according to the procedure outlined in sec. 2.1.2. The results of such a simulation, where pump, signal, and idler beams are in the same spatial mode, are shown in fig. 2.4 (a).

In the normal-dispersion regime, where $\beta(\omega) < 0$ and $\gamma P_p > 0$, we can achieve phase-matching and produce FWM sidebands. Sideband production is restricted by the supported modes of the fiber at a particular wavelength. In the step-index case, this is eqn. 2.13. In the anomalous-dispersion regime, where $\beta(\omega) > 0$, we cannot achieve phase-matching, as seen in fig. 2.4 (a) where the signal and idler pair become degenerate. Therefore, even from a relatively simple simulation, we see the importance of tuning the fiber dispersion, as well selecting the proper pump mode and wavelength.

More precise simulations of fiber dispersion are available. One such method, used commonly for micro-structured PCF, employs finite-element analysis over the fiber cross-section to calculate the modal dispersion at each FWM wavelength, shown in fig. 2.4 (b) [30, 39, 46]. Factors which affect β in these simulations, not accounted for in our silica-strand-in-air simulations, are the size and pitch (spacing) of the air holes of the PCF cross-section. These advanced techniques also allow for simulating intermodal pumping (pumping with two distinct spatial modes) and intermodal

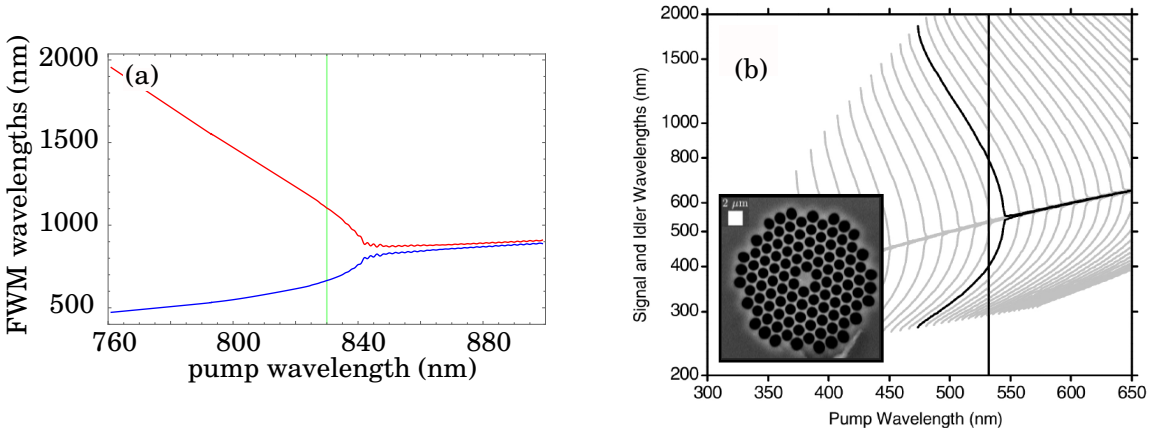

FIGURE 2.4. (a) We performed a numerical phase-matching simulation of a step-index fiber. The green vertical line indicates a particular pump wavelength which corresponds to a signal and idler pair, shown in blue and red, satisfying eqn. 2.9 and eqn. 2.10. Unsmoothed data is result of wavelength step size in numerical simulation. (b, outset) Phase-matching curves at 5% core-diameter increments, reproduced from ref. [39], with pump, signal, and idler in the LP_{02} mode. (b, inset) Scanning electron microscope image of a PCF cross-section, reproduced from ref. [30].

phase-matching (signal and idler in two distinct spatial modes). Note that when the hole size is approximately equal to the pitch, simulations of micro-structured fibers are well-approximated by step-index simulations [30, 39]. This technique is used to fabricate fibers with small effective core sizes for visible-wavelength FWM, as we will see in the next section.

2.1.5 Previous Experimental Work on Visible-Wavelength Four-Wave Mixing

The PCF which we use throughout the experimental efforts discussed in this thesis were fabricated at the University of Bath as part their efforts to push FWM into the UV using PCF [39]. We also use Single-Mode Fiber (SMF)28 to generate visible-wavelength FWM, as described in ref. [47, 48]. In this section, will give a brief review of the experiments reported in ref. [39, 47, 48], as these fibers form an integral part of our own correlated-intensity source.

The novelty of the experiments performed in ref. [39] is the use of a higher-order pump mode to stimulate FWM, and they ultimately measured signal wavelengths down to 393 nm. Because signal wavelengths cannot be less than half of the pump wavelength, according to degenerate FWM phase-matching conditions (eqn. 2.9), one must pump at visible wavelengths to produce blue and UV FWM. In the fundamental LP_{01} mode, this is challenging because of the PCF core and hole diameters required to shift the zero-dispersion wavelength to *e.g.* 532 nm. The small ($\sim 1\,\mu$m) core and large holes are not only difficult to reliably fabricate, but also make the fiber more susceptible to optical damage and loss.

If we consider instead pumping in the LP_{02} mode, with the FWM in this same mode, then the core diameter can be increased to ~ 2.5 µm for a 532 nm pump. This scheme also has the advantage of shallower phase-matching curves, which not only relaxes experimental requirements on the pump laser, but also maintains narrow-band signal and idler wavelengths.

Chen *et al.* [39] drew several lengths of fiber from the same preform, with varying core diameters around ~ 2.5 µm. These few-mode fibers were pumped with an attenuated Teem Photonics NG-10320 laser (0.6 ns pulses at 532 nm wavelength and 7 kHz repetition rate). They employed an in-fiber broadband LP_{02} mode converter to ensure appropriate phase-matching. With 2 m of PCF, they measured UV signal beams at tens of microwatts, with the idler at infrared. They also measured significant Raman scattering at wavelengths near the pump and idler, as well as less-intense anti-Stokes (short wavelength) scattering near the pump.

These higher-order-pump-mode PCF techniques may be used to control fiber dispersion for generating FWM at other novel wavelengths as well. This allows correlated-intensity sources at application-specific measurement wavelengths. In fact, this represents a practical advantage over traditional downconversion sources. While, for example, downconversion crystals may be temperature tuned to adjust the output wavelengths over tens of nanometers [6], they ultimately require a pump wavelength approximately half of the desired twin-beam wavelengths. With fiber FWM sources, one can change the relatively inexpensive fiber rather than the pump laser to access different wavelengths of interest.

More recently, FWM has been observed in commercially available SMF28 when pumped at 532 nm [47, 48]. SMF28e+, the specific type of graded-index SMF used in these experiments, is commonly used in telecommunications applications at 1550 nm, and is multi-mode at visible wavelengths [49].

The pump laser is a bulk-frequency-doubled 1064 nm microchip laser operating at 500 Hz with 680 ps pulses. Pumping monochromatically in the LP_{01} fundamental mode, they observe two sets of FWM peaks: (A) 656 nm and 447 nm in LP_{02} and LP_{01}, respectively; and (B) 650 nm and 449 nm, both in LP_{11}. From discussions in sec. 2.1.2, we expect process (A) to be more efficient, as the pump-FWM spatial mode overlap is greater. This is consistent with the results of ref. [47, 48].

Phase-matching curves for SMF28, modeled as a step-index fiber, are shown in fig. 2.5. Also shown is the stimulated Raman scattering peak wavelength, near the pump wavelength. With the wide FWM separation, much of the optical Raman noise is avoided, though as we will see in sec. 3.2.3, still impacts correlated-intensity measurements. In ref. [47], they achieve 80 µW average FWM power at 2.5 mW average pump power with 25 cm of fiber, necessarily operating in the stimulated FWM regime, attributed to the high peak-power of the pump beam. Note that the authors experienced loss due to fiber bending. As well, they experienced reduced FWM mode coupling because of polarization mixing, also associated with the fiber bending. In experiments performed for this thesis, we also observe these effects, as well as coupling sensitivity, discussed in sec. 3.1.3.

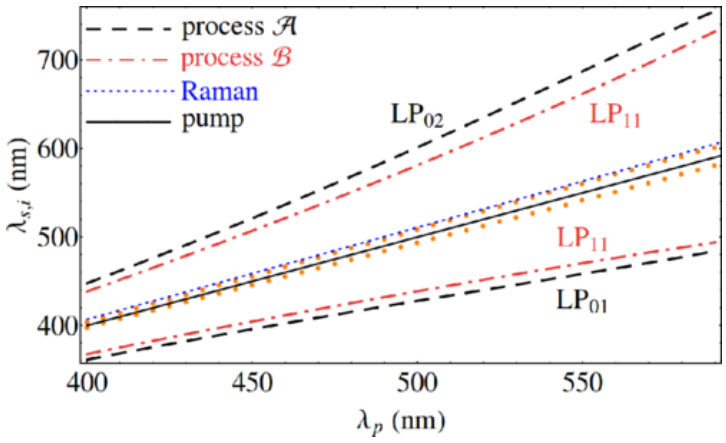

FIGURE 2.5. Phase-matching curves for SMF28, showing the two prominently observed FWM conditions, process $\mathcal{A}$ and process $\mathcal{B}$, reproduced from ref. [48], using degenerate pump spatial modes. The orange dots near the pump wavelength represent FWM from a non-degenerate spatial-mode pump propagating in LP_{01} and LP_{02}. Shown also is the stimulated Raman scattering peak wavelength.

Now that we have an understanding of the principles of FWM, how fiber sources are fabricated to satisfy phase-matching conditions at short wavelengths, and some of the deleterious effects we expect to see in our PCF source, we can discuss in-depth how to characterize the intensity correlations of the signal and idler FWM beams.

2.2 Noise-Reduction Factor Theory and Simulations

In this section, we discuss in detail the metric by which we quantify the mutual multi-beam intensity correlations, called the Noise-Reduction Factor (NRF). We will derive a theoretical model of our correlated-intensity experiment, which predicts NRFs and includes detrimental effects of photon loss, uncorrelated optical noise, and uncorrelated detector noise. This is the most complete model we have of our experiment, and it exhibits many features which have been observed experimentally, discussed further in sec. 3.2.3. Although we have derived this model specifically for research performed in this thesis, it is applicable to many similar such experiments which aim to perform classical or quantum intensity-correlated parameter estimation [2, 6, 10, 11, 13, 14].

Initially used to study the ionization from charged particles [50], the Fano factor has become an important metric in quantum optics for characterizing individual beam statistics [11, 14, 51, 52]. Before formally introducing the NRF for quantifying inter-beam correlations, we first consider how one may quantify the intensity statistics of a singular beam using its Fano factor. The Fano factor F_i for random variable N_i is defined as

$$F_i = \frac{\mathrm{Var}\left[N_i\right]}{\mathrm{E}\left[N_i\right]}, \tag{2.16}$$

where $\mathrm{Var}[N_i]$ is the variance and $\mathrm{E}[N_i]$ is the expected value. The random variable N_i, throughout this chapter's discussions, is the intensity distribution of beam i. For a beam which exhibits ideal Poissonian statistics, such as from a coherent state, where $\mathrm{Var}[N_i] = \mathrm{E}[N_i]$, we find $F_i = 1$. Super-Poissonian statistics, such as thermal states, are characterized by $F_i > 1$. Beams exhibiting $F_i \in [0,1)$ are called squeezed states, and may be generated via nonlinear processes such as down-conversion or second-harmonic generation, wherein the amplitude-uncertainty of a measurement is decreased, at the expense of increased phase-uncertainty [53]. We note that while one can achieve sub-Poissonian beam statistics using nonlinear optics, we will only be considering the case $F_i \geq 1$, which represents our experiment.

Thus, we similarly quantify our degree of correlation between beams N_1 and N_2 using

$$\sigma = \frac{\mathrm{Var}[N_1 - N_2]}{\mathrm{E}[N_1 + N_2]}, \tag{2.17}$$

where σ is the NRF. As before, $\sigma \in [0,1)$ represents sub-Poissonian inter-beam intensity correlations. In this regime, further discussed in sec. 2.3, one can perform parameter estimation better than the classical precision limit of Poisson statistics, called the Shot-Noise Limit (SNL), which corresponds to $\sigma = 1$.

We verify this classical NRF limit by expanding the numerator of eqn. 2.17 as

$$\mathrm{Var}[N_1 - N_2] = \mathrm{Var}[N_1] + \mathrm{Var}[N_2] - 2\mathrm{Cov}[N_1, N_2],$$

where $\mathrm{Cov}[N_1, N_2]$ is the covariance of N_1 and N_2. We consider now the ideal classical case of unit detection efficiency and Poisson-distributed N_1 and N_2. The two beams are also mutually uncorrelated in intensity. One could realize this scenario by shining a coherent state on a lossless beam-splitter, and comparing the outputs. For beams which are uncorrelated, $\mathrm{Cov}[N_1, N_2] = 0$, and $\sigma = 1$. Therefore, $\sigma \in [0,1)$ necessarily corresponds to quantum-correlated beams, and this is the metric by which we will gauge the performance of our experiment.

We will now derive a model of our experiment, adding layers of complexity, to develop an intuition for the experiment and which parameters most influence measured NRFs.

Our starting point is the NRF eqn. 2.17. As previously discussed, we may expand the numerator, and rewrite the denominator using $\mathrm{E}[N_1 + N_2] = \mathrm{E}[N_1] + \mathrm{E}[N_2]$, as

$$\sigma = \frac{\mathrm{Var}[N_1] + \mathrm{Var}[N_2] - 2\mathrm{Cov}[N_1, N_2]}{\mathrm{E}[N_1] + \mathrm{E}[N_2]}. \tag{2.18}$$

In the case of Poisson-distributed, twin-beam N_1 and N_2, we have the following relations:

$$\mathrm{Var}[N_i] = \mathrm{E}[N_i] = \eta_i \mathrm{E}[N] = \eta_i \mathrm{Var}[N], \tag{2.19}$$

where $\eta_i \in [0,1]$ is the channel detection efficiency, and N is the number of correlated photon pairs generated before loss. We also have

$$\mathrm{Cov}[N_1, N_2] = \eta_1 \eta_2 \mathrm{Var}[N]. \tag{2.20}$$

While eqn. 2.20 is derived for a two-mode squeezed state in ref. [54] using quantum operator notation, and in earlier work regarding correlated photon statistics [55–57], we offer an alternative proof in box 2.1, which considers the statistics of a bivariate Poisson distribution.

Substituting eqn. 2.19 and eqn. 2.20 into eqn. 2.18, we find

$$\sigma_p = 1 - \frac{2\eta_1\eta_2}{\eta_1 + \eta_2}, \tag{2.21}$$

where σ_p represents the Poisson-statistics contribution to the measured NRF. There are a few conceptual features of eqn. 2.21 to note. Firstly, in the absence of a correlated twin beam ($\eta_2 = 0$), the best one can achieve is $\sigma = 1$, which does not allow parameter estimation beyond the coherent-state classical limit. In other words, when there are no noise sources, one always expects to outperform a classical experiment with the introduction of a twin beam. Secondly, one always achieves better NRFs by improving detection efficiency, which may seem obvious, but which is not the case for super-Poissonian N, as will be discussed shortly.

BOX 2.1. Alternative derivation of $\mathrm{Cov}[N_1, N_2] = \eta_1\eta_2\mathrm{Var}[N]$.

In eqn. 2.20, we state that $\mathrm{Cov}[N_1, N_2] = \eta_1\eta_2\mathrm{Var}[N]$ for correlated, Poisson-distributed N_1 and N_2. While this statement has been proven in ref. [54] for two-mode squeezed states, it also has been erroneously derived by asserting $N_i = \eta_i N$, as in ref. [10], where they use the relation $\mathrm{Cov}[N_1, N_2] = \mathrm{Cov}[\eta_1 N, \eta_2 N]$. This assertion is false for Poissonian N_i, as η_i relates expected values of random variables, and not random variables themselves. Indeed, $N_i = \eta_i N$ implies that $F_i = \eta_i$, where N_i is only Poissonian for $\eta_i = 1$. Here, we offer an alternative proof that $\mathrm{Cov}[N_1, N_2] = \eta_1\eta_2\mathrm{Var}[N]$, which does not rely on this incorrect relation.

Consider Poisson-distributions N, N_1, and N_2, which may be characterized as

$$\mathrm{E}[N_1] = \eta_1\mathrm{E}[N] = \lambda_{10} + \lambda_{11}$$
$$\mathrm{E}[N_2] = \eta_2\mathrm{E}[N] = \lambda_{01} + \lambda_{11},$$

where $\lambda_{\{10,01,11\}} \geq 0$ are rate parameters, and $0 \leq \eta_{\{1,2\}} \leq 1$. It is shown in ref. [58], that the covariance of such distributions is $\mathrm{Cov}[N_1, N_2] = \lambda_{11}$. Using the ansatz $\lambda_{11} = \eta_1\eta_2\mathrm{E}[N]$, we may rewrite the previous equations as

$$\mathrm{E}[N_1] = \mathrm{E}[N_1](1 - \eta_2) + \eta_1\eta_2\mathrm{E}[N]$$
$$\mathrm{E}[N_2] = \mathrm{E}[N_2](1 - \eta_1) + \eta_1\eta_2\mathrm{E}[N],$$

which satisfies the requirement of $\lambda_{\{10,01,11\}} \geq 0$. Indeed, this is the only solution which satisfies this requirement, as any $\varepsilon > 0$ perturbation of $\lambda_{11} \to \lambda_{11} + \varepsilon$ would imply $\lambda_{\{10,01\}} \to \lambda_{\{10,01\}} - \varepsilon$, which may take negative values for $\eta_{\{1,2\}} = 0$.

The scaling of σ_p with relative detection efficiency is shown in fig. 2.6 (a). Also shown is simulated data for $\eta_1 = 0.7$, which agrees well with our model. Specifics of this simulation and other simulations within this section are discussed in box 2.2.

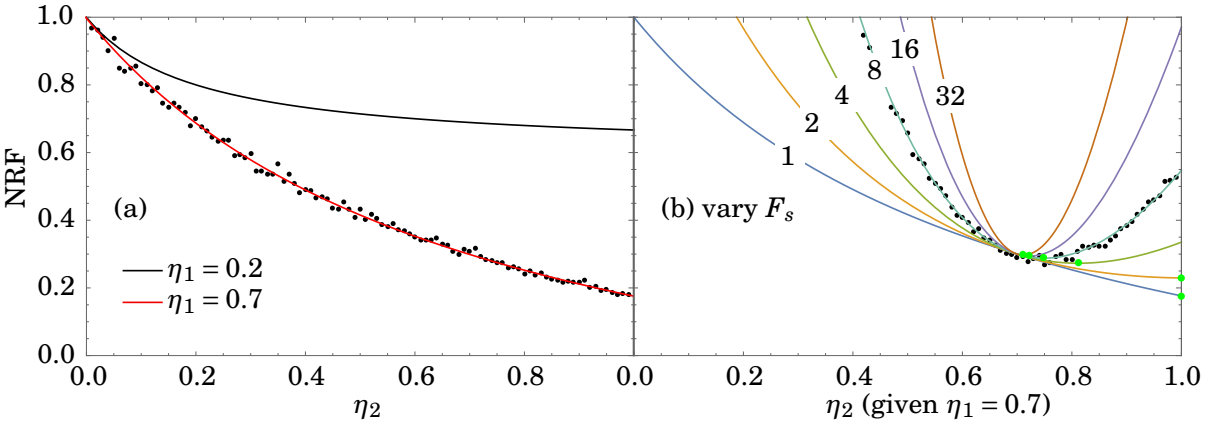

FIGURE 2.6. (a) A plot showing how the NRF scales with (a) channel efficiency for Poissonian twin beams, and (b) varying the twin beam Fano factors F_s. Green markers indicate the minimum NRF for each value of F_s. Example simulation data is shown in each subfigure, with fits.

We can generalize our twin-beam model now, as is done in ref. [10], to describe the scaling of the NRF for super-Poissonian N. The statistics of such beams may be written as [55–57]

$$\mathrm{Var}[N] = \mathrm{E}[N] + \beta \mathrm{E}[N]^2 \tag{2.22}$$

$$\mathrm{Var}[N_i] = \mathrm{E}[N_i] + \beta \mathrm{E}[N_i]^2, \tag{2.23}$$

where $\beta \geq 0$ is a parameter which accounts for super-Poissonian intensity fluctuations of the twin beams, and $i \in \{1,2\}$. Note that β is a fundamental parameter associated with the lossless beams' statistics, and is therefore unchanging from eqn. 2.22 to eqn. 2.23. From eqn. 2.22, we find $\beta \mathrm{E}[N] = F_s - 1$, where F_s is the Fano factor of N, allowing us to simplify eqn. 2.23 to

$$\mathrm{Var}[N_i] = \eta_i \mathrm{E}[N] + \eta_i^2 (F_s - 1)\mathrm{E}[N]. \tag{2.24}$$

Similarly to eqn. 2.20, we also have $\mathrm{Cov}[N_1, N_2] = \eta_1 \eta_2 (\mathrm{E}[N] + \beta \mathrm{E}[N]^2)$ [56].

Finally, for super-Poissonian, correlated beams N_1 and N_2, substituting eqn. 2.24 into eqn. 2.18 yields

$$\sigma = 1 - \frac{2\eta_1\eta_2}{\eta_1 + \eta_2} + \frac{(\eta_1 - \eta_2)^2 (F_s - 1)}{\eta_1 + \eta_2}$$

$$\sigma = \sigma_p + \sigma_{sp},$$

where σ_{sp} is the NRF contribution associated with the super-Poissonian fluctuations of N. Qualitatively, σ_{sp} is quite different from σ_p. First, we see that σ_{sp} has a minimum at $\eta_1 = \eta_2$. Considering this, the minimum NRF is achieved when

$$\eta_2 = \eta_1 \left(\frac{\sqrt{2(F_s-1)(2F_s-1)}}{F_s-1} - 1 \right) \quad \text{for} \quad F_s \geq \frac{\eta_1^2 - 2\eta_1 - 1}{3\eta_1^2 - 2\eta_1 - 1}; \tag{2.25}$$

otherwise, σ can always be improved by increasing detection efficiency. We also see a dependence on F_s in σ_{sp}, indicating that larger classical fluctuations will make sub-Poissonian correlations more difficult to measure. Indeed, if detection efficiency is not balanced according to eqn. 2.25, in the limit of large F_s, it may be impossible to measure $\sigma < 1$, even if N_1 and N_2 are initially well-correlated.

BOX 2.2. Details of NRF simulations for experimental model.

In this section, we derive a theoretical model of our experiment and compare it to simulated intensity-correlated twin beams, including detrimental effects such as loss, super-Poissonian beam statistics, and uncorrelated optical and detector noise. The simulations shown in fig. 2.6 and fig. 2.7 were performed in Mathematica [59], according to the procedure outlined in this box.

We first define the distributions N, N_ϱ, and N_d from which the signal counts and optical and detector noise counts are sampled. Because Poisson distributions are well-approximated by normal distributions for large mean values, we sample from normal distributions with means of order hundreds. Writing the distributions in this way allows one to also account for super-Poissonian statistics by increasing the variance of the normal distribution greater than the mean, changing F_s, F_ϱ, and F_d.

We also define the number of samples s for the data to be averaged over, as well as channel detection efficiencies η_i. For each count source, an integer list of length s is generated, with each element sampled from the corresponding distribution. This represents the number of photons or detector dark counts before loss, for each measurement trial.

A loop is performed over η_2 from zero to one, in specified increments. Within this loop, a loop over s is performed, where for each sample and each count source, a list of pseudo-random numbers between zero and one, inclusive, is generated according to the the specified element from the previous step. These pseudo-random numbers are compared to the corresponding defined channel efficiency, and replaced with a one if the pseudo-random number is less than η_i, zero otherwise. The list is then summed and stored as the number of detected counts for that trial. In this way, we can simulate the random loss associated with the photon-count sources. Note that for the detector dark counts, because they are independent of detection efficiency, no comparison is made to η_i.

Finally, the NRF is calculated for the specified η_2, and η_2 is incremented.

This result may be counter-intuitive, as one might expect that improving detection efficiency is always beneficial to measuring better correlations. The rationale for this result is that the excess photons detected on the more efficient channel do not, on average, have detected correlated photons in the less efficient channel. These excess photons, exhibiting super-Poissonian intensity fluctuations, appear as uncorrelated noise on our measurement. In fig. 2.6 (b), our simulations agree well with this intuition and the theoretical results.

To illustrate this concept further, we include the following example. Consider measurement trials a, b, and c, where twin-beams are generated with intensities $N_a = 1000$, $N_b = 100$, and $N_c = 10$. Also, assume detection efficiency is unbalanced such that $\eta_1 = 1.0$ and $\eta_2 = 0.5$. Despite the beams initially being perfectly correlated, because of the unbalanced detection, we measure $N_1 - N_2 = 500$, 50 and 5 for trials a, b, and c, respectively. One can see that although an equal number of photons was initially produced in each of the twin-beam channels, the unequal detection efficiencies exaggerate the super-Poissonian intensity fluctuations of the source. Indeed, this example corresponds to a NRF of 270.

Now, we include uncorrelated noise photons N_ϱ on one of the channels, in addition to the signal:

$$N_2' \rightarrow N_2 + N_\varrho.$$

In our experiment, these noise photons will be due to Raman scattering, but could more generally be any photon-noise source. In this derivation, we will not include noise on N_1, but the following procedure could be straightforwardly adapted to accommodate such noise. We begin by expanding eqn. 2.17 in terms of N_1 and N_2':

$$\begin{aligned}\sigma &= \frac{\mathrm{Var}\left[N_1 - N_2'\right]}{\mathrm{E}\left[N_1 + N_2'\right]} \\ &= \frac{\mathrm{Var}\left[N_1\right] + \mathrm{Var}\left[N_2\right] - 2\mathrm{Cov}\left[N_1, N_2\right] + \mathrm{Var}\left[N_\varrho\right]}{\mathrm{E}\left[N_1\right] + \mathrm{E}\left[N_2\right] + \mathrm{E}\left[N_\varrho\right]},\end{aligned} \tag{2.26}$$

where $\mathrm{Cov}\left[N_1, N_\varrho\right] = \mathrm{Cov}\left[N_2, N_\varrho\right] = 0$ because the noise photons are uncorrelated with the FWM signal. To simplify this expression further, we must better define the nature of N_ϱ. Because the Raman noise is of similar wavelength to the FWM signal, it is detected with efficiency $\eta_\varrho \approx \eta_2$. As well, for a given pump power, the noise intensity is some constant fraction $\varrho \geq 0$ of the source intensity, $\mathrm{E}\left[N_\varrho\right] = \varrho\eta_2\mathrm{E}\left[N\right]$. Finally, the noise photons are allowed to fluctuate with some Fano factor $F_\varrho - 1 = \varrho(F_s - 1) \geq 0$, because they are generated via different processes than the signal. These assumptions give us the following set of equalities

$$\begin{aligned}\mathrm{Var}\left[N_\varrho\right] &= \mathrm{E}\left[N_\varrho\right] + \beta\mathrm{E}\left[N_\varrho\right]^2 \\ &= \eta_2\varrho\mathrm{E}\left[N\right] + \eta_2^2\varrho(F_\varrho - 1)\mathrm{E}\left[N\right].\end{aligned} \tag{2.27}$$

Substituting eqn. 2.27 into eqn. 2.26 and simplifying as before yields

$$\begin{aligned}\sigma' &= 1 - \frac{2\eta_1\eta_2}{\eta_1+(1+\varrho)\eta_2} + \frac{(\eta_1-\eta_2)^2(F_s-1)}{\eta_1+(1+\varrho)\eta_2} + \frac{\eta_2^2\varrho(F_\varrho-1)}{\eta_1+(1+\varrho)\eta_2} \\ &= \sigma'_p + \sigma'_{sp} + \sigma'_\varrho,\end{aligned} \tag{2.28}$$

where the prime denotes the presence of uncorrelated noise photons, and σ'_ϱ is the NRF contribution associated with this noise.

With the inclusion of uncorrelated noise photons, the minimum attainable NRF is no longer set by σ_p, but increased according to ϱ and F_ϱ. Indeed, as $\varrho \to \infty$, then $\sigma \to 1+\eta_2(F_\varrho-1)$. Related to this, the minimum NRF is no longer given by eqn. 2.25, but by

$$\begin{aligned}\eta_2 &= \eta_1 \frac{\sqrt{\frac{F_s(\varrho+2)^2+\varrho(F_\varrho-\varrho-3)-2}{F_s-1+\varrho(F_\varrho-1)}}}{1+\varrho} \quad \text{for} \quad F_s, F_\varrho > 1 \text{ and } \varrho, \eta_1 > 0 \\ &\geq \eta_1.\end{aligned} \tag{2.29}$$

The difference between η_1 and η_2 decreases with ϱ because there is a compromise between reducing the detection efficiency on the noisy channel to reduce the detrimental effects of the noise, but also maintain the signal correlations. The scaling of the NRF with several values of ϱ is shown in fig. 2.7, and agrees well with our simulations.

We also consider how the introduction of N_ϱ affects the Fano factor of N'_2:

$$\frac{\mathrm{Var}\left[N'_2\right]}{\mathrm{E}\left[N'_2\right]} = 1 + \frac{\eta_2(F_s-1)+\eta_2\varrho(F_\varrho-1)}{1+\varrho}.$$

As we decrease ϱ, $F'_2 \to 1+\eta_2(F_s-1)$, the super-Poissonian NRF associated with measuring only N_2. As we increase ϱ, $F'_2 \to 1+\eta_2(F_\varrho-1)$, the super-Poissonian NRF associated with measuring only N_ϱ, as expected.

So far, we have analyzed three experimental scenarios: noiseless Poisson-distributed twin beams, noiseless super-Poissonian twin beams, and super-Poissonian twin beams with uncorrelated optical noise on one channel. We will finally consider the effects of detection noise. For simplicity, we will consider the detection noise to be the same for both channels, and add this noise to the otherwise-noiseless super-Poissonian twin beam case, before finally stating the full NRF equation.

Let the mean dark counts of each detection region $\mathrm{E}\left[N_d\right]$ be some fraction d of $\mathrm{E}\left[N\right]$, with corresponding Fano factor F_d. Factors which affect the mean and variance of N_d could be the size of the detector, integration time, readout rate, gain, temperature, *etc.*, but detector noise is independent of η_1 and η_2. We can write similar equations to the uncorrelated-optical-noise case for detector noise as

$$\begin{aligned}\mathrm{Var}\left[N_d\right] &= \mathrm{E}\left[N_d\right] + \beta\mathrm{E}\left[N_d\right]^2 \\ &= d\,\mathrm{E}\left[N\right] + d(F_d-1)\mathrm{E}\left[N\right].\end{aligned} \tag{2.30}$$

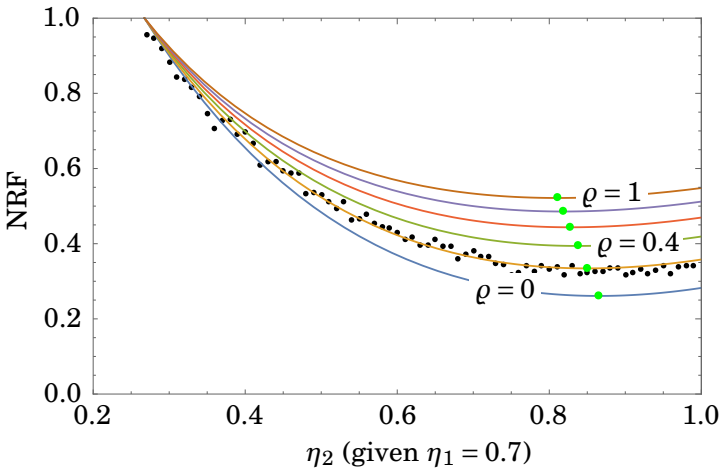

FIGURE 2.7. A plot showing the NRF against channel efficiency, for $\varrho = 0$ to 1 in steps of 0.2, and $F_s = 3$, $F_\varrho = 1$. Green markers indicate the minimum NRF for each ϱ, calculated according to eqn. 2.29. Example simulation data is also shown, with fit.

The covariance for each detection region with each other and the optical signals is zero, uncorrelated. Solving for the NRF in a similar manner to the previous case, but using eqn. 2.30, yields

$$\begin{aligned}\sigma^* &= 1 - \frac{2\eta_1\eta_2}{\eta_1+\eta_2+2d} + \frac{(\eta_1-\eta_2)^2(F_s-1)}{\eta_1+\eta_2+2d} + \frac{2d(F_d-1)}{\eta_1+\eta_2+2d} \\ &= \sigma_p^* + \sigma_{sp}^* + \sigma_d^*,\end{aligned} \tag{2.31}$$

where the asterisk indicates the inclusion of detector noise. In the limit of low detector noise, the minimum NRF is given by eqn. 2.25, as expected.

Finally, we can write a NRF which accounts for correlated, super-Poissonian N_1 and N_2, as well as uncorrelated, super-Poissonian N_ϱ and N_d, combining the results eqn. 2.28 and 2.31, as

$$\sigma'^* = \sigma_p'^* + \sigma_{sp}'^* + \sigma_\varrho'^* + \sigma_d'^* \tag{2.32}$$

$$\sigma_p'^* = 1 - \frac{2\eta_1\eta_2}{\eta_1+(1+\varrho)\eta_2+2d} \qquad \sigma_{sp}'^* = \frac{(\eta_1-\eta_2)^2(F_s-1)}{\eta_1+(1+\varrho)\eta_2+2d}$$

$$\sigma_\varrho'^* = \frac{\eta_2^2\varrho\,(F_\varrho-1)}{\eta_1+(1+\varrho)\eta_2+2d} \qquad \sigma_d'^* = \frac{2d(F_d-1)}{\eta_1+(1+\varrho)\eta_2+2d}.$$

While we were not able to determine an analytical expression for the minimum NRF, which accounts for uncorrelated optical and detector noise, the previous examples suggest that it is reached for $\eta_2 \approx \eta_1$ as noise increases. The minimum could also be numerically solved for, given knowledge of the relevant experimental parameters.

In fig. 2.8, we compare the scaling of NRF with relative channel efficiency – from the ideal, Poissonian twin-beam case, to the full model including uncorrelated optical and detector noise.

Using realistic values for the experimental parameters of eqn. 2.32 (see sec. 3.2.3), there is a relatively large deprovement of the NRF when including optical noise compared to detector noise. With a realistic upper-limit of $\eta_2 = 0.75$, the classical intensity fluctuations of the twin beams limits observation of sub-Poissonian inter-beam correlations to $\eta_2 \in [0.34, 0.75]$, whereas the minimum NRF is achieved at $\eta_2 = 0.85$.

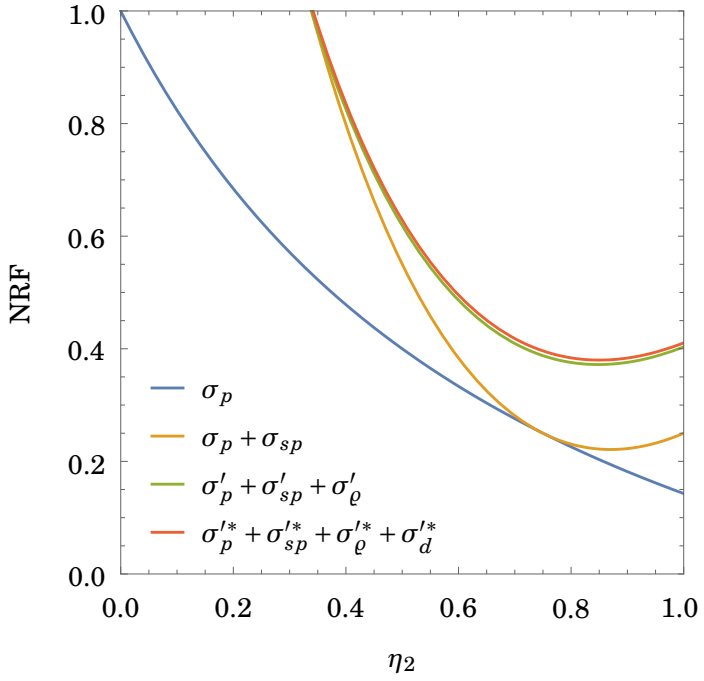

FIGURE 2.8. A plot comparing NRF scaling with relative channel efficiency, adding the noise sources discussed in this section, using realistic experimental parameters. Here, $\eta_1 = 0.75$, $\varrho = 0.45$, $d = 0.003$, $F_s = 4$, $F_\varrho = 1$, and $F_d = 3$.

Considering that we have derived this model with a particular experiment in mind, the model and the techniques used to derive it apply to many similar experiments [2, 6, 10, 11, 13, 14]. Most importantly, the intuition offered by this model is crucial for a complete understanding of the experiments discussed in this thesis. In sec. 3.2.3, we will revisit this theoretical framework, including experimental data, to gain insight into how one can practically optimize such a correlated-intensity experiment.

2.3 Absorption Estimator Theory

Now that we have an experimental model which predicts how well one can measure intensity correlations of twin beams, we would like to use these correlations to estimate physical parameters. In this section, we will introduce classical and quantum absorption estimators, as well as discuss their respective advantages and limitations for parameter estimation.

First, what is an estimator? Given a sample of measured data from a larger population, an estimator is a rule applied to this sample which approximates some parameter associated with the population. Estimators are mathematical tools used to extract information about a given physical parameter, using finite data sets. Two common examples of estimators are the sample mean and standard deviation:

$$\mathrm{E}[x] = \sum_{i=1}^{n} \frac{x_i}{n}$$
$$\mathrm{SD}[x] = \sqrt{\frac{1}{n-1}\sum_{i=1}^{n}(x_i - \mathrm{E}[x])^2}.$$

Because we cannot take data for an infinite amount of time, any statistical information we calculate from our data will be a sample estimation. We would like for this sample estimation to represent the population in an unbiased manner – meaning that if we, for example, repeatedly calculated the mean of our population over many samples, the mean of the sample means would converge to the population mean. In the previous two examples, one finds that $\mathrm{E}[x]$ is unbiased, and $\mathrm{SD}[x]$ is biased because of the nonlinear scaling of the square-root function (to be discussed further in sec. 3.3).

Estimators are also used to determine physical parameters of biological or chemical samples. One such parameter used to characterize samples – the parameter which our experiment estimates – is spectral absorption $\alpha(\lambda)$. Typically, for a given wavelength λ, this procedure involves comparing the intensity of a laser beam with and without a sample in its path:

$$\alpha_c = 1 - \frac{n_p'}{\mathrm{E}[n_p]},$$

where α_c is the direct classical absorption estimator, and n_p is the probe beam intensity for each measurement trial, and the prime denotes beam intensity after a lossy interaction with the sample. To be clear, $\mathrm{E}[n_p] = \eta_p \mathrm{E}[n]$, and $\mathrm{E}[n_p'] = \eta_p(1-\hat{\alpha})\mathrm{E}[n]$, where $\hat{\alpha} \in [0,1]$ is the actual sample absorption. Assuming that the mean intensity of the probe beam does not change from calibration to measurement stage, this is an unbiased estimator, in that $\mathrm{E}[\alpha_c] = \hat{\alpha}$.

In the limit of low-light-level illumination, the precision of such an absorption measurement is fundamentally limited by the quantum nature of light. The intensity noise of an ideal laser beam, a coherent state, is governed by Poisson statistics. Therefore, the limit of precision of a classical direct absorption measurement, the SNL, is

$$\begin{aligned}\mathrm{Var}[\alpha_c] &= \mathrm{E}[\alpha_c^2] - \mathrm{E}[\alpha_c]^2 \\ &= \frac{(1-\hat{\alpha})\eta_p}{\mathrm{E}[n_p]},\end{aligned} \tag{2.33}$$

where η_p accounts for probe-channel loss to consider the ideal case of perfect detection efficiency [2, 10]. Therefore, to compare our measurements to the performance of an experiment with equal detection efficiency, we omit the factor of η_p.

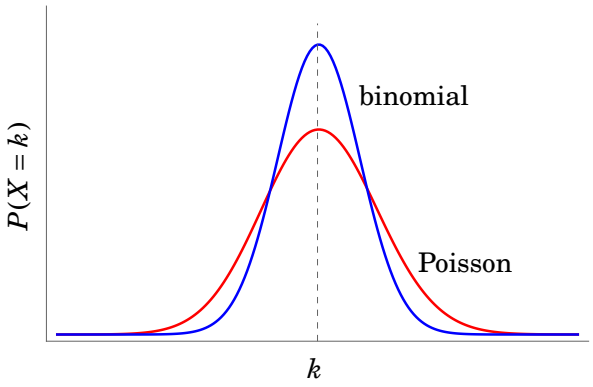

FIGURE 2.9. A plot comparing equal-mean Poisson and binomial distributions, where $P(X = k)$ is the probability that random variable X equals k.

Correlated-intensity twin beams enable increased absorption estimation precision beyond the SNL of an ideal coherent beam [2, 6, 10, 13, 14]. Such states are generated via momentum- and energy-conserving processes (*e.g.* downconversion or FWM, discussed in sec. 2.1), wherein beams exhibiting quantum-correlated intensities are generated. A sample placed in one of the twin beams, the probe beam, allows the other to be used as an intensity reference. In an ideal lossless case, uncertainty on the probe beam intensity becomes binomially distributed, as either a probe photon was absorbed or not, compared to the reference beam [6]. The variance of a binomial distribution is less than that of a Poisson distribution of equal mean, as shown in fig. 2.9. Therefore, for a given mean intensity or photon number, we obtain more statistical information per exposed photon, defined as the inverse of the measurement variance. Indeed, ref. [6] shows that binomial-distributed intensity fluctuations on the probe beam yield a $1/\hat{\alpha}$ improvement on absorption estimation precision compared to a classical, Poisson-distributed source.

As discussed in sec. 2.2, the measured degree of correlation of twin beams σ, the NRF, is degraded by loss and uncorrelated noise. For two independent coherent beams limited by Poisson statistics, we have $\sigma = 1$. For $\sigma \in [0,1)$, we necessarily have quantum-correlated twin beams exhibiting sub-Poissonian statistics and the ability to make sub-SNL absorption measurements, given an appropriate absorption estimator.

We will give examples of two absorption estimators which exploit multi-beam intensity correlations. The first was presented in ref. [2] and further explored by ref. [14]:

$$\alpha_l = 1 - \gamma \frac{n'_p}{n_r},$$

where n_r is the reference beam intensity, and $\gamma = \eta_r/\eta_p$ accounts for unbalanced detection efficiency. Note that this estimator is biased for small $\mathrm{E}[n_r]$ or η_r [2]. In the experiments performed for this thesis, however, we do not suffer from either of these issues.

In the case of balanced detection efficiency, one may write

$$\mathrm{Var}[\alpha_l] = \mathrm{Var}[\alpha_u] + 2\frac{(1-\hat{\alpha})^2}{\mathrm{E}[n_p]}\sigma, \tag{2.34}$$

where $\mathrm{Var}[\alpha_u] = \hat{\alpha}\mathrm{Var}[\alpha_c]$ is the ultimate quantum limit of an absorption measurement, associated with binomial measurement statistics, attainable with *e.g.* Fock states or, equivalently, when

$\sigma = 0$ [6, 14]. To compare this multi-beam estimator to the classical direct case, we define

$$\Gamma_i = \frac{\mathrm{Var}\,[\alpha_i]}{\mathrm{Var}\,[\alpha_c]},$$

for estimator i. When $\Gamma_i \in [0,1)$, the measurement precision is sub-SNL. This regime is exclusive to quantum states of light, similar to $\sigma < 1$.

Comparing eqn. 2.33 and eqn. 2.34 here yields

$$\Gamma_l = \hat{\alpha} + 2(1-\hat{\alpha})\sigma, \tag{2.35}$$

when comparing to a direct classical measurement of equal detection efficiency. One finds $\Gamma_l > 1$ for all $\sigma > 0.5$, shown graphically in fig. 2.10 (a). Thus, even though beams may display quantum, sub-Poissonian intensity correlations $\sigma \in (0.5, 1)$, we cannot perform sub-SNL absorption measurements with this sub-optimal estimator. This counter-intuitive result is explored in detail later in this section. For now, one can gain insight into this issue by considering how α_c is an even less optimal absorption estimator for the multi-beam case, as $\Gamma_c \geq 1$ for all values of σ.

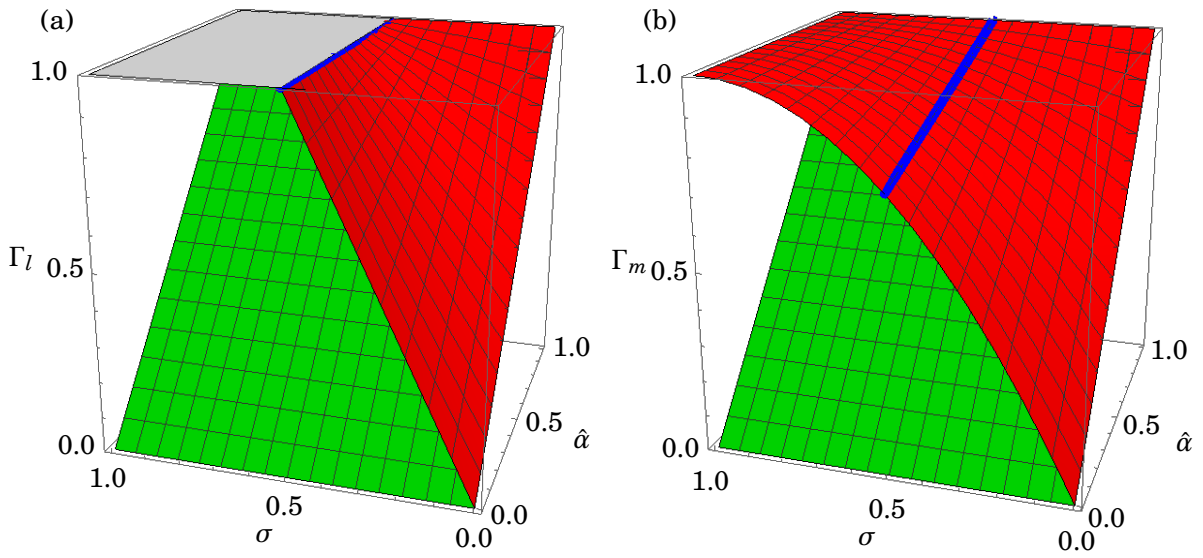

FIGURE 2.10. Plots comparing relative SNL performance metrics (a) Γ_l and (b) Γ_m in the case of balanced detection efficiency. The green plane $\Gamma = \hat{\alpha}$ is the ultimate quantum limit, and the blue line is the $\sigma = 0.5$ contour.

A second multi-beam absorption estimator, which is unbiased and accounts for super-Poissonian beam statistics, is presented in ref. [10]:

$$\alpha_m = 1 - \frac{n_p' - k\delta n_r + \delta E}{\mathrm{E}\,[n_p]}, \tag{2.36}$$

where $\delta n_r = n_r' - \mathrm{E}[n_r]$, δE is a correction factor that is used to ensure that the estimator is unbiased, and k is a weight factor used to minimize the estimator uncertainty. Note that k and δE are both determined in the calibration phase of the experiment, and represent intrinsic properties of the beam fluctuations and detection scheme. As well, the prime in this case denotes the measurement stage in general, and the sample is only placed in the path of the probe beam.

We may perform a similar analysis as the previous estimator, now with

$$\mathrm{Var}[\alpha_m] = \mathrm{Var}[\alpha_u] + 2\frac{(1-\hat{\alpha})^2}{\mathrm{E}[n_p']}\sigma(1-\frac{\sigma}{2})$$

in the case of balanced detection and optimized k [14]. Again comparing this to the classical direct measurement with equal loss,

$$\Gamma_m = \hat{\alpha} + 2(1-\hat{\alpha})\sigma(1-\frac{\sigma}{2}). \tag{2.37}$$

Using this absorption estimator, we now find sub-SNL $\Gamma_m < 1$ for all $\sigma < 1$, and $\Gamma_m < \Gamma_l$ for all $\sigma > 0$. The performance of α_m and α_l is compared graphically in fig. 2.10. We see in this figure that α_m is a superior estimator to α_l when appropriately calibrated, although it may not be optimal, as it does not saturate α_u for all $\hat{\alpha}$ and σ.

In an experiment discussed in detail in sec. 4.11, we measure strong sub-Poissonian twin-beam correlations at $\sigma = 0.47 \pm 0.04$, and yet do not observe sub-SNL statistics on our absorption measurement, with $\Gamma_m = 1.02 \pm 0.16$. From the previous discussion, however, we expect that α_m should yield sub-SNL statistics for all values of $\sigma < 1$. The discrepancy lies in that real experiments may not, as in our case, exhibit Poisson-distributed intensity fluctuations on the individual twin beams. As well, loss on the probe and reference channels may not be balanced, a simplifying assumption made in deriving eqn. 2.37. To see the effect of unbalanced detection and super-Poissonian beams statistics on Γ_i, we will now show how Γ_l may degrade with increasing γ, and apply this intuition to Γ_m.

For unbalanced detection efficiency, eqn. 2.35 takes the form

$$\Gamma_{l,\gamma} = \hat{\alpha} + 2(1-\hat{\alpha})\sigma_\gamma, \tag{2.38}$$

where

$$\sigma_\gamma = \frac{1}{\gamma}\frac{\mathrm{Var}[n_r - \gamma n_p]}{\mathrm{E}[n_r + \gamma n_p]}.$$

Note in the case of balanced detection, $\sigma_1 = \sigma$, where σ is the NRF typically used to quantify multi-beam correlations [14]. Considering the case of super-Poissonian twin beams and unbalanced detection efficiency, we write eqn. 2.38 in terms of σ and detection efficiencies as

$$\Gamma_{l,\gamma} = \hat{\alpha} + 2(1-\hat{\alpha})\left(\frac{\sigma}{2}\left(1+\frac{\eta_p}{\eta_r}\right) - \frac{(\eta_p-\eta_r)^2(F_s-1)}{2\eta_r}\right),$$

where $\Gamma_{l,\gamma}$ is only sub-SNL when

$$\sigma < \frac{\eta_r}{\eta_p + \eta_r} + \frac{(\eta_p - \eta_r)^2 (F_s - 1)}{\eta_p + \eta_r},$$

compared to the balanced, Poissonian twin beam case, which requires $\sigma < 0.5$. Finally, $\Gamma_{l,\gamma}$ performs worse than Γ_l when $\gamma < 1$ and $\sigma > \eta_p(F_s - 1 + \gamma(1 - F_s))$.

In this analysis, we did not include effects such as Raman or detector noise, but one would expect α_l (as well as α_m) to perform even worse in this case, based on the analyses of the previous sec. 2.2. This result highlights the importance of reducing noise on the twin beams, as well as appropriately adjusting γ, for optimal parameter estimation.

2.3.1 Accuracy Advantage Using Multi-Beam Absorption Estimator

To conclude this section, we will show that α_m is not only more precise than α_c, but also more accurate for measuring $\hat{\alpha}$. In a general absorption measurement, we estimate $\hat{\alpha}$ in two stages: calibration and measurement. In the calibration stage, we determine the mean beam intensity $\mathrm{E}[n_p]$ without a sample present. Then, we probe the sample with the same beam, where the measurement beam intensity per trial is given as $n'_p = (1 - \hat{\alpha})\mathrm{E}[n_p] + \delta n_p$.

In a typical experiment, however, the mean intensity of the source may drift from the calibration stage to the measurement stage. Without knowledge of the extent of this drift, we expect it would bias the absorption estimation away from the true sample absorption. We may write this as $\mathrm{E}[n'_p] = (1 - \hat{\alpha})(\mathrm{E}[n_p] + \varepsilon \mathrm{E}[n_p])$, where ε is a constant that quantifies the source's intensity drift. Substituting this into eqn. 2.33, we find $\mathrm{E}[\alpha_c] = \hat{\alpha} + \varepsilon(1 - \hat{\alpha})$. Because we have no knowledge of ε, we cannot unbias our estimator α_c.

In the multi-beam case, we have two intensity-correlated beams, such that

$$\mathrm{E}[n'_p] = (1 - \hat{\alpha})(\mathrm{E}[n_p] + \varepsilon \mathrm{E}[n_p]) \quad \text{and} \quad \mathrm{E}[n'_r] = \mathrm{E}[n_r] + \varepsilon \mathrm{E}[n_r]. \tag{2.39}$$

Taking an average value of eqn. 2.36 also yields $\mathrm{E}[\alpha_m] = \hat{\alpha} + \varepsilon(1 - \hat{\alpha})$, with optimized k. We can write $\hat{\alpha}$ in terms of the absorption estimate as

$$\hat{\alpha} = \frac{\mathrm{E}[\alpha_m] - \varepsilon}{1 - \varepsilon}.$$

Thus, for the multi-beam estimator to be unbiased, we must determine ε, as in the direct-classical case. In the multi-beam case, however, we know from eqn. 2.39 that $\varepsilon = (\mathrm{E}[n'_r]/\mathrm{E}[n_r]) - 1$, and we can unbias $\mathrm{E}[\alpha_m]$. Note that when considering the presence of uncorrelated optical noise on one or both of the correlated beams, one cannot directly apply this procedure, as α_m is biased according to this noise.

The multi-beam absorption estimator is therefore not only more precise, but also more accurate than the direct classical absorption estimator. One could consider a classical absorption measurement using the multi-beam estimators, wherein a coherent state is shown onto a beam

splitter, with one of the outputs used as the signal and the other as the reference, as shown in fig. 2.11 (b). This classical differential measurement can, in principle, achieve the same measurement accuracy as the quantum differential measurement, shown in fig. 2.11 (c). The caveat is that in the classical differential measurement, as in the quantum one, the relative shot-noise is increased to account for the reference beam. In the experiments performed in this thesis, we are interested in improving measurement precision beyond the ultimate classical precision limit, and so we will compare our measurement precision to the lower-noise ideal direct classical measurement, shown in fig. 2.11 (a).

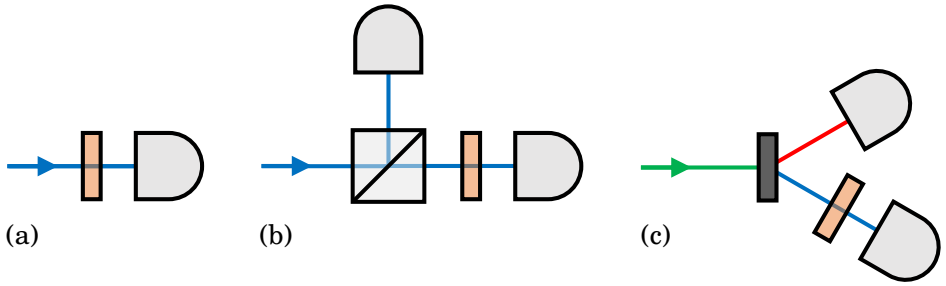

FIGURE 2.11. Schematics comparing the (a) classical direct absorption measurement, (b) classical differential absorption measurement, and (c) quantum differential absorption measurement.

2.4 Conclusion

In this chapter, we discussed the origin of correlated-intensity twin beams, and specifically the four-photon process which we use to generate visible-wavelength beams, called FWM. We also showed in sec. 2.2 how to quantify the degree of multi-beam correlations using the NRF, and how deleterious effects of uncorrelated optical and detector noise affect measured correlations. The derivations in this section were performed to understand how correlated-intensity experiments should be optimized with respect to various noise sources. Finally, in sec. 2.3, we compared three absorption estimators, and showed how unbalanced detection, as well as uncorrelated noise, could limit sub-SNL absorption estimation. We therefore have demonstrated that sub-Poissonian intensity correlations are necessary, albeit not sufficient, to observing sub-SNL measurement precision. This is experimentally demonstrated in sec. 4.11.

Now that we have the tools to characterize multi-beam intensity correlations, as well as estimate sample absorption, we will discuss in the following chapter the general experimental features of our correlated-intensity experiment.

CHAPTER 3

GENERAL EXPERIMENTAL FEATURES AND DATA ANALYSIS TECHNIQUES

Chapter outline: *In this chapter, we discuss the general experimental features of our correlated-intensity experiments performed for this thesis. First, we characterize the nonlinear fibers used to generate twin beams. Second, we apply this characterization to the noise-reduction factor model of our experiment. Finally, we discuss the data analysis code which we use to analyze our intensity data.*

Declaration of contribution: *This chapter is primarily novel work performed by me, one major exception being that the photonic crystal fiber was designed and fabricated at University of Bath by senior lecturer Dr. Peter J. Mosley. I performed the fiber spectral characterizations of sec. 3.1.1 to confirm work which is presently in the literature [39, 47]. Discussions which rely on results which I myself did not obtain are cited accordingly in the text, specifically experimental discussions related to fiber damage mechanisms (sec. 3.1.4) and theoretical discussions related to normally-distributed intensity data (sec. 3.3).*

3.1 Nonlinear Fiber Characterizations

In sec. 2.1, we discussed how one may use Four-Wave Mixing (FWM) to generate intensity-correlated twin beams in χ^3-dominant nonlinear fibers. FWM at blue and ultraviolet wavelengths has been demonstrated using Photonic Crystal Fiber (PCF) in an effort to develop practical short-wavelength lasers [30, 39]. As well, FWM at visible wavelengths has been observed in Single-Mode Fiber (SMF)28, standard telecommunications fiber [47, 48]. However, neither the PCF nor SMF28 sources have been previously characterized in terms of their intensity correlations or used for parameter estimation. In this section, we will detail our own experimental results in characterizing these fibers, as well as comparing the fibers to determine their appropriate respective applications for quantum-enhanced absorption spectroscopy and imaging.

3.1.1 Pump, Four-Wave Mixing, and Raman Spectra

To measure the FWM spectrum of optical fibers, we used the experimental setup shown in fig. 3.1. The general features are that a monochromatic pump beam is coupled into a length of nonlinear fiber. The fiber output is collimated, spectrally filtered to remove the relatively bright residual pump, and coupled to a Multi-Mode Fiber (MMF) to be guided to a spectrometer. We use a flip mirror to switch coupling between spectral characterization of the fiber and measuring the multi-beam intensity correlations, discussed later in this section. Note that we chose for the spectrometer beam path to be associated with the mirror-up position, as the MMF is more robust to pointing instability associated with the flip mirror than the intensity-correlation measurements, wherein beam wandering on the CCD camera may complicate data analysis and reduce the optical signal to electronic noise.

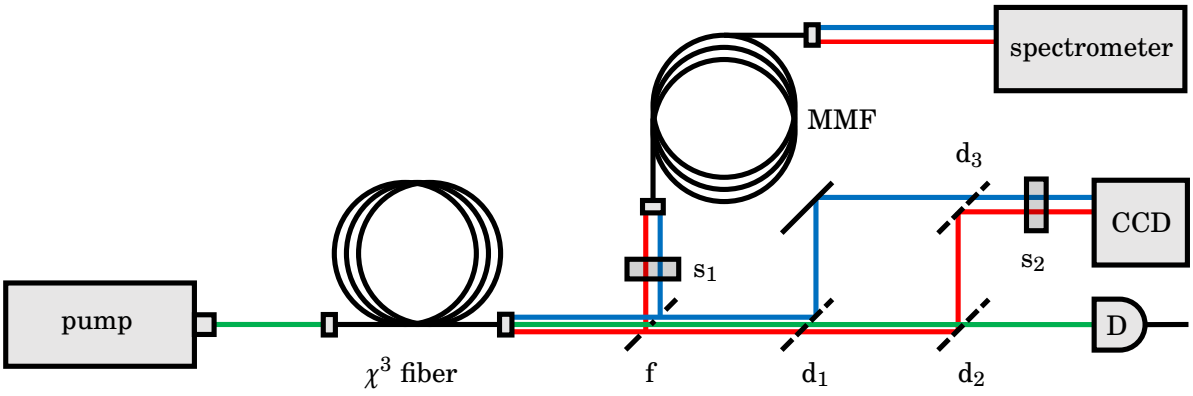

FIGURE 3.1. Schematic of the experimental setup used for spectral characterization of nonlinear fibers and intensity-correlation measurements. f: flip mirror; $d_{\{1,2,3\}}$: dichroic mirrors; $s_{\{1,2\}}$: spectral filters; D: silicon photodiode detector.

In this experiment, the pump we use is a ns-pulsed, 532 nm wavelength, 7 kHz repetition-rate laser. Though the source was iterated several times throughout this thesis (see sec. 4.7), in general it is a frequency-doubled, passively Q-switched 1064 nm laser, manufactured by Teem Photonics [60, 61]. These laser heads have an 11.5×2.9 cm^2 footprint, and cost €5000 at the time of purchase. From an engineering perspective, their small size and low cost make them well suited towards our goal of developing a technology which may be easily transported and implemented in other laboratory settings. The choice of pump wavelength was informed by the results described in sec. 2.1.5, wherein visible-wavelength FWM was generated from a 532 nm source [30, 39, 47, 48]. We have not rigorously characterized the output spatial mode of this pump, due to challenges associated with using low-repetition-rate lasers with commercial beam profilers (see sec. 4.7.2), as well as the high peak power being incompatible with the CCD camera with which we take our correlated-intensity data. We do, however, expect the pump beam to be multi-mode, as we observe by eye several distinct spatial modes in the far field when shining the laser onto a white alignment card. Note that this is in contradiction with the datasheets for the pump lasers, which state that the output is a single fundamental mode [60, 61]. The pump power is adjusted with a half-wave plate and Polarizing Beam Splitter (PBS), meaning the input beam to the fiber is necessarily polarized.

We used an Andor Shamrock 750 [62] spectrometer with attached Andor Newton 970 [63] Electron-Multiplying CCD (EMCCD) camera (> 80% detection efficiency over $450 - 790$ nm wavelengths) to capture spectral data of the various nonlinear fibers used in this experiment. The spectral resolution this arrangement achieves with a fully-open spectrometer slit is 1 nm, with an accuracy of approximately 2 nm. While reducing the camera slit width would increase the spectral resolution, it would reduce the intensity of the signal beam, not allowing measurement of relatively low-power features such as Raman scattering. The current resolution is sufficient for our fiber alignment and spectral characterization purposes. Note also that we operate the EMCCD camera in conventional CCD mode, without electron multiplication, as our signal is bright enough not to require it.

The procedure to align nonlinear optical fibers in our experiment, whether for spectral characterization or intensity-correlation measurements, is first to cleave and secure the nonlinear fiber at both ends, such that pump light may be efficiently coupled in and out. Cleave quality is important to ensure proper FWM mode coupling, as will be discussed later in sec. 4.7.2.2. At this stage, alignment is optimized to achieve maximum pump-power throughput. Once achieved, we apply spectral filtering to the output beam, and couple the beam to the spectrometer via ~ 4 m of MMF (Thorlabs GIF625, with core diameter 62.5 µm [64]). Fiber input coupling is then further adjusted to efficiently excite the desired FWM phase-matching condition, based on live-updated spectrometer data.

We characterized and compared four 1 m pieces of PCF fabricated at the University of Bath, with varying core diameters, as well as 1 m of SMF28. The PCFs were originally fabricated for

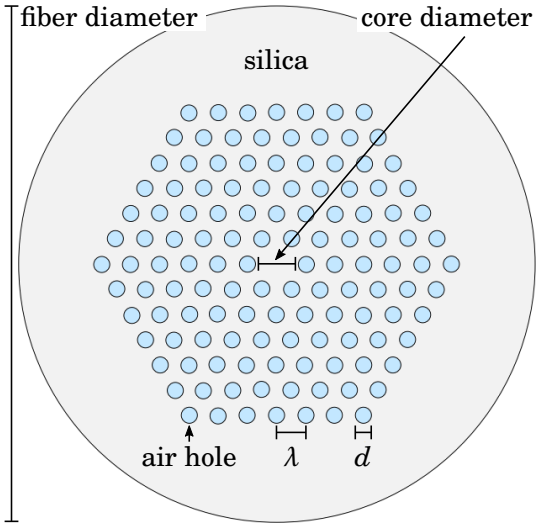

FIGURE 3.2. A PCF cross-section with relevant fabrication parameters labeled. Note that this cross-section is not drawn to scale with the specifications of tab. 3.1.

experiments performed in ref. [39], with their simulations and results featured in sec. 2.1.4 and sec. 2.1.5. Each length of PCF was drawn with the same pressure and temperature to consistently achieve the same hole-diameter-to-pitch-ratio, d/λ (see fig. 3.2), and exhibit < 0.1 dB/m loss over the visible wavelength spectrum [65]. Their respective fiber and core diameters are shown in tab. 3.1 according to ref. [66]. Results of our PCF spectral characterizations are shown in fig. 3.3.

In measuring these spectra, we have coupled into several of the available FWM modes to demonstrate the available wavelengths in each PCF, using our pump. We have applied bandpass filtering (Semrock FF01-450/660-25 and FF01-620/14-25 [67]) to remove pump photons when measuring the FWM signals, and a notch filter (Semrock NF03-532/1064E [67]) to remove bright pump components when measuring the pump spectrum. Only a representative Stokes spectrum is shown for PCF3, as the spectra for the other fibers is similar, and the idler wavelengths calculable from eqn. 2.9.

There are several features to notice in the spectral characterizations of our PCF. First, as the PCF core diameter increases, so does the spectral separation of the FWM. This is consistent with the simulations performed in ref. [30, 39], shown in fig. 2.4 (b).

TABLE 3.1. Fabrications specifications of four PCFs

fiber designation	fiber diameter (μm)	core diameter (μm)	d/λ
PCF1	80	2.35	0.95
PCF2	85	2.50	0.95
PCF3	90	2.65	0.95
PCF4	95	2.80	0.95

Second, due to the multi-mode nature of our pump beam, as well as the multi-mode nature of the PCF, we may simultaneously satisfy several FWM phase-matching conditions. The mode coupling to a specific set of FWM wavelengths may be improved by adjusting the pump alignment with the fiber, filtering the pump mode, or choosing the appropriate fiber coupling lens to overlap the spatial mode of the pump with the desired FWM mode. By doing this, typically one FWM set

becomes dominant, but other modes are still present due to physical perturbations in the fiber causing mode mixing.

Third, there is Raman scattering at the FWM Stokes wavelength, observed in all the PCFs. This is expected, as discussed in sec. 2.1.3, due to the material properties of silica glass [28]. This result is also consistent with previous experimental work discussed in sec. 2.1.5 [30, 39]. We measure both Stokes and anti-Stokes inelastic pump broadening, and stimulated Raman scattering at 560 nm. We can be sure that the pump spectrum has inelastically broadened by comparing its bandwidth to the measured FWM, which should be similar when using a single pump beam.

Note that the optimal FWM coupling efficiency may not correspond to the optimal pump power coupling. In the data shown in fig. 3.3 for PCF3, for example, the pump power measured after the PCF was 65% of the input pump power, although a maximum pump coupling efficiency of about 70% was attainable. This may be attributed to several experimental factors such as pump alignment to the optic axis of the fiber end, as well as the pump and FWM spatial modes.

The fiber which we use for the remainder of the discussions in this chapter is PCF3, which we will simply refer to as PCF. This choice was made because PCF3 allowed access to wavelengths well-separated from the pump, where we measure reduced Raman scattering. We also empirically found that coupling to the preferred FWM modes is more efficient in PCF3 than PCF4, considering our fiber coupling lens and pump modes of the laser. The wavelengths and coupling efficiencies are sufficient to pursue experiments in measuring FWM intensity correlations, and it is a topic of future study to design fibers which access different wavelengths and demonstrate better noise properties.

The SMF28 which we characterized is commercial telecommunications fiber. Specifically, we use Corning SMF-28e+ bare fiber, a graded-index solid-core fiber with core diameter of 8.2 µm [49]. This is the same type of fiber used in ref. [47, 48] to generate visible-wavelength FWM. The results of our SMF28 spectral characterizations are shown in fig. 3.4.

The measured FWM wavelengths for SMF28 are consistent with previous work [47, 48], within spectrometer accuracy. We applied bandpass filtering to remove pump photons when measuring the FWM signals (Semrock FF01-450/660 and FF01-663/18-25 [67]). Because of the lower χ^3 nonlinear response of the SMF28 compared to the PCF due to the guided mode area, measured in the following section, higher average pump powers are required to achieve the same FWM power as in PCF. For this reason, we measure increased Raman scattering for a given FWM power using the SMF28. Because uncorrelated optical photons are detrimental to measuring twin-beam intensity correlations, this suggests that the PCF is a better nonlinear candidate to generate twin beams. As we will see in the remainder of this chapter, such a comparative analysis is not so simple.

Because we necessarily must operate at higher pump powers to achieve bright FWM in SMF28, we also measure uncorrelated anti-Stokes Raman scattering which spectrally overlaps

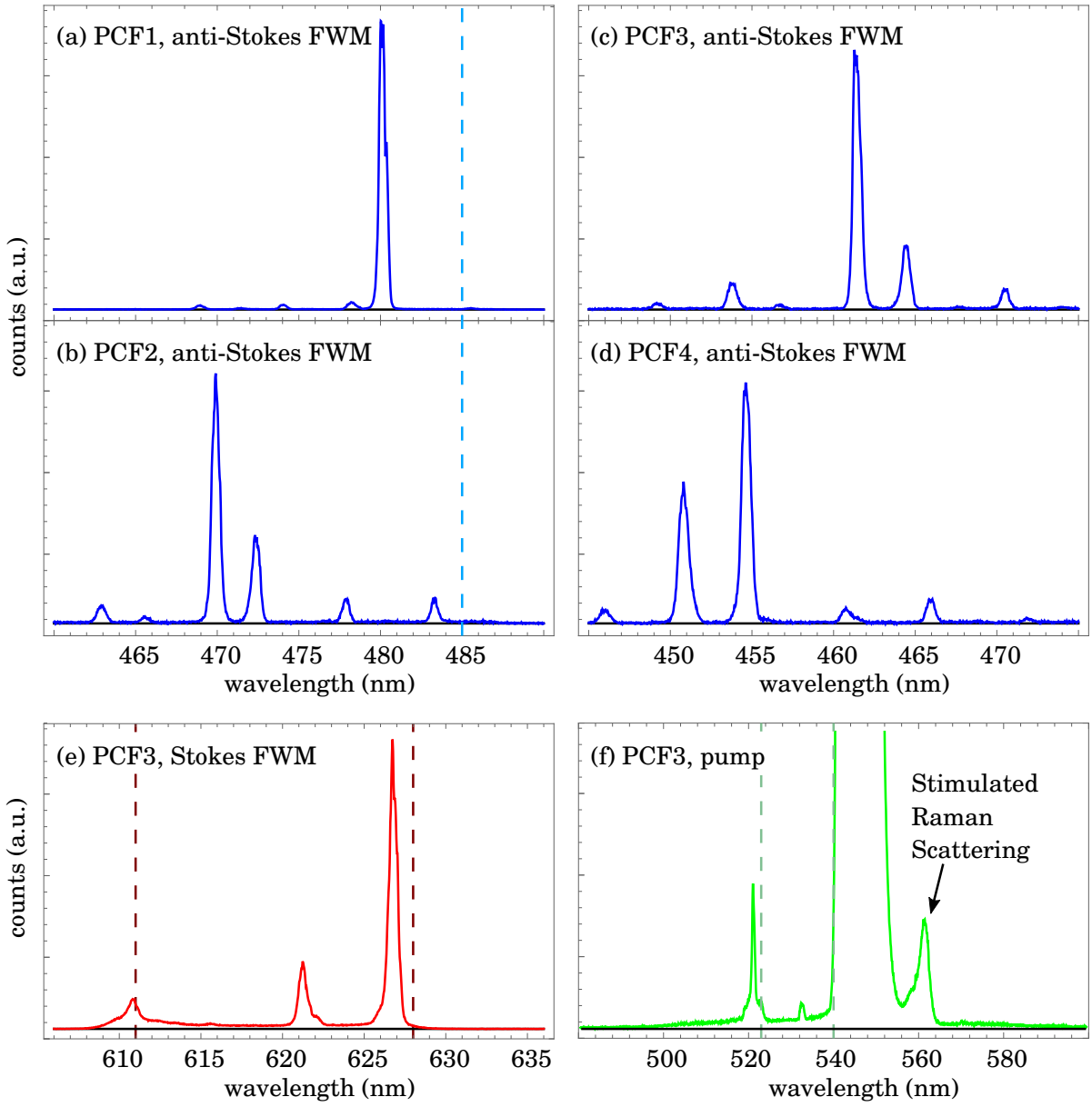

FIGURE 3.3. Results from the spectral analysis of the four 1 m lengths of PCF are shown. Each PCF (a)-(e) was pumped at 532 nm wavelength, 1 mW average power. Also shown is a spectrum of the pump (f), post-PCF, with notch filter to remove bright components and observe inelastic photon scattering features. The spectrometer integration time for each plot was 0.5 s, bandpass filtering (dashed lines, nominal values from datasheets) was used to measure the FWM spectra, and additional neutral-density filters were used to measure the pump spectrum. Note that there is indeed a FWM peak at 610 nm in (e), attenuated by the bandpass filter. The black line in each spectrum represents the average background counts of the camera without incident light.

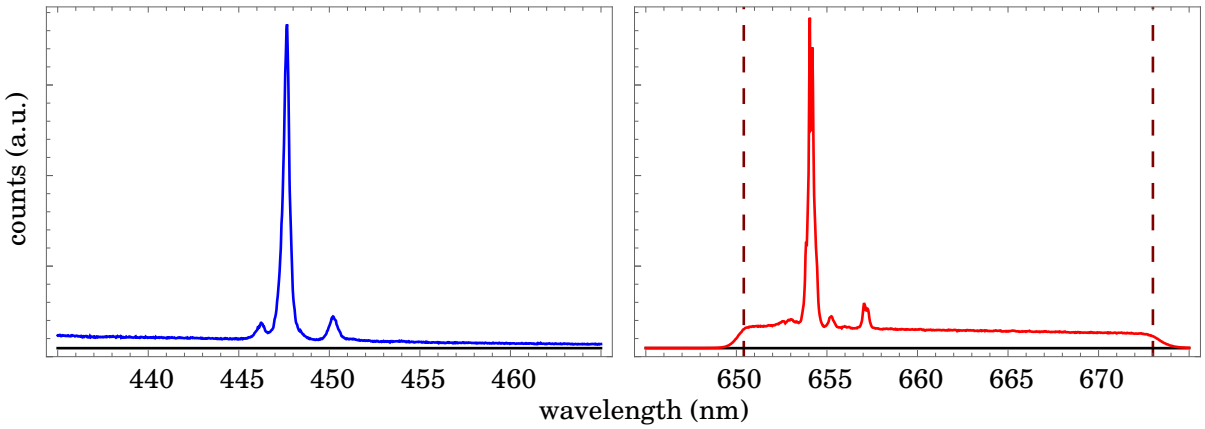

FIGURE 3.4. Results from the spectral analysis of 1 m of SMF28 is shown pumped at 10 mW average power. The spectrometer integration time was 0.5 s, bandpass filtering was used to measure the FWM spectra (dashed lines, nominal values from datasheets). The black line in each spectrum represents the average background counts of the camera without incident light.

with the anti-Stokes FWM peak. As Raman scattering processes are a property of the fiber material, we would expect to observe this in the PCF also. However, because of the low anti-Stokes phonon population factor and high nonlinear response of PCF, we do not reach high enough average pump powers to measure detrimental amounts of anti-Stokes scattering. Note that at 1 mW average pump power, we do not measure bright anti-Stokes scattering in SMF28.

One advantage thus far of using SMF28 compared to PCF is the larger core diameter (8.2 µm compared to 2.5 µm). The larger core size not only makes the SMF28 more robust to optical damage, but also simplifies alignment insofar as initially coupling the pump beam into the fiber. Because there are relatively fewer supported FWM conditions in the SMF28 at our wavelengths of interest, optimizing and maintaining coupling to specific phase-matching conditions is simplified. For these reasons, SMF28 is generally a simpler and more robust source of twin beams than PCF, albeit with a lower nonlinear response and corresponding worse optical noise performance. The nonlinear response is discussed in the following section.

3.1.2 Four-Wave Mixing and Raman Power Scaling with Pump Power

As stated in the previous section, SMF28 exhibits a lower χ^3 nonlinear response than the PCF, due to the reduced nonlinear parameter γ. The implications of this are that SMF28 requires higher pump powers for a given FWM power, thereby increasing the rate of Stokes and anti-Stokes Raman scattering in the signal beams. In this section, we will rigorously demonstrate this comparison.

For each nonlinear fiber, we measured the FWM spectrum around 450 nm at several pump

powers using the spectrometer. We then integrated each spectrum over the bandwidth of the FWM signal to fairly calculate its power, which accounts for differences in the signal's optical bandwidth in each fiber. Note that for the SMF28, we also fit and subtracted the anti-Stokes Raman scattering, following the procedure outlined in sec. 3.2.1. These results are shown in fig. 3.5.

We fit the data with gain factor

$$G = 1 + \left(\frac{\gamma P_p}{g}\right)^2 \sinh^2(gL), \tag{2.6}$$

which relates input and output FWM power [28]. There is good agreement of this model with the data of fig. 3.5. As seen in the data, and importantly for our goal of obtaining high-power twin beams, FWM power increases exponentially in both nonlinear fibers once a threshold pump power is reached. Note that in acquiring the PCF data, fiber coupling was readjusted for each data point, as pump beam deflections from the half-wave plate of the attenuator were found to misalign the coupling sufficiently to no longer be optimally coupled into the desired FWM mode.

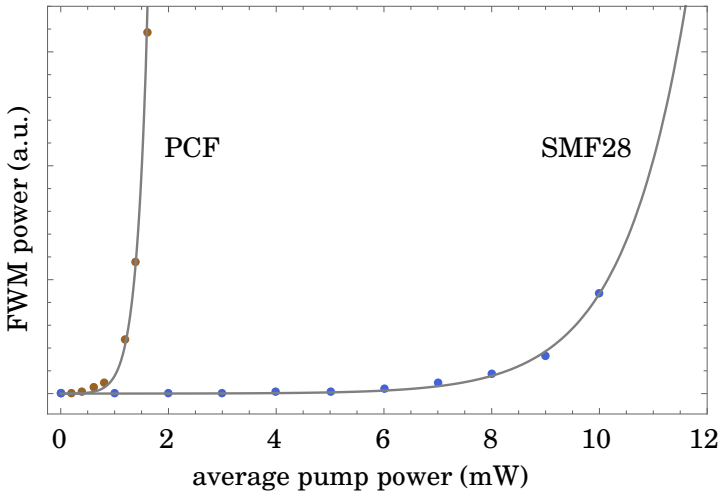

FIGURE 3.5. Plots of measured FWM power produced by PCF and SMF28 against pump power, fit according to eqn. 2.6.

If we assume perfect phase-matching, $\kappa = 0$, then we can simplify eqn. 2.6 to

$$G = \cosh^2(P_p L / A_{\text{eff}}),$$

where $\gamma \approx 1/A_{\text{eff}}$ if all FWM and pump beams are in the same spatial mode, with effective mode area A_{eff} [28]. Fitting the data under this assumption yields $\gamma_{\text{SMF28}}/\gamma_{\text{PCF}} = 0.11$, and thus $d_{\text{PCF}}/d_{\text{SMF28}} = 0.34$, where d is the fiber diameter, in good agreement with our expected fiber core sizes ($d_{\text{SMF28}} = 8.2\,\mu\text{m}$ and $d_{\text{PCF}} = 2.65\,\mu\text{m}$).

Therefore, by increasing pump power, we can increase FWM power exponentially until the fiber damage threshold is reached. The mechanisms by which this occurs are discussed more

thoroughly in sec. 3.1.4, but for PCF, we found that the average pump power threshold is ~ 3 mW, and ~ 12 mW for SMF28. We have reliably measured FWM signal powers up to 2 µW with PCF and 0.5 mW for SMF28. Thus, although the SMF28 has a lower nonlinear coefficient, the fact that it is more robust to optical damage indicates its potential for use in applications two orders of magnitude brighter than our current PCF source.

3.1.3 Effects of Bending on Four-Wave Mixing Spectra and Power

While working with the SMF28, we found the FWM efficiency to be dependent on the physical stresses imposed on the fiber (*e.g.* bend radius, twisting, number of bends, *etc.*). Because the SMF28 supports many modes at visible wavelengths, these physical perturbations modify the coupling efficiency of the pump between the desired FWM modes and other supported core and cladding modes of the fiber. As well, perturbations or fiber manufacturing imperfections may cause birefringence-related polarization changes in the pump and FWM beams along the length of the fiber, reducing the phase-matching efficiency [28].

In SMF28, this bending effect is more pronounced than in the PCF, as one might expect, because the smaller core diameter of the PCF means that it is less multi-mode than the SMF28 at visible wavelengths. Loss and reduced FWM gain directly impact the signal-to-noise ratio of the FWM to Raman scattering, and so fiber position should be accounted for when optimizing the source. Indeed, we see in fig. 3.6, that for a given pump power and fiber length, FWM efficiency in SMF28 may be improved by manually adjusting the fiber flexure on the optical bench.

Unfortunately, we were not able to determine any set of fiber parameters (*e.g.* smallest bend radius) that could be systematically adjusted to optimize the FWM efficiency. To this end, we coiled the fiber around cylinders of various diameters, from 11.8 cm to 21.6 cm, and found that even once coiled, moving the cylinders along the table could significantly change the mode coupling. We also mounted the fiber into a manual fiber polarization controller (Thorlabs FPC560 [68]) to see the effects of systematic polarization adjustments on FWM gain. The small loop diameter (56 mm) of the polarization controller, however, significantly reduced the FWM power, and we were not able to observe the effects of further polarization adjustments.

Ultimately, we developed a system of mounting the fiber to relatively heavy, unclamped optics pedestal mounts, which by then moving allowed for arbitrary fiber position adjustment, shown in fig. 3.7. Once a local maximum of FWM power was found, the fiber position could be maintained by fixing the pedestals to the optics bench. Using this method with a length of SMF28, we were able to quickly improve the Noise-Reduction Factor (NRF) (see sec. 2.2 for definition) from 0.79 ± 0.08 to 0.64 ± 0.07 only by adjusting the fiber position.

Related to this fiber-bending phenomenon, we do not measure any preferential polarization of the FWM signal at the fiber output. Although the pump is polarized at the input, adjusting the polarization did not produce any measurable effect on the output signal power. As well, we did not measure any FWM power change when shining the beams onto a PBS, and rotating the PBS.

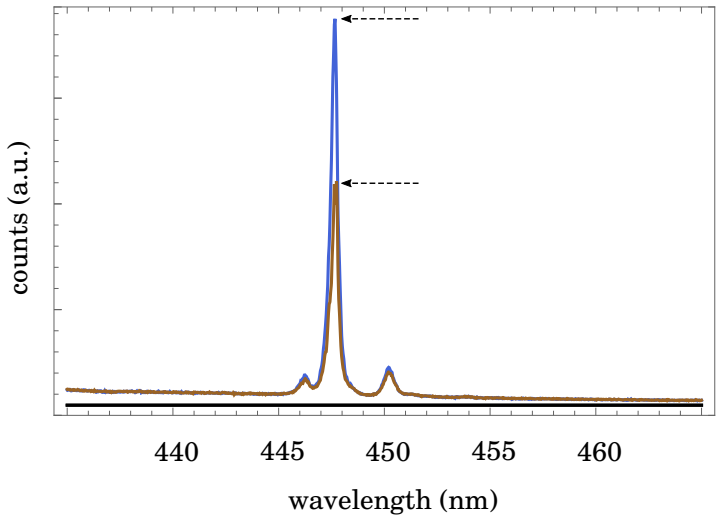

FIGURE 3.6. A comparison of two physical states of SMF28, showing the effects of bending on FWM gain. Pump power and other experimental parameters are constant between both data sets, except the dark-blue data represents an improved fiber position. The black line above the wavelength axis represents the average background counts of the camera without incident light, and the dashed lines indicate peak spectral amplitudes of the SMF28 in two different positions.

This is due to the aforementioned polarization mixing in the fiber.

One could imagine an experiment wherein the fiber is mounted straight, rather than coiled, such that it experiences no bending or twisting along its entire length. While this could, in principle, reduce these loss- and polarization-related effects which we observe, it is impractical. Because we require fiber lengths on the order of a few meters to achieve sufficient FWM power, this would represent a considerable increase in the experiment's physical footprint. In the interest of directing this technology towards practical applications, and because FWM coupling can be sufficiently optimized according to the previously-described method, such that we still measure sub-Poissonian intensity correlations, we did not pursue this line of experimentation.

These mode-mixing discussions also inform why it may not be practical to use very long (tens of meters) nonlinear fibers to generate twin beams. Indeed, following along the discussions of sec. 2.1.1, FWM gain scales exponentially in fiber length once the exponential-gain threshold is reached. However, with long fibers it becomes experimentally challenging to optimize on specific FWM phase-matching conditions, as the modes tend to mix more with increasing fiber length. In the absence of narrowband spectral filtering about the FWM wavelengths of interest, the signal intensities may be contaminated with undesirable FWM or Raman scattering from pump light coupled into fiber cladding modes, worsening measured intensity correlations. We have empirically found that PCF and SMF28 on the order of 2 m to 4 m are an appropriate compromise between fibers too short to produce high-power twin beams and too long such that uncontrollable

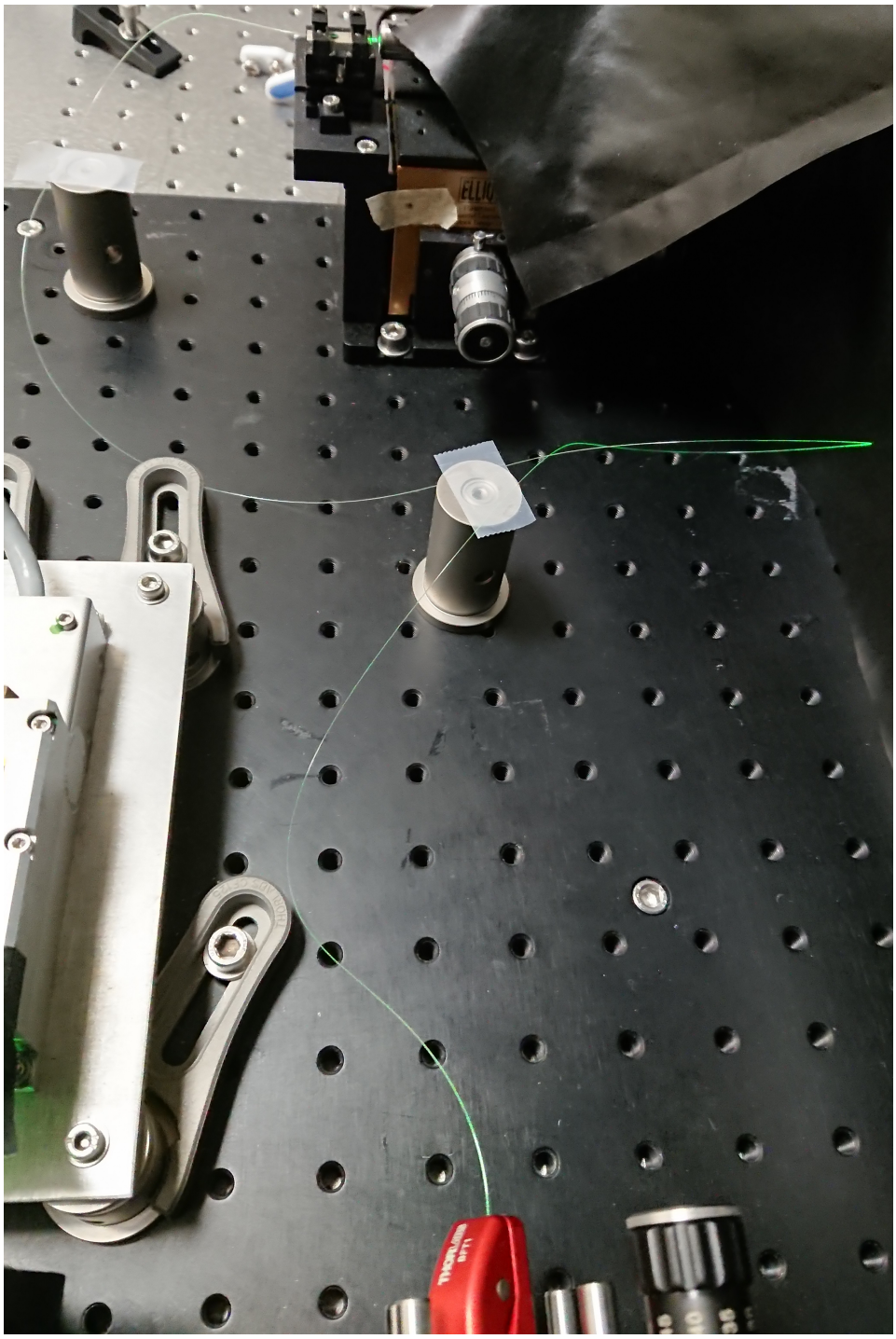

FIGURE 3.7. A photograph of nonlinear fiber fixed to stationary pedestal mounts for position optimization.

intermodal coupling becomes an issue.

3.1.4 Fiber Optical Damage Mechanisms

Optical fibers undergo mechanical deformations when exposed to intense optical fields. These deformations may, as in our case, lead to a loss of ability to achieve efficient FWM mode coupling. Throughout our own experiments, we have observed two characteristic damage pathways: (1) slow optical damage, on the order of minutes, and (2) instantaneous, catastrophic damage. In both cases, we are not able to effectively recouple into the previously-coupled FWM mode.

The mechanism by which the catastrophic damage occurs is called dielectric damage. It may occur when laser energy densities at the glass-air interface reach a threshold energy determined by the material properties of the glass, at which point the glass melts or boils [69, 70]. For picosecond and nanosecond pulsed lasers with high peak powers, this damage pathway represents a particular issue.

Let us briefly consider an example, using our own experimental parameters, to see where this threshold may lie. We use an aspheric microscope objective lens with an effective focal length of 3.1 mm (Thorlabs C330TMD-A [71]) to couple into our nonlinear fibers. With a Gaussian pump beam diameter of 2 mm, and wavelength of 532 nm, this corresponds to a minimum spot size of diameter 1.05 µm. Pumping with 3 mW average power at 7 kHz repetition rate, we calculate an energy density of 49.5 J/cm^2. Comparing this to quoted values for dielectric damage in fused silica, ~ 45 J/cm^2, we find very good agreement with our own experience using PCF [69].

The question is then, why do we observe dielectric damage in the PCF near 3 mW of average pump power, and not in the SMF28, as mentioned in sec. 3.1.2? The answer is that the pump beam is not focused to its diffraction limit on the face of the fiber. When focused beyond the fiber end face, the energy density is reduced to safe operational levels at the glass-air interface. In the PCF, however, the pump beam may drift outside of the relatively small 2.5 µm core over the air holes, due to laser pointing instability or thermal and mechanical fluctuations in the experiment (discussed further in sec. 4.7.2). When focused at the air holes, the pump beam energy densities may now reach the threshold for damaging the microstructures near the end face of the fiber, nearly instantaneously impairing FWM mode coupling.

The second damage pathway is slower, occurring over the course of minutes. While we typically observe this effect in the SMF28 rather than the PCF because the lower catastrophic-damage threshold of the PCF is dominant, it has been seen in both fibers. Characteristic effects of this damage mechanism are shown in fig. 3.8 for SMF28 and PCF.

In fig. 3.8 (a), FWM power is stable at 470 µW for over 30 min when exposed to 13.2 mW of average pump power, as measured with a Thorlabs S130C optical power meter [72]. Increasing the pump power to 18 mW, fiber damage is seen to deteriorate the previous FWM coupling.

As well, post-damage we cannot re-optimize the mode coupling, shown in fig. 3.8 (b). Here, a length of PCF was exposed to 3.3 mW average pump power for 1 hr, initially producing anti-Stokes

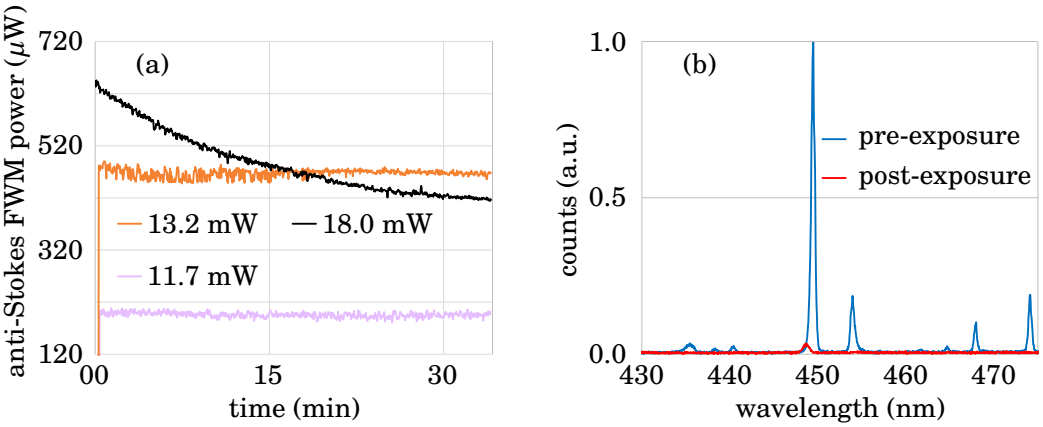

FIGURE 3.8. (a) SMF28 anti-Stokes FWM power over 30 min exposure to several quoted average pump powers. (b) Optimized PCF anti-Stokes FWM mode coupling pre- and post-exposure to 3.3 mW of average pump power for 1 hr.

FWM at 10 µW average power. Prior to exposure, we achieved phase-matching with several FWM modes. Following exposure, however, optimized coupling produces FWM only 4% as intense as pre-exposure.

While we do not fully understand this slow damage mechanism, we propose the following explanations. First, we do not believe it can be attributed to color-center formation in the silica. Color-center formation typically occurs in rare-earth-doped silica fibers (which ours are not), over longer timescales than we observe (several hours), and there is no silica-defect color-center absorption peak near our anti-Stokes FWM wavelength [73, 74]. We also do not observe any damage reversability, as seen in some doped fibers [74].

A possible explanation is dielectric damage exacerbated by surface structural defects. It has been observed that surface defects in silica reduce the optical damage threshold [75, 76]. Considering that we manually prepare each fiber for our experiments and do not polish or etch them, their end faces will have surface defects. It may be the case that optical dielectric damage occurs at the more-susceptible surface-defect sites, reducing efficient mode coupling, without damaging the bulk fiber structure, which would otherwise lead to the previously-described catastrophic damage. This explanation is consistent with the PCF having a lower fast and slow damage threshold than the SMF28.

Both of these damage mechanisms can be mitigated by improving fiber coupling stability, which includes reducing pump-beam wandering, as we explore in sec. 4.7.2. In an effort to mitigate catastrophic PCF damage, we collapsed the fiber end face such that the pump beam would be focused through a more robust piece of solid silica before being guided by the microstructures of the PCF. This procedure and associated results are discussed further in sec. 4.8. In practice, since empirically determining the catastrophic and slow damage thresholds for both nonlinear fibers, we limit pump power beneath these thresholds.

3.1.5 Qualitative Comparison of Nonlinear Fibers

We now summarize the characterizations we performed on our nonlinear fibers which we use to generate visible-wavelength FWM, as each fiber offers advantages depending on experimental design constraints and desired optical properties. Note that the figures quoted in tab. 3.2 are as they relate to our experimental setup, and may change if, for example, a lower peak-power pump laser is used.

TABLE 3.2. Comparison of nonlinear fiber sources.

PCF	SMF28
spectral properties	
visible-wavelength FWM, with signal and idler pairs at ~ 450 nm and ~ 650 nm (fig. 3.3)	visible-wavelength FWM, with signal and idler pairs at 448 nm and 654 nm (fig. 3.4)
wavelength tuneable by structure and phase-matching, for fixed pump (fig. 3.3)	fixed wavelength for fixed pump (fig. 3.4)
nonlinearity	
high χ^3 nonlinear response (fig. 3.5)	low χ^3 nonlinear response (fig. 3.5)
several microwatts of FWM achievable (sec. 3.1.2)	hundreds of microwatts of FWM achievable (fig. 3.8 (a))
no detectable anti-Stokes Raman scattering (fig. 3.3)	increased Stokes and anti-Stokes Raman scattering for given FWM power (fig. 3.4)
power handling	
catastrophic optical damage at $3-4$ mW average pump power (sec. 3.1.4)	catastrophic optical damage at >20 mW average pump power (sec. 3.1.4)
slow optical damage at $3-4$ mW average pump power (sec. 3.1.4)	slow optical damage at $14-16$ mW average pump power (fig. 3.8)
ease of use	
sensitive to pump alignment (sec. 3.1.1)	robust to pump misalignment (sec. 3.1.1)
robust to bend loss and fiber position (sec. 3.1.3)	sensitive to bend loss and fiber position (fig. 3.6)
bespoke (sec. 3.1.1)	commercially available (sec. 3.1.1)

3.2 Noise-Reduction Factor Theory with Experimental Data

In sec. 2.2, we derived a theoretical model of our intensity-correlation experiment, including deleterious effects such as loss, optical noise, and detector noise. We showed how each of these

factors affects the measured multi-beam correlations, giving insight into experimental design. In practice, however, we may not have control over all of the experimental parameters of the model presented in this section. For example, Raman scattering is a noise process associated with the material properties of the optical fibers. It may be reduced via narrowband spectral filtering, or fiber cooling if the FWM photons are spectrally near the pump (see sec. 2.1.3 for theoretical details, and sec. 4.12 for experimental details), but cannot be entirely filtered at the FWM wavelengths, setting a lower-limit on this particular experimental parameter.

In this section, we will characterize the parameters of our theoretical model in terms of practical experimental parameters, and show how the NRF scales accordingly.

3.2.1 Four-Wave Mixing and Raman Power and Noise Characterization

Before beginning our theoretical discussions, we will describe the main experimental features of an intensity-correlation measurement, shown in fig. 3.1. Twin beams (or, in general, any two beams) are generated via the nonlinear processes previously discussed. These beams are spatially separated using, for example, dichroic mirrors or a PBS if the signal and idler photons are orthogonally polarized. Spatially separating the beams along separate paths allows them to be independently spectrally filtered, if required. The twin beams are then focused onto their respective intensity detectors, and their correlations quantified according to the NRF equation.

In our experiments, the detector used for picowatt measurements is a high-detection-efficiency, commercially-available scientific EMCCD camera (Andor iXon Ultra 897 [77]). Because our correlated beams are bright (not single photon), we operate the camera in conventional, non-electron-multiplying mode, as electron multiplication may introduce stochastic noise onto detection of bright signals. The camera is quoted to have greater than 85% detection efficiency at our probe

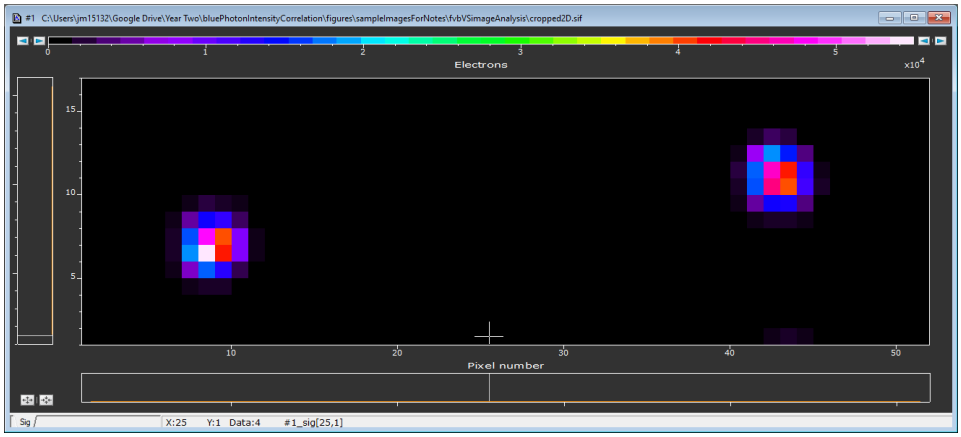

FIGURE 3.9. An example data image for correlated-intensity measurements, using a low-noise CCD camera. Two distinct regions associated with the probe and reference beams are visible.

and reference wavelengths, and we characterize this in sec. 3.2.2. A sample data image is shown in fig. 3.9, wherein two distinct regions associated with the probe and reference beams are visible. The counts in each detection window are vertically binned, summed, and their difference compared across many images according to the NRF equation. The size of each detection window may be selected by the user, and depends on the spot size of the focused beams. Because of dark counts associated with the CCD camera, larger detection windows necessarily increase the detection noise, as we shall see later in this section.

The camera is primarily operated in two readout modes for our experiments: 2D image and Full Vertical Binning (FVB). In 2D image mode, each row of pixels is horizontally and vertically shifted through the readout register, according to the user-defined Horizontal Shift Speed (HSS) and vertical shift speed. Faster shift speeds allow for faster data acquisition, but generally introduce more electronic noise to the data. In 2D image mode, the user can define a sub-region of the CCD to read out smaller than the full array, thereby increasing allowable acquisition rates. Using FVB, all of the CCD rows are vertically shifted before being horizontally shifted simultaneously. Because only one horizontal shift is performed, we expect faster readout times and less electronic noise than using 2D image mode. Noise and speed comparisons of both of these modes are performed in sec. 3.2.2.

We now revisit the NRF equation:

$$\sigma'^{*} = \sigma'^{*}_{p} + \sigma'^{*}_{sp} + \sigma'^{*}_{\varrho} + \sigma'^{*}_{d} \tag{2.32}$$

$$\sigma'^{*}_{p} = 1 - \frac{2\eta_1\eta_2}{\eta_1 + (1+\varrho)\eta_2 + 2d} \qquad \sigma'^{*}_{sp} = \frac{(\eta_1 - \eta_2)^2(F_s - 1)}{\eta_1 + (1+\varrho)\eta_2 + 2d}$$

$$\sigma'^{*}_{\varrho} = \frac{\eta_2^2\varrho\,(F_\varrho - 1)}{\eta_1 + (1+\varrho)\eta_2 + 2d} \qquad \sigma'^{*}_{d} = \frac{2d(F_d - 1)}{\eta_1 + (1+\varrho)\eta_2 + 2d}.$$

where, as before, η_i is channel i detection efficiency, including loss, $F_i = \mathrm{Var}\,[n_i] \,/\, \mathrm{E}\,[n_i]$ is channel i Fano factor, $\mathrm{E}\,[n_\varrho] = \varrho \mathrm{E}\,[n]$ is uncorrelated Raman noise on the reference beam, and $\mathrm{E}\,[n_d] = d\mathrm{E}\,[n]$ is uncorrelated detector noise on both signal and reference channels. We would like to write eqn. 2.32 in terms of parameters which we can experimentally control, namely average pump power p and the size w of the detection region on the CCD. There are other parameters which we can control, *e.g.* camera temperature, but we have already experimentally determined their optimal operating conditions (see box 3.1), which are used for all of the following described measurements, except when noted otherwise.

Specific experimental details for the following measurements are that we are capturing data using FVB at CCD temperature −20°C, with an image integration time 0.07 s, at HSS 80 kHz, and analyzing the data in 10 sets of 100 images. The CCD is internally fan cooled. We are also using a 20 nm bandpass filter and adjustable pinhole filters on the Stokes FWM channel to remove some of the Raman scattering noise. A 1 m length of PCF was used for this data.

BOX 3.1. Camera CCD Temperature Optimization.

In sec. 3.2, we characterize the optical and detector properties of our correlated-intensity experiment. Prior to this characterization, we determined the optimal camera CCD temperature at which to take our data, taking into account dark counts and F_d, the detector Fano factor.

In fig. 3.10, we measure the average dark counts over some camera integration region and F_d, as a function of camera temperature. The camera CCD was allowed to cool for 5 min before each measurement. We find that although the Fano factor generally increases as the camera cools, the number of total counts reaches a minimum around −20°C. We also plot $\mathrm{E}[n_d](F_d - 1)$, similar to the detector noise contribution in eqn. 2.32, and see that this metric also reaches a minimum around −20°C. Our data will therefore be taken at this temperature, as a compromise between total dark counts and Fano factor.

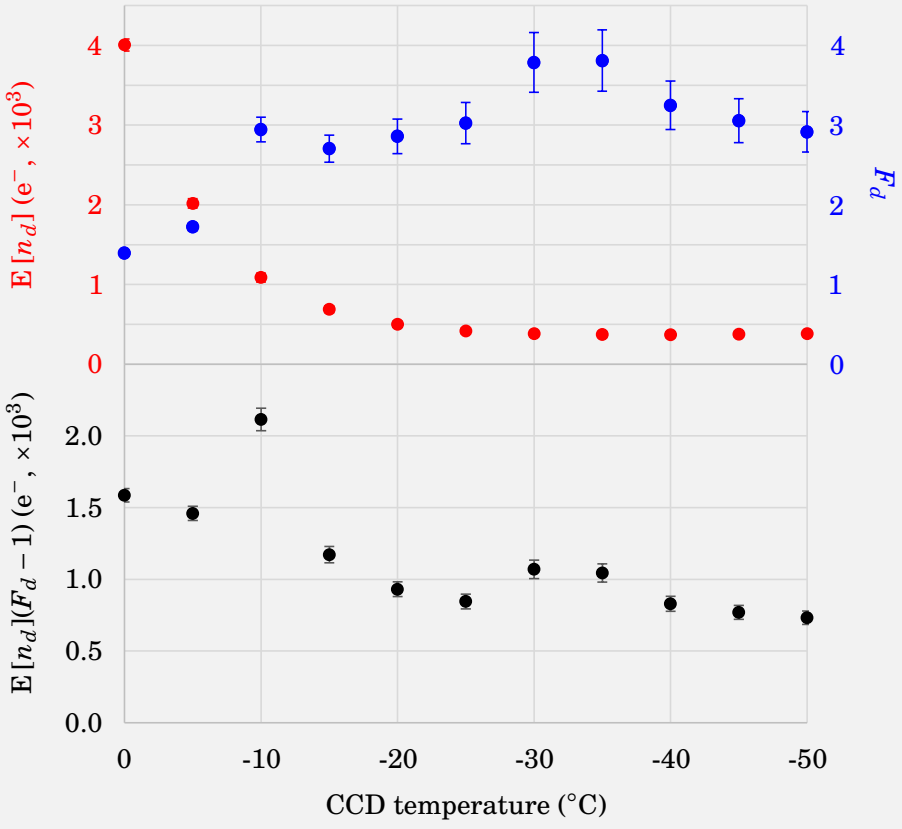

FIGURE 3.10. Plots showing the scaling of the camera dark counts $\mathrm{E}[n_d]$, Fano factor F_d, and $\mathrm{E}[n_d](F_d - 1)$ as a function of temperature, with decreasing temperatures to the right. All data was taken in FVB mode, with 0.01 s integration time at 1 MHz HSS.

First, let us consider $F_s(p)$, which is independent of the detector window size. Each beam is focused onto the CCD as previously described, and the Fano factor calculated according to

$$F_i = \frac{\mathrm{Var}[n_i]}{\mathrm{E}[n_i]}. \tag{2.16}$$

We measure the average pump power before the fiber input lens using a Thorlabs S130C optical power meter. The results of this measurement are shown in fig. 3.11.

The average FWM power data is fit according to eqn. 2.6, and we see good experimental agreement with the theoretical model [28]. Also important to notice is that the average detected power on the Stokes and anti-Stokes beams do not precisely match. This is because, at low power, Stokes Raman scattering dominates the FWM signal. Indeed, the Raman noise represents 35% of the total measured Stokes power at $p = 412\,\mu\mathrm{W}$, when comparing to the anti-Stokes beam which we assume to be otherwise noiseless, and after adjusting for unbalanced detection efficiency.

The Fano factor data of fig. 3.11 is fit according to an exponential function $F_s(p) = ap\exp(bp)$, where a and b are fitting parameters. One would expect the Fano factor of the pump to increase constantly with average power, as well as the FWM Fano factor, according to discussions from sec. 2.2:

$$\mathrm{Var}[n] = \mathrm{E}[n] + \beta\mathrm{E}[n]^2 \tag{2.22}$$

$$\mathrm{Var}[n_i] = \mathrm{E}[n_i] + \beta\mathrm{E}[n_i]^2. \tag{2.23}$$

However, because of the exponential nature of the FWM gain, the Fano factor scales accordingly. Note that because of inefficient charge collection and transfer beyond the saturation level of the CCD, the camera no longer responds linearly in this regime [78, 79]. The effect of saturation on our data is that the Fano factor at optical powers beyond camera saturation increases greater than predicted by the fit curve shown in fig. 3.11, which worsens the measured NRF.

To measure $\varrho(p)$, the ratio of Raman-to-Stokes-FWM power, we use the spectrometer, not the CCD camera. The justification for this is that it is difficult to confidently determine the total Raman power, separate from the FWM, on the camera images due to dispersion from the lenses and other optical components. A sample data image is shown in fig. 3.12 (a), with a 20 nm bandpass filter in place. For each data image at each pump power, we first determined the wavelengths associated with FWM. Performing a linear fit to the spectral data allowed us to approximate the Raman spectrum over these wavelengths. We then determined $\varrho(p)$ by taking the ratio of the integral under the FWM and Raman spectrum, subtracting the Raman integral from the FWM integral to get an accurate estimate of the true FWM power. Note that this approximation of the Raman spectrum and $\varrho(p)$ represents a lower-bound, as Raman scattering may be stimulated at the FWM wavelength by the FWM itself [28]. Repeating this process for each pump power, we plot our FWM Stokes power, Raman power, and ϱ as a function of average pump power, as shown in fig. 3.12 (b). The FWM and Raman power increase exponentially and

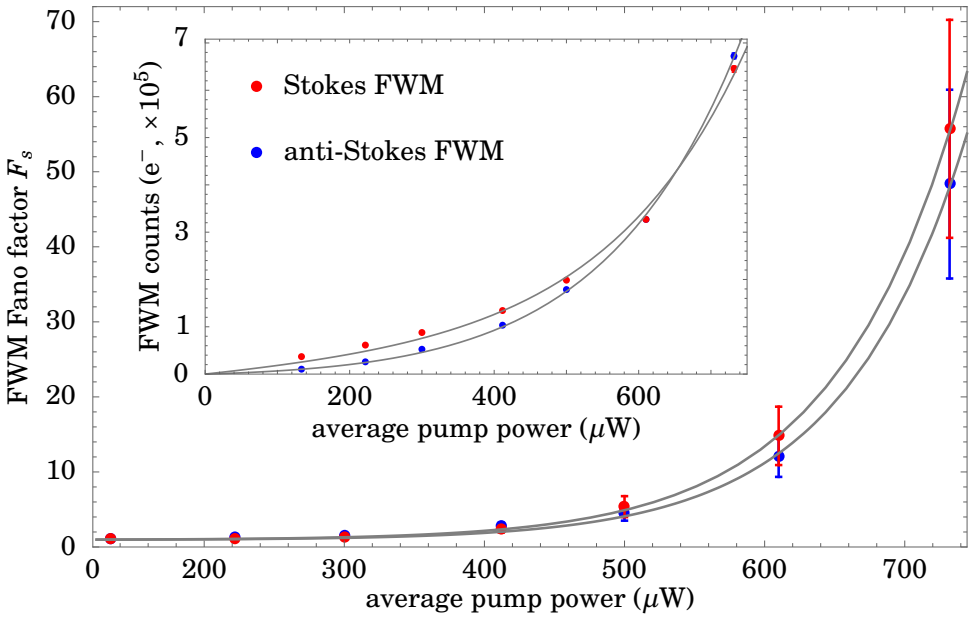

FIGURE 3.11. (outset) Exponentially increasing FWM Fano factor, as pump power increases. (inset) Exponentially increasing FWM average counts as a function of pump power. Error bars on inset figure are comparable to point size.

linearly, respectively, in good agreement with our theoretical discussions of sec. 2.1. Dividing these two fits shows good agreement with our $\varrho\,(p)$ data.

Because we do not have precise spectral filtering about our FWM signal, we simulated spectral filtering bandwidths by varying the Raman integration limits. This is equivalent to varying the slope parameter s of the linear fit to the Raman power $\mathrm{E}\,[n_\varrho]$. In practice, one achieves better spectral filtering with narrower bandwidth absorptive or reflective filters, or using a pinhole to block the dispersed Raman scattering, detailed further in sec. 4.9. Varying s allows us to predict the NRF improvement for various degrees of spectral filtering. Shown in fig. 3.12 (c) is a plot of s against $\varrho\,(404\,\mu\mathrm{W})$. We find good agreement of this data with an exponential fit, so we can precisely predict $\varrho\,(p,s)$.

Next, we measure the Stokes Raman Fano factor as a function of pump power $F_\varrho(p)$, using the CCD camera. To perform this measurement, we removed the pinhole filter, allowing all of the Raman which was not bandpass filtered to be incident upon the camera. Then, the Raman Fano factor was calculated as typically done with the FWM signal, but the integration window was centered on the tail of the FWM Stokes region, dominated by Raman noise (example data image shown in fig. 3.12 (d)). The results of this measurement are shown in fig. 3.13. Because Raman intensity varies linearly with average pump power, as we are not in the stimulated regime, we expect $F_\varrho(p)$ to change linearly with pump power. Due to poor measurement precision associated with super-Poissonian pump intensity fluctuations, this trend is difficult to measure. We see,

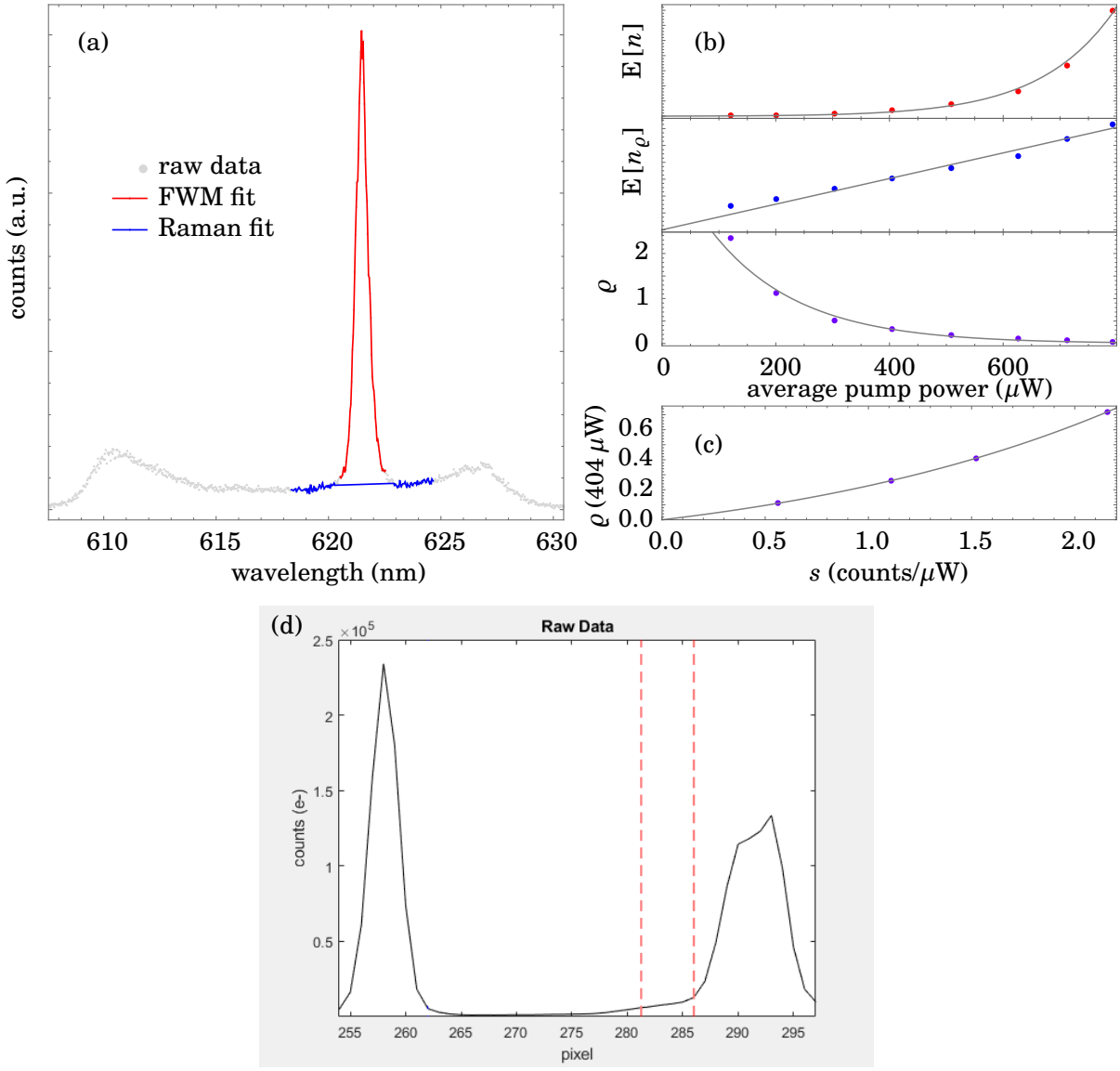

FIGURE 3.12. (a) A sample spectral data image used to calculate $\varrho\,(p)$, with FWM and Raman linear fits highlighted. This data image represents $\varrho\,(303\ \mu\text{W}) = 0.78$. (b) FWM power, Raman power, and ϱ as a function of pump power. (c) Scaling of $\varrho\,(404\ \mu\text{W})$ against s, the slope parameter of $\text{E}\,[n_\varrho]$. Error bars are not drawn for these data, as each point is taken from one spectral image – the data serve as an approximation for our model, and confirm the characteristics which we expect to see in our experiment. (d) Example data image showing the demarcated Raman scattering for calculating $\text{E}\,[n_\varrho](p)$ and $F_\varrho(p)$.

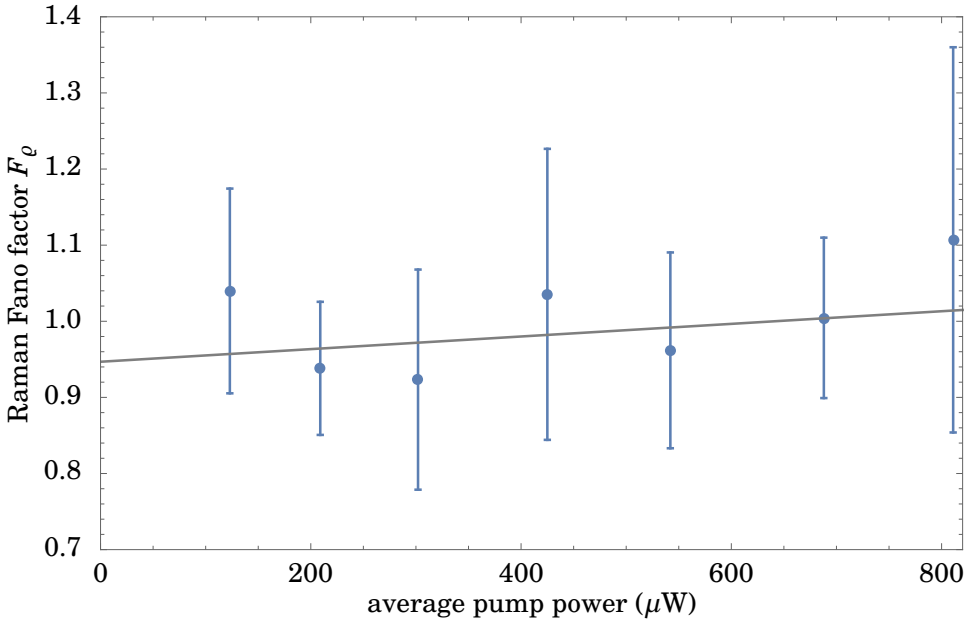

FIGURE 3.13. A plot showing the Raman Fano factor scaling with pump power. A weighted linear fit is also shown.

however, that the data are all 1 within one standard deviation, so we will use this value for our later simulations.

Thus far, we have characterized optical noise components $F_s(p)$, $F_\varrho(p)$, and $\varrho\,(p,s)$ of our intensity-correlation measurements, from eqn. 2.32. To fully simulate eqn. 2.32, we also require knowledge of the detector efficiency and noise properties, which will be the subject of the following section.

3.2.2 CCD Camera Detection Efficiency and Noise Characterization

In this section, we discuss our characterizations of the CCD camera with which we perform our intensity-correlation measurements. In particular, we estimate the camera efficiency at the Stokes and anti-Stokes FWM wavelengths, and measure the noise properties of the camera so that we may write the dark counts as a function of pump power and integration window size.

The initial experimental design to measure the efficiency of the camera was using an unpolarized cube Beam Splitter (BS) in the path of the Stokes or anti-Stokes beam, depending on which is being calibrated. One output of the BS was shone onto the CCD, and the other to a NIST-traceable* calibrated reference power meter (Thorlabs S130C) to which the CCD counts

*The National Institute of Standards and Technology (NIST), "develops and maintains the U.S. national standards for the characterization of lasers, along with detectors and other optical and optoelectronic components used with lasers and in laser-based systems" [80].

could be compared. We used SMF28 rather than PCF for this experiment because of the brighter available FWM produced using SMF28, reducing the optical shot noise as well as producing powers compatible with the reference power meter. In our initial experiment, however, we operated at several picowatts of FWM power to not saturate the CCD camera.

Before calibrating the CCD, we first had to measure the splitting ratio of the BS. The BS ratio was measured using two Thorlabs optical power meters, one at the reference output and one at the signal output, which would otherwise be incident on the CCD in the absence of the power meter. Note that we do not need to know the loss introduced by the BS, so long as we have well-calibrated the power ratio of the BS outputs. The signal power meter was then removed, allowing calibration of the CCD.

In our initial tests at −25°C, we measured a BS splitting ratio of 0.65 at 462 nm, and a camera efficiency of less than 0.01. Because we expect 0.86 at 25°C, according to the camera datasheet [77], we measured the camera efficiency again at 10°C to check if we would observe any efficiency change closer to the factory-calibrated temperature, although we do not expect to see any change in camera efficiency with temperature (see fig. 3.14). Again, we measured less than 0.01 camera efficiency.

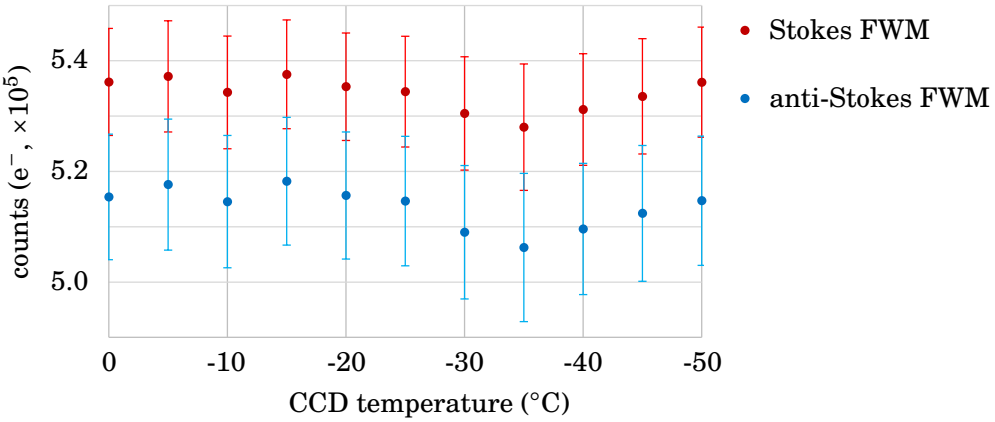

FIGURE 3.14. Plot of average number of counts per image for various CCD temperatures, using the same average pump power. We see that the efficiency of the camera does not change with temperature, below 0°C. Fluctuations in average power are due to super-Poissonian pump intensity noise.

The problem with our initial tests was that the reference power meter was not operating reliably at picowatts of power, near the quoted noise floor of the power meter, 500 pW. To resolve this, we implemented two solutions, both of which reduced the power incident on the CCD so that the FWM power could be increased well above the noise floor of the power meter: (1) use a BS with a splitting ratio which favored the reference power meter, and (2) filter most of the incident light to the CCD with Neutral-Density (ND) filters to avoid camera saturation at high optical powers. This procedure requires careful calibration of the new BS as well as all ND filters.

We used a 1 mm-thick non-anti-reflection-coated glass slide angled at approximately 45° as the new BS. The splitting ratio was measured as before, using the SMF28 as a source, but at several FWM powers to assure that there would be no nonlinearity affecting our calibration at different powers, and to determine error bars. Because this procedure is similar to how the ND filters were calibrated, the data from this measurement is shown in fig. 3.15. We measured the splitting ratio of the BS to be ref/sig = 3.15 ± 0.04, satisfying objective (1) above. As well, calibration of the BS, ND filters, and CCD camera are taken at microwatts of FWM power, satisfying objective (2) above.

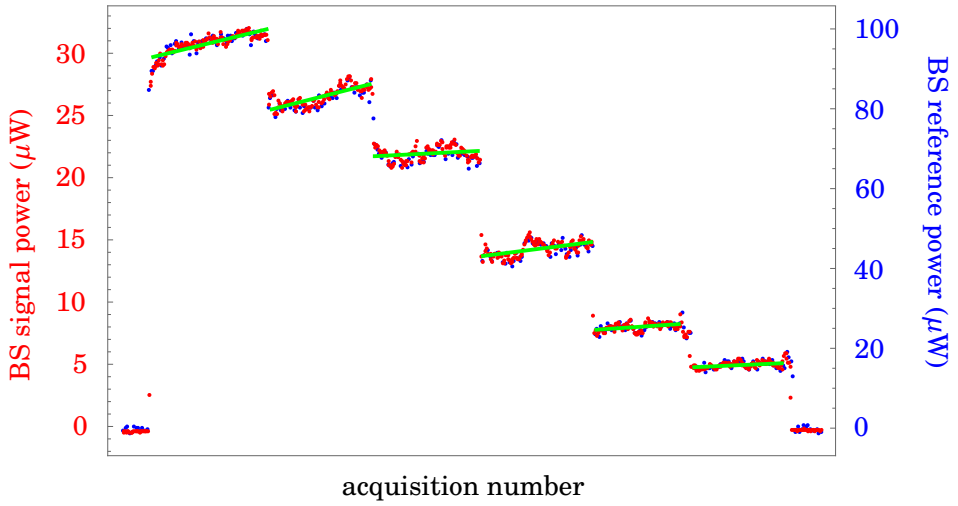

FIGURE 3.15. The power measured by the signal and reference power meters, to determine the splitting ratio of the BS. At each pump power, a linear fit was used to determine the average power at each output, and the ratio of these powers gives us a splitting ratio of the BS.

To reduce the optical power on the signal channel (microwatts) to safe operational powers for the CCD camera (picowatts), we require a ND filter with Optical Density (OD) of order 6, where OD is defined as $\mathrm{OD} = \log_{10}(1/T)$, and T is the filter transmission. Because measuring the transmission of an OD6 filter with calibrated optical power meters would present the same problems as initially encountered with the camera efficiency measurement, we measured several weaker ND filters, which were then placed in succession in the signal beam path for the final camera efficiency measurement. The transmission of each ND filter was measured by placing the filter in the pre-calibrated signal path. We measured a filter with a quoted OD of 1 to be 1.053 ± 0.006, and two filters with quoted ODs of 2 to be 2.218 ± 0.006 and 1.995 ± 0.006. Placing these in succession yields an OD of 5.27 ± 0.01.

Now, measuring the camera quantum efficiency as before, but with the new BS and ND filters in place, we measure 0.84 ± 0.01 at 462 nm and -25°C, in close agreement with the datasheet [77]. The camera data for this measurement is shown in fig. 3.16, where the power meter data P

may be converted to number of photons n using $n = Pt\lambda/hc$, where t is the camera integration time, λ is the wavelength, and h and c are Planck's constant and the speed of light, respectively. Measuring the transmission of, and using datasheet values for, the other optical components along the anti-Stokes FWM path (two lenses, two dichroic mirrors, and a bandpass filter), we determine that the total channel efficiency, including the camera efficiency, is approximately 0.75.

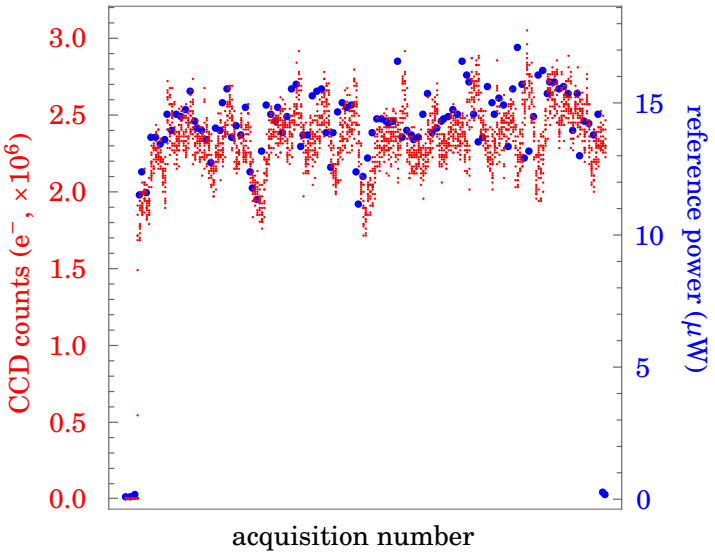

FIGURE 3.16. The power measured by the CCD and reference power meter, to determine the quantum efficiency of the CCD.

Measuring the camera efficiency at the Stokes FWM wavelength (626 nm) is not as straightforward, due to broadband Raman noise contaminating the signal, increasing our estimated quantum efficiency. Our approach to estimating the camera detection efficiency at the Stokes wavelength is as follows. At higher pump powers, FWM tends to dominate the Raman noise, as seen in fig. 3.11, allowing us to approximate the camera efficiency. We assume that the FWM beams are well-correlated at the fiber output, measure the loss or refer to datasheets for the optical components along the Stokes beam path, and compare the average counts of each camera measurement region E $[n_2]$/E $[n_1] = \eta_2/\eta_1$ at high average pump powers, given that we have already measured $\eta_1 = 0.84 \pm 0.01$. Following this procedure, we calculate that the camera efficiency at 626 nm is $\eta_2 = 0.81 \pm 0.01$, while the datasheet quotes 0.92 [77]. We may similarly estimate the transmission of the Stokes FWM channel as before, calculating a total channel efficiency of approximately 0.74. The drawbacks of these approximations are that there is still considerable Raman noise measured in the Stokes beam, even with filtering. Also, because of wavelength-dependent loss in the fiber, the twin beams are not perfectly intensity correlated at the fiber output, although this is approximately true for the 1 m lengths of fiber which we are using.

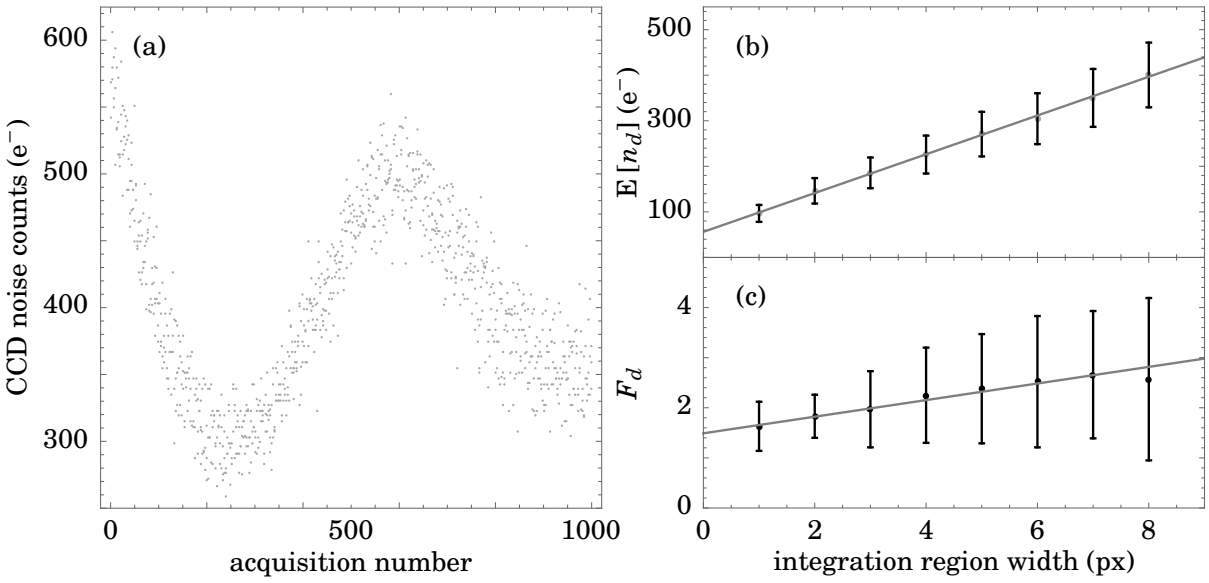

FIGURE 3.17. (a) Data set for $w = 8$ px, used to calculate $d(p,w)$ and $F_d(w)$. (b) Plot of mean camera dark counts as a function of pixel width, with weighted linear fit. (c) Plot of camera dark count Fano factors as a function of pixel width, with weighted linear fit.

We may also approximate the CCD efficiency at the PCF FWM wavelengths. Although the typical anti-Stokes and Stokes wavelengths of the SMF28 and PCF differ by −12 nm and +25 nm, respectively, and we have not measured the CCD efficiency directly at our PCF wavelengths, we do not expect the efficiency difference to vary more than a few percent, according to the camera datasheet [77]. We will therefore use the stated efficiencies here as an approximation. Considering these approximations, our camera quantum efficiency measurements are sufficiently accurate to retrieve useful information from the proceeding simulations, as will be discussed in sec. 3.2.3.

Finally, we measure the noise properties of our CCD camera for various integration-region widths w, which directly relates to the focusing conditions of the FWM beams. In principle, the focused FWM spots may not be the same size, but for simplicity here, we will assume that they are. The procedure for measuring the average camera dark counts $d(p,w)$ and Fano factor $F_d(w)$ is the same as described for measuring the Raman noise, but with the camera shutter completely closed. The integration width was varied from realistic values of 1 to 8 pixels, and a weighted linear fit to the data performed, as shown in fig. 3.17. We see good agreement with the linear fits, and the large error bars are due to camera temperature fluctuations about −20°C, seen in fig. 3.17 (a). The linear fit for the mean dark counts does not have zero intercept. The y-intercept of the mean counts therefore represents a fundamental readout noise associated with the camera, approximately 56 electrons for our camera settings. Note that these noise characterizations are only valid for the integration time, HSS, temperature, and other specific operational parameters

described in these sections.

As the camera noise is independent of pump power p and detection efficiency η_i for each region, $d(p,w)$ decreases exponentially relative to FWM power for a given integration width w.

We have now characterized all of the experimental parameters of eqn. 2.32, which predicts NRFs and includes deleterious effects such as optical and detector noise, in terms of average pump power p, optical noise filter bandwidth s, and beam focusing condition w. In the following section, we apply these characterizations to the theoretical model of the experiment to investigate effects of, for example, noise filtering and detector efficiency balancing.

3.2.3 Noise-Reduction Factor Revisited

Since we have measured or approximated all of the parameters of the experimental NRF eqn. 2.32, we rewrite it as

$$\sigma'^{*}(p,s,w) = 1 - \frac{2\eta_1\eta_2 + (\eta_1-\eta_2)^2(F_s(p)-1) + 2d(p,w)(F_d(w)-1)}{\eta_1 + (1+\varrho\,(p,s))\eta_2 + 2d(p,w)}, \tag{3.1}$$

where $F_\varrho(p) = 1$, from results presented in sec. 3.2.1. The remaining fits according to our experimental characterizations are

$$F_s(p) = 1 + 0.00004pe^{0.01p} \qquad \varrho\,(p,s) = 0.65se^{-0.0065p+0.33s}$$

$$d(p,w) = (0.98w + 1.27)e^{-0.0041p}/p \qquad F_d(w) = 0.17w + 1.5$$

$$\eta_1 = 0.75 \qquad \eta_2 = 0.74.$$

Because of the low-noise properties of our detection scheme, we see in fig. 3.18 (a) that decreasing integration region width has only a small effect on our measured intensity correlations as pump power (and consequently FWM power) increases. As $p \to 0$, our model approaches only camera noise, as expected.

In fig. 3.18 (b), by contrast, we see a much more dramatic effect on the NRF as we vary the FWM-to-Raman ratio. We consider three forms of $\varrho\,(p,s)$, using $\varrho\,(404\ \mu\text{W})$ as a benchmark. For $\varrho\,(404\ \mu\text{W}) = 0.1$, we are in the case of perfect filtering about our FWM. Increasing to $\varrho\,(404\ \mu\text{W}) = 0.35$ represents a realistic intermediate scaling of $\varrho\,(p,s)$, using spectral bandpass and pinhole filtering. Without pinhole filtering, we have $\varrho\,(404\ \mu\text{W}) = 2.5$, according to fig. 3.12 (a). From this data, we learn that for intermediate pump powers, reducing Raman noise is a valuable technique for improving the measured intensity correlations.

In fig. 3.18 (c), we vary the relative channel efficiency, with our predicted $\eta_2 = 0.74$ shown for comparison. Increasing or decreasing η_2 by only 0.04 in either direction can seriously increase the NRF at high power. Assuming the datasheet value $\eta_2 = 0.92$ at 650 nm, and 10% loss due to optics, we have an upper limit on detection efficiency of $\eta_2 = 0.83$, which is in fact worse than the balanced detection case of $\eta_2 = 0.75$. According to this model, as FWM power increases, balancing detection efficiency becomes more critical (assuming super-Poissonian F_s). As discussed

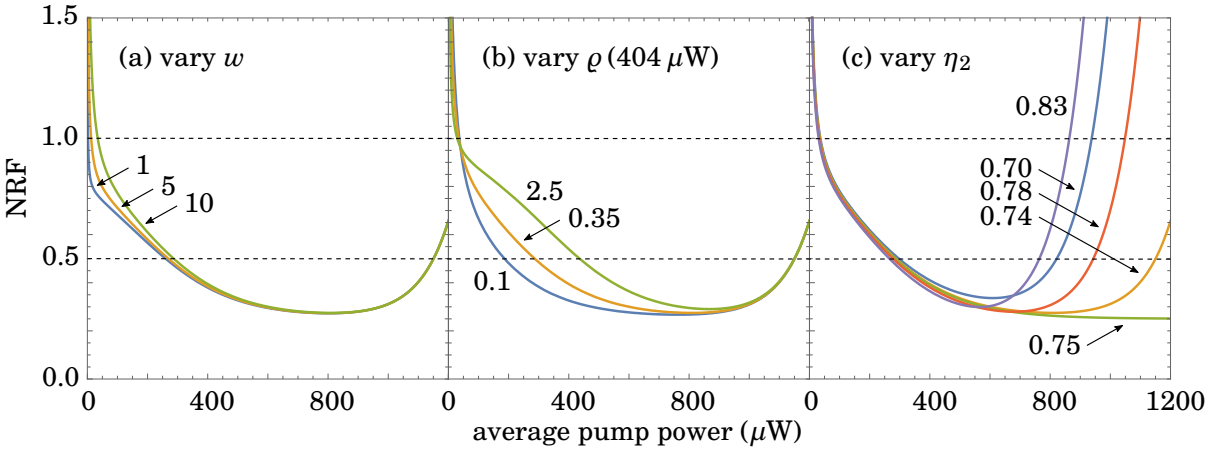

FIGURE 3.18. Plots of eqn. 3.1 varying (a) camera integration region width w, (b) Raman-noise-to-FWM-signal $\varrho(p,s)$, and (c) relative detection efficiency. In (a), we let $\varrho(404\,\mu\text{W}) = 0.35$, $\eta_1 = 0.75$, and $\eta_2 = 0.74$. In (b), we let $w = 10$, $\eta_1 = 0.75$, and $\eta_2 = 0.74$. In (c), we let $w = 10$, $\eta_1 = 0.75$, and $\varrho(404\,\mu\text{W}) = 0.35$.

before, this is because the correlated photons on the more-efficient channel do not, on average, have their correlated pair photon detected, and fluctuate with super-Poissonian F_s. High-power intensity-correlation experiments should therefore implement classical noise suppression, or balance detection efficiency.

There are several drawbacks to the presented model which affect its accuracy, but not its general features. Above, we assumed that there are no noise photons in the anti-Stokes FWM channel. This is not true, however. Because our pump laser is multi-mode, we excite several FWM modes simultaneously in the nonlinear fibers. While we do optimize on a particular mode for each experiment by adjusting the coupling mirrors and fiber position, there are always other modes excited. These modes are only relatively weakly excited, but because their Stokes pair is typically beyond the bandwidth of our bandpass filter, the Stokes pairs are not detected. The effect of this is increasing the minimum measurable NRF and disimproving the NRF scaling for intermediate powers, similar to fig. 3.18 (b). We also observe anti-Stokes Raman scattering in the SMF28, as discussed in sec. 3.1.1, which has a similar effect.

A second drawback, not necessarily of this model, but of using it to precisely predict the outcome of a given experiment, is that several of the parameters which we do not have direct experimental control over can change from measurement to measurement, requiring re-characterization of the experiment. For example, we know from sec. 3.1.3 that changing the fiber position can change the FWM gain, but we do not have a repeatable way to optimize this position. If the fiber requires cleaving or is otherwise moved, or if a new length of fiber is used, then $F_s(p)$ and $\varrho(p,s)$ may no longer be accurate.

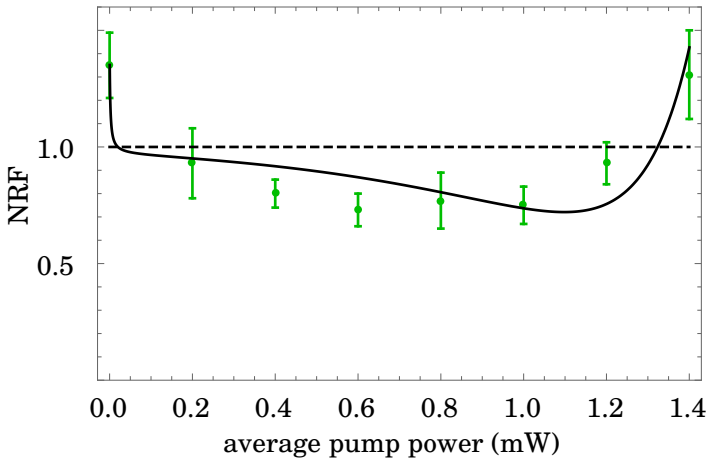

FIGURE 3.19. Plots showing experimentally measured NRFs with average pump power, fit according to eqn. 3.1 with one free parameter, η_2.

Finally, in producing the plots shown in fig. 3.18, we have had to infer η_2 from several other measurements, as direct measurement is complicated by the Raman noise. Specifically for the PCF, we have had to assume that the camera efficiency does not change significantly over 25 nm from the inferred SMF28 η_2. While these approximations are reasonable, we see the importance of balancing detection efficiency at intermediate and high FWM powers. Therefore, accurate predictions using this model at high pump power require careful detector calibration.

Despite these drawbacks, we see in fig. 3.19 that the experimental model eqn. 3.1 well-fits a sample data set, with only one free fit parameter, η_2. The experimental parameters $F_s(p)$, $d(p,w)$, $F_d(w)$, and $\varrho\,(p,s)$ were all characterized in one hour of lab time using two data sets: a spectrum of the Stokes FWM and Raman scattering at 1 mW pump power, and intensity data of the FWM counts against pump power, including 0 mW to establish camera noise.

To reiterate from sec. 2.2, considering that we have derived this model with a particular experiment in mind, the model and the techniques used to derive it apply to many similar experiments [2, 6, 10, 11, 13, 14]. Most importantly, the intuition offered by this model is crucial for a complete understanding of the experiments discussed in this thesis.

3.3 Normally-Distributed Intensity Data and Unbiased Sample Estimators

At the end of this chapter, we will outline various protocols which we use to analyze our intensity data. To fairly analyze and report the data, however, we require unbiased estimates of the population mean, variance, and standard deviation. Practical limitations may also restrict sizes of data sets, and under these conditions, we would like to know if one can still retrieve meaningful

population estimates from small sample sizes. In this section, we will discuss the aforementioned estimators, and under what assumptions they are unbiased. We will also show that our data satisfy these assumptions, and that we can retrieve meaningful sample statistics over small sample sizes.

There are several reasons why a particular experimental setup might favor acquiring small data sets. For example, one's source may exhibit high-frequency average power fluctuations. As well, in an imaging application, the sample may evolve on timescales comparable to image-acquisition rates. If we then calculate the NRF of our data and its uncertainty over 5 sets of 100 images, or 100 sets of 5 images, are either one of these scenarios more statistically significant?

To show that we can retrieve meaningful information from small sample sizes, we need to find an unbiased estimator for the population mean and standard deviation of the data set, and show that our data fits whatever requirements these estimators impose to be unbiased.

Because we cannot take data for an infinite amount of time, any statistical estimation we make of our data will necessarily be a sample estimation. We would like for this sample estimation to represent the population in an unbiased manner – meaning that if we, for example, repeatedly calculated the mean of our population over many samples, the mean of the sample means would converge to the population mean. It will not be proved here, but the sample mean $\mathrm{E}[x] = \sum_{i=1}^{n} x_i/n$ is an unbiased estimate of the population mean [81]. For clarity, in this section we will denote sample estimates with lower-case variables, and population estimates with upper-case, *e.g.* $\mathrm{E}[x]$ and $\mathrm{E}[X]$.

We will now discuss an unbiased estimation of the population variance for normal distributions. Though we will not rigorously prove all statements made in this section, we will try to offer some intuition, and mathematical proofs may all be found in ref. [81, 82]. Assuming that we already know the population mean, we calculate the sample variance using the following unbiased estimator:

$$\mathrm{Var}[x] = \frac{1}{n}\sum_{i=1}^{n}(x_i - \mathrm{E}[X])^2. \tag{3.2}$$

However, when we do not know the population mean *a priori*, and we only have access to the sample mean, then we necessarily will underestimate the population variance using eqn. 3.2 (unless $\mathrm{E}[x] = \mathrm{E}[X]$) because the data with which we calculate the variance are correlated with the sample means rather than population mean. To unbias the sample variance estimator, we use Bessel's correction, where n in the denominator of eqn. 3.2 is replaced with $n-1$:

$$\mathrm{Var}[x] = \frac{1}{n-1}\sum_{i=1}^{n}(x_i - \mathrm{E}[x])^2. \tag{3.3}$$

If we would like to report our mean and uncertainty in the same units, then we must take the square root of the sample variance, yielding the sample standard deviation. This standard deviation estimator is biased, however, as the square root is a nonlinear function. To unbias this

estimator, we introduce a correction factor $c_n = \sqrt{(n-1)/(n-1.5)}$, which depends on the number of measurements in our sample, such that $\mathrm{SD}[x] = c_n \mathrm{SD}[X]$. For a normal distribution, c_n quickly converges to one, with $c_5 = 0.94$, $c_{10} = 0.97$, and $c_{25} = 0.99$. Instead of implementing c_n, however, the sample standard deviation estimator for a normal distribution may also be approximately unbiased with the replacement of $n-1$, as in eqn. 3.3, with $n-1.5$. Using this approximation, there is a 0.4%, 0.08%, and 0.01% bias for $n = 5$, 10, and 25, respectively [82].

This amount of bias is acceptable for the precision of the data which we are acquiring, but we must first prove that our data is normally distributed to have access to this unbiasing approximation. To do this, we shone our FWM signal on to the CCD camera, with an integration time of 0.1 s, counted the number of electrons registered in the blue channel for each of 1000 images, and compared a histogram of this data to a normal distribution. The results of this analysis are shown in fig. 3.20.

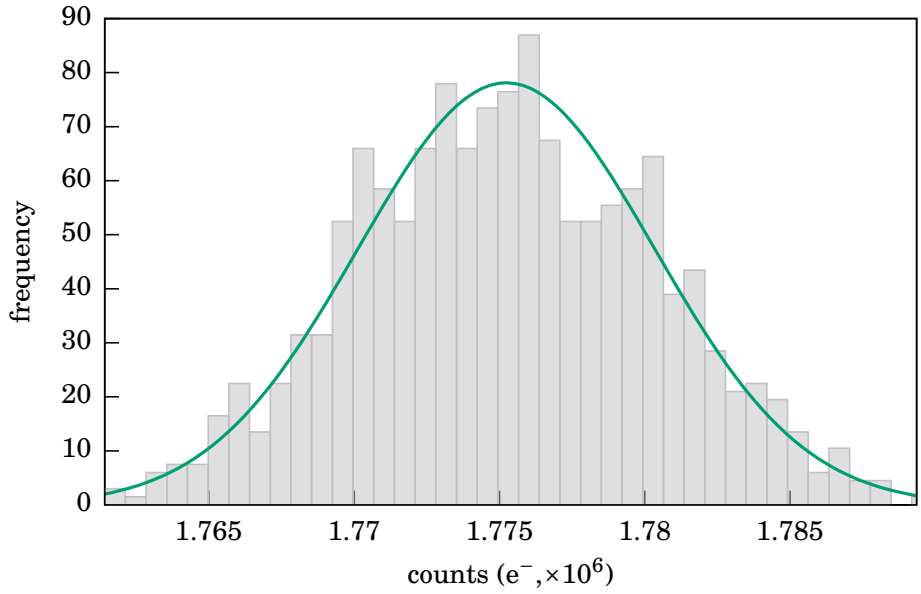

FIGURE 3.20. A histogram showing that the distribution of our raw FWM counts agrees with a normal distribution with 95% confidence. Sample mean and standard deviation of the fitted normal distribution are 1.775×10^6 and 5107, respectively.

These data yield $\chi^2/\nu = 0.90$, where $\nu = 36$ is our number of degrees of freedom (non-empty histogram bins minus estimated model parameters), and $\chi^2_{\nu,0.05}/\nu = 1.42$, where 0.05 is our significance level for testing the model. Thus, we can conclude that our raw count data is normally distributed with at least 95% confidence [83], and use the above detailed estimators to calculate the population mean and standard deviation over small data sets.

We also can use the fact that our counts are normally distributed to predict the distribution

of the NRF. Although deriving the distribution from the NRF equation itself is difficult, we make assumptions based on previous discussions to determine the likely form of the distribution, and verify this with our data. Again, most of the mathematical techniques we use will not be rigorously proved here, but are addressed in ref. [84, 85].

Because our raw counts n_1 and n_2 are normally distributed, so are $n_1 - n_2$ and $n_1 + n_2$, according to

$$\sum_i \text{Normal}(\text{E}[n_i], \text{Var}[n_i]) \sim \text{Normal}\left(\sum_i \text{E}[n_i], \sum_i \text{Var}[n_i]\right).$$

Therefore, the variance of the sample variance of $n_1 - n_2$, which we calculate for each data set, is proportional to a χ^2 distribution [84]. The unbiased sample mean of $n_1 + n_2$ is $\text{E}[n_1 + n_2]$. Because we expect a non-zero-mean distribution, we expect the NRF to follow a non-central χ^2 distribution, which is a special case of a gamma distribution [85]. We will use the gamma distribution then as our ansatz.

The gamma distribution has two parameters, shape $\alpha > 0$ and scale $\beta > 0$, where the mean and arithmetic standard deviation of the distribution are $\alpha\beta$ and $\sqrt{\alpha\beta^2}$, respectively. Shown in fig. 3.21 is a normalized histogram of NRFs calculated from a 10000-sample data set, with a gamma distribution overlaid. Our data represents a gamma distribution with at least 95% confidence, and thus we conclude that our ansatz is appropriate.

3.4 Noise-Reduction Factor Data Analysis Code

As the experimental setup evolved and matured, so did the code which we used to analyze the data it produced. In this section, we will describe the various data analysis techniques we employed to quantify multi-beam correlations using the CCD camera.

The first several versions of data analysis techniques are based on data captured in 2D image mode, rather than FVB mode. This was due to an incomplete understanding of CCD camera technology. As we shall see later in this section, FVB offers improved readout fidelity, as well as faster data acquisition.

3.4.1 Version One with 2D Image Mode

The first iteration of analysis code was inspired by astronomy data-processing techniques, wherein a series of flat-field and dark-current images are taken prior to data acquisition, for later bias subtraction [86]. In our case, a series of dark images is taken with the pump laser off, but otherwise normal operating conditions, to account for ambient uncorrelated light. The dark images are averaged and subtracted from each data image.

The user defines the coordinates of the data image regions associated with the Stokes and anti-Stokes FWM. All data images are then loaded individually, and each pixel in each region of each image is compared to the same pixel of the average background image. If the count in the data image is within 3 standard deviations of the background count, the data image pixel is set

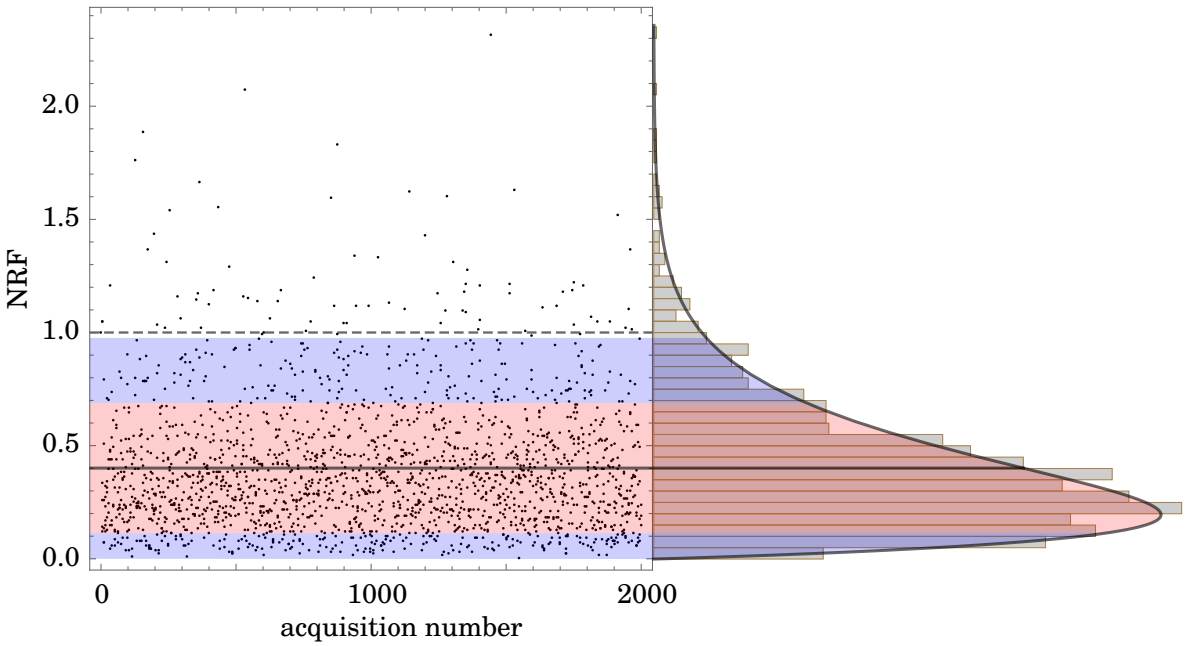

FIGURE 3.21. Two plots showing the calculated NRFs and a histogram representation of the data, with overlaid gamma distribution. This data represents 10000 images analyzed in 2000 sets off 5 images. Shown also is the mean value at 0.40 ± 0.29, and one and two standard deviations in red and blue, respectively.

to value 0. Pixels above this threshold are unaltered. An example of this is shown in fig. 3.22. Within each user-defined region of interest, the counts are then summed, stored, and the value of the correlation parameter is displayed once all images have been analyzed.

While this method of analysis does work, it is slow. Average data analysis times using this method last several hours to a day with a standard desktop computer, depending on the size of the integrated regions and number of data images. As well, as we showed in sec. 3.2.3, detector noise is small compared to the bright FWM signals.

This analysis technique may also bias the measured intensity correlation, as we will discuss in sec. 3.4.4.

3.4.2 Version Two with 2D Image Mode

The second version of the data analysis code is similar to the method described in sec. 3.4.1. The difference between this and the previous iteration is that the background-zero threshold may be varied independently and optimized for each region of interest. The motivation for this change was that the optical noise power may be different within in each defined FWM region (*e.g.* Raman scattered photons are present in the Stokes but not the anti-Stokes FWM). As with the

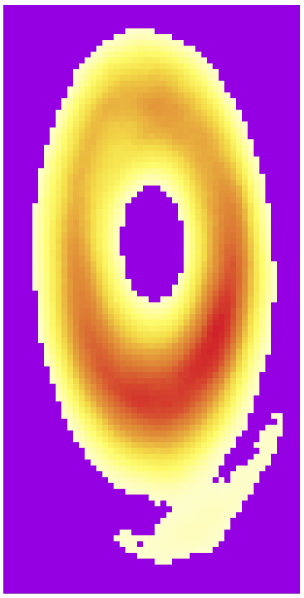

FIGURE 3.22. Shown is one of the regions of interest around a focused FWM spot on a data image, from fig. 4.1. Purple pixels have been set to value 0, and scaled pixels are the unaltered signal.

previous version, each data image is loaded individually, and the analysis is made even slower by the optimization of the background-noise threshold, now on the order of days. This is because the threshold for each region is varied independently, and the NRF fully recalculated for each threshold value.

For example, assume that we have 100 images in a data series. The Stokes and anti-Stokes background thresholds are varied independently from 100 counts to 1000 counts with a step size of 10 counts. The program, throughout its runtime, will load $90 \times 90 \times 100 = 810000$ images. If each image takes one second to load and analyze, and the rest of the program runtime is negligible, the software would take over 9 days to run.

As well, while varying the background threshold does return improved NRFs, this method of analysis may also bias the data, similar as before.

3.4.3 Version Three with 2D Image Mode

This improved software version can analyze the same data with the same parameters as the previous version, now in less than 2 min. The improvement is due to each image being loaded only once. When an image is loaded, the software will analyze each user-defined region of the image for each background threshold value associated with that region, storing the number of counts for each threshold value along the row of a matrix. Each new image's data are stored along a new row of the matrix until all images have been analyzed. Then, the matrix columns of each

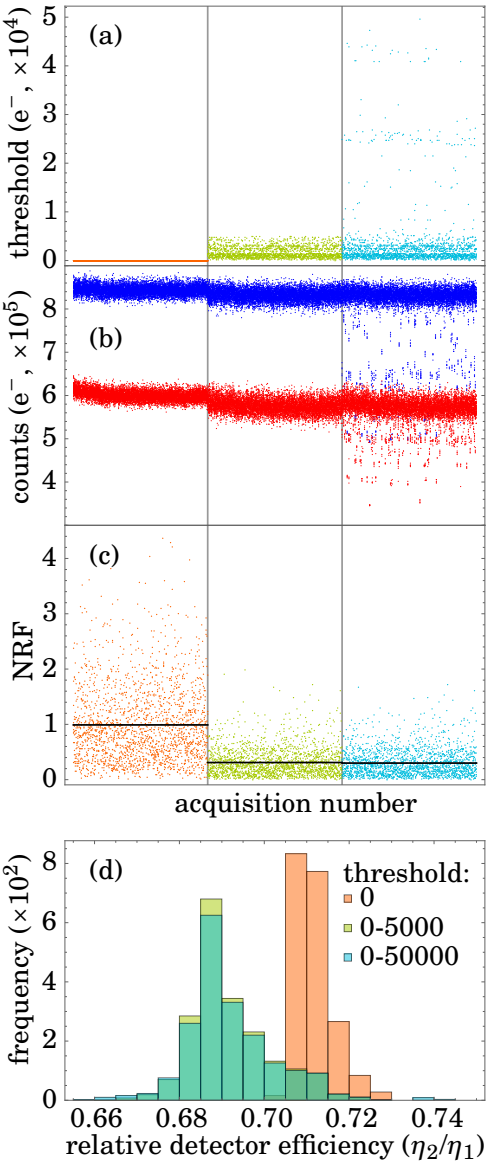

FIGURE 3.23. Plots comparing three thresholding settings for the same data set, from 10000 images analyzed in 2000 sets of 5 images. Plots showing (a) the applied threshold for each data set, (b) counts with each applied threshold, (c) calculated NRFs, with mean values indicated, and a (d) histogram of relative channel efficiency for each data set.

defined region are compared pairwise to return the NRF associated with that pair of threshold values. Finally, the software returns the threshold values associated with the minimum NRF.

The option of background subtracting the images may be selected as well, allowing for comparison of minimum correlation parameters associated with each of these options. The code can also produce a number of `.csv` files related to a defined data image for, for example, producing contour plots.

This software version not only improves runtime over previous versions and includes features allowing for further data analysis, but also improves general productivity, as optimizing experimental parameters no longer requires hours or days waiting for data to analyze.

3.4.4 Biased Data Analysis With Background Thresholding

During the course of our experimental efforts, it was found that the data analysis methods discussed above were positively biasing the measured NRF. The method which we were previously using to analyze the data was to readout 2D images from the CCD camera, then manually define the Stokes and anti-Stokes FWM within the analysis code. The code would then sum the number of counts from each pixel within the defined regions that were above some background threshold. This threshold was fixed for each data set, but allowed to vary from data set to data set, optimized to most reduce the NRF for each data set.

The idea was that as the classical power fluctuated, the Raman noise would fluctuate accordingly, and this variable thresholding would

account for the varying Raman from data set to data set. There are a few issues with this analysis. First, we showed in sec. 3.2.1 that over the timescales of our measurements, the Raman noise does not fluctuate significantly to warrant the range of threshold values which were allowed (typically 0 to ones of thousands, adjusted *ad hoc* based on how bright the signal was). The several distinct thresholding values shown in fig. 3.23 (a), particularly visible in the $0-50000$ data set, may be due to beating effects of the pump noise frequency with the image acquisition frequency.

Secondly, variable thresholding was shown to increase the Fano factor of the anti-Stokes beam, as in fig. 3.23 (b). While we might expect some increase in Fano factor for the Stokes channel as Raman, which has a relatively lower Fano factor compared to the FWM, is removed (see sec. 2.2 and sec. 3.2.1), we have no such noise source to be removed in the anti-Stokes channel using the PCF.

Finally, and most importantly, we have no way to ensure that the algorithm is only removing counts associated with uncorrelated optical and detector noise, and not FWM signal. Even with low threshold values, dispersion from the various optics would spatially overlap the noise and signal photons. Ultimately, this method of analysis could lead us to underestimate the number of photons in the Stokes channel, thereby artificially inflating our per-photon advantage. In fig. 3.23, we compare three analysis methods: one with no applied thresholding, and the others with variable thresholding.

We see that when allowed to threshold at increasingly large values, the algorithm minimizes the NRF ($\sigma_0 = 0.99 \pm 0.69$, $\sigma_{5000} = 0.31 \pm 0.25$, and $\sigma_{50000} = 0.30 \pm 0.24$). It is not immediately obvious why this is the case, as the algorithm both reduces the mean value of counts in each channel and increases the Fano factor of the whole data set, shown in fig. 3.23 (b). We expect that both of these effects would increase the measured NRF. What is likely occurring that reduces the NRF is that the algorithm is optimizing the channel imbalance for a given level of Raman noise and FWM power, a somewhat counter-intuitive result which is explained in sec. 2.2.

For these reasons, one should exercise caution when implementing similar data analysis protocols. In the next section, we describe a faster, unbiased technique for analyzing the data which allows real-time NRF calculation, ideal for optimizing various alignment aspects of the experiment.

3.4.5 Version Four with Full Vertical Binning

The most significant experimental change which allowed us to develop a faster, unbiased data analysis is that the data is now read out via FVB, rather than in 2D image mode. This has several advantages.

First, when reading out in image mode, one may choose to crop the image (fig. 3.24 (c)) or not (fig. 3.24 (a)). If one does not crop the image, the long readout time means that more light is incident on the camera while the image is still being read out. This manifests in a dragging effect,

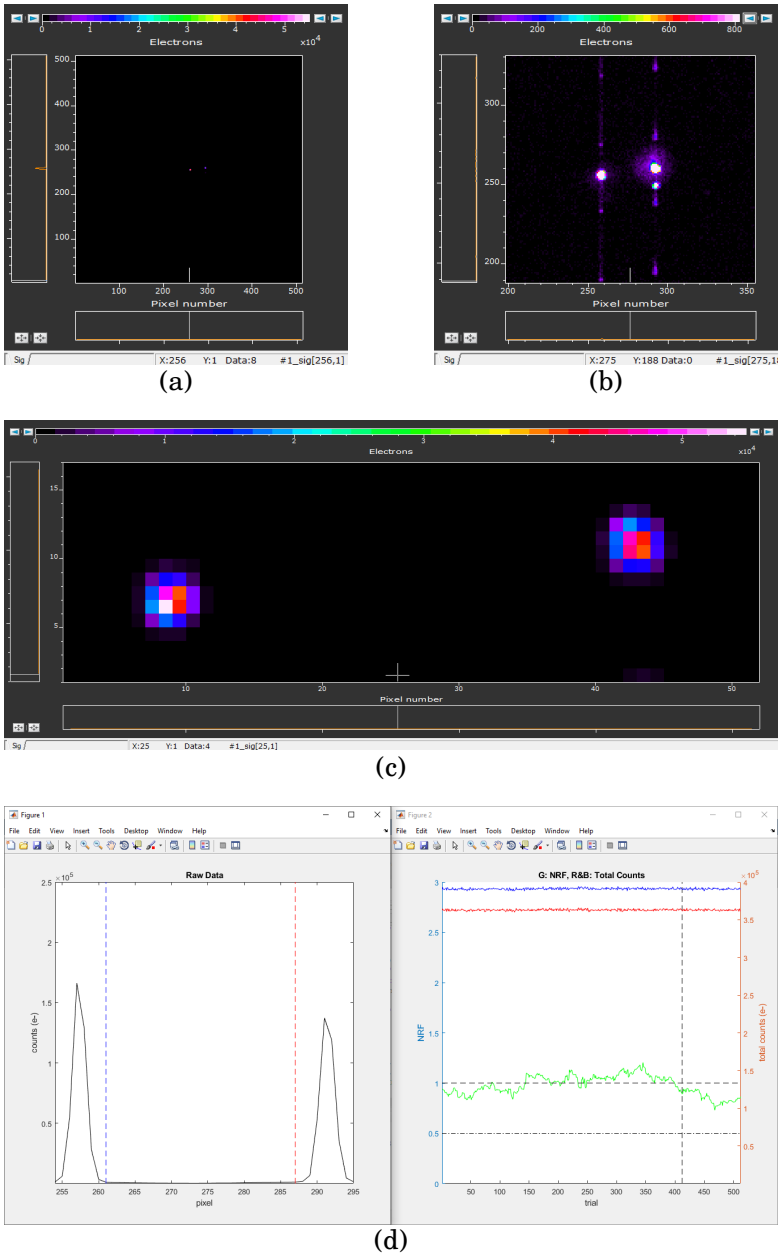

FIGURE 3.24. (a) Screenshot of a sample data image, taken in 2D image mode with no cropping. (b) Cropped and rescaled version of (a) to show dragging effect associated with long image readout times. (c) Screenshot of a sample data image, taken in 2D image mode, cropped around area of interest. (d) Screenshot of MATLAB data analysis. On the left is the FVB of (a), with regions of interest defined by the vertical dashed lines. The plot on the right shows the total counts in each region of interest for the most recent 512 images, as well as the NRF calculated over the most recent 100 images. The dashed horizontal lines indicate a NRF of 1 and 0.5, and the dashed vertical line indicates the most recent data used to calculate the NRF. All data is taken using the SMF28 fiber, at the same pump power and 0.02 s acquisition time.

shown in fig. 3.24 (b), which may introduce noise in the measurement and makes monitoring total incident photons difficult during data analysis. Cropping the image reduces this effect, yielding higher quality data and better measured NRFs. Because each row is not individually horizontally shifted using FVB, there is less noise introduced per pixel.

Secondly, FVB allows faster data acquisition, as the camera does not have to horizontally shift each row individually to construct a 2D image, but rather only horizontally shifts once at the end of each acquisition.

A comparison of readout times and camera noise properties are shown in tab. 3.3. We see that for realistic integration regions, FVB is 8 times faster than even the cropped 2D image mode. As well, the total background noise counts are less, with reduced Fano factors across all FVB HSSs, even compared to the least noisy image mode HSS. FVB has the advantage over both full and cropped 2D image methods in that one can record all 512 pixels faster than the smallest practical image window size, and with less noise per pixel.

TABLE 3.3. A comparison of camera readout modes, for 0.02 s acquisition time. Bg noise for 80 kHz image mode is not shown because the acquisition time must be longer than 0.02 s for this HSS and (50 × 15) px window.

camera mode	HSS (MHz)	window size (px)	readout time (s)	mean background counts (e^-)
image	1	512 × 512	0.291869	
image	1	50 × 15	0.016857	
FVB	1	512	0.002372	
image	1	10 × 10		372 ($F_d = 6.1$)
image	3	10 × 10		619 ($F_d = 17.3$)
FVB	0.08	10		226 ($F_d = 1.5$)
FVB	1	10		227 ($F_d = 3.2$)
FVB	3	10		245 ($F_d = 7.5$)

Note that using this data analysis method, we perform no background thresholding, accounting for all incident photons as well as detector noise.

The camera is now also directly interfaced via MATLAB [87], rather than the manufacturer's software, which allows mathematical operations on the data to be performed real-time. The ability to optimize fiber coupling, beam alignment, camera settings, spectral filtering, and other experimental parameters with immediate feedback on measured NRFs greatly increases lab working efficiency over the previous software versions. A screenshot of the functioning program is shown in fig. 3.24 (d), as well as a comparison to the Andor software. The manufacturer software does still include functionality which is useful for alignment, particularly real-time image rescaling in 2D image mode, but all data collection is now done via MATLAB script.

3.5 Conclusion

In this chapter, we characterized many of the general experimental features which will appear throughout our discussions in the next chapters. In particular, we characterized the FWM and Raman spectra (see sec. 3.1.1), power scaling (see sec. 3.1.2), intensity fluctuations (see sec. 3.2.1), and damage mechanisms (see sec. 3.1.4) of our PCF and SMF28. We also measured the detector noise properties of our experiment to simulate how this and the aforementioned factors affect measured multi-beam intensity correlations. Finally, in sec. 3.4, we discussed several data analysis techniques, their shortcomings, and improvements made with each iteration. Moving forward, we will detail our experimental progression towards ultimately realizing high-power, visible-wavelength, sub-Poissonian twin beam correlations.

CHAPTER 4

EXPERIMENTAL EFFORTS TOWARDS MEASURING SUB-POISSONIAN INTENSITY CORRELATIONS AT PICOWATTS OF FOUR-WAVE MIXING AVERAGE POWER

Chapter outline: *In this chapter, we discuss the chronological progression of our correlated-intensity experiments, showing how changing various aspects related to the twin-beam source, based on the photonic crystal fiber discussed in chapter 3, and detection affect measured correlations. We ultimately demonstrate intensity correlations 3 dB below coherent state statistics with visible-wavelength twin beams at 5 pW average power.*

Declaration of contribution: *This chapter represents novel work performed by me, the exceptions being the fiber collapsing discussed in sec. 4.8 and BluPhoton demonstrator work in box 4.1, performed by postdoctoral colleague Dr. Alex McMillan.*

Previous quantum metrology experiments have realized sub-Poissonian intensity correlations and sub-Shot-Noise Limit (SNL) abosorption estimation, albeit at infrared wavelengths and single-photon (femtowatt) optical powers [6, 8, 10, 11]. In this chapter, since we have discussed the general theoretical and experimental features of our experiments in previous chapters, we now detail our experimental efforts towards measuring intensity-correlated twin beams below the classical limit. We ultimately measure strong sub-Poissonian correlations at picowatts of average optical power, 1000 times brighter than previous work. We measure a Noise-Reduction Factor (NRF) of $\sigma = 0.47 \pm 0.04$, and measure a sample's absorption at the SNL, $\Gamma_m = 1.02 \pm 0.16$.

As the work performed for this thesis represents new experimental efforts, we present this chapter in a mostly chronological order, demonstrating in detail how changes to the experiment may increase or decrease the measured NRFs. The relative importance of each change is quantified by the NRF at each iteration of the experimental setup.

4.1 First Attempt at Measuring Sub-Poissonian Intensity Correlations

Because the primary experiment of this thesis does not build upon previous infrastructure, it underwent several iterations to ultimately measure bright, sub-Poissonian twin-beam intensity correlations. The initial experimental setup used is shown in fig. 4.1. As our source, we employed a 1064 nm wavelength, 1 ns pulse width, 5 kHz repetition rate laser with 60 mW average output power (Teem Photonics SNP-08E-100 [60]), frequency doubled via Second-Harmonic Generation (SHG) to 532 nm using an external temperature-controlled Lithium triBOrate (LBO) crystal. After collimating the pump beam, we used a Half-Wave Plate (HWP) to achieve efficient phase-matching with the LBO crystal for SHG. Both the lens which focused the pump beam into the LBO crystal, as well as the collimating lens after the LBO crystal, were mounted on unidirectional translation stages to optimize focusing conditions. We achieved a maximum 532 nm average power of 20 mW.

The 532 nm beam was attenuated to safe operating powers via a HWP and Polarizing Beam Splitter (PBS) in succession. A third HWP was implemented before coupling into the Photonic Crystal Fiber (PCF), as we did not know at the time how effected Four-Wave Mixing (FWM) efficiency in our PCF is by pump polarization (see sec. 3.1.3 for details about mode-mixing in fiber). A narrowband 532 nm bandpass filter (Thorlabs FLH532-4 [88]) removed residual 1064 nm radiation before the nonlinear fiber.

The PCF was cleaved and clamped at both ends to separate three-axis translation stages, with 20 nm resolution along each axis (Elliot Martock MDE122 [89]). We used short focal-length microscope objectives to couple light in and out of the fiber.

After the fiber, a 532 nm notch filter removed bright pump components. As shown in sec. 3.1.1, however, inelastic pump scattering spectrally broadened the beam beyond the bandwidth of the

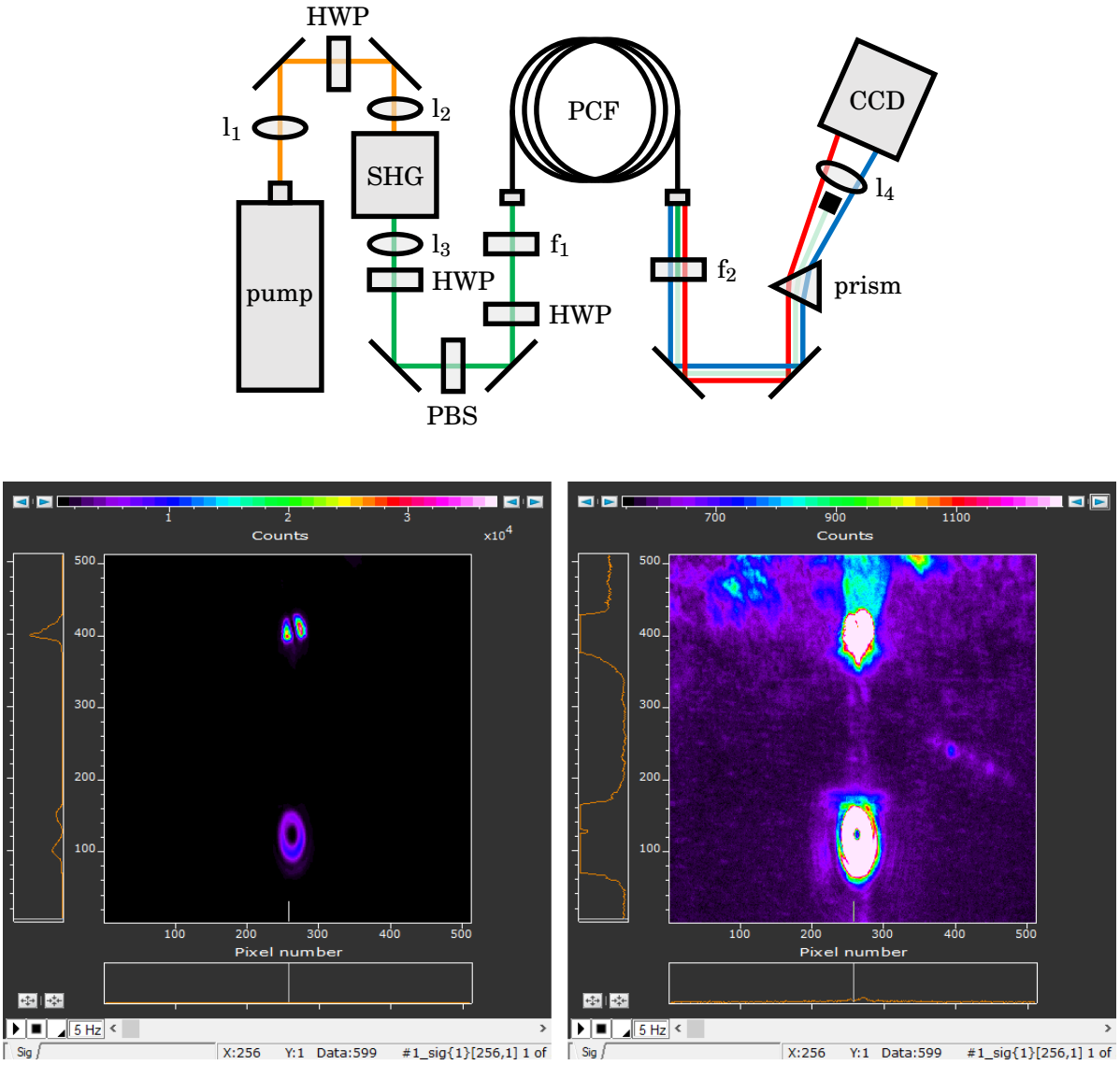

FIGURE 4.1. (top) A schematic of the experimental setup used for first attempts at measuring sub-Poissonian intensity correlations. pump: 1064 nm wavelength, pulsed laser; $l_{\{1,3\}}$: collimating lenses; $l_{\{2,4\}}$: focusing lenses; f_1: 532 nm bandpass filter; f_2: 532 nm notch filter.

(bottom) A sample data image with (left) natural intensity scaling and (right) scaling adjusted such that dim image features become visible. The Stokes beam is incident on the upper region of the CCD, and the anti-Stokes on the bottom. Both images are at an average pump power of 0.92 mW, with camera exposure time 0.1 s. Axes represent pixel number, and are non-essential for qualitatively analyzing the data.

filter, as shown in fig. 3.3.

As the pump and FWM beams are collinear, we spatially separated them according to their wavelengths with a fused-silica dispersion prism (Thorlabs AFS-FS [90]). Once separate, the remaining pump beam was blocked with narrow bespoke beam dumps. These self-fashioned beam dumps were sections of black, absorptive, laser-safe card, cut and mounted to an optical post for positioning. Finally, a 250 mm focal-length, Anti-Reflection (AR)-coated lens simultaneously focused the Stokes and anti-Stokes beams onto a CCD camera.

Since at this stage we did not yet have a mature understanding of the CCD camera functionality, the CCD was not cooled, and left at an unstabilized internal temperature of 15°C (camera noise properties as a function of temperature are discussed in box. 3.1). We collected data in 2D image readout mode, and did not crop the field of view, leading to readout times of 0.3 s plus image acquisition time (camera noise properties for various readout parameters are compared in tab. 3.3). A sample data image is shown in fig. 4.1.

In the naturally-scaled image, we see two regions associated with the Stokes and anti-Stokes FWM beams. The far-field mode shapes are distinguishable, indicating that the FWM spatial modes are mutually distinct, and therefore we are operating in a sub-optimal coupling regime (see sec. 2.1.1). The focused spots are also large compared to data acquired with more mature experimental setups (see fig. 4.7), thereby introducing more electronic noise in the signal regions.

In the rescaled image, noise photons and scattering are visible. The anti-Stokes beam has a diffraction pattern associated with its being partially blocked by the beam dump. As well, because the experiment is not shielded well from ambient light, we see optical noise in the Stokes region of the image.

From this data, we measured $\sigma = 389 \pm 270$ from 5 sets of 10 images, well above the classical limit of $\sigma = 1$ (see sec. 2.2). Aside from the issues noted above, this experiment was difficult to align. The pump beam dump could not be reliably fashioned or placed such that it did not also partially block the FWM beams, as the dispersion prism had to placed physically near the camera because of the small CCD size.

4.2 Second Attempt with Improved Spectral Filtering and Low Peak-Power Laser

In the second iteration of the experiment, we used a different pump laser, and improved spectral filtering both before and after the PCF.

Previously, we used a 60 mW average power, 1 ns pulsed, 7 kHz microchip laser. In our second experimental setup, we employed a 250 mW average power, 7 ps pulsed, 80 MHz, 1064 nm wavelength fiber laser (Fianium FP-1060-0.25-DUAL). The rationale of this change is that we expected the Fianium laser to be more stable both in regards to output power and pulse spectrum, from previous experiments performed with this laser by postdoctoral colleagues, compared to the

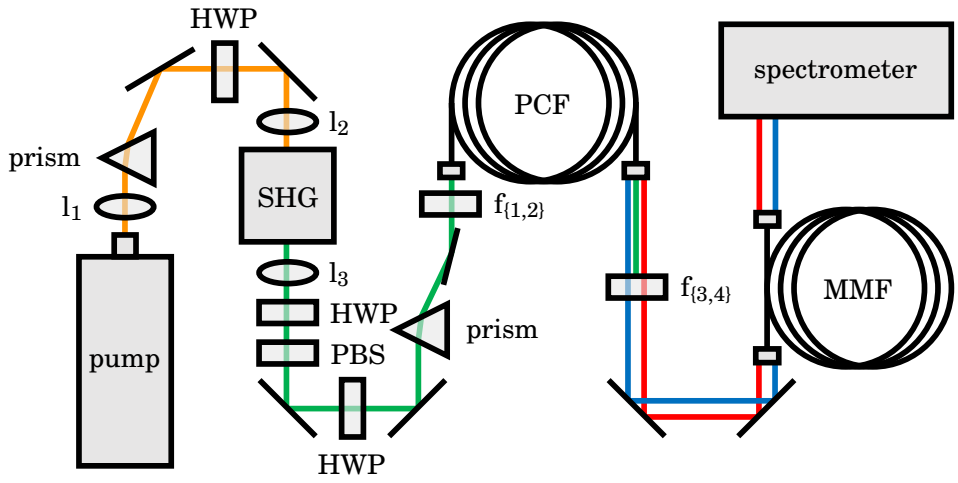

FIGURE 4.2. A schematic of the experimental setup used for characterizing the FWM spectrum using the Fianium laser. pump: 1064 nm wavelength, pulsed laser; $l_{\{1,3\}}$: collimating lenses; l_2: focusing lens; $f_{\{1,2\}}$: 532 nm bandpass filters; f_3: 532 nm notch filter; f_4: 450/660 nm multi-bandpass filter.

passively Q-switched Teem Photonics laser. The disadvantage of using this laser is that although it may achieve much greater average power, the peak power is lower (1.75 pJ compared to 8 µJ). As high peak powers are required to reach the exponential FWM threshold (see sec. 2.1.1 and ref. [28, 37]), this compromise proved detrimental in observing high-power FWM beams.

To ensure spectral filtering of the pump, we included two dispersion prisms before the PCF, as well as a second 532 nm bandpass filter, in addition to the preexisting 532 nm bandpass filter and PBS. The experimental setup is shown in fig. 4.2.

We have also implemented a second filter post-PCF in addition to the 532 nm notch filter. The multi-bandpass filter is designed to have an Optical Density (OD) of 6 at the pump wavelength, effectively attenuating the pump beam without requiring the need for a bespoke beam dump. The blocking bandwidth of the multi-bandpass filter is 125 nm, compared to 15 nm of the notch filter. The pump spectrum with and without bandpass filtering, as well as the FWM spectrum, with filtering, is shown in fig. 4.3.

To produce fig. 4.3 (a) and (b), we shone the pump beam, attenuated with appropriate Neutral-Density (ND) filtering, directly to the spectrometer, via Multi-Mode Fiber (MMF). Although we achieved high SHG efficiency, there is residual 1064 nm pump measured. The residual 1064 nm light is well-attenuated with a 532 nm bandpass filter, quoted to be OD6 at 1064 nm, and is also not efficiently phase-matched in the PCF for FWM.

Fig. 4.3 (c) is a spectrum taken from coupling the Fianium pump beam to a 1 m length of PCF, similar to the measured PCF spectra produced by the Teem Photonics pump laser, fig. 3.3. To measure bright FWM, we pumped with 7.5 mW average power. This had the effect of increasing the Raman noise relative to the Stokes FWM signal.

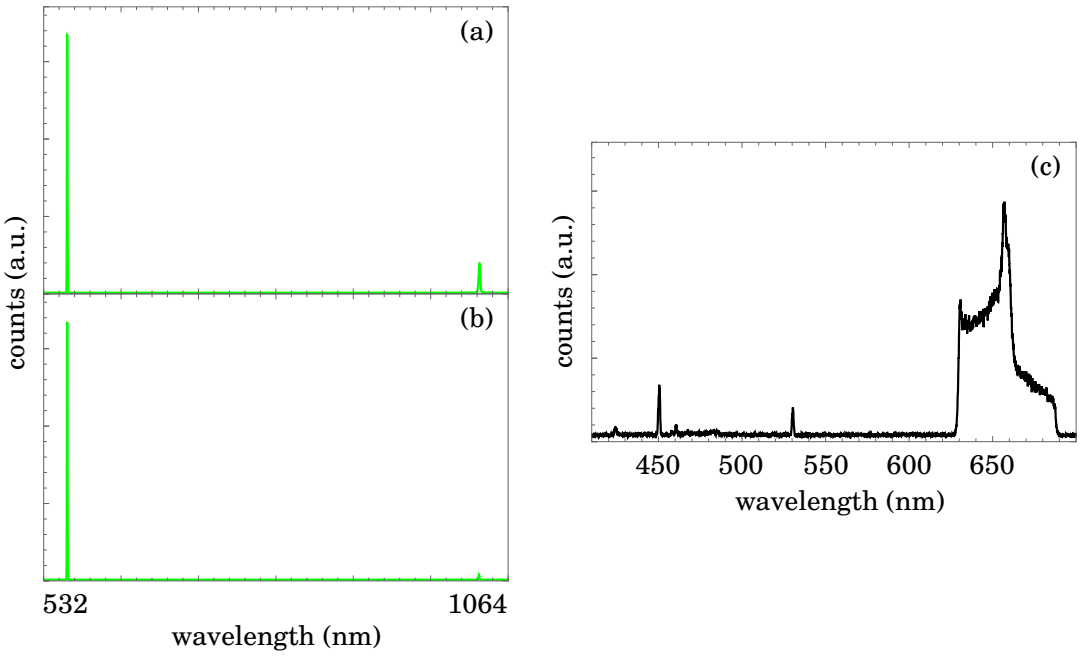

FIGURE 4.3. Spectra of the Fianium pump (a) without and (b) with spectral filtering (532 nm bandpass filter), and (c) a 1 m length of PCF. Note that in (a) and (b), the 532 nm signal has saturated the spectrometer CCD, and is relatively brighter than the 1064 nm signal than shown. The spectrum (c) appears unbalanced because of improper spectrometer coupling for measuring large-bandwidth spectra, although the important features of the spectrum here are still visible. We fix this problem in following spectra by appropriately adjusting alignment and focusing conditions.

Although this experimental setup is more cumbersome to align than the previous experiment due to the extra optical components, and although we measure reduced FWM Signal-to-Noise Ratio (SNR) because of the high average pump power and low peak power, this experiment did have value. We achieved improved spectral filtering with the introduction of the multi-bandpass filter after the PCF, eliminating our need for narrow bespoke beam dumps, described previously.

Note that we did not attempt to measure any NRFs with this experiment, because of the aforementioned drawbacks.

4.3 Third Attempt with Improved Spectral Filtering and High Peak-Power Laser

The following experimental effort represents a combination of the previous two. First, we return to using the Teem Photonics laser which has higher peak power. We also replaced the dispersion prism before the CCD camera for spatially separating the FWM beams. And from the previous iteration of this experiment, we implemented better spectral filtering of the pump beam after the

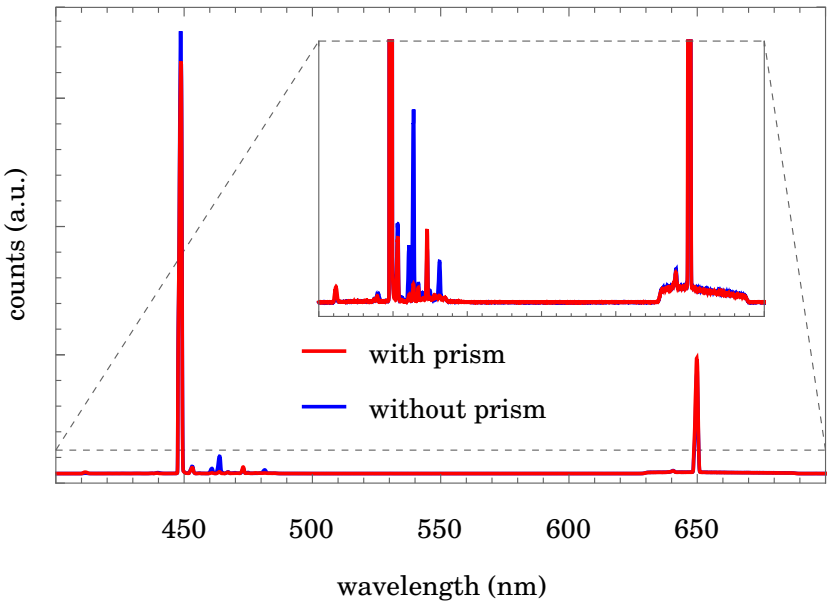

FIGURE 4.4. The spectrum of 60 cm of PCF3, using improved pump filtering post-fiber, comparing the efficacy of pre-fiber pump filtering with and without dispersion-prism filtering. Inset figure is zoomed-in spectrum, showing low-power spectral features, such as Stokes Raman scattering.

PCF, no longer using a beam dump.

As discussed previously, the Fianium laser did not produce sufficient peak power to stimulate FWM well enough above the Raman background. The Fianium laser also has a larger physical footprint compared to the Teem Photonics laser (~ 600 cm^2 compared to ~ 36 cm^2). The Teem Photonics laser is therefore not only the more scientifically useful choice, but also the cheaper, smaller, and lighter choice.

We again characterized the PCF spectrum to determine not only the efficacy of the improved spectral filtering using the ns-pulsed laser, but also whether having two dispersion prisms before the PCF sufficiently improves the pump spectrum to warrant the added complexity. These spectra are shown in fig. 4.4.

At 3.3 mW average pump power, the multi-bandpass filter and notch filter sufficiently attenuate the pump such that it is not detectable above background noise on the spectrometer.

We now compare the FWM spectra with and without using a dispersion prism before pump SHG. According to fig. 4.4, it initially appears that the prism reduces spurious FWM. However, the decreased noise is likely due to decreased pump power (evidenced by comparing the anti-Stokes peak power in the spectra) and altered mode coupling between the two spectra. As will be discussed in sec. 4.6, the three-axis translation stages on which the PCF is mounted did not reliably maintain pump-fiber coupling. For these reasons, and because the noise is dim compared to the signal, we removed the pre-SHG dispersion prism, to use it instead to spatially separate

the FWM beams for intensity measurement.

The experimental setup with these considerations is shown in fig. 4.5. We also implemented a Flip-Mirror (FM) to quickly transition between calibrating the PCF coupling using the spectrometer and measuring intensity correlations on the CCD camera, improving lab-working efficiency. Because the spectrometer fiber coupling is robust to small beam misalignment, due to the fiber's large core diameter (see sec. 3.1), the up-position of the FM was set to correspond to using the spectrometer. The focal length of l_4 depends on a number of factors: the size of the CCD array (8.2×8.2 mm^2), the collimation of the FWM beams, and the distance between the prism and CCD. That is, if the focal length of the lens is not properly selected, then the FWM beams will have spatially diverged beyond the dimensions of the CCD array before the beams are sufficiently focused. Through trial-and-error, we selected an AR-coated lens with focal length 250 mm.

Shown also in fig. 4.5 is a sample intensity-correlation data image captured with this experiment, both with a natural scaling and a rescaling to see fainter features. We see, compared to fig. 4.1, less optical noise and no diffraction caused previously by the pump beam dump. Secondary, less-intense FWM, as seen in the spectrum of fig. 4.4, are also measured, and spatially overlap the desired FWM.

Again, as we did not yet have a mature understanding of camera functionality, the CCD was not cooled. This data is captured at an unstabilized internal temperature of 18°C. Data was recorded in 2D readout mode at 1 MHz Horizontal Shift Speed (HSS), with an exposure time and readout time of 0.5 s and 0.3 s, respectively.

Although we had initially analyzed the data using background thresholding, this data analysis method is biased, as discussed in sec. 3.4.4. Reanalyzing the data in 10 sets of 10 data images, with no background threshold, we measure $\sigma = 4.74 \pm 2.59$. This represents two orders-of-magnitude improvement over the initial experimental results $\sigma = 389 \pm 270$ (see sec. 4.1).

4.4 Fourth Attempt with Independent Beam Focusing and CCD Cooling

In the following iteration of the correlated-intensity experiment, we made several notable changes. First, we added black, laser-safe, absorptive cardboard shielding to insulate the experiment from ambient light sources. The shielding was placed between the source (which includes the laser, SHG, and PCF) and the experiment (which includes the dispersion prism, focusing lenses, and camera). Comparing background data images from the previous experiment, however, we see no change in ambient light on the camera CCD. This is because the camera itself was not insulated from ambient room light, only the other experimental components.

A more impactful change to the setup was the addition of a Dichroic Mirror (DM) and separate focusing lenses for the two FWM beams. Because of chromatic dispersion at the out-coupling fiber lens, the two spectrally disparate Stokes and anti-Stokes FWM beams cannot be simultaneously

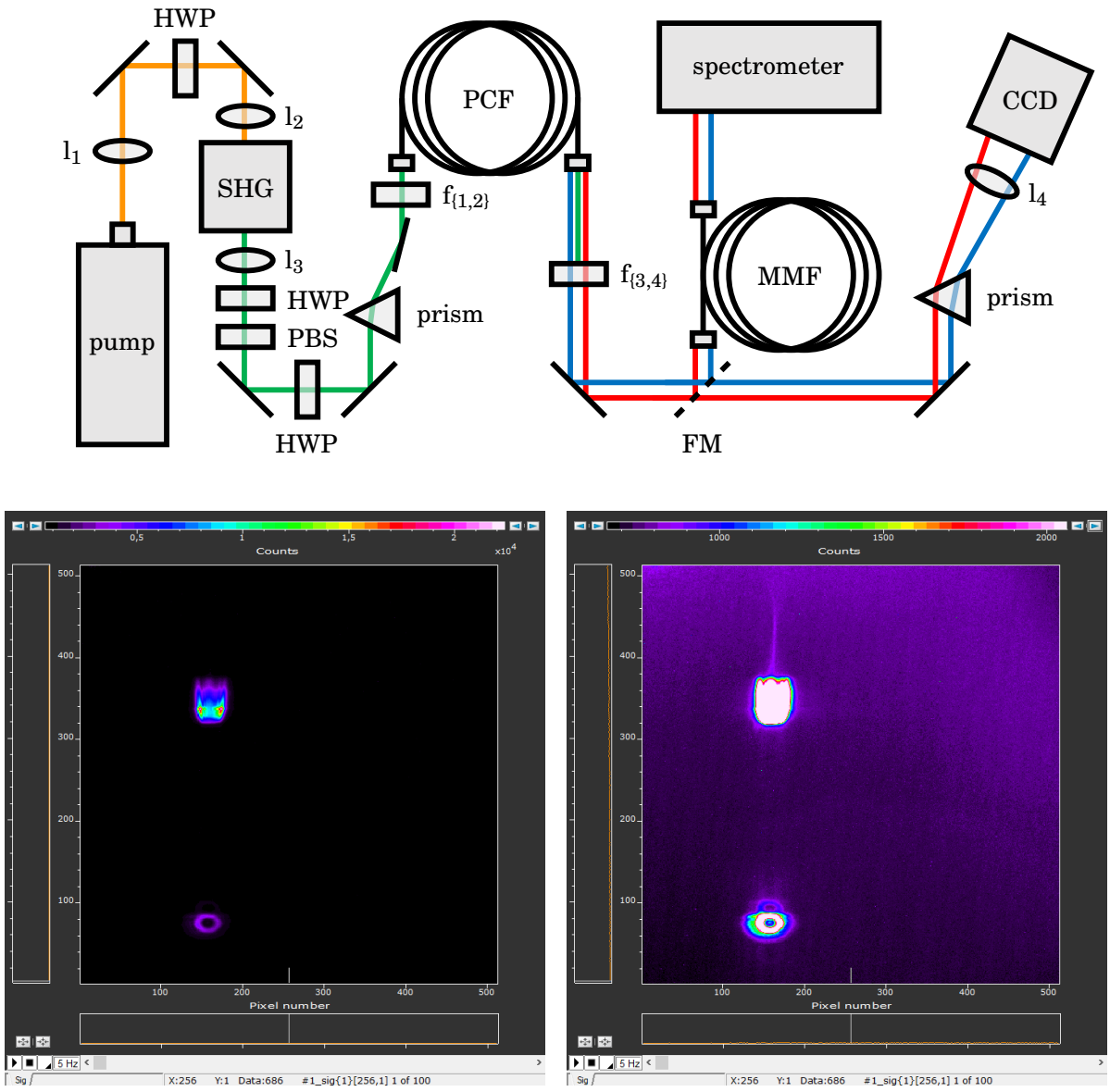

FIGURE 4.5. (top) A schematic of the experimental setup which allows for quick transition between observing the laser spectrum and measuring intensity correlations with the CCD camera. pump: 1064 nm wavelength, pulsed laser; $l_{\{1,3\}}$: collimating lenses; $l_{\{2,4\}}$: focusing lenses; $f_{\{1,2\}}$: 532 nm bandpass filters; f_3: 532 nm notch filter; f_4: 450/660 nm multi-bandpass filter.

(bottom) A sample data image with (left) natural intensity scaling and (right) scaling adjusted such that dim features become visible. The Stokes beam is incident on the upper region of the CCD, and the anti-Stokes on the bottom. Both images are at an average pump power of 3.3 mW, with camera exposure time 0.5 s. Axes represent pixel number, and are non-essential for qualitatively analyzing the data.

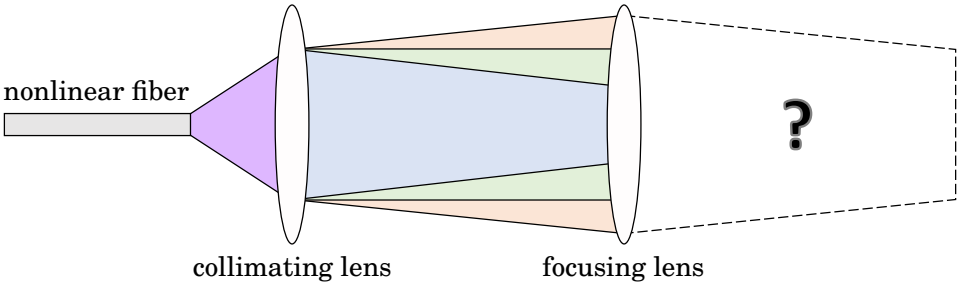

FIGURE 4.6. A graphical representation of chromatic dispersion for collimating disparate wavelengths, showing the pump beam collimated by the collimating lens, but the FWM beams refracted at unknown angles.

collimated such that quoted lens focal lengths used for focusing the beams are reliable, as shown in fig. 4.6. Experimentally, we mitigate this issue by spatially separating the two signal beams with a DM after the dispersion prism, and focus both beams independently on the CCD camera. For alignment consistency, we collimate the fiber output beam according to the relatively bright pump beam.

We also removed the 532 nm notch filter after the PCF, as it was found to be redundant with the multi-bandpass filter in place. The multi-bandpass filter was mounted directly on the camera aperture, as well as an optional ND filter. The rationale of adding an ND filter was to allow for more pump power to be launched into the PCF, thus generating brighter FWM signals compared to optical noise processes such as Raman scattering. Now, with a better understanding of the experiment, and following the experimental characterizations of sec. 3.2, we know that this would increase our measured NRFs because of the increased channel loss and increased FWM Fano factor. The Stokes beam was focused with a stationary lens by moving the camera along a unidirectional translation stage, and the anti-Stokes beam focused by a lens mounted on a separate unidirectional translation stage. A schematic of the described experiment is shown in fig. 4.7.

Another advancement since the previous experiment was a better understanding of the camera functionality as it relates to noise in the data. The camera temperature settings were adjusted from room temperature to $-35°$C. As discussed in sec. 3.2.2, this reduces electronic readout noise.

A minor change to the data acquisition was to save data in number of excited electrons per pixel, as apposed to the post-processed counts, which represents the number of electrons accounting for pre-amplifier gain and bias offset. This allows for direct comparison to number of exposed photons, assuming we know the camera quantum efficiency, simplifying data analysis. We also reduced the pre-amplifier gain setting from 3 to 1, which allows for brighter signals before camera saturation, at the cost of reduced count resolution.

Although cumbersome to align, the ability to independently focus each FWM beam, as well as

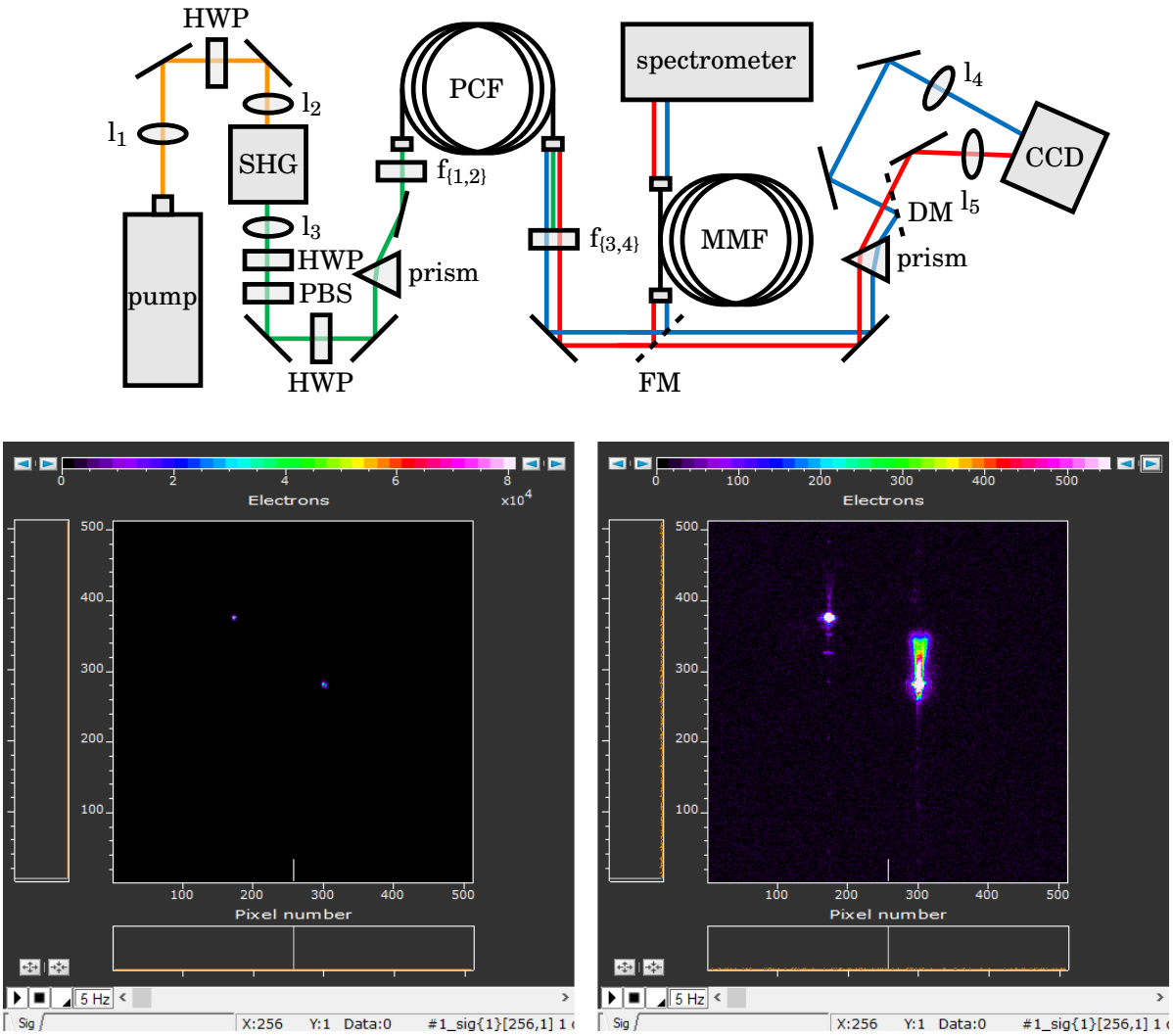

FIGURE 4.7. (top) A schematic of the experimental setup which allows for independent focusing of the two FWM beams. pump: 1064 nm wavelength, pulsed laser; $l_{\{1,3\}}$: collimating lenses; $l_{\{2,4,5\}}$: focusing lenses; $f_{\{1,2\}}$: 532 nm bandpass filters; f_3: 450/660 nm multi-bandpass filter; f_4: optional ND filter.

(bottom) A sample data image with (left) natural intensity scaling and (right) scaling adjusted such that dim features become visible. The Stokes beam is incident on the right region of the CCD, and the anti-Stokes on the left. The camera exposure time is 0.5 s. Axes represent pixel number, and are non-essential for qualitatively analyzing the data.

the reduced camera temperature, improved data quality over previous experimental iterations, as evident in fig. 4.7.

In this data, we measure reduced background counts compared to fig. 4.5. We also achieve a reduction in focused beam area by a factor of nine, thereby decreasing electronic noise in the regions of interest. Visible in the rescaled data image is Raman scattering in the Stokes beam, and secondary FWM modes in the anti-Stokes beam.

Using this data, we measure $\sigma = 6.40 \pm 4.02$, however. This does not indicate that our changes necessarily improved data quality and measured correlations. This is primarily due to the inclusion of the ND filter, which at the time we believed would allow us to increase our SNR. Indeed, using an OD2 filter reduces transmission by a factor of 100, and also increased the FWM Fano factor because we then operated in high-pump-power regimes. With unbalanced detection, both of these factors may severely impact measured NRFs (see sec. 3.2).

4.4.1 Photonic Crystal Fiber Numerical Aperture Characterization

While performing the experiments described in this section, we found that the PCF output collimating lens introduced $\sim 14\%$ optical loss due to clipping. This is because the Numerical Aperture (NA) of the collimating lens was less than the NA of the fiber. That is, at the lens distance at which the PCF output is collimated, the PCF is emitting light at a wider angle than the lens can collect it. Loss may be detrimental to observing sub-Poissonian intensity correlations (see sec. 2.2). In this subsection, we will characterize the NA of the PCF, with the aim of improving component-selection requirements and reducing optical loss.

Initially, clipping was discovered while adjusting the pump beam collimation to various distances for aligning the PCF output beam. After suspecting that the lens may be clipping the beam, we measured the power of the collimated beam compared to the output power of the fiber without the collimating lens, and a 14% power decrease was measured. This loss cannot be attributed to absorptive loss introduced by the AR-coated microscope objective. To determine a suitable replacement for the collimating lens, we measured the NA of the PCF.

We performed this characterization with the experimental setup shown in fig. 4.8. The frequency-doubled laser was coupled in to the PCF as usual. The fiber output was mounted on a rotation stage marked with 2° increments. We placed a pinhole several centimeters from the fiber output, followed immediately by an optical power meter. Careful attention was paid to align the pinhole vertically along the center of the beam output to not negatively bias the fiber NA measurement.

The fiber output was rotated over 70°, recording the power at regular intervals. We performed this measurement twice with the pinhole set to two different opening diameters. The data for the wider pinhole setting, along with a Gaussian fit, is shown in fig. 4.9. To calculate the fiber NA, we assume that our beam profile is Gaussian, which agrees well with fig. 4.9. Under this assumption, where the standard deviation of the beam's transverse intensity profile is r', and $2r$

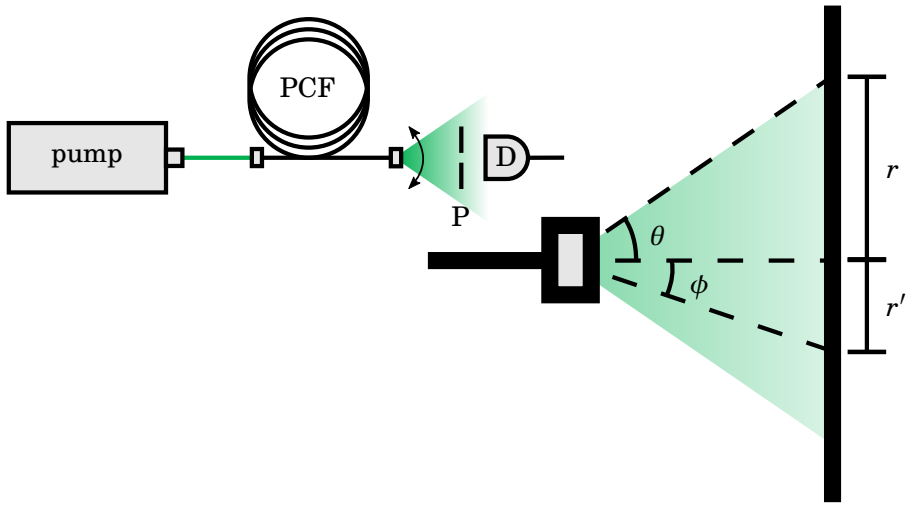

FIGURE 4.8. The experimental setup for measuring the fiber NA, as well as a zoomed in section of the fiber output, showing relevant quantities for calculating the fiber NA. P: pinhole; D: optical power meter.

is the beam's $1/e^2$ diameter, we have $r \approx 1.7\sqrt{2\ln 2}\, r'$. We may then write the fiber NA as

$$\begin{aligned} \mathrm{NA} &= \sin\theta \\ &= \sin\left[\arctan\left(1.7\sqrt{2\ln 2}\,\tan\phi\right)\right], \end{aligned}$$

where ϕ is the standard deviation of the Gaussian fit of fig. 4.9.

Applying this to the data, we calculate NA = 0.34 ± 0.05 for the PCF. Therefore, to avoid clipping the fiber output, the output coupling lens NA should be about twice that of the fiber, NA ≈ 0.7 [91]. We selected two AR-coated aspheric microscope objectives with NAs 0.7 and 0.64, and respective focal lengths 3 mm and 4 mm (Thorlabs C330TMD-A [71] and Thorlabs C340TMD-A [92]). Using the 0.64-NA lens at the fiber input, we were able to increase maximum pump coupling efficiency from 65% to 80%, likely due to better spatial overlap of the pump beam with the supported fiber modes. Using the 0.7-NA lens at the fiber output, we no longer measure clipping loss. The SMF28 has a quoted NA of 0.14, so the generated FWM will also not be clipped by the aforementioned high-NA objective lenses.

Note that the fiber NA may also be written as $\mathrm{NA} = \sqrt{n_{\mathrm{co}}^2 - n_{\mathrm{cl}}^2}$, where n_{co} and n_{cl} are the fiber core and cladding refractive indices. This form of the NA, similar to the fiber's V parameter (see sec. 2.1.2), implies that fibers with higher NAs guide more strongly in the core, and are less prone to bend loss [93]. This is consistent with our own results of sec. 3.1.3, comparing the bend loss and mode mixing of our PCF and SMF28.

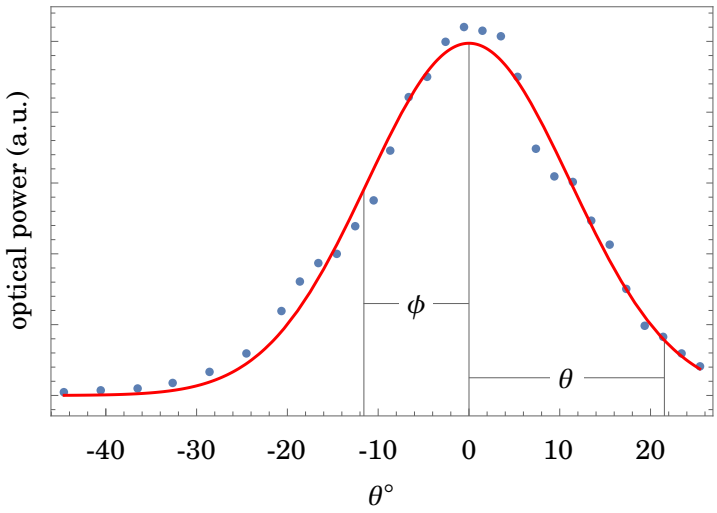

FIGURE 4.9. A sample data set for calculating the PCF NA, fit with a zero-mean Gaussian, showing relevant quantities for calculating the fiber NA. The standard deviation ϕ of the fit distribution is 11.2°.

4.4.2 Improved Camera Settings from Experiments with Downconversion

Building upon our camera-temperature changes earlier in this section, we performed a series of experiments with the objective of empirically determining more appropriate camera settings for our intensity-correlation application, as we did not yet have a sound technical understanding of CCD camera functionality nor the theoretical understanding presented in sec. 3.2.3. The camera settings which we tested were temperature and HSS. To decouple the unknown camera detection parameters from our unknown source parameters, we employed an infrared Spontaneous Parametric DownConversion (SPDC) source which had already previously been shown to exhibit sub-Poissonian intensity correlations by postdoctoral colleague Javier Sabines-Chesterking [13].

The characterized SPDC source produces $\sim 2 \times 10^5$ single-photon pairs per second at 808 nm wavelength, for which the CCD camera is quoted to be 75% efficient. Each of the pair photons from the source were separately MMF-coupled, with the output ends mounted to separate three-axis translation stages, each with a microscope objective for collimating. A non-AR-coated lens was used to focus both beams simultaneously on to the CCD, with a sample data image shown in fig. 4.10.

We first measured the NRF as a function of HSS, with the three available settings, shown in fig. 4.10 (a). In sec. 3.4.5, we measured that faster camera shift rates correspond with increased electronic noise because of reduced charge transfer efficiency. Because camera noise is relatively dim compared to the optical signal for these data, however, our results do not conclusively show a corresponding improvement in NRF for slower readout rates. We nonetheless proceed using slower HSSs when acquisition times are not thusly limited.

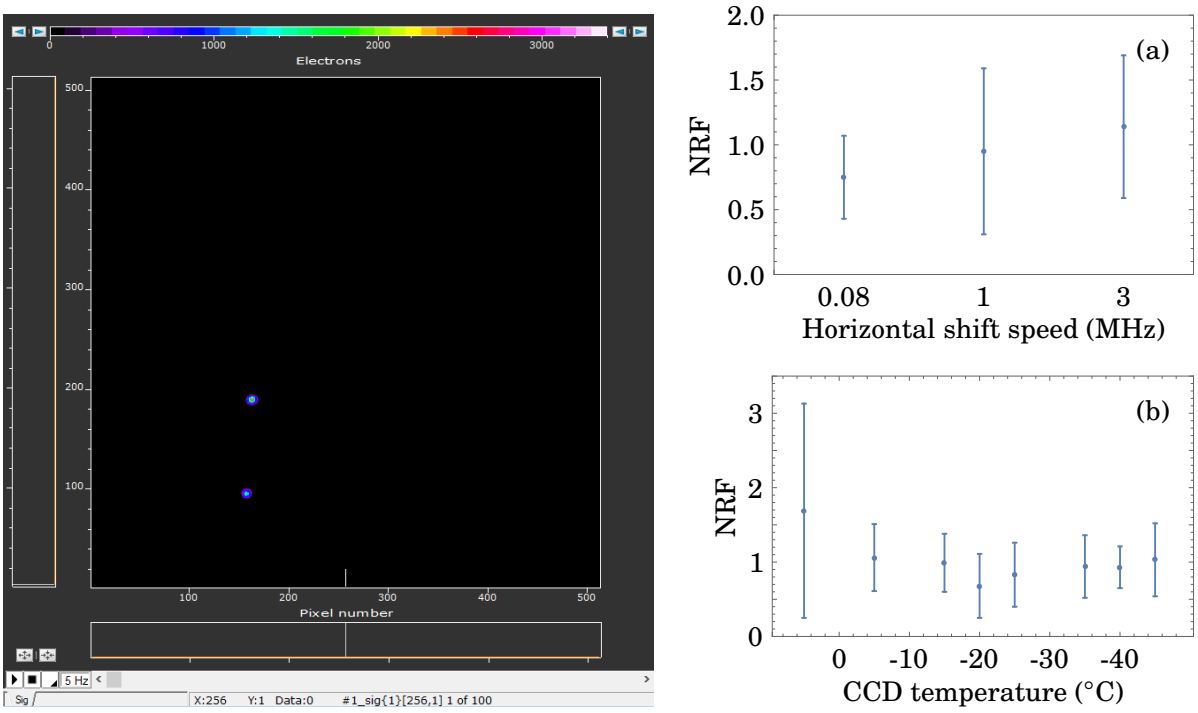

FIGURE 4.10. (left) A sample data image using an SPDC source. The camera settings for this data set are: 0.4 s exposure time, −25°C, and 0.08 MHz HSS. Axes represent pixel number, and are non-essential for qualitatively analyzing the data. (a) A plot showing measured NRF against allowed camera HSS. (b) A plot showing measured NRF against camera CCD temperature, with increasingly negative values to the right.

In fig. 4.10 (b), we compare the air-cooled camera CCD temperature and measured NRFs. The NRF and data precision improve down to −20°C, where the data then becomes inconclusive. These results do agree with previous measurements in box 3.1 which suggest that lower camera temperatures improve data quality by reducing electronic noise.

Importantly, in these experiments we showed that it is possible to measure sub-Poissonian intensity correlations using our specific CCD camera (Andor iXon Ultra 897 [77]), operating at experimental parameters suitable to our application of measuring bright intensity correlations.

4.5 Fifth Attempt with Improved Camera Settings

From the experiments performed with the SPDC source, we learned that CCD camera settings should be optimized for particular measurement applications. Specifically, both decreasing HSS and camera temperature may reduce detection noise. As well, decreasing focused signal spot sizes reduces detection noise, as fewer pixels, each with independent electronic noise, must be integrated over. Finally, depending on the frequency of optical noise in the signal beams, it

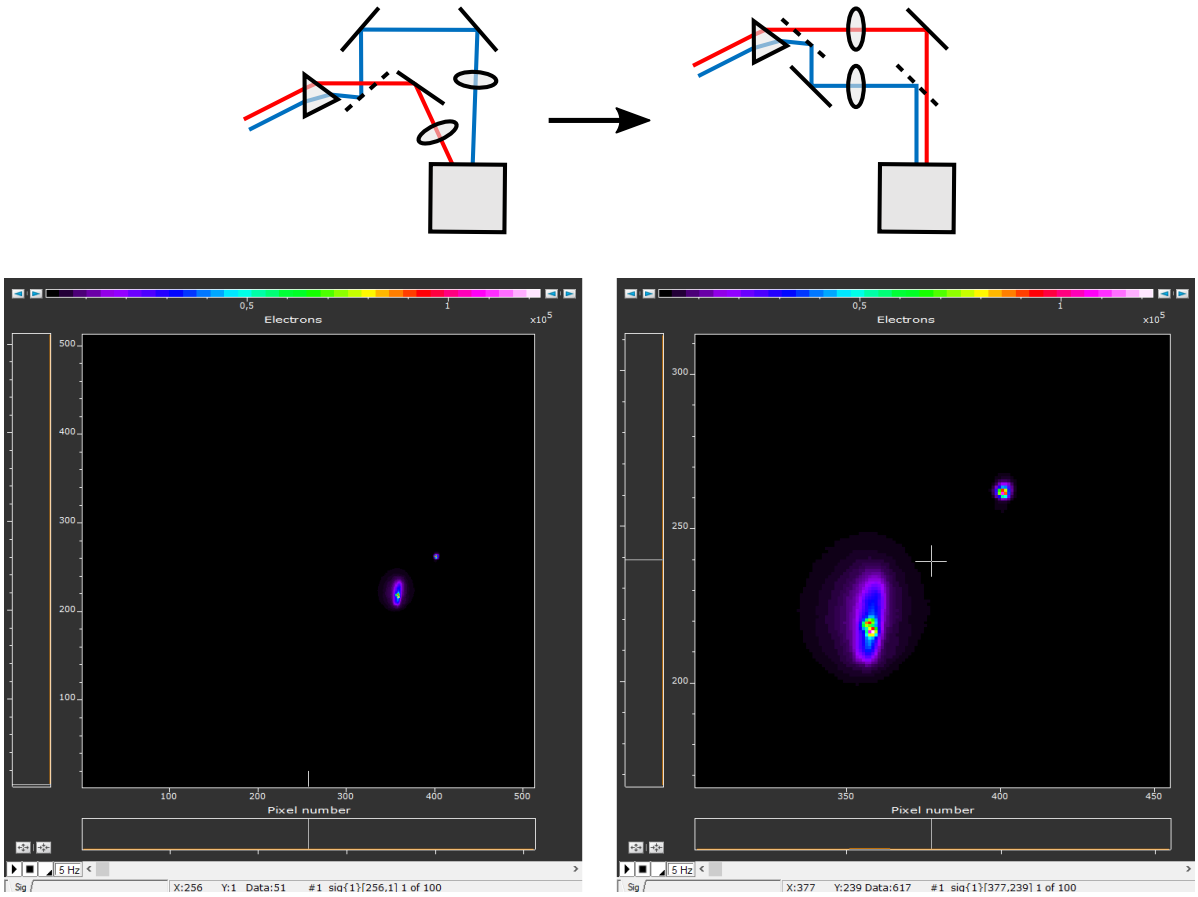

FIGURE 4.11. (top) Improved optical arrangement for multi-beam detection.

(bottom) A sample (left) uncropped and (right) cropped data image. The Stokes beam is incident on the left region of the CCD, and the anti-Stokes on the right. The camera exposure time is 0.1 s. Axes represent pixel number, and are non-essential for qualitatively analyzing the data.

may be advantageous to decrease the image acquisition time, discussed in sec. 3.3. With these considerations and the other experimental changes described later in this section, we improved our previous best-measured NRF from $\sigma = 4.74 \pm 2.59$ (unstabilized temperature, 0.5 s acquisition, 1 MHz HSS, ~ 900 px^2 spot size) to $\sigma = 1.87 \pm 0.97$ (-25°C, 0.1 s acquisition, 0.08 MHz HSS, ~ 49 px^2 spot size).

Shown in fig. 4.11 is a sample data image from the data set which obtained $\sigma = 1.87 \pm 0.97$. We see characteristics typical of the previous example data images, in particular Stokes Raman scattering. In this data set, we have improved focusing conditions of the signal beams due to using independent focusing lenses for each beam, as implemented in the previous experimental iteration. We have, however, improved the arrangement of optical components for the detection

scheme, as shown in fig. 4.11. In the previous experiment, beam alignment was made difficult by the long beam path-lengths required so that optical components would not clip the beam, while having both Stokes and anti-Stokes beams well-focused. In this iteration, the signal beams are spatially separated and recombined using dichroic mirrors, simplifying alignment and removing the need for long beam path-lengths, which may introduce pointing instability to the detection. Note that the signal beams are not interfered on the second dichroic mirror, as is often the case in quantum optics experiments.

The dichroic mirrors together introduce between 5% and 15% loss on each beam, according to datasheet values. The other main source of loss in this detection scheme is the fused-silica dispersion prism, which introduces 10% loss. Thus, the estimated total loss on each arm is between 15% and 25%. Including the detector efficiencies, we estimate $\sim 30\%$ detection loss, consistent with measured values in sec. 3.2.2.

The final experimental improvement is the inclusion of an opaque lens tube mounted directly before the camera shutter to insulate detection from ambient light, as well as an adjustable pinhole, reducing ambient-light at the CCD without a large cardboard enclosure around the camera.

4.6 First Measurement of Sub-Poissonian Intensity Correlations

We finally measure evidence of sub-Poissonian intensity correlations at $\sigma = 0.55 \pm 0.28$, which is 1.6 standard deviations below Poisson statistics. Several experimental modifications were made to achieve this.

First, we found that the three-axis translation stage on which the PCF input was mounted was defective. Prior to replacing the defective stage, the PCF would require realignment roughly every twenty minutes, as the z-alignment would drift away from the set value. As stated before, this alignment procedure involves optimizing pump coupling using an optical power meter, then monitoring the FWM coupling on the spectrometer for further optimization. Not only did this severely impact lab productivity, but also produced inconsistent data, making it difficult to improve other aspects of the experiment. Replacing the stage with a non-defective version improved alignment stability such that the fiber only had to be realigned once per working day, as apposed to several times per hour.

Secondly, we removed the dispersion prism to simplify alignment and reduce loss along the detection channels. While this impedes our ability to spatially filter Raman scattering, this issue may be mitigated with more precise spectral filtering. Indeed, we implemented a narrower-bandwidth spectral filter (Semrock FF01-663/18-25 [67]) in addition to the multi-bandpass filter, which reduced relative Raman scattering power in the Stokes beam by $\sim 40\%$. Adjustable pinholes were also added in each beam path to reduce stray light from unintended reflections.

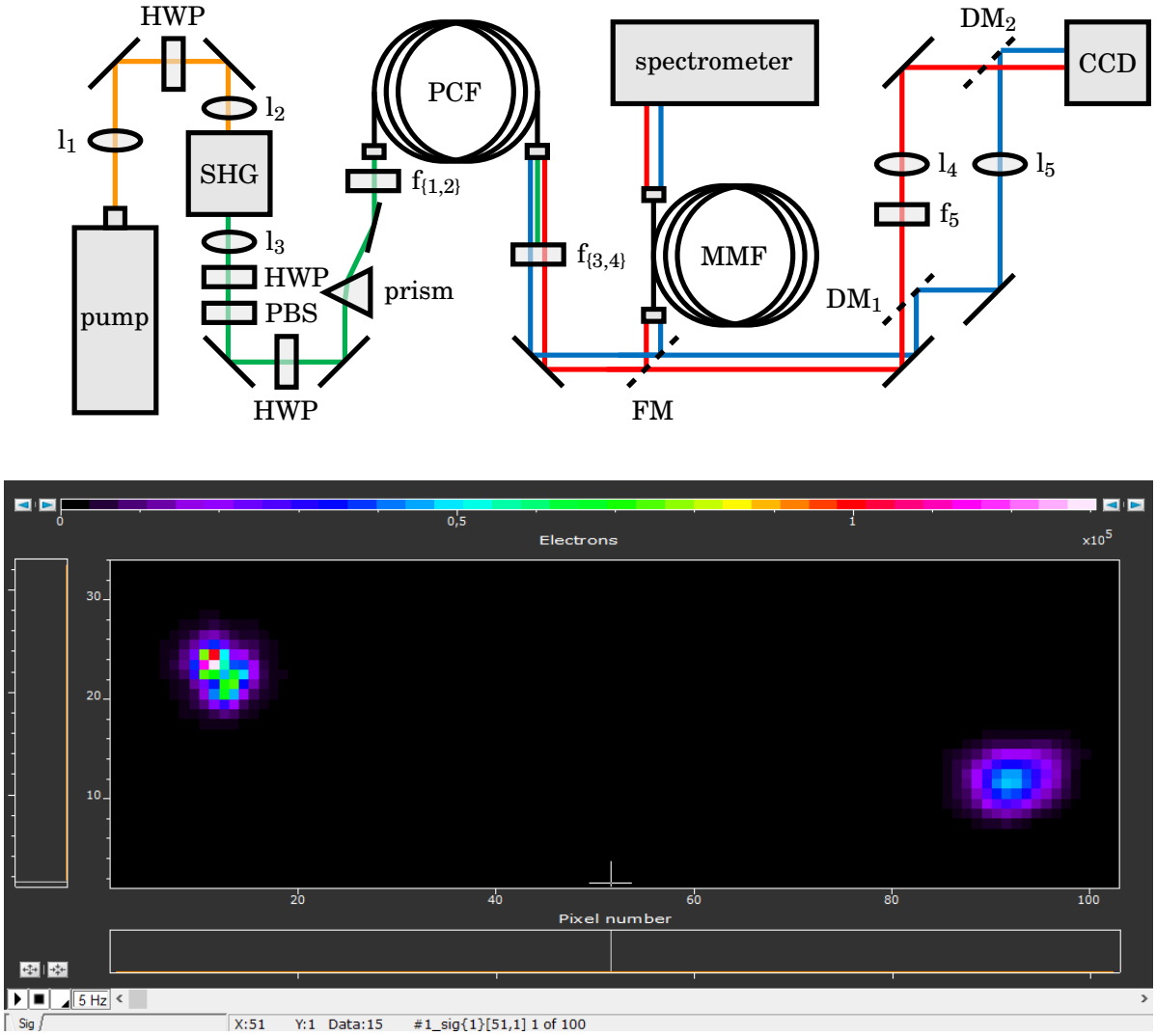

FIGURE 4.12. (top) A schematic of the experimental setup which allows for independent focusing of the two FWM beams. pump: 1064 nm wavelength, pulsed laser; $l_{\{1,3\}}$: collimating lenses; $l_{\{2,4,5\}}$: focusing lenses; $f_{\{1,2\}}$: 532 nm bandpass filters; f_3: 450/660 nm multi-bandpass filter; f_5: 663 nm bandpass filter; FM: flip mirror; $DM_{\{1,2\}}$: dichroic mirrors.

(bottom) A sample data image from our first observation of sub-Poissonian intensity correlations using visible-wavelength FWM. The Stokes beam is incident on the left region of the CCD, and the anti-Stokes on the right. Axes represent pixel number, and are non-essential for qualitatively analyzing the data.

Thirdly, cropped 2D image capturing was implemented. As measured in sec. 3.4.5, cropped 2D image mode is both faster and less electronically noisy than full 2D image mode. This has the advantage that we can acquire data faster than observed average power fluctuations, as well as more quickly analyze the smaller-sized data files. The increased speed with which we could analyze data meant that we could more quickly effect experimental improvements. To this end, we increased the HSS from 0.08 MHz to 1 MHz to acquire data faster. We also focused the signal beams near each other on the CCD, overall reducing the readout region from 512×512 px^2 to 100×34 px^2, and readout time from 0.3 s to 0.02 s. A sample data image according to these changes is shown in fig. 4.12.

These experimental changes led to a first observation of sub-Poissonian multi-beam correlations $\sigma = 0.55 \pm 0.28$ over 10 sets of 10 data images, at 450 nm and 660 nm wavelengths and 0.1 nW average FWM power. To improve this value further, particularly the precision of the reported NRF, we next consider how we may improve the FWM Fano factor by reducing the pump power fluctuations. As discussed in sec. 2.1.3 and sec. 3.2.3, reducing classical beam noise is also essential for observing higher-power sub-Poissonian intensity correlations.

4.7 Improving Pump Power and Pointing Stability

Although we did not at this point yet have a full theoretical understanding of our experiment, as outlined in sec. 2.2, we expected that pump power and pointing fluctuations over measurement timescales could increase measured NRFs by increasing the Fano factor of the FWM beams and decreasing the SNR if the pump beam becomes misaligned. As well, there are practical considerations to improving the power stability of the pump beam. Because we coarsely align the nonlinear fiber coupling based on the pump throughput, as well as optimize the coupling based on FWM power as measured by the spectrometer, pump power fluctuations are scientifically as well as practically limiting. A similar argument can be made for improving pump pointing stability, as this affects FWM mode coupling, as well as optical fiber damage.

4.7.1 Characterizing and Mitigating Pump Power Instability

We first characterized the power stability of the pump laser with a Thorlabs optical power meter mounted directly before the PCF input, optically insulating the power meter from ambient light using a lens tube and laser-safe cardboard. The laser power fluctuations shown in fig. 4.13 therefore includes all optical components prior to fiber coupling (*i.e.* temperature-controlled bulk LBO crystal, dispersion prism, filters, *etc.*).

In fig. 4.13, we see power fluctuations over several-minute measurement timescales. As pump power is quadratically related to the number of spontaneous FWM pairs generated, and exponentially related to the number of stimulated FWM pairs (see sec. 2.1.1), pump fluctuations are amplified in the intensity-correlation data (see sec. 3.1.2). Note that this power measurement

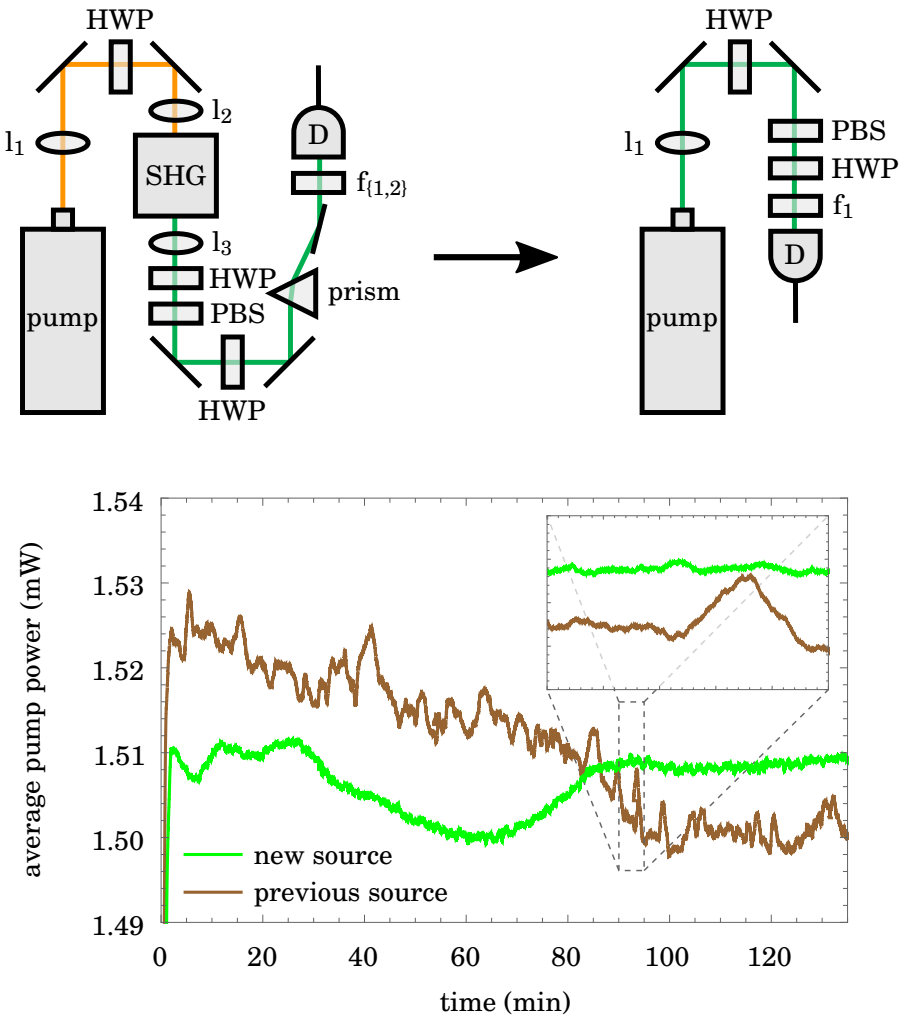

FIGURE 4.13. (top) A comparison of experimental setups using the (left) previous 1064 nm pump and (right) new 532 nm pump. $l_{\{1,3\}}$: collimating lenses; l_2: focusing lens; $f_{\{1,2\}}$: 532 nm bandpass filters; D: optical power meter.

(bottom) A comparison of the power fluctuations of the previous 1064 nm pump and new 532 nm pump. (inset) A 5 min data segment. Data was acquired with a Thorlabs optical power meter, and fit with a moving average to remove effects of laser pulsing.

does not include effects of pointing instability caused by the long pump beam path-length and other optical components, which are also detrimental to FWM power stability, discussed in detail in sec. 4.7.2.

The short-timescale power variations are due to poor LBO temperature stability, as SHG phase-matching in LBO is temperature dependent [94]. Long-term instability is likely due to ambient temperature variation misaligning the pump from optimal SHG phase-matching.

Both of these issues have been mitigated by replacing the externally frequency-doubled 1064 nm laser (Teem Photonics SNP-08E-100 [60]) with a 532 nm pulsed source (Teem Photonics SNG-03E-100 [61]). The new source is essentially the same as the previous, albeit with a quasi-phase-matched periodically-poled LBO crystal [95] integrated into the front of the laser head for SHG, which does not require external temperature control. The new pump laser, including SHG, has the same footprint at the previous 1064 nm laser itself. Comparing the complexity and power stability of these two pumps is shown in fig. 4.13.

We see that once both lasers have stabilized around 90 min operation, the 532 nm source is more stable on both long and short timescales compared to the 1064 nm source. As well, due to the shorter beam path from the pump to nonlinear fiber ($\sim$ 1 m to, ultimately, $\sim$ 0.4 m), mode-coupling issues related to pump pointing instability are reduced.

4.7.2 Characterizing and Mitigating Pump Pointing Instability

As discussed in sec. 3.1.4, dielectric damage may occur in PCF when high-energy optical pulses are incident on the PCF microstructures. Also, pump-fiber alignment directly affects coupling into desired FWM modes, which may decrease the SNR if the pump becomes misaligned. Sources of pointing instability affecting fiber coupling efficiency are the pump laser itself, optical components, and component mounts along the beam path (*e.g.* mirrors, lenses, HWPs, translation stages, post and pedestal mounts). We already identified and replaced one primary source of noise in sec. 4.6, the defective three-axis translation stage on which the nonlinear-fiber input was mounted, which contributed to our first measurement of sub-Poissonian intensity correlations. In this section, we characterize the effects on laser pointing from various optical components, as well as test several solutions to mitigate these issues, including fiber splicing and optical cage systems.

We characterized pump beam wandering using a Thorlabs BP209-VIS beam profiler [96] mounted $\sim$ 65 cm from the laser output, including any intermediate optical components. The distance 65 cm was chosen as an expected beam path length based on previous experiments and the reduced footprint of the 532 nm laser, compared to bulk frequency-doubling the 1064 nm laser. We measured the beam wandering of several optical components: the laser mounted on 7.5 cm post mounts, the laser mounted on 2.5 cm pedestal mounts, and the laser wandering while rotating the second HWP which controls pump polarization. The results are shown in fig. 4.14.

A collimating lens was mounted between the laser and the beam profiler, as well as an attenuator (HWP and PBS), as these are essential experimental components. In the measure-

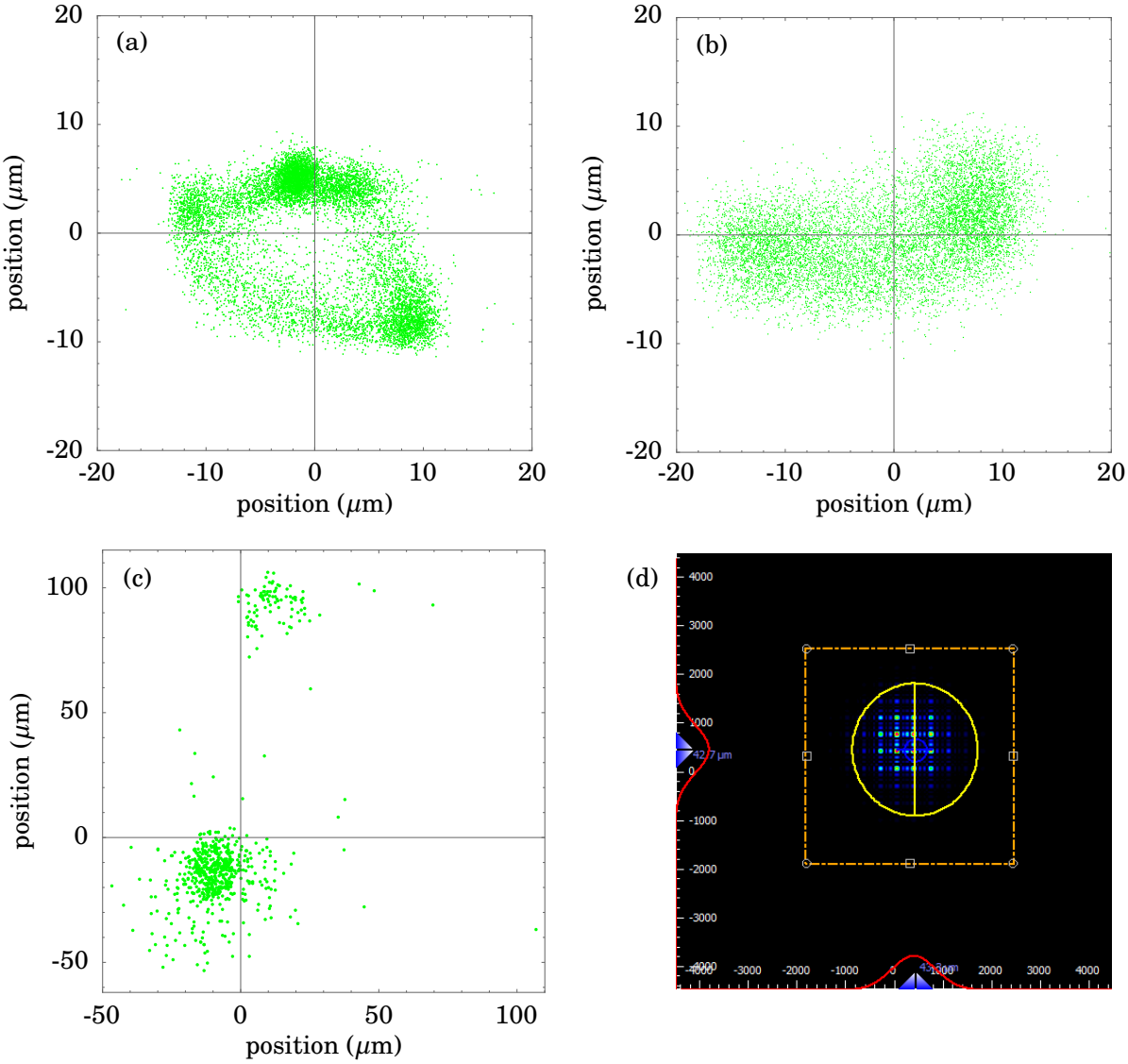

FIGURE 4.14. Pump beam wandering of (a) the laser mounted on 7.5 cm post mounts, (b) the laser mounted on 2.5 cm pedestal mounts, (c) the laser divergence from a rotating HWP, and (d) a sample data set captured with a Thorlabs BP209-VIS beam profiler. In (a), (b), and (c), the green markers indicate the pump beam's centroid for each position measurement. The average beam position is marked by the figure cross hairs. In (d), the axes represent position in microns, and are non-essential for qualitatively analyzing the data. The yellow circle indicates the calculated beam perimeter; the red curves on each axis are the beam cross sections with Gaussian fits. The specle pattern of the beam profile is due to the low-frequency beating of the beam profiler's scanning slit with the slow laser repetition rate.

ment of beam deflection due to HWP rotation, only the HWP after the PBS (see fig. 4.13, for example) was rotated, keeping the optical power on the beam profiler constant and consistent with previous beam stability characterizations. Measurements were taken over a 12 min period, with a sample data image shown in fig. 4.14 (d). The grid pattern is not a true feature of the beam profile, but rather a beating effect of the slow-pulsed laser with the scanning slit of the beam profiler. To achieve consistent beam tracking, beam profiler settings were optimized to give a true representation of the beam's centriod. A limiting factor of these characterizations is the low scan rate of the beam profiler, operating at 20 Hz, too slow to see the pulse-to-pulse wandering of the kilohertz-pulsed pump beam.

We can see from fig. 4.14 (a) and 4.14 (b) that the pump laser mounting does not significantly change beam pointing stability when comparing short post and pedestal mounts. Indeed, measuring the average radial beam distance ρ from the beam's average position, we calculate $\rho_{\text{post}} = 7.8 \pm 3.0$ µm and $\rho_{\text{pedestal}} = 8.3 \pm 3.8$ µm. Note that these estimates do not include systematic errors introduced by beam-profiler vibrations.

While rotating the HWP over even a few degrees, the pump beam is deflected as far as 100 µm, which is greater than ten times the wandering measured of the beam itself, as shown in fig. 4.14 (c). This is due to the nature of multi-order HWP design and fabrication, wherein a beam will refract through the birefringent plate depending on the beam's polarization relative to the optical axis of the HWP. Previously it had been observed that rotating the second HWP could increase or decrease the measured power of the FWM beams, suggesting that the FWM process was polarization-dependent in our fibers. We, however, do not expect this to be the case because of mode-mixing along the fiber length. From this data, we conclude that this phenomenon was actually due to beam deflections of the HWP altering mode coupling at the fiber input. This HWP was therefore removed from the experiment.

4.7.2.1 Experiments with SM450 to Improve Pump Coupling

As a first attempt to mitigate pump pointing stability issues, we spliced a length of Single-Mode Fiber (SMF) (Thorlabs SM450 [97]) to the PCF. We anticipated that this approach would improve the pump mode quality, using the SM450 as a mode filter for the multi-mode pump beam. As well, because of the larger solid-core size of the SM450 relative to the PCF (~ 5 µm diameter and 2.5 µm diameter, respectively), it is more robust to pointing issues and damage, as discussed in sec. 3.1.4. Finally, the splice would maintain constant coupling conditions into the appropriate FWM modes of the PCF. Despite these potential advantages, this solution was found to be unfeasible, as we will now discuss.

The principle of fiber splicing is to orient two fiber end faces near each other, and then to apply a powerful electric arc across the fibers' interface to melt the two ends together. If performed correctly, this creates a robust joint between the two fibers, which efficiently guides light from one to the next. To perform our fiber-splicing experiments, we used a Fitel S183 PM II splicer [98]

along with a mechanical fiber cleaver (as opposed to the ceramic tile that had been previously used to manually cleave fiber ends). The prepared ends of 5 m of PCF and 10 m of SM450 were loaded into opposite-facing ends of the splicer. The fibers were automatically aligned by the splicer, and their relative x-, y-, and z-positions manually adjusted to optimize coupling before the splicing arc was initiated. To optimize fiber orientations and positions while in the splicer, we pumped the SM450 with our usual 532 nm source, and measured the spectrum of the PCF using a spectrometer. Settings related to the fiber positions, arc power, arc duration, and number of arcs were all adjusted from factory settings to increase coupling efficiency before and after the splice. Note that we achieved only ~ 50% coupling efficiency of the pump laser into the SM450 itself, likely low due to the poor pump laser mode.

The first issue with this experiment was the spectrum of the output beam from the SM450, before being launched into the PCF, shown in fig. 4.15. When pumped with our 532 nm source at 190 µW average power, we measure a stimulated Stokes Raman peak at 545nm, and anti-Stokes peak at 525 nm, with broadband Stokes scattering to beyond 700 nm. With low SM450 coupling efficiency and loss due to the imperfect fiber splice into the PCF, and because we require high pump power to achieve bright FWM, this Raman scattering is detrimental to measuring sub-Poissonian intensity correlations. That is, the broadband Stokes Raman scattering spectrally overlaps with the PCF Stokes FWM wavelength, which necessarily deproves measured correlations (see sec. 2.2) and cannot be spectrally filtered at the splice joint.

One could use a shorter length of SM450 for guiding, which would linearly reduce (but not eliminate) the Raman scattering power with fiber length at our Stokes FWM wavelength. There are, however, two other issues associated with splicing the SM450 to the PCF: mode coupling efficiency into the desired FWM mode, and SM450 power handling, which will be discussed later in this section.

In regards to poor mode-coupling efficiency, although we are able to align the two fibers in the splicer such that we measure FWM at the appropriate wavelengths on the spectrometer, coupling is severely degraded after the electrical arc splices the fibers. With poor PCF-SM450 coupling efficiency, as well as SM450-pump coupling efficiency, the required pump power to observe bright FWM becomes infeasible in regards to optical noise and fiber power handling.

Finally, obtaining optimal coupling into the specific FWM modes is challenging, if not impossible, without an intermediate fiber lens or fiber tapering. This is because the mode field diameter of SM450 at 532 nm wavelength is ~ 3.5 µm according to the fiber datasheet [97]. This is 1 µm larger than the core size of the PCF itself, therefore not allowing optimal focusing into the desired FWM modes of the PCF. Because of this reason, as well as the challenges associated with SM450 optical noise and poor splicing efficiency to the microstructured PCF, we did not pursue this option further. This technique is not practical when using the SMF28 as the FWM source either because of the low χ^3 nonlinearity requiring high pump power. As well, as discussed in sec. 3.1.5, the larger solid core of the SMF28 already makes it less susceptible to pump beam wandering.

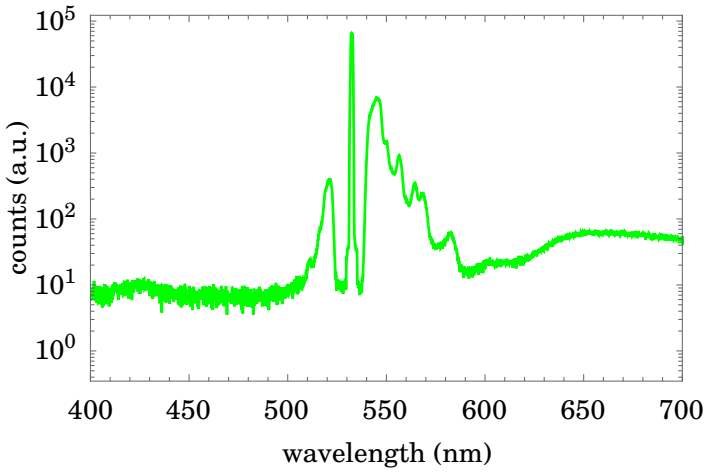

FIGURE 4.15. The spectrum of 10 m of SM450 fiber, pumped with 190 µW of 532 nm pulsed laser average power.

Following our discussions of pointing stability in sec. 4.7.2, as well as our intention to design a portable optics experiment, we have mounted all sensitive optical components in optical cage systems. Such optical cage fixtures have successfully been used in previous experiments performed by postdoctoral colleagues to achieve long-term stability in SPDC sources [13]. Cages, the pump laser, and coupling mirrors have also been mounted on 1 cm to 1.5 cm pedestal mounts, reducing the physical footprint of the FWM source.

The current iteration of the FWM source is shown in fig. 4.16. The pulsed 532 nm pump laser is collimated, attenuated via a single HWP and PBS, and coupled into a 1 m length of connectorized SM450. The SM450 fiber input is mounted on an xy-translation stage (Thorlabs ST1XY [99]), and the coupling lens is a Thorlabs C330TMD-A, the same lens used to couple in to the PCF, mounted on a z-translation stage (Thorlabs SM1Z [100]). The SM450 output is collimated and aligned with a Schäfter-Kirchoff fiber beam coupler. After filtering the Raman scattering from the SM450 output with a 532 nm bandpass filter, the pump beam is coupled into the PCF input, mounted the same as the SM450 input. Note that the PCF itself is not connectorized, but rather clamped in an FC/PC bare fiber adapter (Thorlabs BFT1 [101]) to interface with the cage.

In this way, the SM450 output was mounted within 10 cm of the PCF input in a rigid optical cage to maintain alignment, decoupling effects of beam wandering from the laser and beam deflections from the HWP.

Although this source did demonstrate long-term stability, requiring realignment only once every few days, there were two primary drawbacks. The first was that the Schäfter-Kirchoff fiber beam coupler was not practical for repeated realignment in the cage mount, as access to alignment screws was obstructed by the cage rods. The second drawback was that the SM450

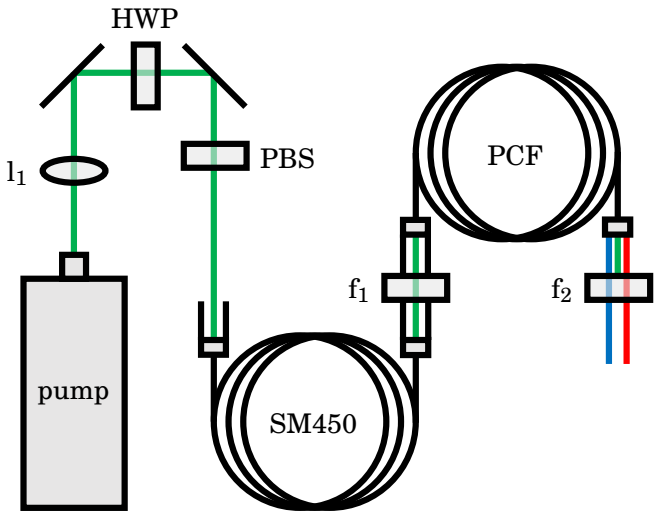

FIGURE 4.16. A schematic of the experimental setup using optical cage mounts and SM450 to stabilize PCF coupling. l_1: collimating lens; f_1: 532 nm bandpass filter; f_2: 450/660 nm multi-bandpass filter. Microscope objectives to couple into the SM450 and PCF are mounted on z-translation stages within the cage. The SM450 output is collimated and aligned via a Schäfter-Kirchoff fiber beam coupler within the cage. PCF output is mounted to a three-axis translation stage, as before. All fiber inputs and outputs within the optical cage are mounted to xy-translation stages.

could not handle sufficient pump power to achieve bright FWM before the SMF450 fiber input was optically damaged.

While calibrating the SM450 output power against pump input power, it was found that the output average power did not increase beyond ~ 1.8 mW, while increasing pump power. During this calibration, the pump power was increased beyond the dielectric damage threshold (see sec. 3.1.4), which resulted in permanent damage to the SM450. Because the core of the SM450 is solid, as is the SMF28 core, we expect it to have a similar damage threshold of tens of milliwatts average power with our laser. However, the SM450 has a doped germanosilicate core, and because the epoxy used to connectorize the SM450 has a lower optical damage threshold, the energy required to damage the fiber ends is reduced.

So far we have found that splicing SM450 and PCF together to improve mode coupling and mitigate beam wandering does not work, as splicing introduces loss and negatively affects mode coupling. SM450 is also impractical for mode filtering due to power handling issues, especially as we would like to demonstrate higher power FWM from the PCF. Ultimately, we removed the SM450 from the experiment, and replaced it with a pinhole, to accomplish a similar task.

4.7.2.2 Experiments with Pinholes to Improve Pump Coupling

As an alternative to using SMF mode filtering and guiding, we implemented a high-precision pinhole. The pinhole has the advantage of better power handling so long as the beam is well-focused through the hole and not on the surrounding material. Pump beam wandering then appears as power fluctuations on the filtered beam (similarly to the SM450), but reduces pointing and mode instability at the PCF input so long as the pinhole is stable relative to the fiber. Practically, the pinhole was found to be easier to align than the SM450, as all components are mounted in accessible two-axis translation stages in the optical cage.

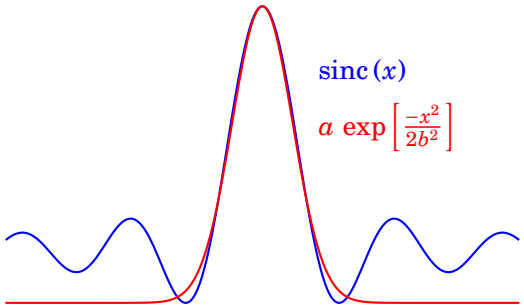

FIGURE 4.17. An approximation of the zero-order sinc mode with a Gaussian function.

The pump beam profile will not, however, be in the fundamental LP mode, as the Fourier transform of a rectangular function (the pinhole) is a sinc function, assuming that the input beam may be approximated as a plane wave. However, the zero-order mode of a sinc function is well-approximated by a Gaussian, as shown in fig. 4.17.

We used a 40 mm lens to focus the collimated pump beam through a 20 µm pinhole (Thorlabs P20D [102]), then recollimated the beam with a second 40 mm lens. The pinhole-filter and PCF were all mounted in a single optical cage, as shown in fig. 4.18. We chose these components based on our estimated pump beam diameter and diffraction-limited spot size of the 532 nm wavelengths pump. Specifically, we calculate the spot size D according to

$$D = \frac{2\lambda f}{d},$$

where λ is the pump wavelength, f is the lens focal length, and d is the beam diameter incident on the lens. In our specific case, $D \approx 14$ µm. We chose a pinhole with a diameter larger than 14 µm to avoid excessive clipping, 20 µm. The beam was then recollimated to its original diameter with a second 40 mm lens so that coupling conditions into the PCF would not be affected, as we did not change the input microscope objective.

We achieved ~ 80% coupling efficiency through the pinhole, with a visible sinc beam profile, when viewed in the far-field with a white laser-safe card. FWM at the desired wavelengths was observed with this source.

As with our nonlinear fibers, the pinhole is prone to optical damage at high pulse energies due to the 25 µm-thick foil from which it is made. Optically damaging the central pinhole may affect mode shape and coupling stability. Indeed, while aligning the experiment, we burned an irregular-shaped hole through the material while pumping at several milliwatts average power.

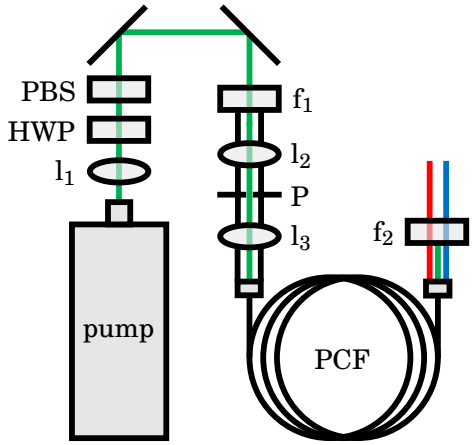

FIGURE 4.18. A schematic of the experimental setup using optical cage mounts and a pinhole to stabilize PCF coupling. $l_{\{1,3\}}$: collimating lenses; l_2: focusing lens; f_1: 532 nm bandpass filter; f_2: 450/660 nm multi-bandpass filter; P: 20 µm pinhole. The microscope objective to couple into PCF and l_2 are mounted on z-translation stages within the cage. The pinhole and l_3 are mounted on xy-translation stages.

While this pinhole could still be used with care taken to align through the proper central hole, we implemented a more robust pinhole to mitigate the risk of further optical damage to the experiment. The newly implemented pinhole has a datasheet-specified continuous-wave damage threshold of 75 MW/cm^2 (Newport 910PH-20 [103]), compared to the previous < 0.001 MW/cm^2. The high-power pinhole allowed for mode coupling into the desired FWM modes, as with the previous implementation, and extra care was taken to align the pinhole precisely before increasing the pump power.

4.7.2.3 Mode-Coupling Sensitivity to Fiber Cleaving

In our initial experiments using the pinhole filtering, we measured FWM peaks which were always excited in pairs, as shown in fig. 4.19. For example, as fiber coupling was optimized to excite the 449 nm anti-Stokes FWM condition, the 454 nm condition was always equally satisfied. Upon recleaving the fiber input several times, we measured the same phenomenon. This indicated that this was a feature of the newly-implemented pinhole filtering, we believed caused by the mode overlap of the sinc-profile pump beam with the supported FWM modes of the fiber.

The doubly-satisfied FWM condition effect is detrimental to measuring sub-Poissonian twin-beam correlations, as the reduced coupling efficiency into any single FWM mode decreases the SNR, especially at the optically-noisy Stokes FWM wavelengths.

However, after recleaving the fiber several more times, we no longer observed the doubly-satisfied FWM condition effect. The red herring can either be attributed to a series of poor cleaves or a defective short length of fiber, which happened to coincide with our implementing a new source design.

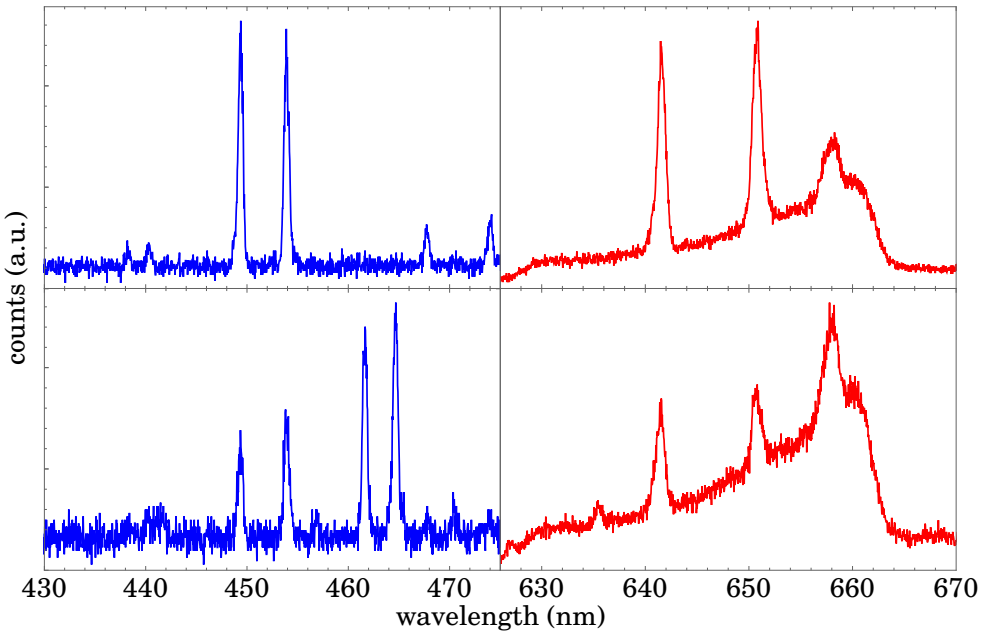

FIGURE 4.19. Sample spectra showing doubly-satisfied FWM conditions. Stokes and anti-Stokes FWM pairs with different fiber coupling alignment are shown in the top and bottom spectra.

4.7.2.4 Fiber Coupling Using an Optical Cage and No Mode Filtering

We also found, during the interim of waiting for the high-power pinhole, that the source remained stable over the period of one week when coupling directly to PCF without any form of pump or mode stabilizing. We therefore removed the added complexity of pinhole or SMF pump filtering. This simplified experiment is shown in fig. 4.20, with reduced physical footprint, and pump-beam path-length of ~ 40 cm. Fig. 4.20 represents the current FWM source, which we use for the remainder of this chapter.

4.8 Collapsing Fiber Input for Improved Optical Power Handling

As discussed in sec. 3.1.4, the PCF has been observed to be damaged at a few milliwatts of average pump power, with catastrophic dielectric damage occurring above 3 mW. This is due to the microstructures at the PCF end face being exposed to high energy densities of the focused pump beam. In an effort to mitigate this issue so that we might observe FWM at milliwatts of average power, we collapsed the fiber end face such that the pump beam would be focused through a more robust piece of solid silica before being guided in the PCF core. The fiber collapsing was performed by postdoctoral colleague Dr. Alex McMillan, and all spectral and

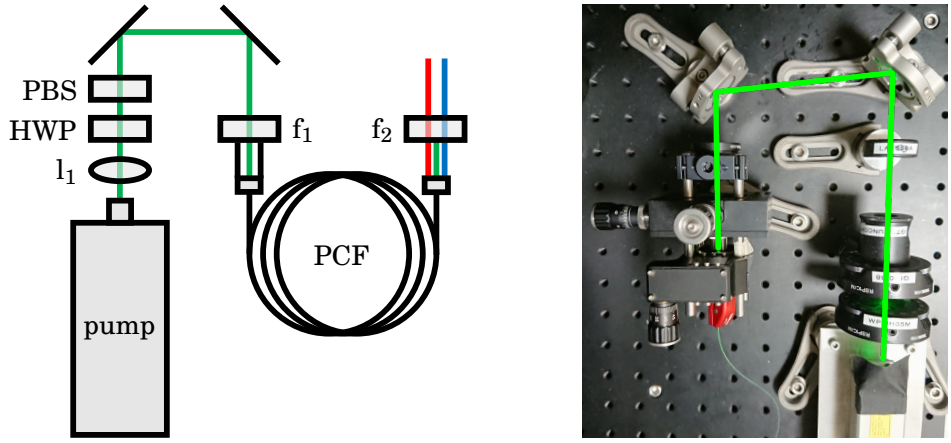

(a) (b)

FIGURE 4.20. A schematic of the current experimental FWM source, using optical cage mounts for improved coupling stability. $l_{\{1,3\}}$: collimating lenses; f_1: 532 nm bandpass filter; f_2: 450/660 nm multi-bandpass filter.

damage characterizations were performed by myself.

We collapsed the fiber in a similar fashion to fiber splicing. Several inches of PCF were first drawn through a bare fiber adapter ferrule for interfacing the fiber with the optical cage after collapsing the input. The exposed end of the PCF was then clamped across both fiber inputs of the Fitel S183 PM II splicer. The splicer arc melted a small section of PCF, which was then drawn back near to the ferrule, as shown in fig. 4.21 (a). Having the collapsed end of the fiber near the

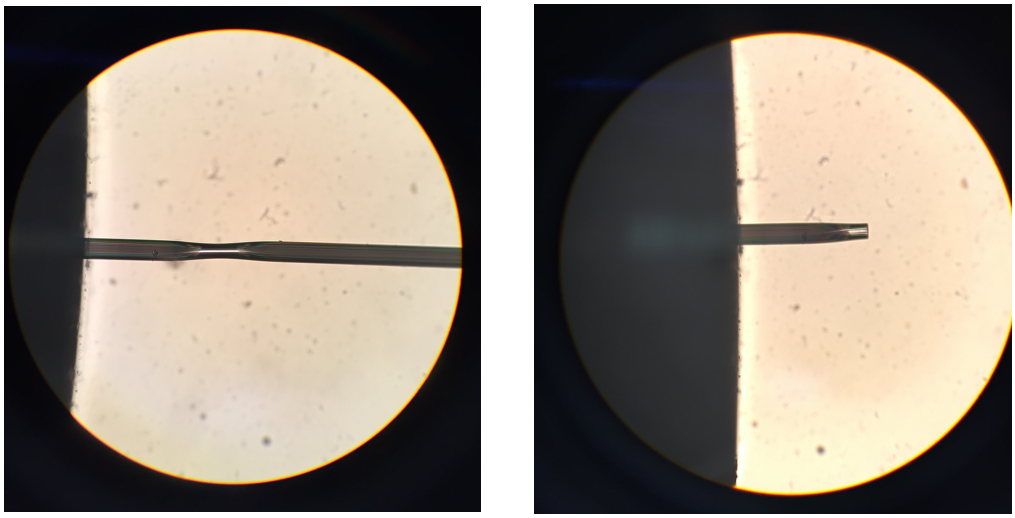

(a) (b)

FIGURE 4.21. A microscope image showing the collapsed fiber (a) pre- and (b) post-cleave.

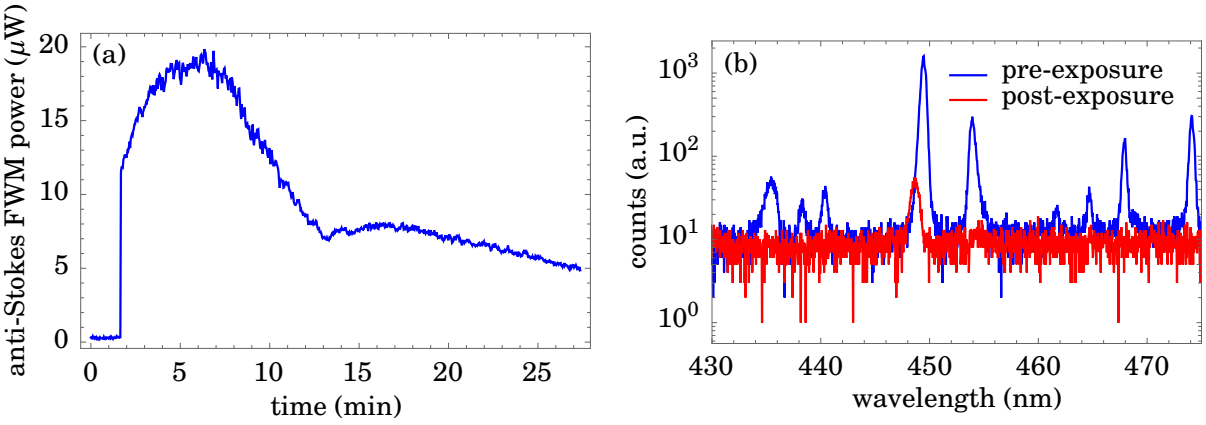

FIGURE 4.22. (a) A plot of average anti-Stokes FWM power over 25 min, with collapsed PCF input face. The zero-power data for the first few minutes is with the pump laser off, so that the noise-floor of the optical power meter can be clearly distinguished from the data. (b) PCF spectra before and after exposing the collapsed PCF to 3.3 mW average pump power for 25 min, plotted with a logarithmic y-axis to see dim spectral features.

ferrule allowed for more precise cleaving in the center of the collapse. The collapsed and cleaved fiber input is shown in fig. 4.21 (b). Note that only the input end of the fiber was collapsed, not the output. We measured no extra coupling loss or reduced available FWM power due to the collapse.

To test the damage properties of the collapsed PCF, we aligned the fiber in the experiment as usual. The FWM spectrum of the fiber was similar as before, shown in fig. 4.22 (b). The pump average power was slowly increased to 4 mW, with no catastrophic dielectric damage observed. The pump power was then reset to 3.3 mW, which initially corresponded to 10 μW of anti-Stokes FWM average power, as measured with a Thorlabs S130C optical power meter. The FWM power was monitored for 25 min, the results of which are shown in fig. 4.22 (a).

Although the fiber did not experience catastrophic dielectric damage, it was still damaged over long timescales. The initial power increase of fig. 4.22 (a) is likely due to fluctuations in average pump power, as we are in the exponential FWM gain regime. Not shown is that anti-Stokes FWM power had decreased to < 1 μW after 40 min exposure. To ensure that the fiber had not simply become misaligned over the 25 min measurement duration, we realigned the fiber according to the spectrometer to optimize coupling, and were only able to achieve FWM coupling efficiency at 5% from pre-exposure, shown in fig. 4.22 (b).

These data suggest that collapsing the PCF end face does not insulate the microstructures well enough to prevent long-timescale optical damage associated with the high peak energy densities of our pulsed laser. Without improved PCF coupling stability or robustness to optical damage, average FWM power is limited to hundreds of nanowatts. As discussed in sec. 3.1.5, however, average FWM powers up to hundreds of microwatts are accessible using SMF28 as the nonlinear gain medium.

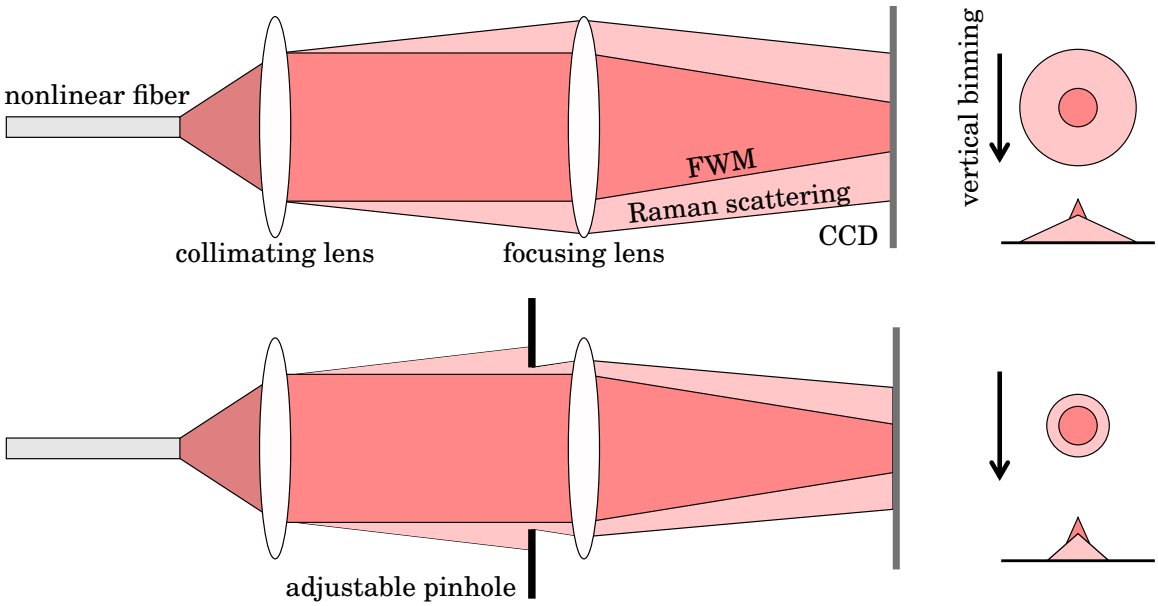

FIGURE 4.23. A graphical representation of how a pinhole may be used for spectral filtering of Raman scattering in the Stokes beam, exploiting the chromatic aberrations of the collimating lens. The bottom figure shows reduced Raman noise due to pinhole filtering, when compared with the top figure.

4.9 Other Techniques for Reducing Raman Noise

Stokes Raman scattering is the primary source of optical noise in our correlated-intensity experiment. Indeed, improved spectral filtering enabled our first measurement of sub-Poissonian intensity correlations (see sec. 4.6). In this section, we discuss two methods of reducing optical Raman noise in the Stokes beam by taking advantage of the chromatic dispersion introduced by the fiber out-coupling lens, and spherical aberrations introduced by the focusing lens.

The principle of the first technique is shown in fig. 4.23. Because the fiber out-coupling lens exhibits chromatic dispersion, wavelengths longer than the Stokes FWM wavelength will refract at larger angles, and reduction of Raman noise along the binning direction increases our SNR. To reduce the Raman noise, we align a mostly-closed pinhole to the center of the Stokes beam, using the CCD camera to monitor optical power and ensure proper alignment. The pinhole diameter is then manually adjusted according to the Full Vertical Binning (FVB) data, to reach a minimum NRF. Implementing this technique, we improved the NRF from $\sigma = 0.68 \pm 0.12$ to $\sigma = 0.61 \pm 0.08$ over 10 sets of 100 data images, all other experimental parameters consistent.

The second technique is shown in fig. 4.24. Here, we exploit the spherical aberrations of the focusing lens to spatially shift the Raman noise photons away from the Stokes FWM photons, perpendicular to the vertical binning direction, by aligning the Stokes beam away from the center

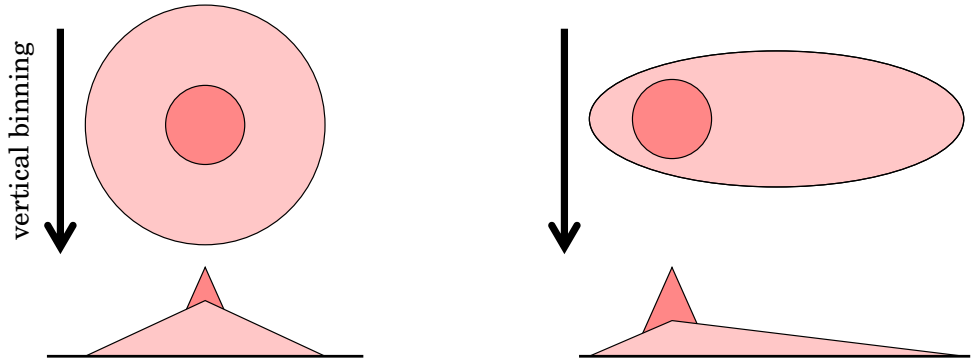

FIGURE 4.24. A graphical representation of how Stokes Raman noise may be spatially distinguised from the FWM signal, exploiting spherical aberrations of the short focal-length focusing lens. (left) The beam is aligned through the center of the focusing lens, and (right) the beam is aligned away from the center of the focusing lens. Note that both triangles which represent Raman power have the same area.

of the short focal-length focusing lens. While not reducing the net power of the Raman noise, the effect is that fewer Raman photons will be aligned vertically over the FWM, thereby increasing our SNR. Using this technique, without pinhole filtering, we were able to quickly reduce a NRF of ~ 0.9 to ~ 0.6.

4.10 Improved Four-Wave Mixing Focusing on CCD Array

A primary challenge associated with this experiment has been finding a simple, reliable method for focusing both FWM beams simultaneously onto the CCD, with $\lesssim 150$ µm spot diameters ($\lesssim 10$ px). This is due to chromatic dispersion introduced by the PCF collimating lens (see fig. 4.6), as high-NA achromatic microscope objectives required by the high-NA PCF are not presently commercially available. Having well-focused beams is not only useful for reducing electronic camera noise in the CCD detection regions (see sec. 3.2), but is also an important practical consideration for imaging techniques.

Typical alignment procedure has been to first collimate the intermediate-wavelength pump beam because it is high-power enough to collimate by eye. The Stokes beam is then focused independently of the anti-Stokes beam with one lens, to a few pixels diameter, as measured with the CCD camera. A second lens was used to focus the anti-Stokes beam independently of the Stokes. Because we do not have precise access to the collimation conditions of the FWM beams, quoted focal lengths for lenses which we might use for detection are unreliable. We therefore determine all lenses and positions heuristically, a task whose difficulty is compounded for each unknown optic used. Nevertheless, we have empirically found a single-lens which focuses both beams to sub-10 px diameter spots, reducing the complexity and optical loss associated with using two separate focusing lenses, as in sec. 4.6.

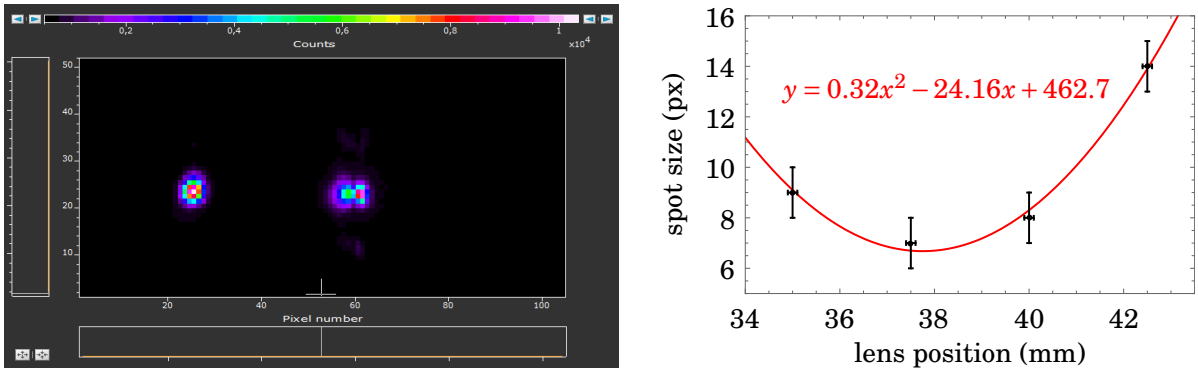

FIGURE 4.25. (left) Sample data image with a 10 cm lens at 37.5 mm in the lens tube, used for determination of optimal lens position. Axes represent pixel number, and are non-essential for qualitatively analyzing the data. (right) Results of lens position optimization, with fitted parabola. Error bars are estimated from the measurement precision of the spanner and camera.

To optimize the single focusing lens position, of quoted focal length 10 cm (Thorlabs LA1509-A [104]), we first adjusted the collimation to the pump beam, as previously described. Then we mounted a 1" optic retainer ring inside of a 3"-long opaque lens tube that could be fixed to the face of the camera. The position of the retainer ring was measured with a spanner wrench (Thorlabs SPW602 [105]). We then shone both FWM beams on the CCD, adjusting the PCF output collimating lens position until both FWM spots were approximately the same width. Because we are using a short focal-length focusing lens, careful attention was paid to aligning the beams parallel to the optic axis, and near the lens center, to minimize spherical aberrations. The spot size of the beams were recorded for several lens positions around what had already been determined to be a near-optimal position. A sample data image, and the results of this optimization are shown in fig. 4.25. From the fitted parabola, we can determine our optimal lens position to be near 37.8 mm, as measured from the end of the lens tube with the spanner wrench. Note that when both beams were optimally focused for a given focusing lens and position, the collimating lens position had to be adjusted such that the pump beam was no longer collimated. If the fiber out-coupling is not adjusted properly, the FWM beams may clip on the 1" optic mounts.

Because reducing the spot size increases the SNR of the FWM to electronic detection noise, we also tried to focus the beams with even shorter focal-length lenses: 11 mm focal-length aspherical microscope objective, and a 6 cm focal-length 1" spherical lens. The short focal length of the microscope objective, however, meant that the microscope lens tube in which it was mounted would come in contact with the external camera shutter before the lens could well-focus the beams. We also tried to optimize a 6 cm focal-length lens, similar to the 10 cm lens. We found in this case that when both beams were equally focused on to the CCD, the required collimation meant that

one of the FWM beams was clipped by the 1" optics. This drawback might be overcome by using higher-NA optics nearer the fiber out-coupling, but the 10 cm lens worked sufficiently well to not warrant such an experimental undertaking. Indeed, we see from sec. 3.2.3 that reducing our spot diameter by one or two pixels does not have a significant impact on the quality of the NRF data at our operating powers.

4.11 First Absorption Measurement at the Shot-Noise Limit Using Sub-Poissonian Intensity-Correlated Beams

In this section, we report an absorption measurement performed at the SNL, using the PCF source. This represents a first demonstration of parameter estimation using visible-wavelength twin beams at 5 pW of average power (1 µW peak power). The experimental advancements which enabled this measurement are (1) fiber position optimization (see sec. 3.1.3), (2) optimization of pump power to balance the detrimental effects of noise photons and unbalanced detection efficiency (see sec. 3.2.3), (3) using FVB rather than image mode to collect less-noisy data (see sec. 3.4.5), (4) simplification and ruggedization of the FWM source (see sec. 4.7.2), (5) the implementation of pinhole filtering and spherical-aberration filtering to remove some of the Raman noise not already removed by the bandpass filter (see sec. 4.9), and (6) the use of only one focusing lens for detection (see sec. 4.10). A schematic of the current version of the experiment is shown in fig. 4.26.

First, we characterized the correlations of our source by measuring the NRF. Parameters such as pinhole width, focusing conditions, camera temperature, HSS, pump power, and camera inte-

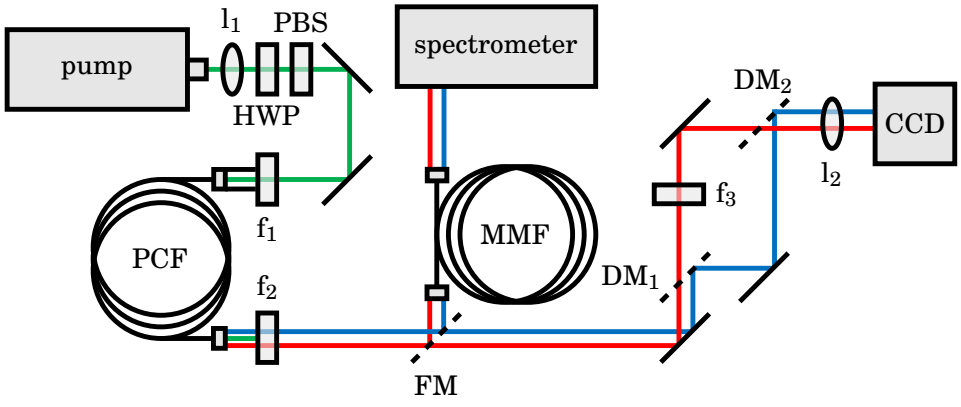

FIGURE 4.26. A schematic of the experimental setup used for current attempts at measuring sub-Poissonian intensity correlations. pump: 532 nm wavelength, pulsed laser; l_1: collimating lenses; l_2: focusing lens; f_1: 532 nm bandpass filter; f_2: 450/660 nm multi-bandpass filter; f_3: narrowband Stokes filter; FM: flip mirror; $DM_{\{1,2\}}$: dichroic mirrors.

gration time were all optimized as described in previous sections, with the live-NRF-monitoring via MATLAB code. We measured $\sigma = 0.47 \pm 0.04$, an average of 10 data sets, each 100 images at 0.07 s integration time, without background noise thresholding or post-selection. This is strong evidence of sub-Poissonian intensity correlations at 13.25 standard deviations below coherent-beam statistics, and an improvement over our previous best results of $\sigma = 0.55 \pm 0.28$ in sec. 4.6.

We then inserted a 1 mm-thick glass slide in the anti-Stokes beam as our absorptive sample. With the glass slide in place, we measure $\sigma = 0.50 \pm 0.07$. This value is comparable to the previous measurement, though we would expect deviations as channel loss increases due to changing detection efficiency (see sec. 2.2). We estimate $\hat{\alpha}$ over a data set of 1000 images according to

$$\hat{\alpha} \approx 1 - \frac{\mathrm{E}[n_2]}{\mathrm{E}[n_1]} \frac{\mathrm{E}[n_1']}{\mathrm{E}[n_2']},$$

where n_1 and n_2 are the probe and reference beams, respectively, and the prime denotes beam power from the sample measurement stage (as opposed to the calibration stage). We measured $\hat{\alpha} = 0.0868 \pm 0.0005$. As discussed in sec. 2.3.1, however, this estimate may be biased due to changes in average pump power affecting the ratio of Stokes Raman scattering against FWM signal. Without precise knowledge of the Raman power scaling and filtering efficiency, this accuracy error cannot be precisely estimated. For the remainder of these discussions, we assume that average pump power has not changed significantly between calibration and measurement stages, which is true up to the measurable precision of the Thorlabs optical power meter used to monitor average pump power, and approximately true according to the data presented in fig. 4.27.

The results of the absorption measurement, comparing single- and multi-beam estimators, is shown in fig. 4.27. In the classical direct measurement (fig. 4.27 (a)),

$$\alpha_c = 1 - \frac{n_1'}{\mathrm{E}[n_1]}, \tag{2.33}$$

we are estimating absorption using only the probe beam, achieving $\Gamma_c = 22 \pm 6$, where $\Gamma < 1$ is sub-SNL. Classical super-Poissonian power fluctuations ($F_s = 20 \pm 6$) are reflected in the absorption data. As well, because the average pump power has changed from calibration to measurement stage, the estimated mean absorption is negatively biased $\mathrm{E}[\alpha_c] = 0.078 \pm 0.008$. The change in mean classical power could be due to many factors, including fluctuations in the pump laser power, fiber misalignment from temperature fluctuations, fiber movement changing mode coupling.

The estimator of fig. 4.27 (b), compared to the single-beam one, has access to the correlated reference channel

$$\alpha_l = 1 - \frac{\mathrm{E}[n_2]}{\mathrm{E}[n_1]} \frac{\mathrm{E}[n_1']}{\mathrm{E}[n_2']}. \tag{2.34}$$

Using this estimator, we measure $\Gamma_l = 1.24 \pm 0.23$, which is still above the SNL of estimating the loss parameter. Some of the classical fluctuations are still visible in the data, although reduced compared to α_c. The mean value $\mathrm{E}[\alpha_l] = 0.087 \pm 0.002$ agrees well with the estimated sample absorption.

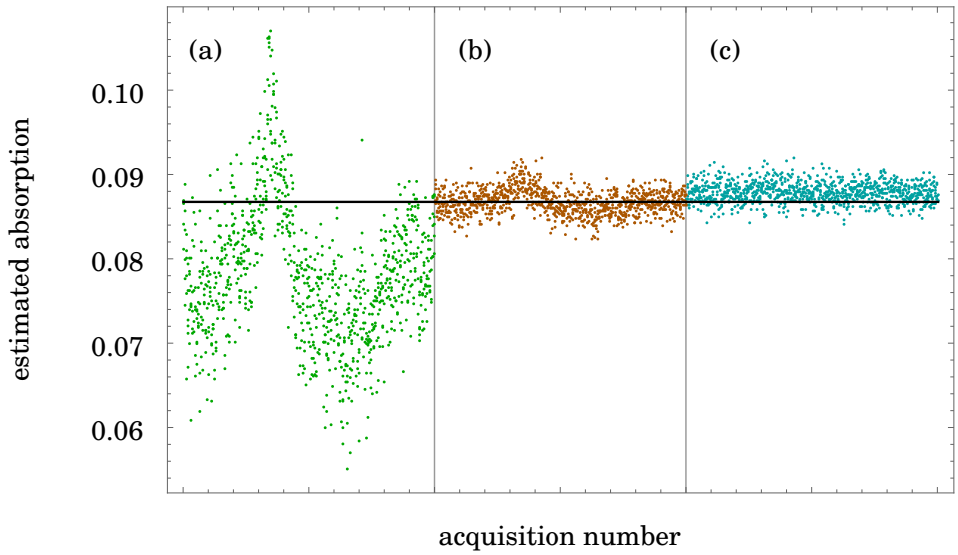

FIGURE 4.27. Plots showing 1000 absorption estimations of a 1 mm-thick glass slide according to (a) a classical direct-measurement estimator α_c (eqn. 2.33), (b) a correlated multi-beam estimator α_l (eqn. 2.34), and (c) an improved correlated-beam estimator α_m (eqn. 2.36). The mean sample absorption over all 1000 images is indicated by a solid black line.

Finally, we estimate the sample absorption according to

$$\alpha_m = 1 - \frac{n_1' - k\,\delta n_2 + \delta E}{\mathrm{E}\,[n_1]}, \tag{2.36}$$

which we know from sec. 2.3 to outperform α_l and α_c in terms of measurement precision. Indeed, we calculate $\Gamma_m = 1.02 \pm 0.16$, close to the SNL ($\Gamma = 1$). We also measure $\mathrm{E}\,[\alpha_m] = 0.088 \pm 0.001$, which agrees with the estimated sample absorption.

These results highlight the importance of optimizing estimators which account well for loss, unbalanced detection, uncorrelated optical noise, and detector noise, as although we measured strong sub-Poissonian intensity correlations, we are not currently able to estimate absorption below the SNL. The theoretical justification for these results are discussed in detail in sec. 2.3.

We have shown that our source can reliably produce sub-Poissonian intensity correlations, and when used with current multi-beam absorption estimators, can perform loss estimation at the SNL. Comparing our experiment to an equally-noisy classical one with the same detection efficiency, we measure a significant improvement, quantified by the ratio $\Gamma_c/\Gamma_m = 21 \pm 6$.

In the following section, we discuss Liquid Nitrogen (LN2) cooling the fiber, and the effects this has on the optical SNR. We also present box 4.1, which contains recent work by postdoctoral colleague Dr. Alex McMillan on reducing the size and weight of the FWM source. This is evidence of application of our research for outreach and dissemination.

4.12 Preliminary Work on Fiber Cooling

In sec. 2.1.3, we mentioned the temperature-dependence of Raman scattering in optical fiber. Specifically, according to eqn. 2.14 and eqn. 2.15,

$$I_R(\Delta\nu, T) \sim I_0(\Delta\nu) g_R(\Delta\nu)[1 + n(\Delta\nu, T)] \tag{2.14}$$

$$n(\Delta\nu, T) = \frac{1}{\exp(h\Delta\nu/kT) - 1}, \tag{2.15}$$

where I_R is the Raman emission rate, $\Delta\nu$ is the optical frequency relative to the pump frequency, T is temperature, I_0 is the 0 K emission rate, g_R is the Raman gain spectrum, n is the phonon population factor, and h and k are fundamental Planck and Boltzmann constants, respectively. From these equations, Raman power decreases with decreasing temperature and increasing spectral separation from the pump wavelength [45]. As well, because of the reduced density of states, we expect to improve the FWM Fano factor [44, 106]. As reduced optical noise, both uncorrelated photon noise and classical intensity noise, has been shown both theoretically (see sec. 3.2.3) and experimentally to reduce measured NRFs, we explored fiber cooling with LN2 at 77 K as a method to improve measurement precision.

Due to technical challenges associated with cooling PCF, discussed at the end of this section, we have conducted our preliminary tests using SMF28, which we have measured in sec. 3.1.1 to have broadband Stokes and anti-Stokes Raman scattering. The fiber was placed in a polystyrene dish, the fiber held in place by aluminum weights placed on top, and secured at both ends as usual for coupling in and out of the fiber. A polystyrene lid was also made with a hole to support a large-mouth funnel for safe LN2 pouring. The experimental setup is shown in fig. 4.29 (a). The length of fiber was allowed to cool for 20 min from room temperature to 77 K, with ~ 75% of the fiber submerged in LN2. The fiber was not moved before or after cooling, but fiber output required minor realignment because of ambient cooling from the LN2 near the mounting stage. Coupling to the spectrometer was optimized pre- and post-cooling to ensure a fair power comparison. The spectral effects of fiber cooling are shown in fig. 4.29 (b).

BOX 4.1. *BluPhoton* demonstrator for CLEO Europe 2019.

At CLEO Europe 2019, we presented a demonstrator of the FWM source, dubbed *BluPhoton*, using SMF28 as the nonlinear gain medium. This source, shown in fig. 4.28, was designed and assembled by postdoctoral colleague Dr. Alex McMillan based on the experimental efforts described in this thesis. It is approximately $25 \times 25 \times 15$ cm^3, and the enclosure weighs ~ 500 g without the aluminum breadboard. The base plate is PMA, and the sides and top are laser-cut acrylic sheets [107].

Although we have not yet rigorously measured the power stability or performance of the source, it remained well-aligned in an exhibition-hall environment, producing bright, visible-wavelength FWM and requiring alignment optimization only once per day.

Alignment on the showroom floor was performed via piezo-controlled mirror mounts.

This work demonstrates the potential for source miniaturization and long-term stability for other lab environments.

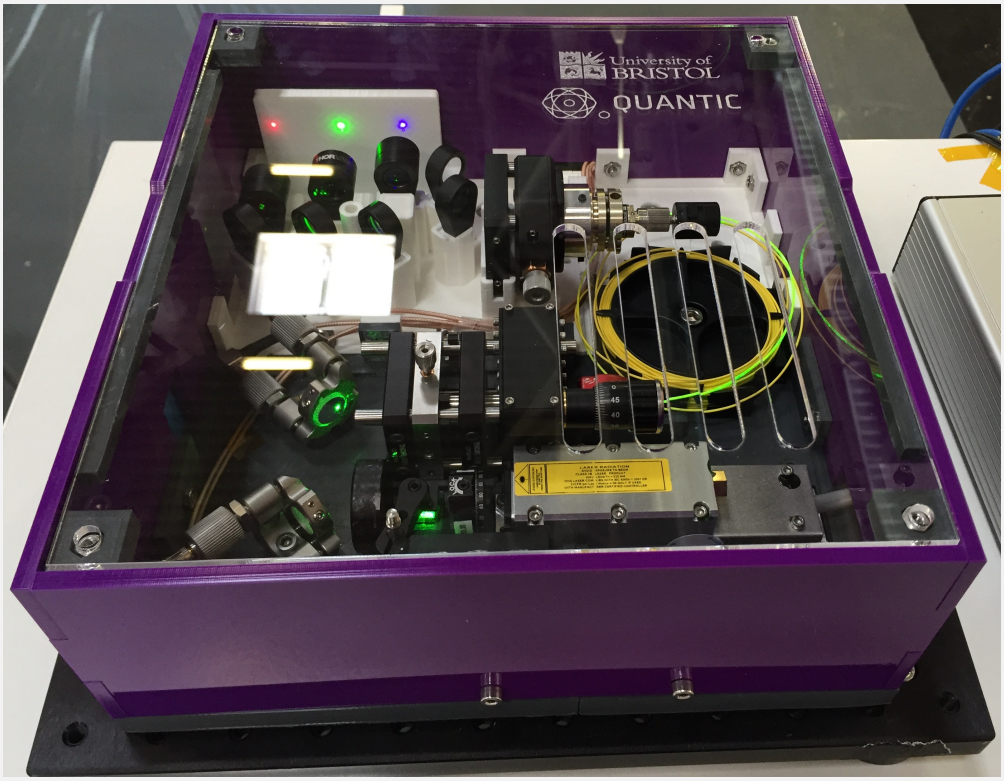

FIGURE 4.28. A photograph of the *BluPhoton* demonstrator for CLEO Europe 2019, with stable, visibly-bright FWM.

First to notice from the results of fig. 4.29 (b) is that Raman power did not measurably decrease at our wavelengths of interest. This is predicted according to the dependence of $n(\Delta\nu, T)$ on T, where we do not expect to see a large reduction in Raman amplitude as temperature changes for Raman wavelengths far from the pump. Considering our case where $\lambda_p = 532$ nm and $\lambda_{FWM} = 650$ nm, reducing the temperature from 300 K to 77 K predicts a reduction in Raman power by a factor of $\sim 10^{-8}$, less than our spectrometer measurement precision can distinguish.

Fiber cooling has also been shown to improve the Fano factor at wavelengths near the pump [44, 106]. Because spontaneous emission along the fiber contributes to the amplified signal, by reducing the temperature we would expect reduced intensity fluctuations. We, however, do not measure an improvement in FWM Fano factor with the camera pre- or post-LN2 cooling, for the same reason that we do not see a reduction in Raman noise amplitude. In fact, for a given pump power, we measure an increase in Fano factor ($3.39 \rightarrow 6.19$). This is due to an increase in FWM

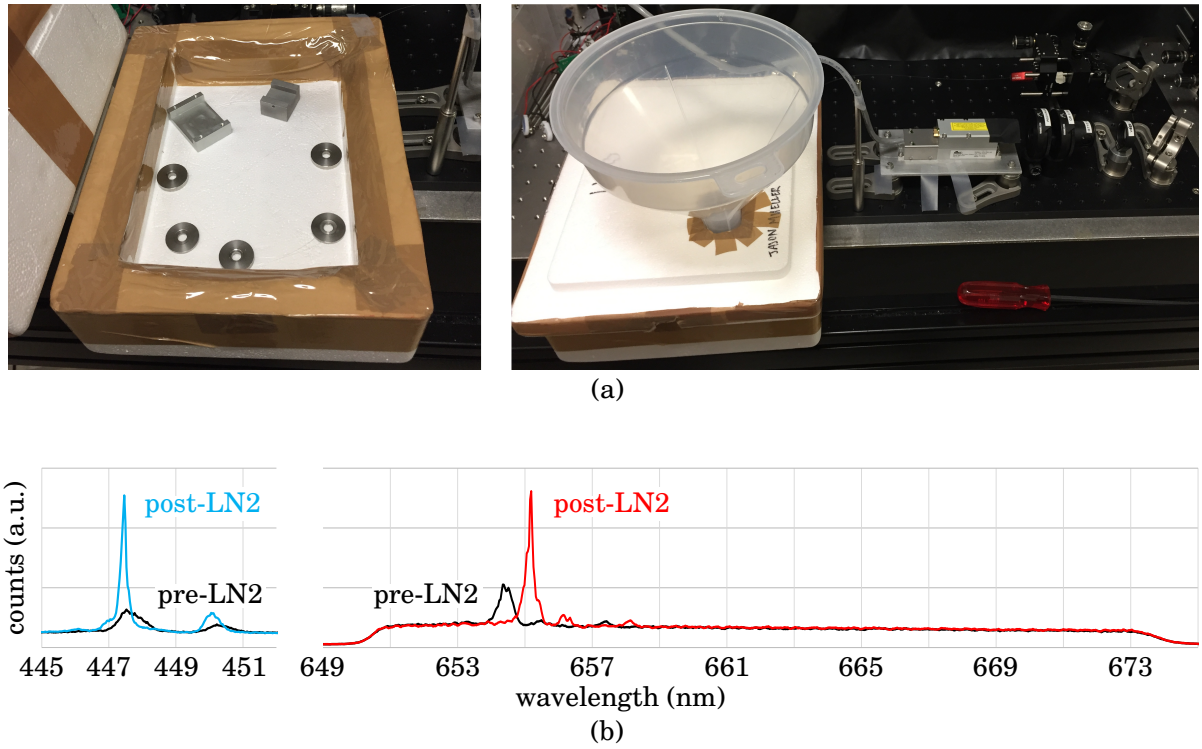

FIGURE 4.29. (a) The experimental setup used to secure and safely submerge the nonlinear fiber in LN2. (b) The spectrum of SMF28 pre- and post-LN2 cooling.

power by a factor of 1.4 at an equivalent pump power. We show in sec. 3.2.1 that the FWM Fano factor increases with pump power because of the exponential gain spectrum, and this increased Fano factor is consistent with the results shown in fig. 3.11. To be sure, for a fixed FWM power, we measure no change in Fano factor.

So far we have discussed that our Raman noise power, and our FWM intensity fluctuations worsen, for a given pump power. It would seem as though LN2 cooling of the fiber is not appropriate towards our goal of improving the SNR. However, we measure a spectral shift and narrowing FWM linewidth in the SMF28. Both of these results can be attributed to the thermal contraction of the fiber changing the dispersion of the FWM modes [44]. More intuitively, one could imagine blueshifting the fiber's FWM phase-matching curve (see fig. 2.5), such that the fixed-linewidth pump intersects a shallower-sloped region of the phase-matching curve. This would have the effect of shifting both FWM wavelengths away from the pump, as well as reducing their linewidths, both effects observed in fig. 4.29 (b).

From ref. [37], decreasing the FWM linewidth, with the pump linewidth constant, produces brighter FWM. This is because the FWM will reach the threshold for exponential gain sooner along the fiber length, with more optical power initially confined to a narrower bandwidth. With increased FWM power at LN2 temperatures for a given pump power, we can therefore increase

the SNR by decreasing the pump power, thereby reducing the Raman noise for a given FWM power. Work is presently ongoing to demonstrate the expected improvement of the measured NRF for a given FWM power, due to the increased SNR.

We have found that PCF cannot be as straightforwardly cooled as SMF28 due to the air-filled holes along the fiber core. Work performed by postgraduate colleague George Atkinson on separate nonlinear hollow-core fibers for their own separate experiments showed a reduction in fiber coupling efficiency when cooled with LN2. This may be due to air being drawn into the fiber and condensing near the end faces or along the fiber length, which also changes the fiber dispersion. Reduced fiber coupling may be mitigated by collapsing both PCF input and output ends, and we are currently pursuing this as a method to improve the SNR of the PCF-generated FWM as well.

4.13 Conclusion

In this chapter we detailed our experimental efforts towards ultimately measuring strong evidence of sub-Poissonian intensity correlations with $\sigma = 0.47 \pm 0.04$. To our knowledge, this is a first demonstration at visible wavelengths from FWM, as well as a first demonstration at high photon flux (picowatts) as measured with a CCD camera.

From the initial experimental setup shown in fig. 4.1 which obtained $\sigma = 389 \pm 270$, a number of improvements were made to achieve sub-Poissonian intensity correlations. In sec. 4.2, we improved spectral filtering using glass filters, removing the need for bespoke beam dumps. In sec. 4.3, the improved spectral filtering was used in conjunction with the high peak-power laser to achieve $\sigma = 4.74 \pm 2.59$. In the following iteration of sec. 4.4, the camera CCD was air-cooled to reduce detector noise, and the FWM beams were independently focused on the CCD. The measured NRF was comparable to the previous iteration, however, because of the inclusion of an ND filter which reduced the overall detection efficiency. In the next section sec. 4.4, implementing these camera temperature and focusing changes, as well as a fiber out-coupling lens with suitably high NA, we measured $\sigma = 1.87 \pm 0.97$. Our first realization of sub-Poissonian correlations finally came after replacing a faulty translation stage, modifying the detection scheme to that shown in fig. 4.12, and improving spectral filtering on the Stokes FWM beam to remove Raman scattering. With these changes, we measured $\sigma = 0.55 \pm 0.28$.

After realizing sub-Poissonian intensity correlations, we further improved the experiment by stabilizing the pump intensity and pointing fluctuations. Specifically, we replaced the 1064 nm frequency-doubled laser with a 532 nm laser head, and mounted the fiber and sensitive optics in a stable optical cage system. Using these techniques, as well as improving data acquisition software and camera measurement settings, we realized $\sigma = 0.47 \pm 0.04$. We used these correlations to estimate a sample absorption at the SNL with $\Gamma_m = 1.02 \pm 0.16$. This represents an experimental confirmation of our theoretical results from sec. 2.3, wherein we show that sub-Poissonian inten-

sity correlations are necessary, but not sufficient, to observing sub-SNL parameter estimation. Improvements to the estimated absorption may come from either improved noise properties of the FWM beams, or the development of estimators which well-account for uncorrelated optical and detector noise.

In the following chapter, we discuss our experimental efforts towards pushing this technology to microwatts average power, designing and fabricating bespoke detectors for our specific application, and highlighting the technical challenges of this pursuit.

CHAPTER 5

DETECTOR DESIGN AND FABRICATION FOR MEASURING SUB-POISSONIAN INTENSITY CORRELATIONS AT MICROWATTS OF FOUR-WAVE MIXING AVERAGE POWER

Chapter outline: *In this chapter, we discuss our efforts towards developing the electronics for silicon photodiode detectors for measuring bright four-wave mixing with low electronic noise at kilohertz frequencies. First, we describe the fundamentals of silicon photodiodes, and the metrics by which we quantify detector performance. Second, we discuss the design and fabrication of two types of photodiode detectors. Along the way, we discuss various noise sources to be mitigated for realizing a low-noise detector.*

Declaration of contribution: *This chapter contains both background research and novel work. The discussed background work is related to photodiode fundamentals, as well as transimpedance amplifiers, although our inclusion of quantization noise to this model is novel. I myself also derived the saturation energy of the photodiode and the passive detector gain including parasitic photodiode effects. Useful discussions with postgraduate colleagues Giacomo Ferranti and Joel Tasker enabled the design and troubleshooting of the two-described detectors, although all simulations, designs, fabrication, and characterizations were performed by me.*

In sec. 3.1.4, we showed that our Four-Wave Mixing (FWM) source can reach average optical powers on the order of hundreds of microwatts using Single-Mode Fiber (SMF)28 as the nonlinear gain medium. We also showed that we can reliably measure sub-Poissnoian picowatt intensity correlations with this FWM source in sec. 4.11. A natural next step is to demonstrate twin-beam correlations at visible wavelengths and microwatts of average power, thereby increasing the scope of applications of our correlated source. Currently, because the CCD camera saturates at picowatts of optical power, the primary challenge of such an undertaking is the development of low-noise, high-efficiency detectors which suit our wavelengths, optical powers, and other technical specifications. Specifically, we would like to measure 450 nm and 650 nm wavelength, 1.5 nJ optical pulses at $> 80\%$ quantum efficiency on a 7 kHz pulse-by-pulse basis, rather than the millisecond integration times of the CCD camera, allowing for faster imaging and spectroscopy with at least the same detection efficiency as the CCD.

Replacing the CCD camera with Silicon Photodiode Detectors (SiPDs) also offers several other advantages. First, from a design perspective, SiPDs are smaller (~ 15 cm^2), cheaper ($\sim$ £50 each), lighter (~ 20 g), and more rugged than commercially-available CCD cameras. They also offer simplified experimental layouts for detection, as both signal beams may be focused on to independent SiPDs rather than a single 8.2×8.2 mm^2 CCD pixel array.

Second, from a scientific perspective, technically simpler SiPDs, which have been used for low-noise intensity-measurement applications since the 1980s [4, 6, 108, 109], allow greater control over design parameters such as detection bandwidth (speed), efficiency, and noise properties. To this end, we can measure individual pulse energies, or electronically average over many pulses by tuning detector bandwidth, as discussed in sec. 5.2. We can also design detectors which operate at various optical powers by adjusting the detector gain. And although we do not fabricate the silicon photodiodes themselves, the large selection of commercially-available photodiodes allows one to achieve $> 80\%$ detection efficiency over the entire visible spectrum.

In this chapter, we will discuss the theory of operation of SiPDs, our technical detector requirements, as well as the metrics by which we quantify detector performance. We will then present three different detection schemes, increasing in complexity, identifying each scheme's utility as well as key challenges.

5.1 Introductory Photodiode and Detector Characterization Theory

A PIN photodiode consists of three main layers, shown in fig. 5.1. The incident light first enters through a thin (1-3 µm thick) p-layer, which consists of a doped semi-conductor with a higher hole density than electron density, thereby making it positively charged. This is followed by an i-layer (~ 200 µm thick) of an undoped semiconductor, such that the number of holes and electrons are equal. Finally, the n-layer is similar to the p-layer except that it has a higher electron density

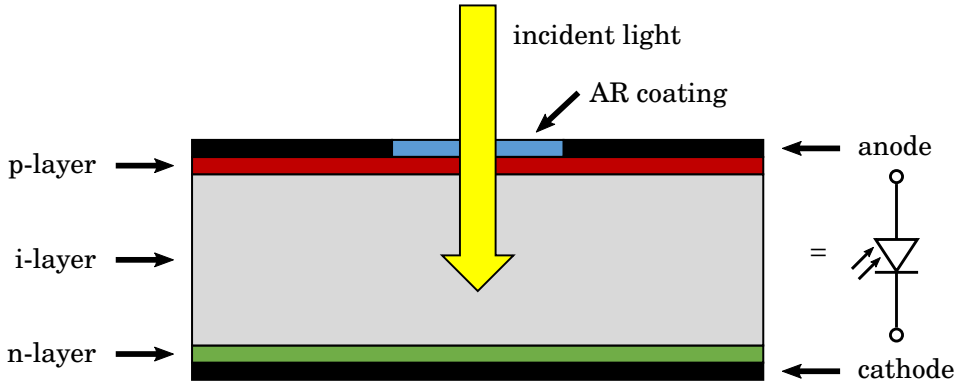

FIGURE 5.1. A simplified diagram of a PIN photodiode, with schematic representation.

than hole density, thereby making it negatively charged. In conjunction, the p- and n-layers create an intrinsic electric field across the i-layer [110].

When light is absorbed in the i-layer, the generated holes and electrons are separated by the electric field in this region, inducing a current across the diode. The charges are collected in the p- and n-layers, which act as electrodes (anode and cathode, respectively). Photodiode manufacturers can tune the quantum efficiency of devices at specific wavelengths by not only changing the p- and n-layer doping agents, but also by tuning the thickness of the three absorptive layers. Indeed, quantum efficiency at short wavelengths may be reduced when light which is absorbed in the initial p-layer does not generate current. The same holds for longer wavelengths absorbed in the n-layer [110].

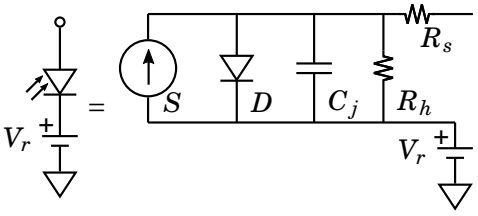

FIGURE 5.2. The equivalent circuit of a PIN photodiode. S: current source; D: diode; C_j: junction capacitance; R_h: shunt resistance; R_s: series resistance; V_r: reverse bias voltage.

Photodiodes are typically used in one of two operating modes: PhotoConductive (PC) and PhotoVoltaic (PV). In PC mode, a voltage of up to 200 V, depending on the specific photodiode and application, is applied across the photodiode electrodes. Increasing the reverse bias increases the electric field (*i.e.* depletion region) in the i-layer, and therefore the detection bandwidth of the detector. The reverse bias also affects the saturation current of the photodiode (see eqn. 5.1), as well as the measured dark current. In PV mode, no external voltage is applied across the photodiode electrodes, but there remains an intrinsic voltage drop of ~ 0.3 V across the p- and n-layers [111].

The equivalent circuit of a photodiode is shown in fig. 5.2. There is a series resistance $R_s \approx 50\,\Omega$ associated with physical contacts of the photodiode, and a shunt resistance R_h associated with the PIN junction. The shunt resistance is also the slope of the photodiode's $I-V$ curve at 0 V reverse bias, and is used to calculate electronic

noise associated with the photodiode itself [112]. Typical values of R_h are tens to thousands of megaohms, where larger values are preferred, as they correspond to reduced dark current. Note that we did not include other representative current sources in this schematic, such as for dark current, as we do not model these effects in our later simulations because photodiode dark current ($\sim 10^{-10}$ A [113]) is negligible compared to our signal current ($\sim 10^{-5}$ A). There is also a junction capacitance C_j across the p- and n-layers, which varies with the dimensions of each layer [111, 112].

We have included V_r in fig. 5.2, the optional reverse bias voltage which may be applied to the photodiode, thus switching it from PV to PC mode. Because the intrinsic voltage drop across a photodiode is small in PV mode, the photodiode is limited in its signal output. For high-gain applications then, the input optical signal must be low-power or else the photodiode will saturate.

We will now discuss the saturation limitations of photodiodes. Let us first define the maximum current I_{sat} produced by a photodiode, according to Ohm's Law:

$$V_j = I_{\text{sat}} R_{\text{tot}},$$

where $V_j = V_i + V_r$ is the voltage across the photodiode, which includes the intrinsic voltage V_i and reverse bias voltage V_r. $R_{\text{tot}} = R_s + R_L$ is the series and load resistance that the current is measured across. Depending on the SiPD design, R_L may vary from effectively 0 Ω (active amplification; see sec. 5.3) to kiloohms (passive amplification; see sec. 5.2). Rewriting I_{sat} in terms of the saturation pulse energy E_{sat} and photodiode responsivity S_λ yields

$$E_{\text{sat}} = \frac{\Delta t (V_i + V_r)}{S_\lambda (R_s + R_L)}, \tag{5.1}$$

where Δt is the electronic pulse width, and S_λ is the photodiode current output per unit optical power at wavelength λ, in units of amperes per watts. Responsivity is a useful metric for designing electronic circuits, and directly relates to a photodiode's quantum efficiency η as

$$S_\lambda = \frac{\mathrm{E}\left[I_{\text{out}}\right]}{\mathrm{E}\left[P_{\text{in}}\right]} = \eta \lambda \frac{q}{hc},$$

where $\mathrm{E}\left[I_{\text{out}}\right]$ and $\mathrm{E}\left[P_{\text{in}}\right]$ are the average output current and incident optical power, q is the electron charge, h is Planck's constant, and c is the speed of light [43]. A typical responsivity plot and calculated quantum efficiency are shown in fig. 5.3.

From eqn. 5.1, there are several practical ways to increase the saturation energy of a photodiode. Firstly, we may decrease the load resistance. While this is not typically applicable to passively amplified detectors as it reduces signal gain, actively amplified detectors have $R_L \approx 0\ \Omega$. One may also increase the reverse bias voltage or electronic pulse length. Increasing V_r is sometimes not possible, depending on the choice of photodiode, as some photodiodes are designed only to function in PV mode. Finally, increasing Δt may be done electronically by placing a capacitor in parallel with the photodiode, as will be discussed in sec. 5.2.

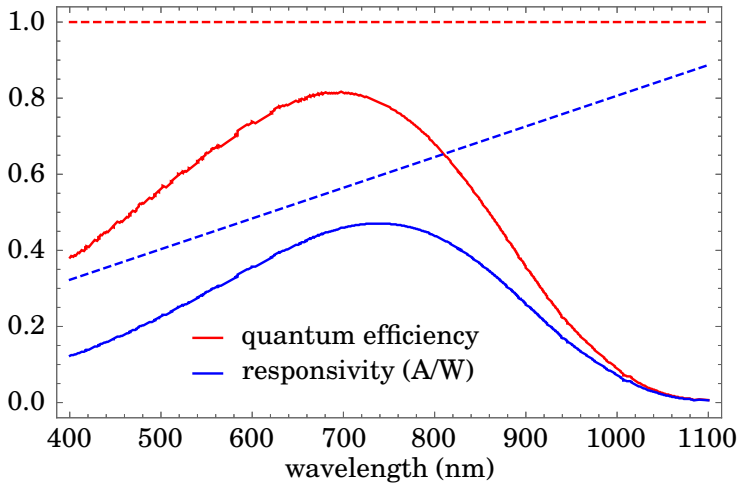

FIGURE 5.3. A typical photodiode responsivity curve (Thorlabs FDS025 [114]), and corresponding quantum efficiency. Dashed lines represent unit detection efficiency.

Now that we have a basic understanding of photodiode principles, which will inform photodiode selection later, we will discuss the metric by which we quantify the performance of an SiPD, called the shot-noise clearance.

Electronic noise clearance is a quantity that compares the measured output electric signal V_o, which corresponds to the input optical signal, to the electronic noise of the detector V_e (*e.g.* current noise from active components, thermal noise from resistors, dark current, voltage noise from supply lines, quantization noise). When the input optical signal is shot-noise limited, we call this metric shot-noise clearance (which we will henceforth refer to simply as clearance, unless otherwise specified), and is defined over the electronic frequency bandwidth $[0, f]$ as

$$\zeta(f) = 10\log_{10}\left(\frac{\mathrm{MSE}\,[V_s(f)]}{\mathrm{MSE}\,[V_e(f)]} + 1\right), \tag{5.2}$$

where $\mathrm{MSE}\,[V(f)]$ is the mean-squared error of the voltage, and $V_o = V_s + V_e$, the sum of the signal and noise voltages [109].

We calculate the MSE of a signal as the integral of that signal's Power Spectral Density (PSD), by Parseval's theorem, which relates the energy of a function and its Fourier transform [115], as the PSD may be defined as the square of the signal's Fourier transform [116]. For example, optical or electronic shot noise, being a stochastic process, would have a constant PSD in frequency. Therefore, the MSE would be a linear function of frequency.

To simplify eqn. 5.2 in terms of experimental parameters, we define the output voltage as $V_s(f) = I_{\mathrm{in}}(f) R_L G(f)$, where $G(f)$ is the frequency-dependent amplifier gain, and $I_{\mathrm{in}}(f)$ is the photocurrent generated by the photodiode. Because we assume a coherent-state optical input whose PSD is constant in frequency (white noise), we may write $\mathrm{MSE}\,[I_{\mathrm{in}}(f)] = 2qS_\lambda \mathrm{E}\,[P_{\mathrm{in}}]f$ [43, 109]. Note that this function increases with detection efficiency and input optical power, as one

would intuitively expect from the nature of shot noise. The amplifier gain and electronic noise depend on the specific SiPD design, and will be discussed in the following sections.

In practice, we do not characterize the clearance of our detectors with an ideal coherent state, as our pump beam typically exhibits super-Poissonian intensity fluctuations. If super-Poissonian intensity statistics are not accounted for, shot-noise clearance is overestimated. To fairly measure the detector clearance, the pump beam with which we characterize our detectors is shone incident on a balanced beam splitter, with each output then incident on separate identical detectors. The subtracted measured intensity of the two detectors represents the optical shot-noise fluctuations at the average pump power which was incident on the beam splitter [32, 108, 117]. The electronic noise of a detector is measured with the pump beam off and the photodiode covered with an opaque rubber cap.

5.2 Passively Amplified Silicon Photodiode Detector

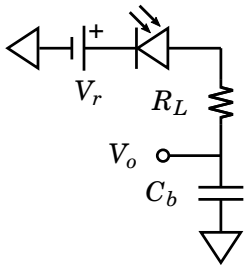

FIGURE 5.4. A circuit diagram of a passively-amplified, reverse-biased photodiode.

A passively amplified SiPD is one in which the amplification stage is itself not externally power supplied, and therefore draws current directly from the photodiode through the load resistor. A schematic of such an SiPD is shown in fig. 5.4. In this circuit diagram, a load resistor and pulse-stretching capacitor are connected in parallel, where the capacitor is used to ensure that the photodiode does not saturate, as discussed later in this section.

The voltage is amplified across R_L according to Ohm's law, and C_b is to ensure that the amplified pulse does not draw so much current from the photodiode that it saturates, according to eqn. 5.1. Indeed, R_L and C_b in parallel form a low-pass filter with 3 dB cutoff frequency

$$f_{3\text{dB}} = \frac{1}{2\pi R_L C_b}.$$

To complicate this somewhat, the photodiode itself has a frequency-dependent impedance. The gain $G(f)$ of this circuit, derived according to the photodiode equivalent circuit of fig. 5.2 and considering the effects of R_L and C_b, is a continued fraction

$$G(f) = \frac{1}{1 + R_L 2\pi i C_b f + \dfrac{R_L}{R_s} + \dfrac{1}{2\pi i C_j f + \dfrac{1}{R_h}}}.$$

In the realistic limit of $R_s \ll R_L \ll R_h$, the cutoff frequency is then

$$f_{3\text{dB}} = \frac{1}{2\pi R_L (C_b + C_j)}. \tag{5.3}$$

Therefore, to accurately model detector properties, one should consider photodiode effects such as junction capacitance if they are comparable to other relevant component values. Note also

that junction capacitance is affected by reverse biasing, the extent of which is given in most component datasheets.

When considering using C_b to pulse stretch, we are interested in the lower and upper limits of Δt from eqn. 5.1. The lower limit is set by the photodiode saturation energy, primarily a function of reverse bias, load resistance, and detection efficiency. For example, considering realistic optical values of eqn. 5.1 to our experiment, and using $R_L = 15$ kΩ, $V_r = 15$ V, and $S_\lambda = 0.3$ A/W, we calculate $\Delta t \approx 420$ ns to avoid photodiode saturation. Ignoring photodiode effects for simplicity ($C_j \ll C_b$), we calculate $C_b \approx 4.4$ pF, and the effects of this implementation are shown in fig. 5.5, simulated in the electronics simulation package LTspice [118].

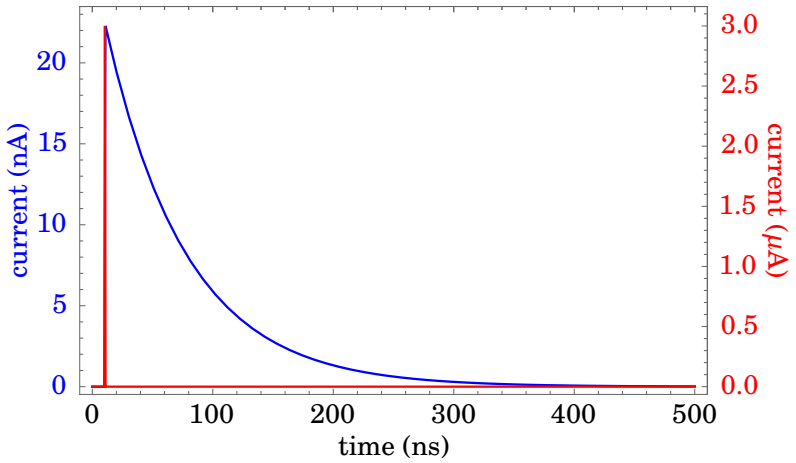

FIGURE 5.5. An example of electronic pulse stretching. The initially 1 ns triangle pulse is stretched over hundreds of nanoseconds to avoid photodiode saturation.

Although in our experiment the optical pulses are ~ 150 μs apart, the upper limit on how long a pulse may be electronically stretched is given by the electron-hole recombination time of the photodiode. If the electrons are not swept from the device before they begin to recombine with the previously-created holes, then the output energy of the photodiode will not be linearly proportional to the input optical pulse energy [110, 119]. While the recombination time varies according to the materials and dimensions of the photodiode, as well as temperature, ref. [110] estimates it to be ~ 20 μs, so we will use this upper limit for the remainder of our discussions.

Finally, we calculate the clearance of this device. The quantities which we must derive are the MSEs of the signal shot-noise and electronic noise, MSE $[V_s(f)]$ and MSE $[V_e(f)]$. As discussed in the previous section, $V_s(f) = I_{\text{in}}(f) R_L G(f)$, which gives

$$\text{MSE}\,[V_s(f)] = \int_0^f |G(f')|^2 df' (2qS_\lambda \text{E}\,[P_{\text{in}}]) R_L^2.$$

The electronic noise is primarily given by the thermal noise of the load resistor as

$$\text{MSE}\,[V_e(f)] = \int_0^f |G(f')|^2 df' (4k_B T R_L),$$

where k_B is the Boltzmann constant, T is the temperature, and $4k_BTR_L$ is the PSD associated with the white, thermal resistor noise [109]. Using these two equations in eqn. 5.2, yields

$$\zeta(f) = 10\log_{10}\left(\frac{q}{2k_BT}S_\lambda \mathrm{E}\left[P_{\mathrm{in}}\right]R_L + 1\right), \tag{5.4}$$

which is independent of electronic frequency f, as the signal and noise gain are equivalent for all frequencies. Therefore, we can always increase the shot-noise clearance by increasing the load resistor, up to the point at which the detector saturates.

Let us now consider an example using values from our experiment to calculate our maximum-attainable clearance. With 10 µW average FWM power and 7 kHz repetition rate, this corresponds to a pulse energy of 1.4 nJ. Electronically broadening the 1 ns pulse to the maximum $\Delta t^{\max} = 20$ µs, and using typical values $S_{650\mathrm{nm}} = 0.45$ A/W, $V_i = 0.3$ V, $V_r^{\max} = 40$ V, and $R_s = 50\,\Omega$, we calculate $R_L^{\max} = 1.25$ MΩ. From eqn. 5.3 with junction capacitance $C_j = 8$ pF, however, the maximum load resistance is reduced to $R_L^{\max} = 0.4$ MΩ, letting $C_b = 0$ F and $f_{3\mathrm{dB}} = 1/20$ µs. Using $R_L^{\max} = 0.4$ MΩ in eqn. 5.4, with corresponding responsivities $S_{650\mathrm{nm}} = 0.45$ A/W and $S_{450\mathrm{nm}} = 0.3$ A/W, we calculate a maximum clearance of 16.8 dB, sufficient for measuring sub-Poissonian intensity correlations.

A final practical consideration for detector design is the technical specifications of the oscilloscope used to measure the current from the SiPD. Digital oscilloscopes introduce quantization noise as the analog signal is processed by the Analog-to-Digital Converter (ADC), as well as $1/f$ (pink) noise from the various electronics. In the following section, we will compare two oscilloscopes in terms of their noise properties to determine appropriate measurement settings for optimal electronic noise clearance.

5.2.1 Characterizing Oscilloscope Quantization and Pink Noise

Initially, we characterized our SiPDs using a Tektronix TDS2014B oscilloscope [120]. During these efforts, we found the electronic noise of the oscilloscope to be detrimental to the measured detector clearance. To mitigate this, we employed a lower-noise, higher-resolution oscilloscope, a Keysight InfiniiVision MSOX3104A [121]. Relevant technical specifications of the two oscilloscopes are compared in tab. 5.1.

TABLE 5.1. A comparison of the maximum specifications of two oscilloscopes.

	Tektronix TDS2014B	Keysight InfiniiVision MSOX3104A
bandwidth	100 MHz	1 GHz
channels	4	4
sample rate	1 GS/s	5 GS/s
ADC	8 bits	8 bits (12 bits in *hires* mode)
vertical sensitivity	2 mV/div to 5 V/div	1 mV/div to 5 V/div
horizontal sensitivity	5 ns/div to 50 s/div	0.5 ns/div to 50 s/div

Because we are measuring slow transient signals, the maximum bandwidth of both oscilloscopes is sufficient for our purposes, ~ 100 kHz, or twice $f_{3\text{dB}}$. Depending on the detector design and measurement scheme, between 1 and 3 channels are required (see sec. 5.2 and sec. 5.4), and again both oscilloscopes are sufficient.

The sample rate depends on the horizontal setting, in that smaller time/div settings may have higher sampling rates. Higher sampling rates improve vertical resolution, and therefore our estimates of optical pulse energy, so the Keysight InfiniiVision MSOX3104A is preferred in this regard. Also, the Keysight oscilloscope may be operated in *hires* mode, wherein the input signal is oversampled and neighboring points are averaged together. This increases the vertical resolution to effectively 12 bits (when operating at ≥ 20 µs/div), at the cost of reduced sampling rate.

The number of ADC bits relates to the quantization noise of the signal, wherein more bits of resolution are preferred. A simple example of quantization error is shown in fig. 5.6. In this example, an analog sine waveform is quantized by a 2-bit ADC, with the resulting quantization error shown. With more ADC bits, the digital signal approaches the analog signal.

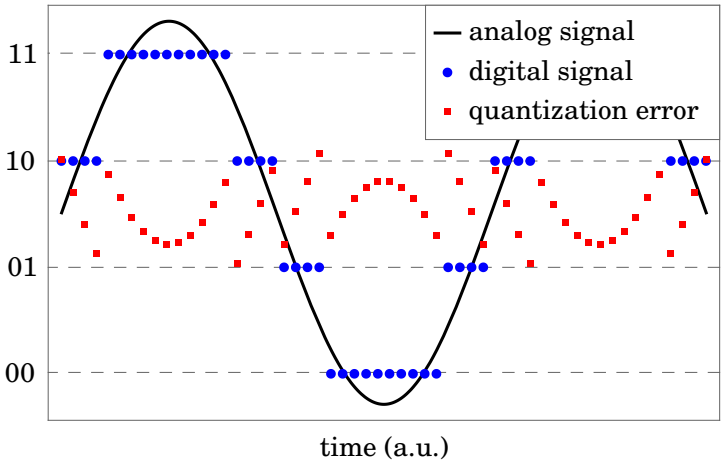

FIGURE 5.6. An example of quantization error from analog-to-digital conversion. A sine wave is quantized by a 2-bit ADC, with quantization error shown. Due to poor digital resolution, the reconstructed analog signal may be over- or under-estimated. For our application, this leads to systematic errors in estimating photon numbers of each optical pulse.

For stochastic signals, the PSD of quantization noise source is white, given by $\Lambda^2/(12\times 2^{2n})$, where Λ is the dynamic range of the vertical oscilloscope setting (10×V/div setting, for our oscilloscope), and n is the number of ADC bits [122]. Because quantization noise is white, and independent of our signal, it is additive in calculating the electronic noise of the detector. We may, for example, rewrite eqn. 5.4, including now quantization noise from the oscilloscope, as

$$\zeta(f) = 10\log_{10}\left(\frac{\int_0^f |G(f')|^2 df'(2qS_\lambda \mathrm{E}\left[P_{\text{in}}\right])R_L^2}{\int_0^f \left[|G(f')|^2(4k_BTR_L)+\Lambda^2/(12\times 2^{2n})\right]df'}+1\right),$$

where

$$\int_0^f |G(f')|^2 df' = \frac{\arctan\left[R_L 2\pi(C_b + C_j)f)\right]}{R_L 2\pi(C_b + C_j)}$$

in the limit $R_s \ll R_L \ll R_h$. Note that the passive-detector clearance is now frequency-dependent, decreasing at higher frequencies as the oscilloscope noise becomes dominant past the detector bandwidth. Using the same values as in the example clearance calculation of the previous section, and realistic values $\Lambda = 10$ mV and $n = 12$ bits, the clearance is reduced from 16.8 dB to 1.3 dB at 100 kHz. Because any additional electronic noise associated with the oscilloscope would reduce the clearance further, we wish to find the lowest-noise settings suitable for our application.

We first compare the electronic noise of the two oscilloscopes. We measured this noise on a single channel, with no detector input, using the same oscilloscope settings, the results of which are shown in fig. 5.7.

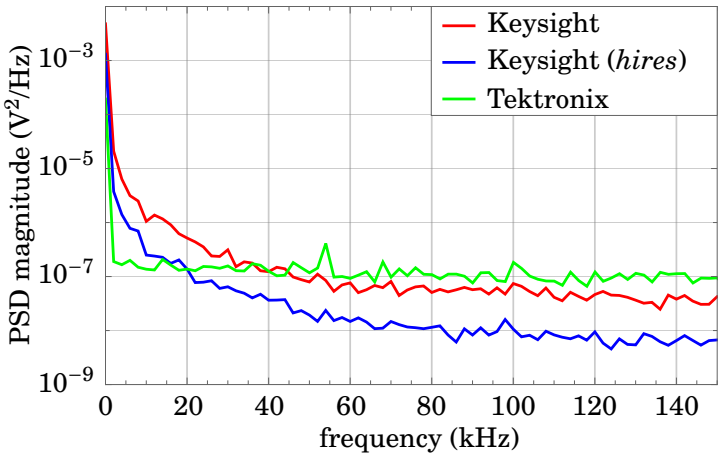

FIGURE 5.7. A comparison of the electronic noise of a Tektronix TDS2014B, Keysight InfiniiVision MSOX3104A, and Keysight InfiniiVision MSOX3104A operating in *hires* mode. In all measurements, the settings are 2 mV/div and 50 µs/div, with internal 20 MHz and 20 Hz low- and high-pass filters applied. These data represent an average of 20 oscilloscope traces.

All spectra exhibit $1/f$ noise, typical in electronic devices [123]. Comparing the Keysight and Tektronix oscilloscopes, at the same ADC 8 bit resolution, the Keysight oscilloscope exhibits less electronic noise. When enabling *hires* mode, the electronic noise is further decreased due to the reduction in quantization noise. We will therefore use the Keysight InfiniiVision MSOX3104A for the remainder of our experiments.

To further optimize the Keysight oscilloscope settings, we measured the electronic noise at increasing vertical and horizontal resolutions. The results are shown in fig. 5.8, with the corresponding settings listed in tab. 5.2. In fig. 5.8 (b), varying vertical resolution from 1 mV/div to 20 mV/div, the noise increases with decreasing resolution, due to quantization error. More significant is the decrease in electronic noise with decreasing horizontal resolution, as shown in

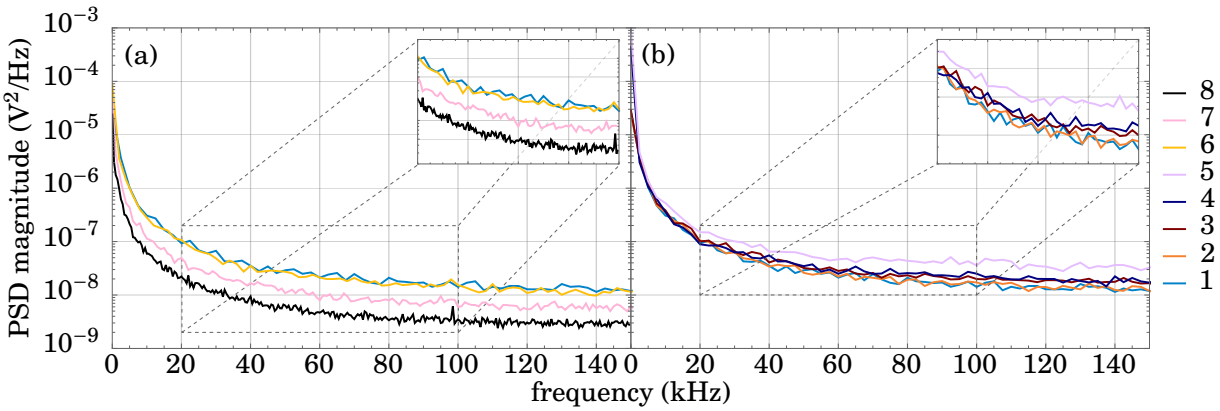

FIGURE 5.8. Electronic noise PSDs of a Keysight InfiniiVision MSOX3104A oscilloscope at different (a) horizontal and (b) vertical resolution settings (see tab. 5.2). (a) Vertical resolution is held constant at 1 mV/div, while varying horizontal resolution from 40 µs/div to 200 µs/div. (b) Horizontal resolution is held constant at 40 µs/div, while varying vertical resolution from 1 mV/div to 20 mV/div. These data each represent an average of 100 oscilloscope traces.

TABLE 5.2. Keysight InfiniiVision MSOX3104A settings used to characterize electronic noise, as shown in fig. 5.8.

setting	vertical resolution (mV/div)	horizontal resolution (µs/div)
1	1	40
2	2	40
3	5	40
4	10	40
5	20	40
6	1	50
7	1	100
8	1	200

fig. 5.8 (a). Decreasing the horizontal resolution increases the low-frequency measurement precision at the cost of decreased measurement bandwidth. Indeed, there is an order-of-magnitude difference in electronic noise at 100 kHz from 50 µs/div to 200 µs/div. The maximum time/div setting is one such that the sampling frequency satisfies the Nyquist-Shannon sampling theorem, is at least twice $f_{3\mathrm{dB}}$ to reconstruct the signal without aliasing [124]. With kilohertz $f_{3\mathrm{dB}}$, this corresponds to hundreds of milliseconds per division, according to the sample rate of the Keysight InfiniiVision MSOX3104A operating in *hires* mode. We have therefore measured the noise properties of our oscilloscope, and found the parameters which most reduce the quantization and $1/f$ electronic noise. Specifically, we would like to operate the Keysight oscilloscope in *hires* mode at the highest-possible vertical resolution (several millivolts per division) and lowest-

possible horizontal resolution (hundreds of milliseconds per division) to achieve a minimum electronic noise over 0 Hz to 100 kHz bandwidth.

5.2.2 Design and Fabrication

So far we have discussed general features of photodiodes (see sec. 5.1) and passive amplification detectors. Putting theory into practice, in this section we discuss simulations, designs, and fabrication of a passive SiPD.

The initially proposed detection scheme using SiPDs is shown in fig. 5.9, wherein each FWM beam is measured on independent detectors, and their signals subtracted in post-processing. We may also use a third SiPD to simultaneously monitor classical intensity fluctuations on the residual pump beam, if desired. This experiment, as compared to using the CCD camera for detection, has the advantage of simplified optical alignment, discussed at the beginning of this chapter.

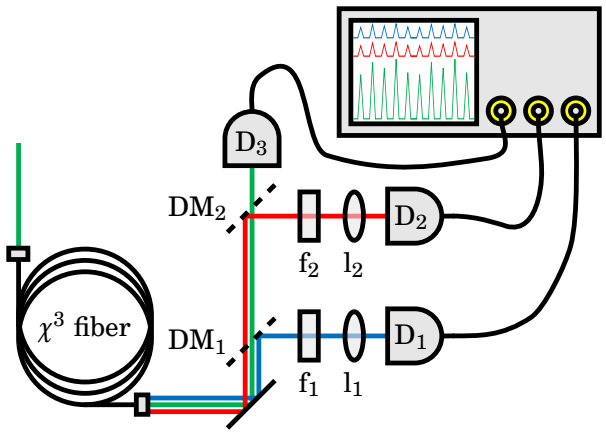

FIGURE 5.9. SiPD detection scheme, measuring all beams independently for post-processing subtraction. $f_{\{1,2\}}$: spectral filters; $l_{\{1,2\}}$: focusing lenses; $DM_{\{1,2\}}$: dichroic mirrors; $D_{\{1,2,3\}}$: SiPDs.

The first detector which we designed is shown in fig. 5.10. We implemented a switch in the detector so that each may be used to measure either FWM intensities, or the relatively-bright pump beam by switching between the two R_L-C_b combinations. The photodiode is reverse biased with 9 V batteries connected in series, whose combined voltage V_p is down-regulated via an adjustable voltage regulator. Decoupling capacitors $C_{d1} = 0.33\,\mu F$ and $C_{d2} = 0.1\,\mu F$ are also implemented according to the voltage regulator's datasheet specifications (Texas Instruments LM317 HVT [125]). We added $R_c = 12\,k\Omega$ to satisfy the minimum current load requirements of the voltage regulator. Without R_c, the regulator imposes kilohertz current noise through the detector,

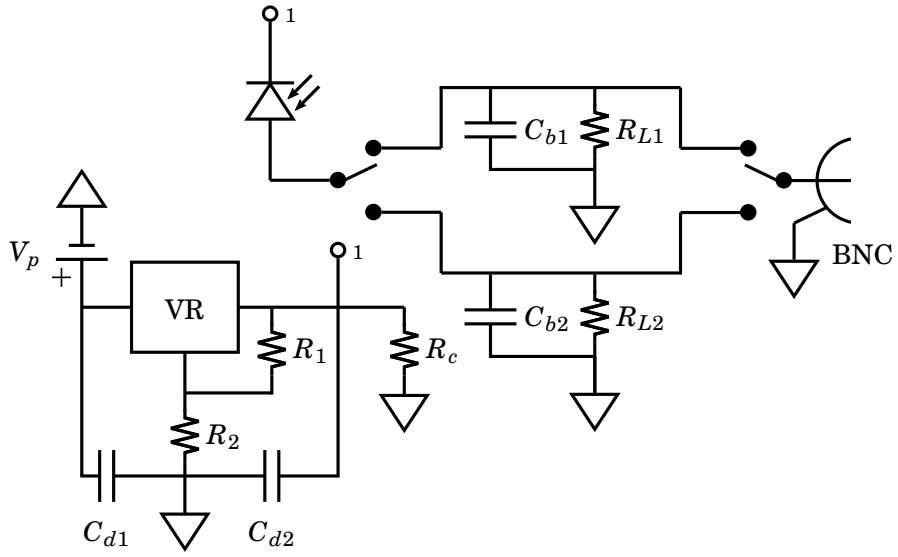

FIGURE 5.10. A schematic for a passive SiPD, switchable between two detection modes. VR: voltage regulator; BNC: coaxial cable connector; $C_{d\{1,2\}}$: decoupling capacitors.

as discussed in detail in sec. 5.4.2. An example simulation of such a detectors output, simulated with LTspice, is shown in fig. 5.5.

Now that we have simulated and produced a schematic for a passive SiPD, we used EAGLE [126] to design the PCB of this detector for fabrication, shown in fig. 5.11. Some specific design considerations were (1) that we wanted to be able to mount the detector on standard optical post mounts and (2) we wanted unencumbered access to any components which may need to be reworked (*e.g.* changing R_L and/or C_b). We implemented (1) via an aluminum M4 screw terminal near the edge of the PCB. Because the PCB is small (40×49 mm^2), the soldered-in screw terminal is sufficient to stabilize the PCB for intensity measurements. For consideration (2), the PCB was intuitively laid out with all amplification components near the labeled switches, with several millimeters between each component for straightforward reworking.

This being our first-fabricated SiPD, there were several practical drawbacks to the design. First, the PCB supply-voltage leads (fig. 5.11 (d), bottom right) had to be soldered to the PCB, making supply-voltage adjustments cumbersome. In subsequent detector iterations (see sec. 5.4), the supply lines are interfaced with the PCB via a screw terminal. The through-hole voltage regulator is also replaced with surface-mount regulators in future detector iterations, reducing the detector footprint and allowing for more compact designs. Finally, for large R_L, comparable to the typically 1 MΩ input impedance of the oscilloscope, the photodiode reverse bias is reduced according to the voltage-divider created by having R_L in parallel with the oscilloscope input resistance.

The specific components which we used are as follows. The photodiode is a First Sensor PC5-

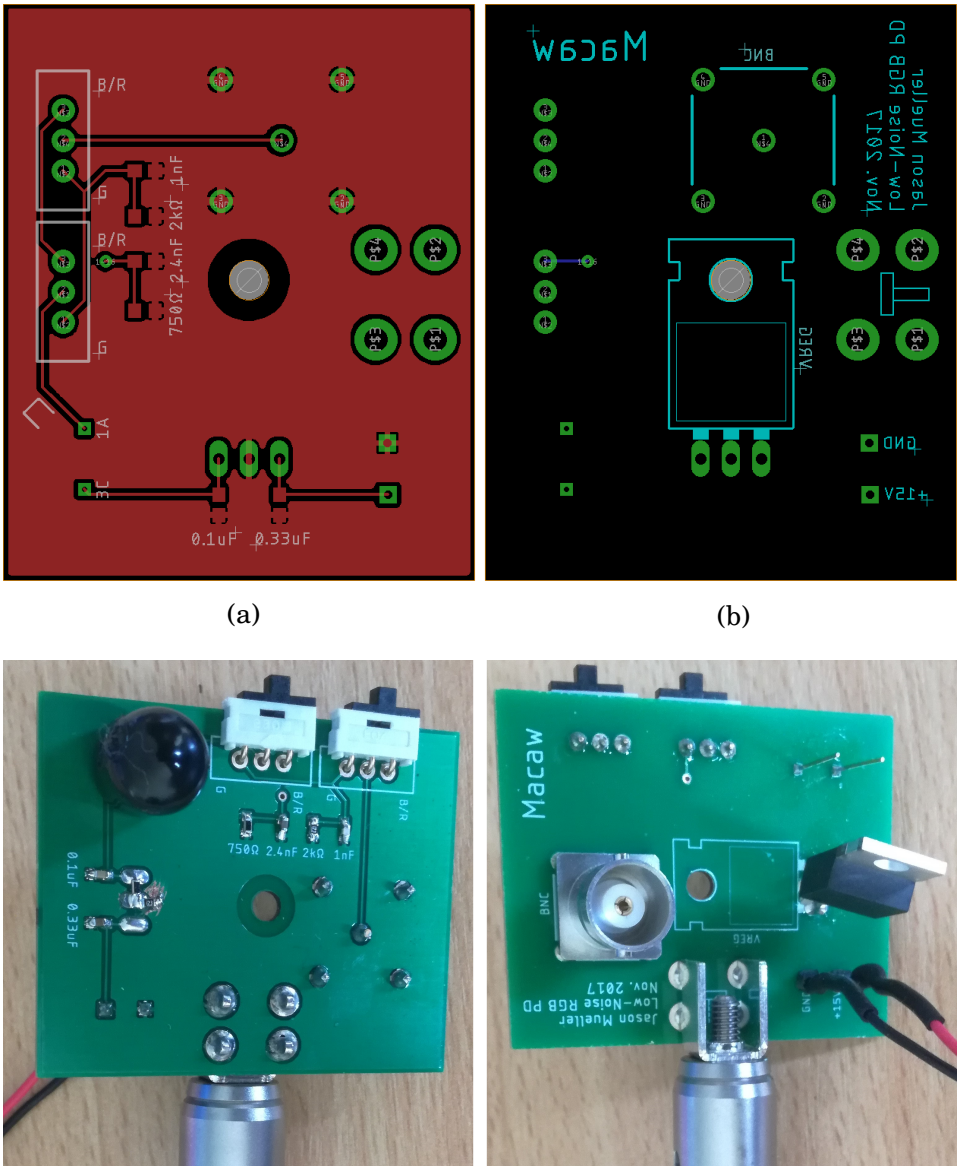

(a) (b)

(c) (d)

FIGURE 5.11. The PCB design and fabrication of a passive SiPD, dubbed *Macaw* after the vibrantly-colored red, green, and blue Scarlet Macaw. (a) represents the top PCB layer, and (b) the bottom (mirrored). (c) and (d) are fabricated PCBs with soldered components, mounted to a standard optical post mount. The dimensions of this PCB are 40×49 mm^2.

6b TO5 [113], designed to be operated in PV or PC mode, with $V_r^{\max} = 50$ V. It is quoted as 85% efficient at 450 nm and 650 nm wavelength. We apply a reverse-bias voltage of $V_1 = 39.5$ V, according to

$$V_1 = 1.25\ \text{V}\left(1 + \frac{R_2}{R_1}\right),$$

where $R_1 = 392\,\Omega$ and $R_2 = 12$ kΩ [125]. The photodiode has a junction capacitance $C_j \approx 8$ pF at this reverse bias. Therefore, to obtain a low-pass cutoff frequency of 50 kHz, we let $R_L = 402$ kΩ and $C_b = 0$ F, according to eqn. 5.3. The results of our detector characterizations using these specifications are discussed in the following section.

5.2.3 Detector Noise and Results

Before measuring the detector clearance, we must first establish the electronic noise of the detector itself. To do this, the detector is connected to an oscilloscope via a 1 m low-noise coaxial cable with the photodiode itself blocked using an opaque rubber cap. The oscilloscope noise is measured as in sec. 5.2.1, and compared to the electronic noise with the photodiode batteries connected. The results are shown in fig. 5.12.

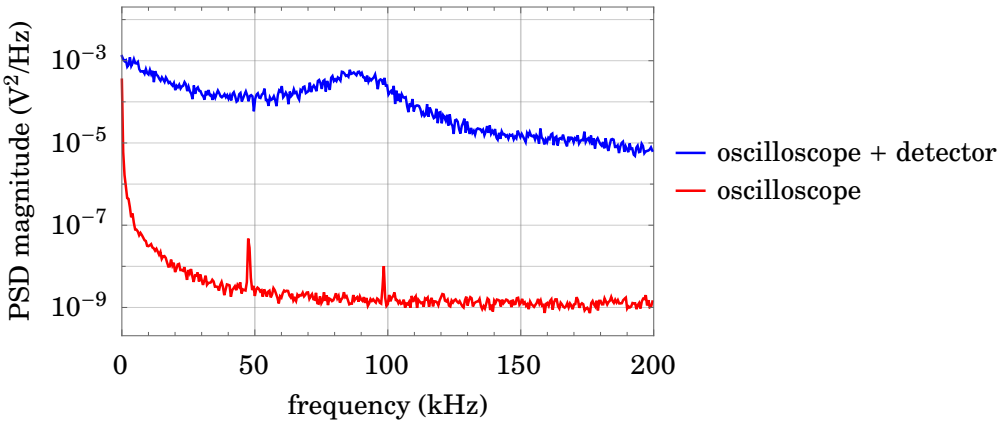

FIGURE 5.12. Electronic noise of the fabricated passive, switched SiPD. These data each represent an average of 25 oscilloscope traces. The 50 kHz and 100 kHz peaks are artifacts of the oscilloscope time/div settings, and not true features of the oscilloscope noise.

The oscilloscope noise is 50 dB less than the detector noise. To be certain that no detector components were faulty or damaged, we measured the noise spectrum across three identical builds of the same detector, with the same results each time. The noise of the detector is primarily due to current noise from the voltage regulator being amplified by the gain resistor, as discussed in sec. 5.4.2.

As the detector noise is tens of decibels greater than the oscilloscope noise over our 100 kHz measurement bandwidth, and because we expect only a few decibels clearance considering only

oscilloscope quantization noise, the detector would not obtain significant shot-noise clearance for our measurement purposes. These detectors were useful, however, in measuring the responsivity of the photodiode for datasheet verification, as well as measuring the repetition rate of the FWM pump laser.

To measure the responsivity of the photodiode, the voltage output is compared to the optical input power, as measured with a NIST-traceable optical power meter. Knowing R_L, we may convert the voltage signal to current, using Ohm's law, and therefore measure the photodiode responsivity.

To perform this measurement, we used a Continuous-Wave (CW) 404 nm wavelength M-Squared Lasers SolTis 500 PSX-F, attenuated with a Half-Wave Plate (HWP) and Polarizing Beam Splitter (PBS). We used a CW laser of similar wavelength to the expected anti-Stokes FWM wavelength (see sec. 3.1.1), rather than our own FWM source, to mitigate potential issues with laser pulsing such as photodiode saturation (which could negatively bias our responsivity estimation) as we had not yet fully characterized the detector response to short optical pulses. Using the second laser also allowed us to work simultaneously on detector characterizations and measuring intensity correlations with the CCD camera. The results of the responsivity measurement are shown in fig. 5.13.

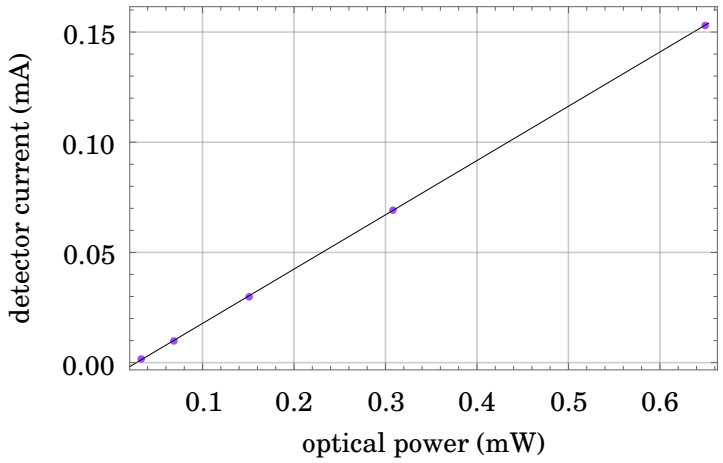

FIGURE 5.13. Measured photodiode responsivity at 404 nm wavelength, using R_L = 2 kΩ. Vertical error bars are smaller than the data markers. The fit line is $y = 0.245x - 0.007$.

The responsivity (slope of linear fit in fig. 5.13), was measured to be $S_{404\text{nm}} = 0.245 \pm 0.001$ A/W, which corresponds to a quantum efficiency of 0.752 ± 0.003, in close agreement with the datasheet value ~ 0.24 A/W [113]. Note that the y-intercept of the linear fit to the data of fig. 5.13, which determines the photodiode dark current, is negative, likely due to ambient light at wavelengths of less photodiode responsivity positively biasing the measured optical power. This bias, however, is consistent across all data points and therefore does not affect the fit slope, which determines

the photodiode responsivity.

We also performed preliminary pulsed-laser tests using these passive SiPDs with the 532 nm wavelength FWM pump beam. In particular, we measured a time series of the pump beam to show that pulses may be individually measured, as well as calculated the repetition rate of the laser from this data, shown in fig. 5.14.

The average pump power of fig. 5.14 (a), as measured with a calibrated optical power meter, was 7.7 µW. Pulse-to-pulse energy fluctuations are visible, corresponding to optical shot noise as well as super-Poissonian power fluctuations. The time-series data reveals a challenge associated with the detection method of fig. 5.9, wherein each FWM beam is measured independently and subtracted post-processing. As the electronic pulses increase in energy, lower oscilloscope vertical resolution settings are required to measure the total pulse energy. Reducing the vertical resolution increases the quantization noise of the data, reducing the detector clearance. This challenge is addressed in sec. 5.4.

Fourier transforming this data, as in fig. 5.14 (b), reveals that the repetition rate of the Teem Photonics SNG-03E-100 is 7.2 kHz, faster than the datasheet-quoted 5 kHz [61]. Higher-order harmonics, spaced at 7.2 kHz, are associated with the pulse shape.

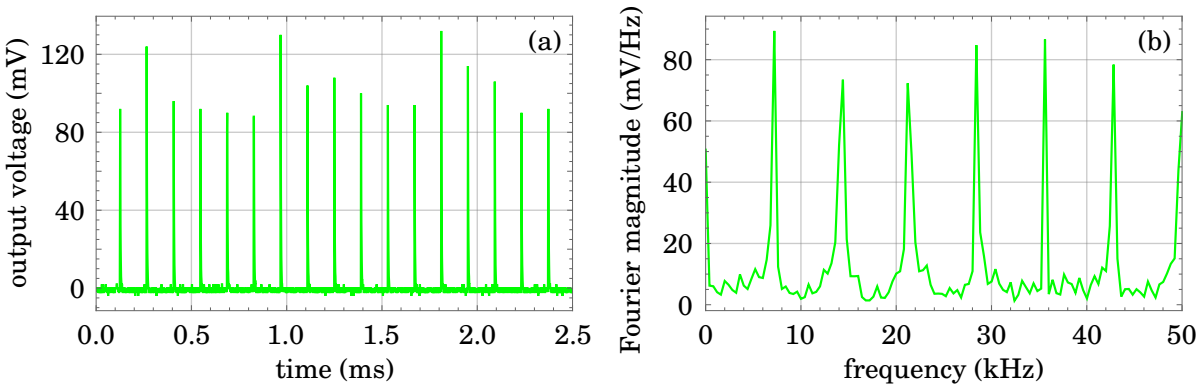

FIGURE 5.14. (a) Time and (b) Fourier series of the 532 nm pump laser, as measured with the passive SiPDs.

5.3 Actively Amplified Silicon Photodiode Detector

A second category of detectors which we will now discuss are actively amplified SiPDs, a simplified schematic of which is shown in fig. 5.15. This schematic is similar to the passively-amplified detector shown in fig. 5.4, but the load resistor R_L is replaced with a transimpedance amplifier circuit, which includes an Operational Amplifier (OA), and a feedback resistor and capacitor R_f and C_f. The purpose of such an amplification stage is that the OA actively maintains a 0 V differential at its two inputs via its own external power supply, ideally reducing the load resistance

on the photodiode to 0 Ω [109]. According to eqn. 5.1, the photodiode saturation energy increases inversely proportionally to the photodiode load resistance, allowing greater amplification before photodiode saturation. The details of such transimpedance detectors are thoroughly discussed in ref. [109], and here we will mention the relevant details to our experiment.

As before, the detector parameters of interest are the cutoff frequency $f_{3\text{dB}}$, gain spectrum $G(f)$, and electronic noise MSE $[V_e(f)]$. The cutoff frequency is given by the OA's Gain-Bandwidth Product (GBP) and capacitance C_{OA}, as well as other detector parameters as

$$f_{3\text{dB}} = \sqrt{\frac{\text{GBP}}{2\pi R_f \left(2C_j + C_b + C_f + C_{\text{OA}}\right)}}. \tag{5.5}$$

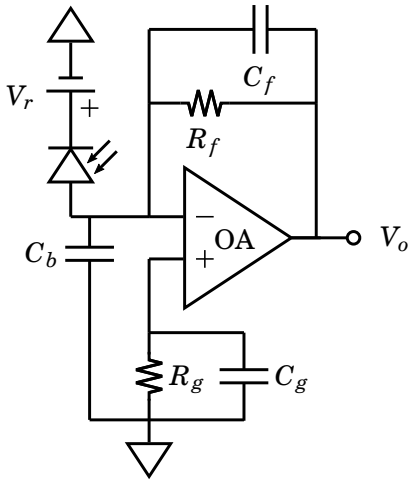

FIGURE 5.15. A circuit diagram of an actively-amplified, reverse-biased photodiode.

GBP is in units of frequency, and is the amplifier gain times the bandwidth at which that gain is measured. For example, if an OA is quoted to have GBP = 1 MHz, then the gain is 1 at 1 MHz. If the amplifier is then wired to have gain 10, it will only have at least this gain up to 100 kHz. Inspection of eqn. 5.5 indicates that an OA with a large GBP is desirable for our application, as larger R_f may then be used for a given cutoff frequency, increasing the detector clearance, discussed in more detail shortly.

The capacitor C_b is a practical consideration used to tune the bandwidth of the detector without having to reduce C_f so much that parasitic PCB trace capacitance (1-3 pF/in [127]) becomes comparable to C_f. Note that C_b is not considered in ref. [109] and similar work, as typically such transimpedance detectors are used with CW or megahertz repetition-rate lasers, where the highest-possible detector bandwidth is desired. Because our application requires lower detection bandwidths due to the duty cycle and energy of our laser pulses, we will consider its effects.

The gain spectrum of this active SiPD is

$$G(f) = \left[1 + i\sqrt{2}\frac{f}{f_{3\text{dB}}} - \left(\frac{f}{f_{3\text{dB}}}\right)^2\right]^{-1},$$

where

$$C_f \overset{!}{\approx} \sqrt{\frac{2C_j + C_b + C_{\text{OA}}}{\pi R_f \,\text{GBP}}} \tag{5.6}$$

to achieve a second-order Butterworth filter. A Butterworth filter is desirable due to its flat frequency response within its bandwidth, as a nonuniform frequency response may cause oscillations within the feedback circuit of the OA if C_f is too small [128]. As an example, in fig. 5.16 we simulate the difference between using too large and too small feedback capacitance values

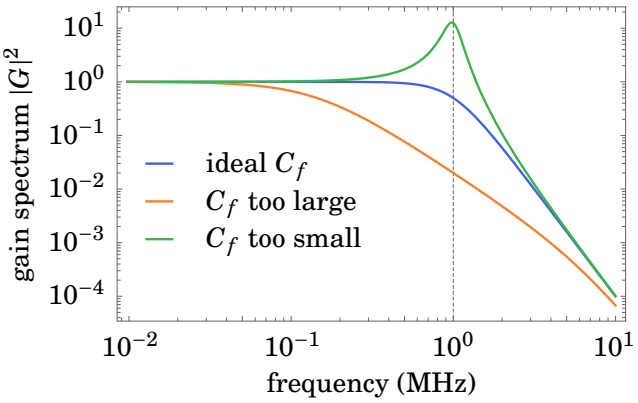

FIGURE 5.16. A comparison of active SiPD gain spectra with varying feedback capacitance C_f, for $f_{3\text{dB}} = 1$ MHz.

and indeed see increased gain at the $f_{3\text{dB}}$ cutoff frequency for small C_f. Increasing C_f greater than the value given by eqn. 5.6 also results in a sub-optimal gain spectrum, decaying before the cutoff frequency.

Now, we examine the noise properties of the detector. The active SiPD is affected by thermal noise sources associated with resistors, oscilloscope quantization noise, as well as current and voltage noise of the OA inputs, MSE $[I_{\text{OA}}(f)]$ and MSE $[V_{\text{OA}}(f)]$, not previously covered in the passive SiPD discussions (see sec. 5.2). From ref. [109], including quantization noise which they do not consider, the active SiPD electronic noise is

$$\text{MSE}\,[V_e(f)] = \int_0^f \left(A(f') + B(f')f^2\right) df',$$

where

$$A(f') = |G(f')|^2(4k_BTR_f + \text{PSD}\,[V_{\text{OA}}(f')] + \text{PSD}\,[I_{\text{OA}}(f')]\,R_f^2) + \Lambda^2/(12\times 2^{2n}),$$

$$B(f') = |G(f')|^2\left(\frac{\text{GBP}}{f_{3\text{dB}}^2}\right)^2 \text{PSD}\,[V_{\text{OA}}(f')],$$

$$\int_0^f |G(f')|^2 df' = -\frac{(-1)^{3/4}}{2} f_{3\text{dB}}\left[\arctan\left(\frac{(-1)^{1/4}f}{f_{3\text{dB}}}\right) + \text{arctanh}\left(\frac{(-1)^{1/4}f}{f_{3\text{dB}}}\right)\right].$$

From the previous equations, we see that MSE $[I_{\text{OA}}(f)]$ is the dominant OA noise source in the high-gain regime at low frequencies, which informs our OA selection, discussed later. We may now write the active SiPD clearance as

$$\zeta(f) = 10\log_{10}\left(\frac{\int_0^f |G(f')|^2 df'(2qS_\lambda \text{E}\,[P_{\text{in}}])R_f^2}{\int_0^f \left(A(f') + B(f')f^2\right) df'} + 1\right).$$

Using the previous set of equations, and imposing a desired cutoff frequency and minimum component capacitance, one may optimize for the largest possible feedback resistance, thereby

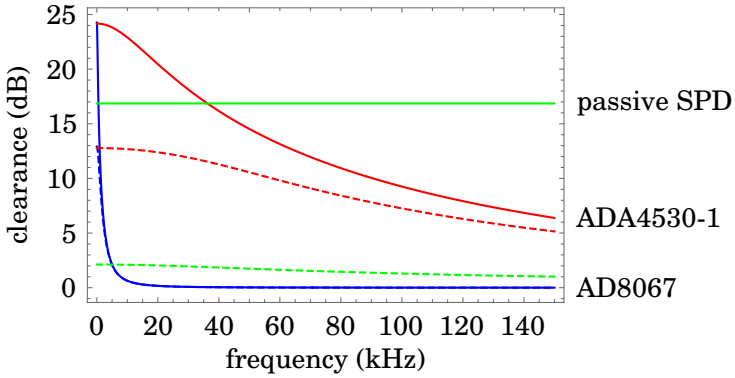

FIGURE 5.17. A comparison of two active SiPD and one passive SiPD clearance spectra. All detectors have a 50 kHz cutoff frequency, and maximal clearance given the technical specifications of their respective OAs. Solid lines are without ADC quantization noise, and corresponding dashed lines with. We have used $R_L = 402\ \text{k}\Omega$, $R_f^{\text{AD8067}} = 2.25\ \text{M}\Omega$, and $R_f^{\text{ADA4530-1}} = 2.21\ \text{M}\Omega$.

TABLE 5.3. A comparison of two OA technical specifications.

	AD8067	ADA4530-1
GBP	300 MHz	2 MHz
PSD $[I_{\text{OA}}(f)]$	0.36 fA^2/Hz	0.0049 fA^2/Hz
PSD $[V_{\text{OA}}(f)]$	43.56 nV^2/Hz	196 nV^2/Hz
C_{OA}	2.5 pF	4 pF

maximizing detector clearance over the measurement bandwidth. Using realistic datasheet values from two low-noise OAs (Analog Devices AD8067 [129] and Analog Devices ADA4530-1 [130], with relevant technical specifications shown in tab. 5.3), and comparing to a passive SiPD of the same 50 kHz cutoff frequency and 10 µW average anti-Stokes FWM power, we find that the active SiPD design can outperform the passive SiPD, as shown in fig. 5.17.

Without considering quantization noise of the oscilloscope, the passive SiPD performs better than the active ones. However, because of the reduced current load on the photodiode, we may implement $R_f \gg R_L$, increasing the amplification of the photocurrent. The clearance is then less reduced by quantization noise, achieving $\zeta(100\,\text{kHz}) = 7.3$ dB for the ADA4530-1. The AD8067 and ADA4530-1 are interesting to compare due to the trade-off between GBP and MSE $[I_{\text{OA}}(f)]$. From our simulations, the reduced OA current noise is more beneficial than the greater GBP when measuring at kilohertz frequencies. Note that these simulations do not include oscilloscope $1/f$ noise or dark current from the voltage regulator, as discussed in sec. 5.2.3.

Although we did design and test an active transimpedance detector, it suffered from similar drawbacks to the passive SiPD. Namely, because of the even greater electronic gain ($R_f/R_L \approx 10^3$), the oscilloscope vertical resolution must be decreased to several volts per division to capture the

full pulse energy, greatly increasing the ADC quantization noise. Instead, we will discuss a final detection scheme, similar to conventional homodyne detection, to reduce measured pulse energy while maintaining sufficient clearance.

5.4 Actively Amplified Subtracted-Signal Silicon Photodiode Detector

The primary drawback of the proposed detection scheme of fig. 5.9 is that because each signal beam is measured independently, intense electrical voltage signals are passed to the oscilloscope. To measure the full energy of each pulse, low oscilloscope vertical resolution settings are required, increasing the ADC quantization noise, reducing the clearance. To mitigate this, we implement a subtracted-signal detector scheme, wherein the photocurrents from the two FWM signal photodiodes are subtracted prior to active amplification, as shown in fig. 5.18. Because of the imbalanced photodiode responsivity at our two signal wavelengths ($S_{650\text{nm}}$ = 0.45 A/W and $S_{450\text{nm}}$ = 0.3 A/W), the less-intense subtracted optical pulses may be measured in the time domain at higher vertical resolution.

For example, consider a twin-beam signal at 10 µW average anti-Stokes power, each beam at our wavelengths of interest. Assuming 1 ns pulses at 5 kHz repetition rate, $R_f = 1\,\Omega$, and an infinite-bandwidth detector, the peak measured voltage for the Stokes and anti-Stokes beams are, respectively, 623 mV and 600 mV. Subtracting the photocurrents prior to amplification yields a reduced peak voltage of 23 mV, relaxing oscilloscope vertical resolution requirements.

Before further discussing the design and implementation of such a subtracted-signal SiPD, we must first show that we have access to all of the parameters required to measure the Noise-Reduction Factor (NRF)

$$\sigma = \frac{\mathrm{Var}\left[n_1 - n_2\right]}{\mathrm{E}\left[n_1 + n_2\right]}, \tag{2.17}$$

discussed in sec. 2.2. In particular, how can we measure the added signal from the subtracted photocurrent to compare our intensity fluctuations to the relative shot noise?

First, to calculate the numerator of the NRF equation, consider the output voltage of the unbalanced subtraction, according to Ohm's law

$$\begin{aligned} V_o &= R_f(I_1 - I_2) \\ &= \frac{qR_f}{\Delta t}(n_1 - n_2) \\ \mathrm{Var}\left[V_o\right] &= \left(\frac{qR_f}{\Delta t}\right)^2 \mathrm{Var}\left[n_1 - n_2\right], \end{aligned}$$

where V_o is the measured output voltage, $I_{\{1,2\}}$ is the photocurrent from each photodiode, and Δt is the electronic pulse width. The variance of the voltage output, as measured on the oscilloscope, therefore corresponds to the variance of the twin-beam intensity difference.

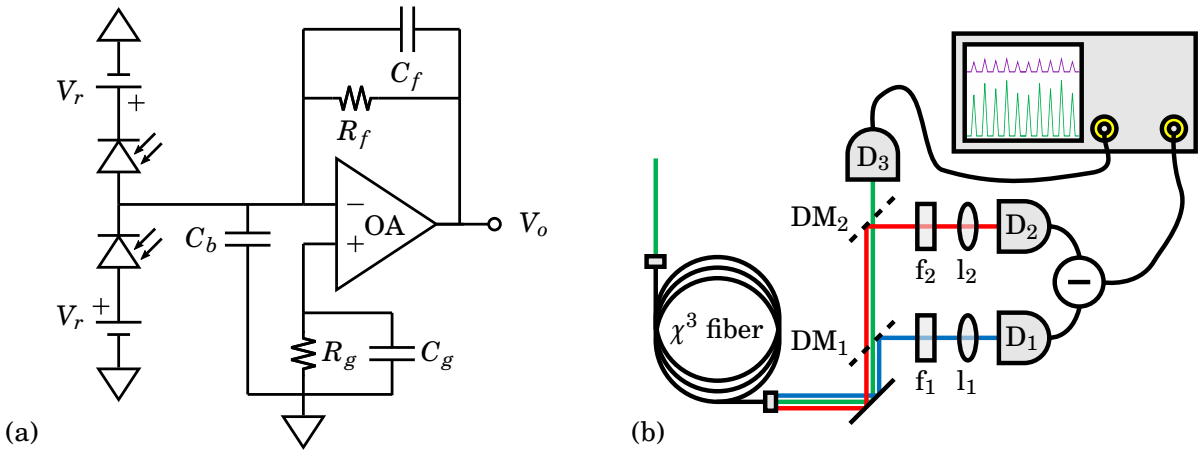

FIGURE 5.18. (a) A schematic of the actively-amplified subtracted-signal SiPD, and (b) the experimental setup used to perform the subtracted-intensity measurement. The photodiode signals are subtracted electronically, rather than in post-processing (see fig. 5.9), to reduce electronic noise, simplify data collection, and increase measurable signal powers. $f_{\{1,2\}}$: spectral filters; $l_{\{1,2\}}$: focusing lenses; $DM_{\{1,2\}}$: dichroic mirrors; $D_{\{1,2,3\}}$: SiPDs.

The denominator of eqn. 2.17 requires us to measure the average twin-beam power, which corresponds to shot-noise in the coherent-state limit. Because the pump beam is largely undepleted, we may correlate its average power $\mathrm{E}[P_p]$ with the FWM average power using a similar characterization as performed in sec. 3.2.1. That is, assuming pump-fiber coupling is constant over the measurement duration, and that pump and FWM average powers have been well-characterized according to some function G, we may infer the average FWM power from the average pump power as

$$\mathrm{E}[P_i] = G_i\left(\mathrm{E}[P_p]\right),$$
$$\mathrm{E}[n_i] = \frac{T\lambda_i}{hc} G_i\left(\frac{\mathrm{E}[V_o^p]}{R_f^p S_p}\right),$$

where $i \in \{1,2\}$, T is the laser repetition rate, V_o^p is the measured voltage associated with the pump beam, R_f^p is the feedback resistor associated with the pump detector, which may in principle differ from that used to measure the FWM beams, and S_p is the responsivity of the photodiode at the pump wavelength. Thus, we have demonstrated how one may calculate the NRF from measured experimental parameters using the subtracted-detection scheme.

The subtracted-signal detector noise and clearance are the same as the previously-discussed active SiPD in sec. 5.3, or in sec. 5.2 if the amplification stage is a passive one. To the best of our knowledge, this is a novel result that is of particular importance to our application of measuring high peak-power, disparate wavelengths in the time domain without saturating the photodiode.

5.4.1 Design and Fabrication

The schematic and PCB design for an active subtracted-signal detector are shown in fig. 5.19. Four adjustable voltage regulators are used to supply the two photodiodes and OA. Two screw terminals are on each board for stable mounting options. As well, there is a terminal block for easily connecting battery packs, which were not included on the previous detector designs 5.2.2. Careful attention has been given to the placement of the photodiodes. One is mounted on each side of the PCB, allowing closest possible positioning to reduce parasitic trace effects along the OA signal input. Two ground planes are required for this detector design to accommodate the surface-mount components on each side. The sutracted detector is smaller and more compact than previous detector iterations, 13.4 cm^2 compared to 19.6 cm^2 from fig. 5.11.

An assembled *Mandrill* detector is shown in fig. 5.20. The PCB substrate is a more-absorptive black (compared to typical green substrates) to reduce noise in the experimental setup from stray or ambient light, and has no effect on electronic performance. We used the same high-efficiency photodiodes as in previous detectors (First Sensor PC5-6b TO5 [113]), reverse biased at 10 V to reduce the junction capacitance as well as increase the saturation energy. The four voltage regulators are positive- and negative-voltage, surface-mount versions of the through-hole regulators from sec. 5.2.2, allowing for more compact PCB design. Finally, in the following discussions, we tested the AD8067 OA with component selection corresponding to $f_{3\text{dB}} = 75$ kHz, as we had not yet a complete understanding of the detector noise properties. As we shall see, however, the current noise associated with the voltage regulators is again dominant, increasing the detector's electronic noise by 40 dB over our measurement bandwidth.

The noise of this SiPD was characterized similarly to the passive detector (see sec. 5.2.3), wherein the photodiodes were covered with an opaque rubber cap, and their output voltage signal compared to the oscilloscope noise. We also measured the subtracted signal for comparison to the electronic noise by equally splitting a 404 nm wavelength CW beam via a HWP and PBS, and shining the two outputs on the two detector photodiodes.

More specifically, the 404 nm CW signal was balanced on each photodiode according to the DC-coupled detector signal measured on an oscilloscope. We balanced detection by adjusting the splitting ratio of the PBS using a HWP, such that the oscilloscope signal was approximately 0 V. We then measured the detector output with no incident signal and the subtracted signal, with results shown in fig. 5.21 (a).

From this data, with $R_f = 3\,\text{M}\Omega$, the detector electronic noise is at least 40 dB greater than the oscilloscope noise at our intended measurement bandwidth. Ultimately, we believe this to be due to voltage regulator current noise, and the process to this determination is discussed in the following section.

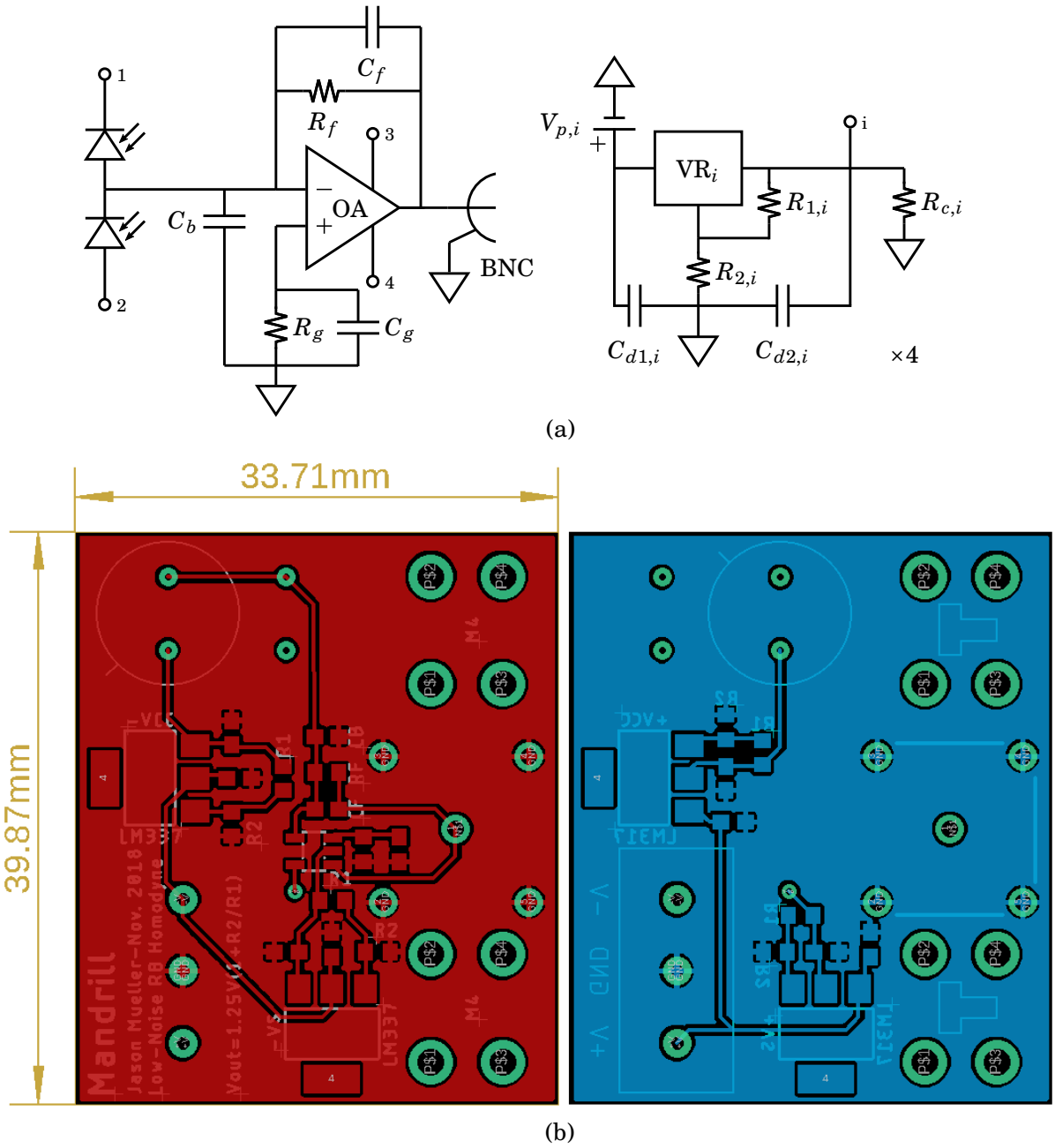

FIGURE 5.19. (a) A schematic for an active subtracted-signal SiPD. VR: voltage regulator; BNC: coaxial cable connector. (b) The PCB design, dubbed *Mandrill* after the vibrantly-colored red and blue muzzle and anus of the mandrill primate.

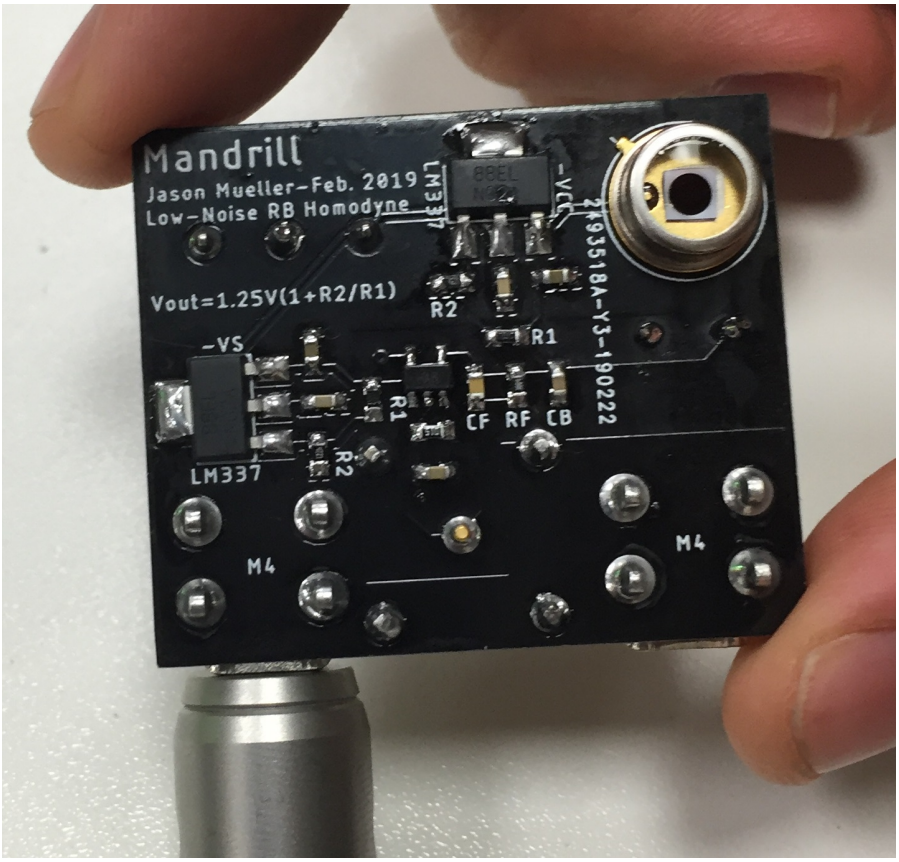

FIGURE 5.20. Photo of an assembled *Mandrill* detector for microwatt correlated-intensity measurements.

5.4.2 Parasitic Voltage Regulator Noise

In our discussions of sec. 5.2.3 and the previous section, we measured electronic noise to be tens of decibels greater than predicted by our theory and simulations. Through a series of experiments to isolate this noise source, we finally believe it to be caused predominantly by the voltage regulators injecting low-frequency dark current through the amplification circuit, as we will detail in this section. This is important in our development of low-noise detectors because we have not only identified a major source of electronic noise within all of our fabricated circuits, but the techniques and principles outlined in this section also inform future component selection and troubleshooting.

As a first step, we built and characterized three identical copies of each *Macaw* and *Mandrill* detectors to ensure that no faulty components were responsible for the 45 kHz and other broadband noise. All detectors exhibited the same noise, indicating that the noise was a feature of the detector design itself and not a defect or manufacturing error.

To minimize ambient low-frequency noise from *e.g.* mains power supplies being amplified

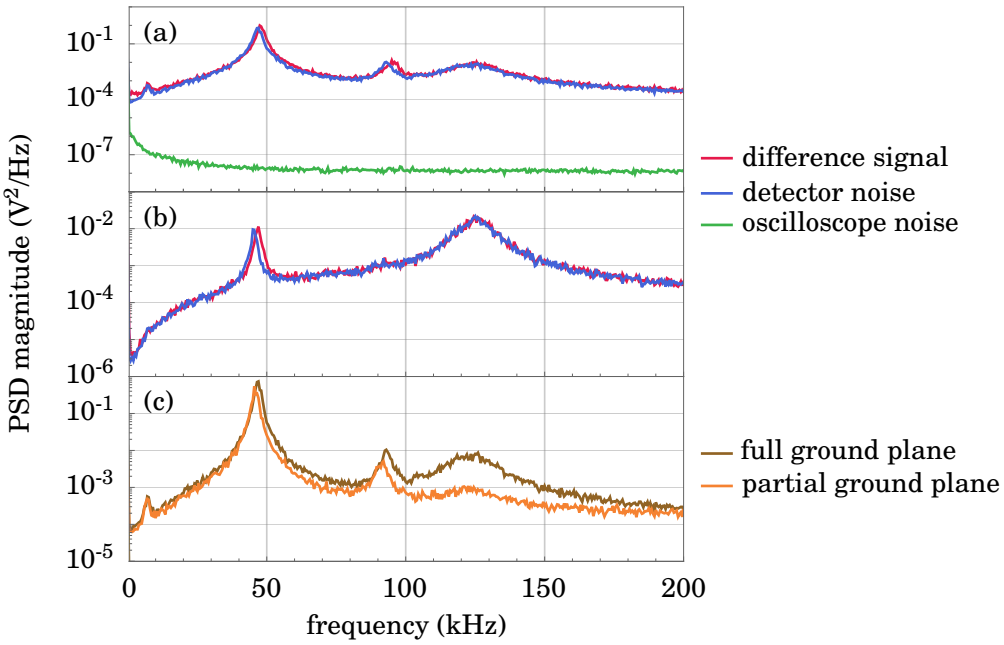

FIGURE 5.21. Electronic noise of the fabricated active subtracted-signal SiPD with (a,c) $R_f = 3\,\mathrm{M\Omega}$, (b) $R_f = 0.3\,\mathrm{M\Omega}$, and (c) comparing parasitic effects of the ground plane. Total signal power was (a) 29 µW and (b) 100 µW. These data each represent an average of 50 oscilloscope traces.

through the high-gain transimpedance circuit, we constructed a home-fashioned Faraday cage, shown in fig. 5.22, and measured the subtracted-signal SiPD noise in two separate labs, one unoccupied, with and without the Faraday cage. The noise across all tests were the same (see fig. 5.21 (a)), indicating that the kilohertz noise is likely not from ambient sources. Note, however, that the skin depth of aluminum at 45 kHz is ~ 0.4 mm, and our home-fashioned Faraday cage may not have been optimally isolating the SiPD.

In a third attempt to mitigate the excess noise, we added decoupling capacitors directly from the photodiode leads to the ground plane to reduce residual voltage noise and trace inductance from the voltage regulators to the photodiodes, although the regulators themselves already had such capacitors in place. This had no effect on the excess electronic noise.

A fourth possibility we considered was that the 45 kHz noise may be caused by a 2π-phase change across the OA at the noise frequency, leading to constructive interference at the OA input. That is, because the photocurrent input is at the inverting pin of the OA, the output signal is π out of phase with the input signal. The OA output will therefore destructively interfere with the input across the feedback circuit. However, if there is an extra π-phase shift across the OA, the output signal will be in phase with the input, and constructively interfere. This scenario is unlikely, however, as OA simulations using LTspice do not predict such a phase shift.

Fifthly, we reduced the feedback resistance from 3 MΩ to 0.3 MΩ, suspecting that the OA may

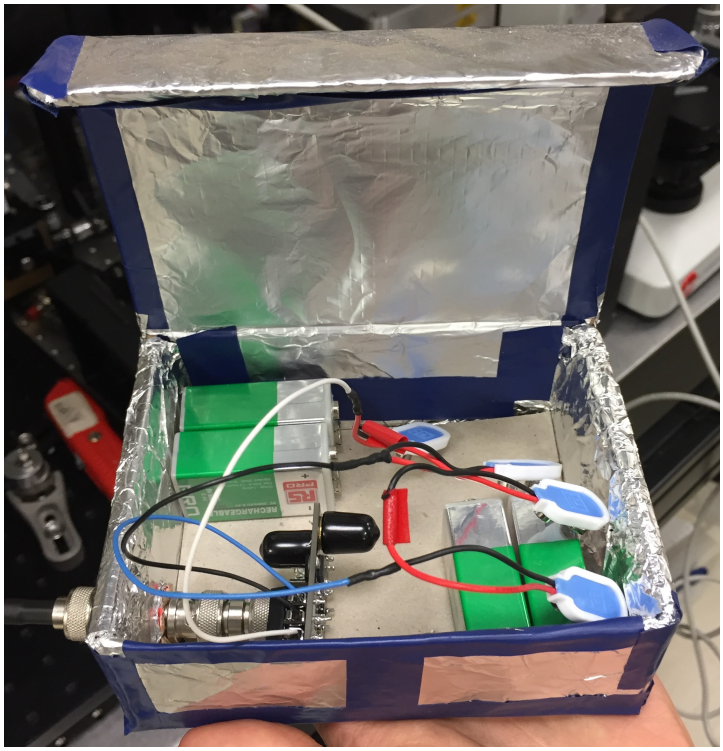

FIGURE 5.22. A photo of the subtracted-signal SiPD in a bespoke Faraday cage. Several layers of aluminum are wrapped around the interior cardboard box, and edges of the box were sealed with aluminum when characterizing the detector with the lid closed.

not be rated for such large R_f. The results are shown in fig. 5.21 (b). While the noise is generally reduced by 10 dB according to the factor of ten reduction in R_f, the characteristic 45 kHz noise remains, indicating that R_f is not the cause. As well, by reducing the feedback resistance, we predict reduced shot-noise clearance. Therefore, reduction of R_f is not a viable option given the FWM power which we expect.

We next suspected that the ground plane beneath the signal electronics (photodiodes, OA, and leads and components connecting them) may be inducing parasitic inductance or capacitance, creating a resonance then amplified by our high-gain transimpedance amplifier. Redesigning the detector, we removed the ground plane beneath the sensitive components and recharacterized the detector noise as before, with the results shown in fig. 5.21 (c). While the ground plane was responsible for the 125 kHz noise, its removal under sensitive components did not reduce electronic noise at our frequencies of interest.

The 45 kHz and associated broadband noise was first observed while using the megaohm-resistance transimpedance amplifiers. Increasing the load resistance of the passive detectors to comparable values, before we had included R_c to meet the minimum current load requirements of the voltage regulator, we measure the same noise features, comparing fig. 5.23 and fig. 5.21.

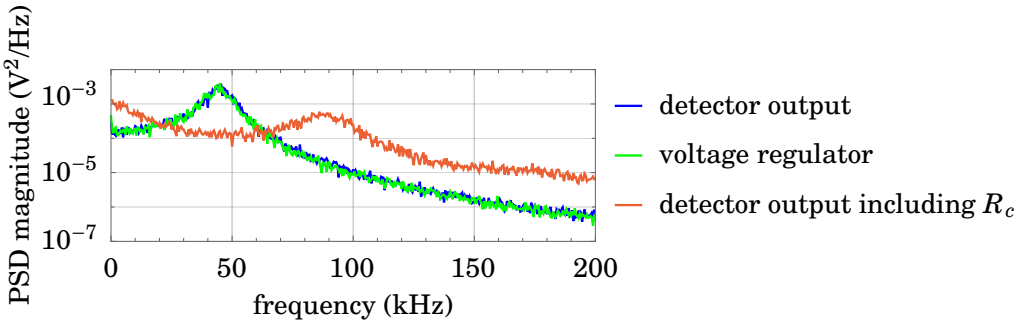

FIGURE 5.23. Noise spectra of the voltage regulator and passive SiPD with and without $R_c = 12$ kΩ to satisfy the voltage regulator minimum current requirements.

This excluded the OA and associated circuitry from being responsible for the excess noise. Indeed, after probing several of the detector components, we found that the noise spectrum of the voltage regulator precisely matched that of the detector noise spectrum. Inserting a 12 kΩ resistor to ground between the voltage regulator and photodiode to satisfy the milliampere current requirement of the regulator mitigated the 45 kHz noise. However, because of the constant current being now drawn from the voltage regulator through the amplification stage, there persists kilohertz broadband noise.

These endeavours to reduce parasitic electronic detector noise are essential to fabricating low-noise SiPDs for measuring sub-Poissonian multi-beam intensity correlations and, ultimately, sub-shot-noise parameter estimation with these detectors.

5.5 Conclusion

In this chapter, we have laid the foundations for designing and fabricating low-noise optical detectors to meet our defined design specifications, namely visible wavelength detection and kilohertz repetition-rate pulses. In sec. 5.1, we discussed relevant background information related to photodiodes, and how we quantify the performance of photodiode detectors. We then discussed two primary classes of detectors, passive and active, and two different detection schemes. The passive detectors of sec. 5.2 were found to suffer from unanticipated electronic noise associated with parasitic voltage regulator effects. The passive SiPDs were useful, however, in characterizing the repetition rate of the laser as well as the responsivity of the photodiodes. The active detectors of sec. 5.3 suffered similar issues, but were shown to be less susceptible to quantization noise of the oscilloscope. Because of the high gain of both of these detectors, the vertical resolution of the oscilloscope must be reduced to levels which introduce excessive noise onto our intensity measurements. To mitigate this, we described a detection scheme in sec. 5.4, similar to traditional homodyne techniques, which allows for simultaneous measurement and electronic subtraction

of the intense optical pulses, such that the oscilloscope may be operated in a low-noise regime. Finally, we discussed techniques for identifying and mitigating parasitic electronic noise from trace capacitance, ground-plane placement, and dark current from voltage supplies.

In the following concluding chapter, we will summarize the methods and results of this thesis, as well as ongoing experimental efforts and outlook.

CHAPTER 6

CONCLUSIONS AND FUTURE WORK

Chapter outline: *In this chapter, we outline the methods and results from the previous chapters. We conclude with a brief discussion of future research directions.*

Declaration of contribution: *This chapter is a summary of previous experimental and theoretical efforts, and contains limited novel work, excepting future research directions discussed at the end of the chapter.*

6.1 Summary of Results

In this thesis, we primarily developed the theoretical and experimental foundations of twin-beam parameter estimation using high-energy optical pulses and disparate, visible wavelengths. The objectives of this and ongoing work were and are to create a portable, low-cost, practical method for improving the precision of absorption imaging and spectroscopy beyond the classical Shot-Noise Limit (SNL). To this end, we have successfully demonstrated strong evidence of sub-Poissonian intensity correlations at $\sigma = 0.47 \pm 0.04$ and SNL parameter estimation ($\Gamma_m = 1.02 \pm 0.16$) at visible wavelengths, four orders of magnitude brighter than previous demonstrations [6–14, 16]. We developed a theoretical framework which accurately describes the results of this experiment, and has broader use in many multi-beam absorption-estimation experiments. And we finally made significant progress towards the realization of low-noise photodiode detectors for sub-SNL applications at microwatts of average power.

In chapter 1, we provided context to our experimental efforts, as well as motivation for its utility in biology and chemistry settings. We also estimated the optical powers required to damage common biological samples, which we demonstrated in the following chapters that we are able to achieve.

In chapter 2, we introduced the process by which we generate our correlated twin beams: Four-Wave Mixing (FWM). This is a parametric process occurring wherein, essentially, two pump photons at one wavelength annihilate to create a photon pair at spectral sidebands determined by the properties of the material in which the optical interaction occurs. By energy conservation, the presence of one FWM photon heralds the presence of the other, and the mutual intensity correlations may be characterized by the Noise-Reduction Factor (NRF). The NRF is disimproved by deleterious effects such as loss, optical and detector noise, and classical intensity fluctuations in the pump beam. All of these effects on the measured NRF are carefully derived and simulated in chapter 2, and these results agree well with experimental data.

We also introduced and compared three absorption estimators used in single- and multi-beam parameter estimation. We found that while multi-beam estimators may be used to improve both the precision and accuracy of an absorption measurement, there is still theoretical work to be done on optimizing such estimators to account for *e.g.* optical noise and classical intensity fluctuations.

In chapter 3, we characterized the spectral, noise, and power properties of our setup of a twin-beam source and CCD detector combined to ultimately show which parameters most-effected the measured intensity correlations at various pump powers. We showed also that in both our tested Photonic Crystal Fiber (PCF) and Single-Mode Fiber (SMF)28, we can consistently achieve average FWM powers on the order of microwatts, due to the exponential gain of the nonlinear fibers and large peak power of the pump beam. The upper limits on FWM power are determined by the optical damage properties of the fibers, which differ for PCF and SMF28, as well as physical fiber perturbations that may cause mode-mixing and reduce FWM efficiency.

The five characterized fibers all generated Stokes and anti-Stokes FWM at ~ 650 nm and ~ 450 nm, respectively. Due to the multi-mode nature of the fibers, as well as the pump beam, multiple FWM modes could be simultaneously excited or optimized on, according primarily to the pump alignment relative to the fiber input. In both the PCF and SMF28, Stokes Raman scattering was found to spectrally overlap with the Stokes FWM, increasing the NRF at low pump powers.

After also characterizing the optical and noise properties of *e.g.* Stokes Raman scattering and CCD dark counts, we showed that the primary contributors to worse-measured NRFs in our experiment were detector noise at low powers, optical noise at intermediate powers, and classical intensity noise at high powers. These simulations proved useful for informing experimental design, and the underlying experimental framework is widely applicable to similar classical and quantum multi-beam parameter-estimation experiments.

Also in chapter 3, we described our various data analysis protocols, increasing their speed and reliability over the course of our experimental efforts. We now use a version of data analysis which allows live-monitoring of the NRF, such that the effects of experimental changes on the measured NRF may be rapidly assessed.

Since describing the theoretical and experimental background of intensity-correlated parameter estimation, in chapter 4 we detailed our efforts towards measuring sub-Poissonian intensity correlations and sub-SNL absorption estimation. With each iteration of the experiment, we systematically improved the measured NRF by identifying and reducing the number of optical components which may introduce parasitic noise, involving careful characterization of *e.g.* the fiber numerical aperture, the pump beam pointing stability, and optical filters. Ultimately, we measured strong evidence of sub-Poissonian intensity correlations, at $\sigma = 0.47 \pm 0.04$ and picowatts average FWM power, which is 3 dB below the classical coherent-state limit. Using the multi-beam correlations, the absorption estimation is improved by a factor of ~ 20 over an equally-classically-noisy data set. Due to optical noise and sub-optimal absorption estimators which do not account for this noise, however, the efficacy of the correlations are reduced such that we measure $\Gamma_m = 1.02 \pm 0.16$, at the SNL.

In chapter 5, we began work on designing, fabricating, and characterizing low-noise Silicon Photodiode Detectors (SiPDs) for microwatt parameter estimation which satisfy our FWM repetition rate, optical power, and spectral requirements, as the CCD camera saturates at tens of picowatts average power and cannot be reliably used for high-power, sub-SNL parameter estimation. We described two broad classes of SiPDs, passive and active, as well as the benefits and limitations of each. After simulating, designing, and testing several models which predict noise clearance at several to tens of decibels, parasitic electronic noise from *e.g.* the oscilloscope and voltage regulators were found to dominate the shot-noise signal which the detectors were designed to measure. Work is currently ongoing to identify and mitigate other such sources of electronic noise, with the ultimate objective of performing microwatt average power (watt peak

power) parameter estimation. We also described a novel technique for measuring the NRF of intense optical pulses in the time domain while maintaining high oscilloscope vertical resolution.

6.2 Applications of Quantum Metrology to Biology

In the literature related to quantum imaging beyond the SNL, there are numerous claims to the practical utility of twin-beam sources for biological imaging applications [2, 7–12, 15]. There are, however, relatively few experimental proposals which implement these sources and show a true quantum advantage [18]. Indeed, an experiment has yet to be realized which demonstrates a sub-SNL precision improvement at a photon flux that simultaneously damages or alters the biological or chemical sample of interest.

One proposed direction of research is characterizing properties of volatile materials related to the spectral absorption of these materials, for example, color. As a specific example, the color of beer and wort may be characterized according to its absorption coefficient at 430 nm wavelength, using the *standard reference method* [131–133]. While blue light is used to characterize the beer's color, blue and UltraViolet (UV) light is also responsible for degradation of riboflavin in the beer. Some of the products of this photochemical reaction are responsible for spoilage and may occur over minute timescales depending on the wavelengths and optical power [134, 135]. Riboflavin concentration in aqueous solutions can be measured using fluorescence techniques [136, 137], thereby allowing a quantifiable determination of sample damage pre- and post-spectral-characterization. Indeed, ref. [135] employs a 0.7 mW tungsten lamp with a UV filter and demonstrate a 5% decrease in riboflavin concentration after 1 hr exposure. Note also that riboflavin is found in many pharmaceutical compounds, as well as other food products [134]. This is an intended application of the work of this thesis.

6.3 Future Work and Outlook

Near-term future research directions include continued work on the development and characterization of high-power silicon photodiode detectors for measuring sub-Poissonian intensity correlations, as well as estimating a non-biological sample absorption. We are also currently investigating techniques to improve FWM mode coupling such as liquid-nitrogen cooling the fiber and fiber tapering, as well as the potential to implement a spatial light modulator, digital micromirror device, or bespoke phaseplate to improve FWM mode coupling. These techniques would increase the optical Signal-to-Noise Ratio (SNR) and improve measured NRFs. Other techniques to improve the SNR are to implement narrow-band spectral filtering around the anti-Stokes and especially the Stokes FWM wavelengths. This requires careful characterization of the FWM wavelengths with a precisely-calibrated spectrometer, and reliable fiber mode coupling, enabled by the aforementioned techniques. Finally, we are continuing theoretical work on absorption

estimator optimization to account for optical and detector noise, improving estimated sample absorption.

The work of this thesis represents an important step in applying techniques found in many physics laboratories to real-world, cross-disciplinary applications. Indeed, the primary motivation of our work was, and continues to be, to bridge the gap between quantum metrology and its near-term applications in biology and chemistry, specifically imaging and spectroscopy applications. Long-term uses of such technologies could be in pharmaceuticals for efficient drug characterization, for early identification of cell cultures, improving diagnosis efficiency of bacterial infections, or characterization of new, optically-sensitive synthetic materials. It is my opinion that for this technology to be seriously considered by disciplines outside of quantum physics, an imaging or spectroscopy measurement must be demonstrated which shows improved precision for a given sample damage threshold. Practically, the technology should also be user-friendly enough that a biologist or chemist without specialist knowledge in quantum mechanics could use it.

To achieve this goal, since we have already demonstrated that it is possible to measure sub-Poissonian intensity correlations at novel visible wavelengths, efforts should be focused primarily in two areas: (1) the development of efficient and reliable fiber-coupling techniques to excite specific wavelengths of interest for a given nonlinear fiber, in conjunction with using low-cost pump lasers, and (2) the fabrication of low-noise, application-specific detectors. Achieving (1) will improve the SNR, making sub-SNL absorption measurements possible even if no improved absorption estimator is found. And achieving (2) will allow for the measurement of correlated beams at optical powers relevant to biological applications.

BIBLIOGRAPHY

[1] J. Mueller, A. McMillan, P.-A. Moreau, J. Sabines-Chesterking, J. Rarity, P. J. Mosley, and J. Matthews, "Sub-Poissonian Twin-Beam Correlations at Blue and Red Wavelengths from Four-Wave Mixing," in *Conference on Lasers and Electro-Optics*, Optical Society of America, 2018.

[2] E. Jakeman and J. Rarity, "The use of pair production processes to reduce quantum noise in transmission measurements," *Optics Communications*, vol. 59, pp. 219–223, 1986.

[3] S. Reynaud, C. Fabre, and E. Giacobino, "Quantum fluctuations in a two-mode parametric oscillator," *J. Opt. Soc. Am. B*, vol. 4, no. 10, pp. 1520–1524, 1987.

[4] A. Heidmann, R. J. Horowicz, S. Reynaud, E. Giacobino, C. Fabre, and G. Camy, "Observation of Quantum Noise Reduction on Twin Laser Beams," *Phys. Rev. Lett.*, vol. 59, pp. 2555–2557, 1987.

[5] K. L. Haller and P. C. D. Hobbs, "Double-beam laser absorption spectroscopy: shot noise-limited performance at baseband with a novel electronic noise canceler," in *Optical Methods for Ultrasensitive Detection and Analysis: Techniques and Applications*, vol. 1435, 1991.

[6] R. Whittaker, C. Erven, A. Neville, M. Berry, J. L. O'Brien, H. Cable, and J. C. F. Matthews, "Absorption spectroscopy at the ultimate quantum limit from single-photon states," *New Journal of Physics*, vol. 19, no. 2, p. 023013, 2017.

[7] G. Brida, L. Caspani, A. Gatti, M. Genovese, A. Meda, and I. R. Berchera, "Measurement of Sub-Shot-Noise Spatial Correlations without Background Subtraction," *Phys. Rev. Lett.*, vol. 102, p. 213602, May 2009.

[8] G. Brida, M. Genovese, and I. Ruo Berchera, "Experimental realization of sub-shot-noise quantum imaging," *Nature Photonics*, vol. 4, no. 4, pp. 227–230, 2010.

[9] P. A. Morris, R. S. Aspden, J. E. C. Bell, R. W. Boyd, and M. J. Padgett, "Imaging with a small number of photons," *Nature Communications*, vol. 6, no. 1, p. 5913, 2015.

[10] P.-A. Moreau, J. Sabines-Chesterking, R. Whittaker, S. K. Joshi, P. M. Birchall, A. McMillan, J. G. Rarity, and J. C. F. Matthews, "Demonstrating an absolute quantum advantage in direct absorption measurement," *Scientific Reports*, vol. 7, no. 1, p. 6256, 2017.

[11] N. Samantaray, I. Ruo-Berchera, A. Meda, and M. Genovese, "Realization of the first sub-shot-noise wide field microscope," *Light: Science & Applications*, vol. 6, no. 7, p. 17005, 2017.

[12] E. Toninelli, M. P. Edgar, P.-A. Moreau, G. M. Gibson, G. D. Hammond, and M. J. Padgett, "Sub-shot-noise shadow sensing with quantum correlations," *Opt. Express*, vol. 25, no. 18, pp. 21826–21840, 2017.

[13] J. Sabines-Chesterking, R. Whittaker, S. K. Joshi, P. M. Birchall, P. A. Moreau, A. McMillan, H. V. Cable, J. L. O'Brien, J. G. Rarity, and J. C. F. Matthews, "Sub-Shot-Noise Transmission Measurement Enabled by Active Feed-Forward of Heralded Single Photons," *Phys. Rev. Applied*, vol. 8, p. 014016, 2017.

[14] E. Losero, I. Ruo-Berchera, A. Meda, A. Avella, and M. Genovese, "Unbiased estimation of an optical loss at the ultimate quantum limit with twin-beams," *Scientific Reports*, vol. 8, no. 1, p. 7431, 2018.

[15] E. Knyazev, F. Y. Khalili, and M. V. Chekhova, "Overcoming inefficient detection in sub-shot-noise absorption measurement and imaging," *Opt. Express*, vol. 27, no. 6, pp. 7868–7885, 2019.

[16] J. Sabines-Chesterking, A. R. McMillan, P. A. Moreau, S. K. Joshi, S. Knauer, E. Johnston, J. G. Rarity, and J. C. F. Matthews, "Twin-beam sub-shot-noise raster-scanning microscope," *Opt. Express*, vol. 27, pp. 30810–30818, Oct 2019.

[17] S. Sofer, E. Strizhevsky, A. Schori, K. Tamasaku, and S. Shwartz, "Quantum Enhanced X-ray Detection," *Phys. Rev. X*, vol. 9, p. 031033, 2019.

[18] M. A. Taylor and W. P. Bowen, "Quantum metrology and its application in biology," *Physics Reports*, vol. 615, pp. 1–59, 2016.

[19] S. Wäldchen, J. Lehmann, T. Klein, S. van de Linde, and M. Sauer, "Light-induced cell damage in live-cell super-resolution microscopy," *Scientific Reports*, vol. 5, p. 15348, 2015.

[20] Y. Fu, H. Wang, R. Shi, and J.-X. Cheng, "Characterization of photodamage in coherent anti-Stokes Raman scattering microscopy," *Opt. Express*, vol. 14, no. 9, pp. 3942–3951, 2006.

[21] E. H. K. Stelzer, "Light-sheet fluorescence microscopy for quantitative biology," *Nature Methods*, vol. 12, no. 1, pp. 23–26, 2015.

[22] M. A. S. de Oliveira, D. S. Moura, A. Fontes, and R. E. de Araujo, "Damage induced in red blood cells by infrared optical trapping: an evaluation based on elasticity measurements," *Journal of Biomedical Optics*, vol. 21, no. 7, pp. 1–5, 2016.

[23] M. L. Denton, M. S. Foltz, L. E. Estlack, D. J. Stolarski, G. D. Noojin, R. J. Thomas, D. Eikum, and B. A. Rockwell, "Damage Thresholds for Exposure to NIR and Blue Lasers in an In Vitro RPE Cell System," *Investigative Ophthalmology & Visual Science*, vol. 47, no. 7, pp. 3065–3073, 2006.

[24] L. Song, E. Hennink, I. Young, and H. Tanke, "Photobleaching kinetics of fluorescein in quantitative fluorescence microscopy," *Biophysical Journal*, vol. 68, no. 6, pp. 2588–2600, 1995.

[25] S. Kalies, K. Kuetemeyer, and A. Heisterkamp, "Mechanisms of high-order photobleaching and its relationship to intracellular ablation," *Biomedical optics express*, vol. 2, no. 4, pp. 805–816, 2011.

[26] F. Forghieri, R. W. Tkach, A. R. Chraplyvy, and D. Marcuse, "Reduction of four-wave mixing crosstalk in WDM systems using unequally spaced channels," *IEEE Photonics Technology Letters*, vol. 6, no. 6, pp. 754–756, 1994.

[27] M. W. Maeda, W. B. Sessa, W. I. Way, A. Yi-Yan, L. Curtis, R. Spicer, and R. I. Laming, "The effect of four-wave mixing in fibers on optical frequency-division multiplexed systems," *Journal of Lightwave Technology*, vol. 8, no. 9, pp. 1402–1408, 1990.

[28] G. Agrawal, *Nonlinear Fiber Optics*. Academic Press, 5 ed., 2012.

[29] J. W. Silverstone, D. Bonneau, K. Ohira, N. Suzuki, H. Yoshida, N. Iizuka, M. Ezaki, C. M. Natarajan, M. G. Tanner, R. H. Hadfield, V. Zwiller, G. D. Marshall, J. G. Rarity, J. L. O'Brien, and M. G. Thompson, "On-chip quantum interference between silicon photon-pair sources," *Nature Photonics*, vol. 8, no. 2, pp. 104–108, 2014.

[30] B. Sévigny, A. Cassez, O. Vanvincq, Y. Quiquempois, and G. Bouwmans, "High-quality ultraviolet beam generation in multimode photonic crystal fiber through nondegenerate four-wave mixing at 532 nm," *Opt. Lett.*, vol. 40, no. 10, pp. 2389–2392, 2015.

[31] A. McMillan, *Development of an all-fibre source of heralded single photons*. PhD thesis, University of Bath, 2011.

[32] U. Hoff and U. Andersen, *Integrated Quantum Optics: Experiments towards integrated quantum-light sources and quantum-enhanced sensing*. PhD thesis, Department of Physics, Technical University of Denmark, 2015.

[33] C. W. Thiel, "Four-Wave Mixing and its Applications," 2000.

[34] Z. Y. Ou and Y. J. Lu, "Cavity Enhanced Spontaneous Parametric Down-Conversion for the Prolongation of Correlation Time between Conjugate Photons," *Phys. Rev. Lett.*, vol. 83, pp. 2556–2559, 1999.

[35] X. Guo, C.-l. Zou, C. Schuck, H. Jung, R. Cheng, and H. X. Tang, "Parametric down-conversion photon-pair source on a nanophotonic chip," *Light: Science & Applications*, vol. 6, no. 5, p. 16249, 2017.

[36] C. K. Hong, Z. Y. Ou, and L. Mandel, "Measurement of subpicosecond time intervals between two photons by interference," *Phys. Rev. Lett.*, vol. 59, pp. 2044–2046, 1987.

[37] O. Alibart, J. Fulconis, G. K. L. Wong, S. G. Murdoch, W. J. Wadsworth, and J. G. Rarity, "Photon pair generation using four-wave mixing in a microstructured fibre: theory versus experiment," *New Journal of Physics*, vol. 8, no. 5, p. 67, 2006.

[38] R. W. Boyd, *Nonlinear Optics, Third Edition*. Academic Press, 3rd ed., 2008.

[39] Y. Chen, W. Wadsworth, and T. Birks, "Ultraviolet four-wave mixing in the LP_{02} fiber mode," *Optics letters*, vol. 38, no. 19, pp. 3747–3750, 2013.

[40] I. N. Chuprina, N. S. Perminov, D. Y. Tarankova, and A. A. Kalachev, "Generating pure single-photon states via spontaneous four-wave mixing in a system of coupled microresonators," *Laser Physics Letters*, vol. 15, p. 105104, aug 2018.

[41] A. W. Snyder and J. Love, *Optical waveguide theory*. Springer Science & Business Media, 2012.

[42] A. W. Snyder and W. R. Young, "Modes of optical waveguides," *J. Opt. Soc. Am.*, vol. 68, no. 3, pp. 297–309, 1978.

[43] R. Paschotta, *Field Guide to Optical Fiber Technology*. SPIE Press, 16 ed., 2010.

[44] T. R. Hart, R. L. Aggarwal, and B. Lax, "Temperature Dependence of Raman Scattering in Silicon," *Phys. Rev. B*, vol. 1, pp. 638–642, 1970.

[45] R. H. Stolen, "Chapter 5 - Nonlinear Properties of Optical Fibers," in *Optical Fiber Telecommunications* (S. E. Miller and A. G. Chynoweth, eds.), pp. 125–150, Academic Press, 1979.

[46] K. Saitoh and M. Koshiba, "Empirical relations for simple design of photonic crystal fibers," *Opt. Express*, vol. 13, no. 1, pp. 267–274, 2005.

[47] H. Pourbeyram, E. Nazemosadat, and A. Mafi, "Detailed investigation of intermodal four-wave mixing in SMF-28: blue-red generation from green," *Opt. Express*, vol. 23, no. 11, pp. 14487–14500, 2015.

[48] H. Pourbeyram and A. Mafi, "Photon pair generation in multimode optical fibers via intermodal phase matching," *Phys. Rev. A*, vol. 94, p. 023815, Aug 2016.

[49] Corning, *SMF-28e+® Optical Fiber*, 2019.

[50] U. Fano, "Ionization Yield of Radiations. II. The Fluctuations of the Number of Ions," *Phys. Rev.*, vol. 72, pp. 26–29, 1947.

[51] D. Glattli, "Course 11 - Introduction to Quantum Conductors," in *Quantum Entanglement and Information Processing* (D. Estève, J.-M. Raimond, and J. Dalibard, eds.), vol. 79 of *Les Houches*, pp. 401–441, Elsevier, 2004.

[52] J. Rarity, P. Tapster, and E. Jakeman, "Observation of sub-poissonian light in parametric downconversion," *Optics Communications*, vol. 62, no. 3, pp. 201–206, 1987.

[53] L. Davidovich, "Sub-Poissonian processes in quantum optics," *Rev. Mod. Phys.*, vol. 68, pp. 127–173, 1996.

[54] N. Samantaray, *Quantum enhanced imaging and sensing with correlated light*. PhD thesis, Politecnico Di Torino, 2017.

[55] E. M. Purcell, "The Question of Correlation between Photons in Coherent Light Rays," *Nature*, vol. 178, no. 4548, pp. 1449–1450, 1956.

[56] L. Mandel, "Fluctuations of Photon Beams and their Correlations," *Proceedings of the Physical Society*, vol. 72, pp. 1037–1048, dec 1958.

[57] L. Mandel, "Fluctuations of Photon Beams: The Distribution of the Photo-Electrons," *Proceedings of the Physical Society*, vol. 74, pp. 233–243, sep 1959.

[58] K. Kawamura, "The structure of bivariate Poisson distribution," *Kodai Math. Sem. Rep.*, vol. 25, no. 2, pp. 246–256, 1973.

[59] W. R. Inc., "Mathematica, Version 11.3." Champaign, IL, 2019.

[60] Teem Photonics, *SNP High Performances IR Microchip Series*, 2019.

[61] Teem Photonics, *SNG High Performances Green Microchip Series*, 2019.

[62] Andor, *Shamrock 750*, 2019.

[63] Andor, *Newton 970*, 2019.

[64] Thorlabs, *GIF625 - Graded-Index Multimode Fiber, ∅62.5 µm Core / ∅125 µm Cladding, OM1, 0.275 NA*, 2019.

[65] Y. Chen, Z. Chen, W. J. Wadsworth, and T. A. Birks, "Nonlinear optics in the LP02 higher-order mode of a fiber," *Opt. Express*, vol. 21, no. 15, pp. 17786–17799, 2013.

[66] P. J. Mosley. private communication, 2019.

[67] Semrock, *Semrock 2017 Master Catalog*, 2017.

[68] Thorlabs, *FPC560 - Fiber Polarization Controller, 3 Large Paddles, No Fiber*, 2019.

[69] B. C. Stuart, M. D. Feit, A. M. Rubenchik, B. W. Shore, and M. D. Perry, "Laser-Induced Damage in Dielectrics with Nanosecond to Subpicosecond Pulses," *Phys. Rev. Lett.*, vol. 74, pp. 2248–2251, 1995.

[70] A. V. Smith, B. T. Do, G. R. Hadley, and R. L. Farrow, "Optical Damage Limits to Pulse Energy From Fibers," *IEEE Journal of Selected Topics in Quantum Electronics*, vol. 15, no. 1, pp. 153–158, 2009.

[71] Thorlabs, *C330TMD-A - f = 3.1 mm, NA = 0.7 Mounted Geltech Aspheric Lens, AR: 350 - 700 nm*, 2019.

[72] Thorlabs, *S130C - Slim Photodiode Power Sensor, Si, 400 - 1100 nm, 500 mW*, 2019.

[73] L. Skuja, H. Hosono, and M. Hirano, "Laser-induced color centers in silica," in *Laser-Induced Damage in Optical Materials: 2000*, vol. 4347, 2001.

[74] V. B. Neustruev, E. M. Dianov, V. M. Kim, V. M. Mashinsky, M. V. Romonov, A. N. Guryanov, V. F. Khopin, and V. A. Tikhomirov, "Ultraviolet radiation- and γ radiation-induced color centers in germanium-doped silica glass and fibers," *Fiber and Integrated Optics*, vol. 8, no. 2, pp. 143–156, 1989.

[75] T. I. Suratwala, P. E. Miller, J. D. Bude, W. A. Steele, N. Shen, M. V. Monticelli, M. D. Feit, T. A. Laurence, M. A. Norton, C. W. Carr, and L. L. Wong, "HF-Based Etching Processes for Improving Laser Damage Resistance of Fused Silica Optical Surfaces," *Journal of the American Ceramic Society*, vol. 94, no. 2, pp. 416–428, 2011.

[76] Y. Li, H. Yan, K. Yang, C. Yao, Z. Wang, X. Zou, C. Yan, X. Yuan, X. Ju, and L. Yang, "Surface molecular structure defects and laser-induced damage threshold of fused silica during a manufacturing process," *Scientific Reports*, vol. 7, no. 1, p. 17870, 2017.

[77] Andor, *Andor iXon Ultra Data Sheet*, 2019.

[78] B. Ma, Z. Shang, L. Wang, Y. Hu, Q. Liu, and P. Wei, "The nonlinear photon transfer curve of ccds and its effects on photometry," in *High Energy, Optical, and Infrared Detectors for Astronomy VI*, vol. 9154, 2014.

[79] M. Downinga, D. Baadea, S. Deiriesa, and P. Jordenb, *Bulk Silicon CCDs, Point Spread Function and Photon Transfer Curves: CCD Testing Activities at ESO*. European Southern Observatory, 2009.

[80] "Laser Power and Energy Meter Calibration." `https://www.nist.gov/programs-projects/laser-power-and-energy-meter-calibration`. Accessed: 2019-07-12.

[81] D. Montgomery and G. Runger, *Applied Statistics and Probability for Engineers*. John Wiley & Sons, Inc., 3rd ed., 2003.

[82] R. M. Brugger, "A Note on Unbiased Estimation of the Standard Deviation," *The American Statistician*, vol. 23, p. 32, 1969.

[83] P. Scott, "Physics 133 Lab Manual," 2015.

[84] K. Knight, *Mathematical statistics*. Chapman & Hall/CRC, 1st ed., 2000.

[85] M. Abramowitz and I. Stegun, *Handbook of Mathematical Functions With Formulas, Graphs, and Mathematical Tables*. Dover Publications, 10th ed., 1972.

[86] O. Hainaut, "Basic CCD image processing." `https://www.eso.org/~ohainaut/ccd/`, 1996. Accessed: 2019-07-25.

[87] MathWorks, "MATLAB, Version R2018a." Natick, MA, 2019.

[88] Thorlabs, *FLH532-4 - Premium Bandpass Filter, ∅25 mm, CWL = 532 nm, FWHM = 4 nm*, 2019.

[89] Elliot Scientific, *MDE122 - Elliot Gold Series XYZ Flexure Stage with High Precision Manual Adjusters*, 2019.

[90] Thorlabs, *AFS-FS - Fused Silica Ultrafast Laser Dispersion-Compensating Prism Pair*, 2019.

[91] Thorlabs, *Collimation Tutorial*, 2019.

[92] Thorlabs, *C340TMD-A - f = 4.03 mm, NA = 0.64 Mounted Geltech Aspheric Lens, AR: 350 - 700 nm*, 2019.

[93] R. Hui and M. O'Sullivan, "Chapter 1 - Fundamentals of Optical Devices," in *Fiber Optic Measurement Techniques* (R. Hui and M. O'Sullivan, eds.), pp. 1–128, Boston: Academic Press, 2009.

[94] K. Kato, "Temperature-tuned 90° phase-matching properties of LiB_3O_5," *IEEE Journal of Quantum Electronics*, vol. 30, no. 12, pp. 2950–2952, 1994.

[95] M. M. Fejer, G. A. Magel, D. H. Jundt, and R. L. Byer, "Quasi-phase-matched second harmonic generation: tuning and tolerances," *IEEE Journal of Quantum Electronics*, vol. 28, no. 11, pp. 2631–2654, 1992.

[96] Thorlabs, *BP209-VIS/M - Dual Scanning Slit Beam Profiler, 200 - 1100 nm, ∅2.5 µm - ∅9 mm, Metric*, 2019.

[97] Thorlabs, *SM450 - Single Mode Optical Fiber, 488 - 633 nm, ∅125 µm Cladding*, 2019.

[98] 3SAE Technologies, *Fitel S183 PM II*, 2019.

[99] Thorlabs, *ST1XY-D/M - XY Translator with Differential Drives, Metric*, 2019.

[100] Thorlabs, *SM1Z - Z-Axis Translation Mount, 30 mm Cage Compatible*, 2019.

[101] Thorlabs, *BFT1 - Universal Bare Fiber Terminator (Connectors Not Included)*, 2019.

[102] Thorlabs, *P20D - ∅1" Mounted Precision Pinhole, 20 ± 2 µm Pinhole Diameter*, 2019.

[103] Newport, *High-Energy Pinhole, Molybdenum, 20 µm, 0.875-20 Thread*, 2019.

[104] Thorlabs, *LA1509-A - N-BK7 Plano-Convex Lens, ∅1", f = 100.0 mm, AR Coating: 350-700 nm*, 2019.

[105] Thorlabs, *SPW602 - Spanner Wrench for SM1-Threaded Retaining Rings, Graduated Scale with 0.1" (2.5 mm) Increments, Length = 3.88"*, 2019.

[106] S. A. E. Lewis, S. V. Chernikov, and J. R. Taylor, "Temperature-dependent gain and noise in fiber raman amplifiers," *Opt. Lett.*, vol. 24, no. 24, pp. 1823–1825, 1999.

[107] A. McMillan. private communication, 2019.

[108] E. Allen, *Suppression of Noise in Classical and Quantum Optics*. PhD thesis, University of Bristol, 2019.

[109] A. V. Masalov, A. Kuzhamuratov, and A. I. Lvovsky, "Noise spectra in balanced optical detectors based on transimpedance amplifiers," *Review of Scientific Instruments*, vol. 88, no. 11, p. 113109, 2017.

[110] J. G. Edwards and R. Jefferies, "Analysis and measurement of the speed and linearity of silicon photodiodes for measuring short laser pulses," *Journal of Physics E: Scientific Instruments*, vol. 6, no. 9, p. 841, 1973.

[111] Hamamatsu, *Si photodiodes*, ch. 2. 2019.

[112] OSI Optoelectronics, *Photodiode Characteristics and Applications*, 2019.

[113] First Sensor, *First Sensor PIN PD Data Sheet: Part Description PC5-6b TO*, 2013.

[114] Thorlabs, *FDS025 - Si Photodiode, 47 ps Rise Time, 400 - 1100 nm, ∅0.25 mm Active Area*, 2019.

[115] I. S. Gradshteyn and I. M. Ryzhik, *Table of Integrals, Series, and Products*. Elsevier Inc., 7 ed., 2007.

[116] J. Stein, *Digital Signal Processing: A Computer Science Perspective*. John Wiley & Sons, Inc., 2000.

[117] S. Schmitt, J. Ficker, M. Wolff, F. König, A. Sizmann, and G. Leuchs, "Photon-Number Squeezed Solitons from an Asymmetric Fiber-Optic Sagnac Interferometer," *Phys. Rev. Lett.*, vol. 81, pp. 2446–2449, 1998.

[118] L. Technology, "LTspice, Version XVII." Milpitas, CA, 2019.

[119] D. A. Corder, D. R. Evans, and J. R. Tyrer, "A novel method for energy measurement of short optical pulses," *Measurement Science and Technology*, vol. 8, no. 9, p. 1034, 1997.

[120] Tektronix, *Digital Storage Oscilloscopes TDS1000B Series, TDS2000B Series Data Sheet*, 2009.

[121] Keysight, *InfiniiVision 3000 X-Series Oscilloscopes*, 2018.

[122] L. Tan and J. Jiang, "Chapter 12 - Multirate Digital Signal Processing, Oversampling of Analog-to-Digital Conversion, and Undersampling of Bandpass Signals," in *Digital Signal Processing (Second Edition)* (L. Tan and J. Jiang, eds.), pp. 555–619, Boston: Academic Press, second edition ed., 2013.

[123] A. V. D. Ziel, "Flicker Noise in Electronic Devices," in *Advances in Electronics and Electron Physics* (L. Marton and C. Marton, eds.), vol. 49, pp. 225–297, Academic Press, 1979.

[124] C. E. Shannon, "Communication in the Presence of Noise," *Proceedings of the IRE*, vol. 37, no. 1, pp. 10–21, 1949.

[125] Texas Instruments, *LMx17HV High Voltage Three-Terminal Adjustable Regulator With Overload Protection*, 2015.

[126] Autodesk, "EAGLE, Version 9.4.2." Mill Valley, CA, 2019.

[127] J. Karki, *Effect of Parasitic Capacitance in Op Amp Circuits*. Texas Instruments, 2000.

[128] S. Butterworth, "On the Theory of Filter Amplifiers," *Experimental Wireless and the Wireless Engineer*, vol. 7, pp. 536—-541, 1930.

[129] Analog Devices, *High Gain Bandwidth Product, Precision Fast FET Op Amp*, 2012.

[130] Analog Devices, *Femtoampere Input Bias Current Electrometer Amplifier*, 2017.

[131] Merck, *Analysis Methods for the Brewery Industry*, 2017.

[132] J. A. S. Viggiano, *Spectrophotometric Analysis of Beer and Wort*, 2006.

[133] H. C. de Oliveira, J. C. E. da Cunha Filho, J. C. Rocha, and E. G. F. N. nez, "Rapid monitoring of beer-quality attributes based on UV-Vis spectral data," *International Journal of Food Properties*, vol. 20, pp. 1686–1699, 2017.

[134] M. A. Sheraz, S. H. Kazi, S. Ahmed, Z. Anwar, and I. Ahmad, "Photo, thermal and chemical degradation of riboflavin," *Beilstein Journal of Organic Chemistry*, vol. 10, pp. 1999–2012, 2014.

[135] Y. Sato, M. Yokoo, S. Takahashi, and T. Takahashi, "Biphasic Photolysis of Riboflavine with a Low-intensity Light Source," *Chemical & Pharmaceutical Bulletin*, vol. 30, no. 5, pp. 1803–1810, 1982.

[136] M. G. Duyvis, R. Hilhorst, C. Laane, D. J. Evans, and D. J. M. Schmedding, "Role of Riboflavin in Beer Flavor Instability: Determination of Levels of Riboflavin and Its Origin in Beer by Fluorometric Apoprotein Titration," *Journal of Agricultural and Food Chemistry*, vol. 50, no. 6, pp. 1548–1552, 2002. PMID: 11879035.

[137] A. Bonamore, M. Gargano, L. Calisti, A. Francioso, L. Mosca, A. Boffi, and R. Federico, "A Novel Direct Method for Determination of Riboflavin in Alcoholic Fermented Beverages," *Food Analytical Methods*, vol. 9, no. 4, pp. 840–844, 2016.

DATASHEETS

In this section, we include measured and datasheet-specified technical specifications for several of the key components of the experiments described in this thesis.

Teem Photonics SNG-03E-100 (pump laser)	
wavelength	532 nm
repetition rate	7.2 kHz
pulse width*	0.75 ns
maximum average power	20 mW
maximum peak power*	3.7 kW

Andor iXon Ultra 897 EXF (CCD camera)	
active pixels	512×512
pixel size*	16×16 µm
minimum air-cooled temperature*	−80°C
ADC bits*	16
pixel well depth*	180000 e^-
readout rates*	3, 1, 0.08 MHz
quantum efficiency	0.84 (462 nm), 0.81 (626 nm)

First Sensor PC5-6b TO5 (photodiode)	
active area*	5 mm^2
quantum efficiency*	0.85 (450 nm), 0.85 (650 nm)
junction capacitance*	10 pF (V_r = 20 V, 23°C)
dark current*	0.1 nA (V_r = 20 V, 23°C)
shunt resistance*	600 MΩ
maximum reverse bias*	50 V

Photonic crystal fibers (χ^3 nonlinear gain medium): see tab. 3.1.

*Nominal or inferred value from datasheet.

PUBLICATIONS

In this section, we include publications related to the work of this thesis.

Sub-Poissonian Twin-Beam Correlations at Blue and Red Wavelengths from Four-Wave Mixing

Jason Mueller[1,2], **Alex McMillan**[2], **Paul-Antoine Moreau**[3], **Javier Sabines-Chesterking**[2], **John Rarity**[2], **Peter J. Mosley**[4], **Jonathan Matthews**[2]

[1]*Quantum Engineering Centre for Doctoral Training, Centre for Nanoscience and Quantum Information, University of Bristol, BS8 1FD, United Kingdom*
[2]*Quantum Engineering Technology Labs, H. H. Wills Physics Laboratory and Department of Electrical and Electronic Engineering, University of Bristol, BS8 1FD, United Kingdom*
[3]*School of Physics and Astronomy, University of Glasgow, G12 8QQ, United Kingdom*
[4]*Centre for Photonics and Photonic Materials, Department of Physics, University of Bath, BA2 7AY, United Kingdom*
jason.mueller@bristol.ac.uk

Abstract: We demonstrate sub-Poissonian intensity correlations of twin beams at short wavelengths: 442nm and 665nm. The beams are generated via four-wave mixing in photonic crystal fiber, measured with a CCD camera.

OCIS codes: (270.270) Quantum optics, (120.3940) Metrology, (270.5290) Photon statistics

1. Background

Twin-beam experiments have been used for measuring light intensity [1], absorption imaging [2], and direct absorption measurement [3, 4]. These experiments have all taken place at infrared wavelengths. Here, we pave the way to performing sub-shot-noise-limit (sub-SNL) absorption measurements using twin beams at blue and red wavelengths.

Samples may be characterized by their spectral absorption $\alpha(\lambda)$. This procedure typically involves comparing the intensity of a coherent beam with and without the sample in its path. In the limit of low-light-level illumination, the signal-to-noise ratio of such an absorption measurement is fundamentally limited by the quantum nature of light – the SNL. The noise on an intensity measurement of an ideal laser beam, a coherent state, is governed by Poisson statistics. The SNL limits the precision of an absorption measurement to $\Delta^2\alpha_{cl} = (1-\alpha)/\overline{n}$, where $\Delta^2\alpha_{cl}$ is the variance of the absorption estimate, $\overline{n}$ is the average beam intensity, and $0 \leq \alpha \leq 1$ [4].

Correlated twin beams enable increased absorption estimation precision beyond the SNL of an ideal coherent beam [5]. Such states are generated via momentum- and energy-conserving processes (*e.g.* downconversion or four-wave mixing (FWM)), wherein beams of quantum-correlated intensities are generated. A sample placed in one of the twin beams allows the other to be used as a reference for the number of photons generated. In an ideal lossless case, uncertainty on the probe beam intensity becomes binomially distributed, as either a probe photon was absorbed or not, compared to the reference beam. The variance for this absorption measurement is $\Delta^2\alpha_q = \alpha(1-\alpha)/n$, where n is the beam intensity. Compared to the classical version of this measurement, we see a factor of α improvement in measurement precision.

In practice, the degree of correlation of twin beams is degraded by loss. The intensity correlation is given by the beams' correlation factor $\sigma = \Delta^2(n_1 - n_2)/(\overline{n_1} + \overline{n_2})$. For two independent coherent beams limited by Poisson statistics, we have $\sigma = 1$. For $\sigma < 1$, we necessarily have quantum-correlated twin beams exhibiting sub-Poissonian statistics. Optimized absorption estimators which account for loss and classical intensity fluctuations allow for sub-SNL absorption measurements when $\sigma < 1$, assuming balanced detection [3].

2. Current Work and Results

Fig. 1(a) shows our current experimental setup for generating and measuring correlated twin beams produced via FWM. Photonic crystal fiber (PCF) was used as the FWM medium. The signal and idler frequency modes are unpopulated at the fiber input, and grow initially through spontaneous FWM. Due to the high peak power of the laser, photon pairs generated near the fiber input stimulate further FWM, leading to exponential FWM gain and bright intensity-correlated twin beams. The PCF has a core diameter and hole-to-pitch ratio of approximately 2.5μm and 0.95, respectively. The dispersion of the fiber allows for intermodal phase-matching of the 532nm pump to signal and idler wavelengths of 442nm and 665nm, where the blue beam of interest is in the fundamental guided mode [6].

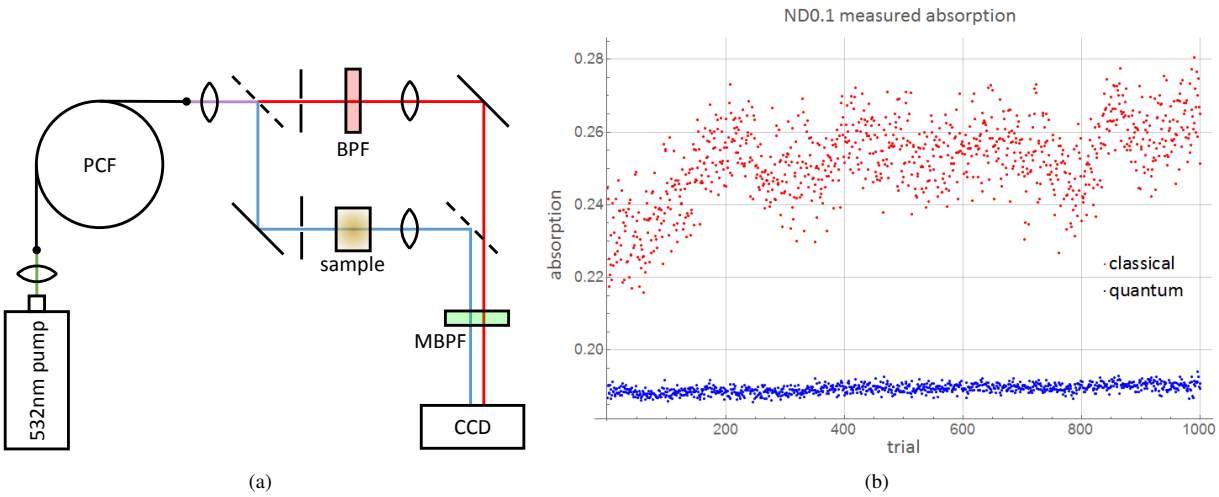

(a) (b)

Fig. 1. (a) Our experimental setup for performing sub-SNL absorption measurements. The sample may be placed in either arm before focusing the beam to a CCD camera. BPF: bandpass filter; MBPF: multi-bandpass filter. (b) Experimental results measuring the absorption of a 0.1 OD neutral density filter, comparing classical and quantum absorption estimators.

Our pump is a 5kHz repetition rate, 1ns pulse width, 1064nm laser (Teem Photonics SNP-08E-100), which has been frequency doubled with an external, temperature-tuned LBO crystal. Spectral filtering is used after the PCF to remove uncorrelated noise photons, primarily Raman-scattered pump light and any remaining pump. We measure the beams simultaneously with a high-efficiency commercial CCD camera (Andor iXon Ultra 897) operating without electron multiplication, set to an integration time of 0.05s. We account for all detected photons in both beams without post selection. At 21pW of FWM power, we measure $\sigma = 0.41 \pm 0.12$, suitable for sub-SNL absorption measurements. The results of such an absorption measurement are shown in Fig. 1(b), comparing using only one arm of the twin beams (classical), to harnessing the quantum correlations of the signal and idler pairs (quantum). We see a 104-fold precision improvement using the quantum correlations for a classically noisy data set with unbalanced detection, measuring the absorption of a 0.1 optical density (OD) attenuator. The large correlation uncertainty and the discrepancy in the mean absorption are due to large classical intensity fluctuations of the laser, which are not accounted for by the classical estimator in the case of Fig. 1(b). Preliminary results show that by monitoring the pump beam as well as the FWM, we are able to account for classical fluctuations and have reduced the correlation factor from 0.91 ± 0.48 to 0.77 ± 0.27 in one example data set.

We have demonstrated sub-Poissonian intensity correlations of twin beams at 442nm and 665nm. Increasing the variety of wavelengths at which quantum light can be generated widens application of correlated photon-pair spectroscopy and twin-beam imaging. Future extensions of this work are to improve the measured correlations with tailor-made silicon photodiodes and to apply the source to bilogically relevant samples.

References

1. A. Heidmann, R. J. Horowicz, S. Reynaud, E. Giacobino, C. Fabre, and G. Camy, Phys. Rev. Lett. **59**, 2555 (1987).
2. G. Brida, M. Genovese, and I. R. Berchera, Nature Photonics **4**, 227230 (2010).
3. P. A. Moreau, J. Sabines-Chesterking, R. Whittaker, S. K. Joshi, P. M. Birchall, A. McMillan, J. G. Rarity, and J. C. F. Matthews, Sci. Rep. **7**, 6256 (2017).
4. R. Whittaker, C. Erven, A. Neville, M. Berry, J. L. O'Brien, H. Cable, and J. C. F. Matthews, New J. Physics **19**, 023013 (2017).
5. E. Jakeman and J. Rarity, Optics Communications **59**, 219 (1986).
6. Y. Chen, W. Wadsworth, and T. Birks, Opt. Lett. **38**, 3747 (2013).

High-Power, Sub-Poissonian Twin-Beam Correlations at Blue and Red Wavelengths from Four-Wave Mixing in Photonic Crystal Fiber

Jason Mueller[1,2], **Alex McMillan**[2], **John Rarity**[1,2], **Peter J. Mosley**[3], **Jonathan Matthews**[2]

1. Quantum Engineering Centre for Doctoral Training, Centre for Nanoscience and Quantum Information, University of Bristol, BS8 1FD, United Kingdom

2. Quantum Engineering Technology Labs, H. H. Wills Physics Laboratory and Department of Electrical and Electronic Engineering, University of Bristol, BS8 1FD, United Kingdom

3. Centre for Photonics and Photonic Materials, Department of Physics, University of Bath, BA2 7AY, United Kingdom

Abstract

We demonstrate sub-Poissonian intensity correlations of twin beams at visible wavelengths. Picowatt beams generated via four-wave mixing in photonic crystal fiber are measured with a CCD camera. Progress towards microwatt demonstration with photodiodes is discussed.

1 Introduction to Sub-Shot-Noise Measurements

Twin-beam sources are enabling tools for high-precision light intensity [1], absorption imaging [2], and direct absorption measurements [3,4]. These experiments typically use infrared wavelengths or few-femtowatt intensities measured with single-photon detectors. For many practical applications, higher powers are desired, as well as access to shorter wavelengths.

Samples may be characterized by their spectral absorption $\alpha(\lambda)$, where the signal-to-noise ratio of a direct absorption measurement is fundamentally limited by the Poissonian quantum nature of light – the SNL. Correlated twin beams enable increased absorption estimation precision beyond the SNL [5]. Such states can be generated via energy-conserving processes (*e.g.* Four-Wave Mixing (FWM)), so a sample placed in one of the twin beams allows the other to be used as an intensity reference. In a lossless case, uncertainty on the probe beam intensity becomes binomially distributed. Compared to the classical version of this measurement, we find a factor of α improvement in measurement precision [4].

In practice, the degree of correlation of twin beams is degraded by loss, where the intensity correlation is given by the beams' correlation factor $\sigma = \Delta^2(n_1 - n_2)/(\overline{n_1} + \overline{n_2})$. For $\sigma < 1$, we necessarily have quantum-correlated twin beams exhibiting sub-Poissonian statistics. Optimized absorption estimators which account for loss and classical intensity fluctuations allow for sub-SNL absorption measurements when $\sigma < 1$ [3,6].

2 Sub-SNL Measurement Scheme

Photonic Crystal Fiber (PCF) was used as the FWM medium. The signal and idler frequency modes are unpopulated at the fiber input, and grow initially through spontaneous FWM. Due to the high peak power of the laser, photon pairs generated near the fiber input stimulate further FWM, leading to exponential FWM gain and bright intensity-correlated twin beams. The PCF has a core diameter and hole-to-pitch ratio of 2.5μm and 0.95, respectively. The dispersion of the fiber allows for intermodal phase-matching of the 532 nm pump to signal and idler wavelengths of 450 nm and 650 nm, in the LP02 and LP11 modes, respectively.

Our pump is a 7 kHz repetition rate, 1 ns pulse width, 532 nm laser (Teem Photonics SNG-03E-100). We measure the generated twin beams simultaneously with a high-efficiency commercial CCD camera (Andor iXon Ultra 897). At 21 pW of FWM power, we measure $\sigma = 0.41 \pm 0.12$, suitable for sub-SNL absorption measurements. We also characterized the system with a fixed 0.1 optical density attenuator, measuring a 104-fold precision improvement using the quantum correlations for a classically noisy data set compared to a direct absorption measurement.

Because the CCD camera saturates near our current working power, we require alternate detection schemes for higher FWM powers which we know are accessible from previous fiber characterization. Current work is on fabricating electronics and characterizing bespoke transimpedance-based silicon photodiode detectors for sub-SNL measurements at microwatts of FWM power using an unbalanced homodyne-detection scheme.

References

[1] A. Heidmann, R. J. Horowicz, S. Reynaud, E. Giacobino, C. Fabre, and G. Camy, Phys. Rev. Lett. **59**, 2555 (1987).

[2] G. Brida, M. Genovese, and I. R. Berchera, Nature Photonics **4**, 227230 (2010).

[3] P. A. Moreau, J. Sabines-Chesterking, R. Whittaker, S. K. Joshi, P. M. Birchall, A. McMillan, J. G. Rarity, and J. C. F. Matthews, Sci. Rep. **7**, 6256 (2017).

[4] R. Whittaker, C. Erven, A. Neville, M. Berry, J. L. O'Brien, H. Cable, and J. C. F. Matthews, New J. Physics **19**, 023013 (2017).

[5] E. Jakeman and J. Rarity, Optics Communications **59**, 219 (1986).

[6] E. Losero, I. Ruo-Berchera, A. Meda, A. Avella, and M. Genovese, Scientific Reports **8**, 7431 (2018)